NASA CR-112202

INFLUENCE OF VIBRATION MODES ON CONTROL SYSTEM STABILIZATION FOR SPACE-SHUTTLE TYPE VEHICLES

By H. G. Greiner

FINAL REPORT
Report No. GDCA-DDE72-005
November 1972

Prepared under Contract No. NAS1-10795 by
CONVAIR AEROSPACE DIVISION OF GENERAL DYNAMICS
San Diego, California
for
NATIONAL AERONAUTICS AND SPACE ADMINISTRATION

INFLUENCE OF VIBRATION MODES ON CONTROL SYSTEM STABILIZATION FOR SPACE-SHUTTLE TYPE VEHICLES

By H. G. Greiner

Report No. GDCA-DDE72-005

Prepared under Contract No. NAS1-10795 by
CONVAIR AEROSPACE DIVISION OF GENERAL DYNAMICS
San Diego, California

for

NATIONAL AERONAUTICS AND SPACE ADMINISTRATION

CONTENTS

FIGURES

INFLUENCE OF VIBRATION MODES ON CONTROL SYSTEM STABILIZATION FOR SPACE-SHUTTLE TYPE VEHICLES

By H. G. Greiner

1 SUMMARY

An investigation was made to determine the feasibility of using conventional autopilot techniques to stabilize the vibration modes at the liftoff flight condition for two different space shuttle configurations. The objective was to determine if these conventional techniques would still be adequate to stabilize the elastic modes for these configurations, which have greater modal density and asymmetry than any previous launch vehicle. One configuration is called the dual flyback vehicle in which both the orbiter and booster vehicles have wings and complete flyback capability. The other configuration is called the solid motor vehicle in which only the orbiter has flyback capability. This latter vehicle consists of four elements: two strap-on solid motors, an external liquid propellant tank and the winged orbiter. The results of the linear stability analyses for each of these vehicles are summarized below.

Dual Flyback Vehicle

Adequate stability margins were provided for all parasitic modes (propellant sloshing and elastic vehicle) at the liftoff flight condition. Considerable latitude was available to establish satisfactory control mode (rigid body) response characteristics. The propellant sloshing modes exhibited small positive damping, but indications were that they would become less stable with increasing flight time. Essentially their stability properties were similar to those that have been witnessed on current operational launch vehicles.

Satisfactory elastic mode stability margins were obtained for the symmetric mode case when the autopilot pitch control plane was configured with the rate sensor located aft of the first body mode antinodes. The forward rate sensor configuration, including the autopilot compensation required to stabilize the first body modes, exhibited one slightly unstable elastic mode. However, indications were that with careful attention to actuator system design, the required stability margins could be provided for this mode.

A two-rate-sensor (forward and aft) configuration also resulted in satisfactory stability margins for all of the elastic modes. This concept would permit a dominant

aft rate sensor configuration early in flight, switching to a dominant forward rate sensor configuration for later flight times when the modal stability with the aft rate sensor typically becomes marginal.

In the antisymmetric mode case, the autopilot yaw control plane exhibited satisfactory stability margins for both the aft rate sensor configuration and the forward rate sensor configuration, with the appropriate first body mode stability compensation included in the latter. The roll control plane was also satisfactorily configured with either a forward or aft mounted rate sensor. Coupling between the yaw and roll autopilot channels was small, with the result that elastic modes in the coupled system exhibited adequate stability margins.

The autopilot configurations that provided satisfactory stability margins were not found to be unusually sensitive to variations in the elastic mode natural frequencies. Only small adjustments in the stability compensation were required to cope with these frequency changes.

It was found that local structural deformations at the autopilot sensor locations, particularly the rate sensor, could significantly alter the stability characteristics that were obtained from equivalent centerline type modal data. This condition was briefly examined in the roll autopilot control plane using the three-dimensional booster antisymmetric mode shapes.

Two anticipated stability problems at the liftoff flight time did not materialize for this vehicle. Negligible coupling was evidenced between the control mode, the propellant sloshing modes, and the lowest frequency elastic modes. Also, the elastic mode frequency density did not appear to be as important a factor as originally anticiplated.

Solid Motor Vehicle

With the exception of the yaw/roll coupled system, positive stability was demonstrated for all parasitic modes at the liftoff flight condition. However, the stability margins for some of the elastic modes were not satisfactory.

The relatively small control thrust available from the orbiter engines required high autopilot gains to obtain satisfactory control mode (rigid body) response characteristics. Propellant sloshing stability was not a factor in this analysis because of the very small sloshing masses relative to the total vehicle mass (less than 1 percent for the oxidizer and 1/2 percent for the fuel). The most dominant sloshing mode was the oxidizer mode, and it assumed a stable root locus configuration that was not

significantly influenced by any of the other oscillatory modes or by the autopilot elastic mode stability compensation that was investigated.

The mode shapes exhibited a high degree of interaction between the vehicle elements through the links that join these elements together. The modal data from these mode shapes, together with the high autopilot gains, produced stability compensation requirements which, in many cases, were not practical with conventional autopilot techniques.

For the symmetric mode case the first orbiter body modes (elastic modes exhibiting classic first mode shape on orbiter) could not be stabilized for either forward- or aft-mounted rate sensors on the orbiter vehicle. The extremely high modal gain in the forward rate sensor case was incompatible with conventional compensation techniques. The aft rate sensor case showed some promise since it exhibited a negative damping ratio of only 2 percent. However, the high modal gain and the opposing nature of the loci from two adjacent open-loop poles made stability compensation relatively ineffective. A brief attempt to stabilize this aft rate sensor configuration by selected variation of mode frequencies produced only a marginally stable condition. Finally the two-rate-sensor configuration was employed, and the results indicated that all elastic modes could be stabilized. This configuration exhibited the greatest potential for providing adequate stability margins for these elastic modes. The stabilizing of these first body modes was significantly complicated by the location of the "tail-wags-dog" frequency in the midst of these first-mode frequencies.

Autopilot sensor locations on the external tank and the solid rocket motors were also investigated. The results exhibited unstable modes that were not amenable to conventional compensation techniques in all cases.

The effect of increasing the control forces was briefly investigated by adding a thrust vector control system to the solid motor rockets. The resulting reduction in the autopilot forward loop gain significantly reduced the elastic modal gains and improved the system stability for the case where the autopilot sensors were located on the orbiter. However, the stability complication posed by the location of the "tail-wags-dog" zero was not appreciably reduced.

In the antisymmetric mode case, all elastic modes were stable for the autopilot yaw control plane with an aft rate sensor located on either the orbiter or the external tank. For the autopilot roll control plane, stable elastic modes resulted with an aft attitude sensor located on either the orbiter or the external tank and an aft rate sensor located on the external tank. However, for considerations similar to those encountered in the symmetric mode case, none of these stable configurations provided satisfactory margins of stability.

Although the stable planar autopilot configurations were used, the yaw/roll coupled system exhibited unstable elastic mode properties. The analysis results indicated that there was significant coupling through the yaw attitude control system and that this coupling was detrimental to system stability.

2 INTRODUCTION

The objective of this study was to conduct a preliminary investigation of the feasibility of using conventional control system techniques to stabilize the vibration modes at the liftoff flight condition for space-shuttle type vehicles. Two quite different space shuttle concepts were considered, both having greater modal density and asymmetry than any previous launch vehicle. They were: 1) a piggy-back configuration with both the booster and the orbiter vehicles having complete fly-back capability, and 2) a strap-on solid motor configuration in which only the orbiter vehicle has fly-back capability. In this report the first configuration is referred to as the dual flyback vehicle, and the second is called the solid motor vehicle.

The study was divided into three parts. Part one derived the perturbational equations that were used in the stability analyses. Part two generated a consistent set of basic data for each of the study configurations. Part three performed the "time slice" stability analyses for each of the vehicles at the liftoff flight condition.

The stability analyses for each vehicle were divided into two parts, which reflected the constraints that were applied to the elastic modal data. The first part considered elastic modal data subject to symmetric vehicle boundary conditions, and the second part used elastic modal data subject to antisymmetric vehicle boundary conditions. In terms of the vehicle attitude control system, the first part included the pitch control plane, and the second part included the yaw and roll control planes. Where practical, variations in parasitic mode (propellant sloshing and elastic vehicle) natural frequencies and damping ratios were considered for their effect on the conventional autopilot parameters.

The basic data used in the dual flyback vehicle analyses were obtained from the final results of an earlier space shuttle study. The solid motor vehicle basic data were primarily obtained from a follow-on to this study. However, due to the timing between the progress of this autopilot study and the advent of the solid motor vehicle concept, these data are not as refined as the data applicable to the dual flyback vehicle. This was particularly true for the critical elastic vehicle models. Thus, it was not considered appropriate at this time to conduct as detailed an analysis for this vehicle as was conducted for the dual flyback vehicle. Instead, the solid motor vehicle analysis attempted to illuminate the most important considerations in applying conventional control system techniques to this vehicle.

As stated earlier, this study considered two vehicle configurations representing two quite different space shuttle concepts. The first configuration was the piggy-back

delta wing vehicle shown in Figure 1. Both the booster and orbiter vehicles have independent flyback capability. During the ascent flight phase, all forward thrust and all control is accomplished with the booster. Forward thrust is obtained from the booster's twelve 2,446,000N (550,000 lb) thrust liquid oxygen/liquid hydrogen rocket engines.

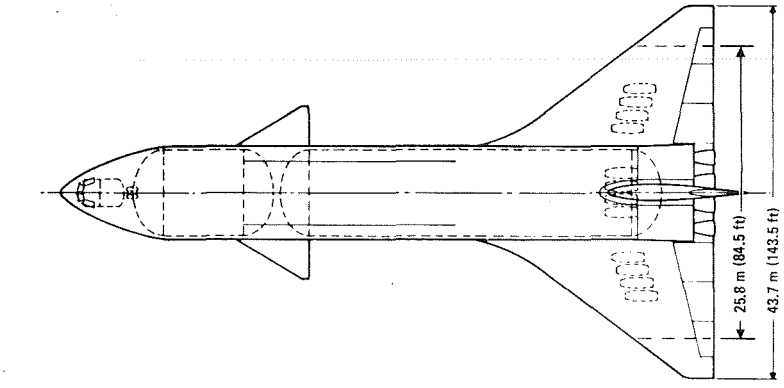

WEIGHT	kg	(lb)
BOOSTER-LIFTOFF	1,900,000	(4,188,000)
ASCENT PROPELLANT	1,534,000	(3,382,000)
CRUISE PROPELLANT (JP)	65,300	(144,000)
LANDING	298,500	(658,000)
AREA	m^2	(ft^2)
EXPOSED WING	469	(5,047)
EXPOSED CANARD	47	(504)
VERTICAL TAIL	139	(1,500)

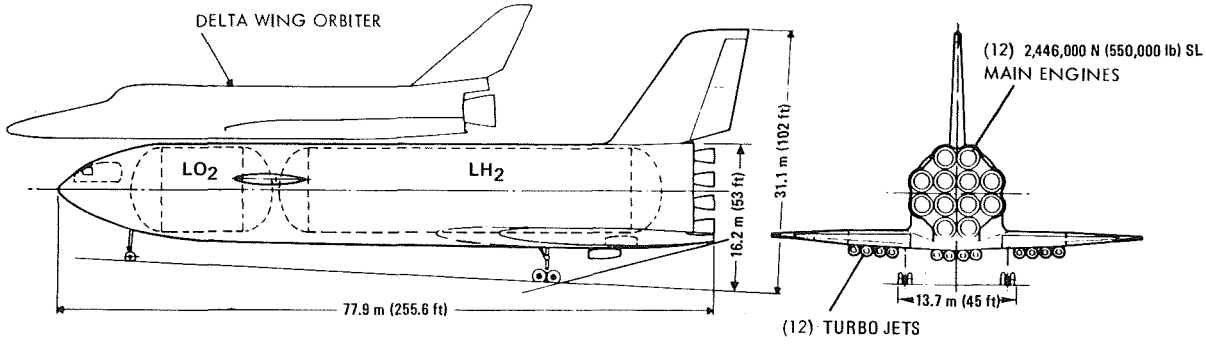

Figure 1. Dual Flyback Vehicle

The size of the booster body is primarily a function of the amount of liquid propellants required to satisfy the mission profiles. This particular configuration contains two 10 M (33 ft) diameter tanks. The forward tank contains the liquid oxygen, and it has a capacity of 1160 M^3 (41,000 ft^3). The liquid hydrogen is contained in the aft tank, which has a volume of 3400 M^3 (120,200 ft^3).

During the ascent flight phase vehicle control is accomplished by gimballing the booster rocket engines. All twelve engines are gimballed in both the pitch and yaw control planes. For roll control all twelve engines are differentially gimballed in both pitch and yaw. This maximum roll control thrust capability is required by the high degree of aerodynamic yaw/roll coupling exhibited by these piggy-back configurations.

The second configuration was the piggy-back solid motor vehicle shown in Figure 2. For this vehicle, only the orbiter has independent flyback capability. Forward thrust is obtained from the two 3.96 M (156 in.) solid rocket motors, each providing 12,450,000 N (2,800,000 lb) of thrust and the three 1,650,000 N (370,000 lb) thrust liquid propellant main orbiter engines.

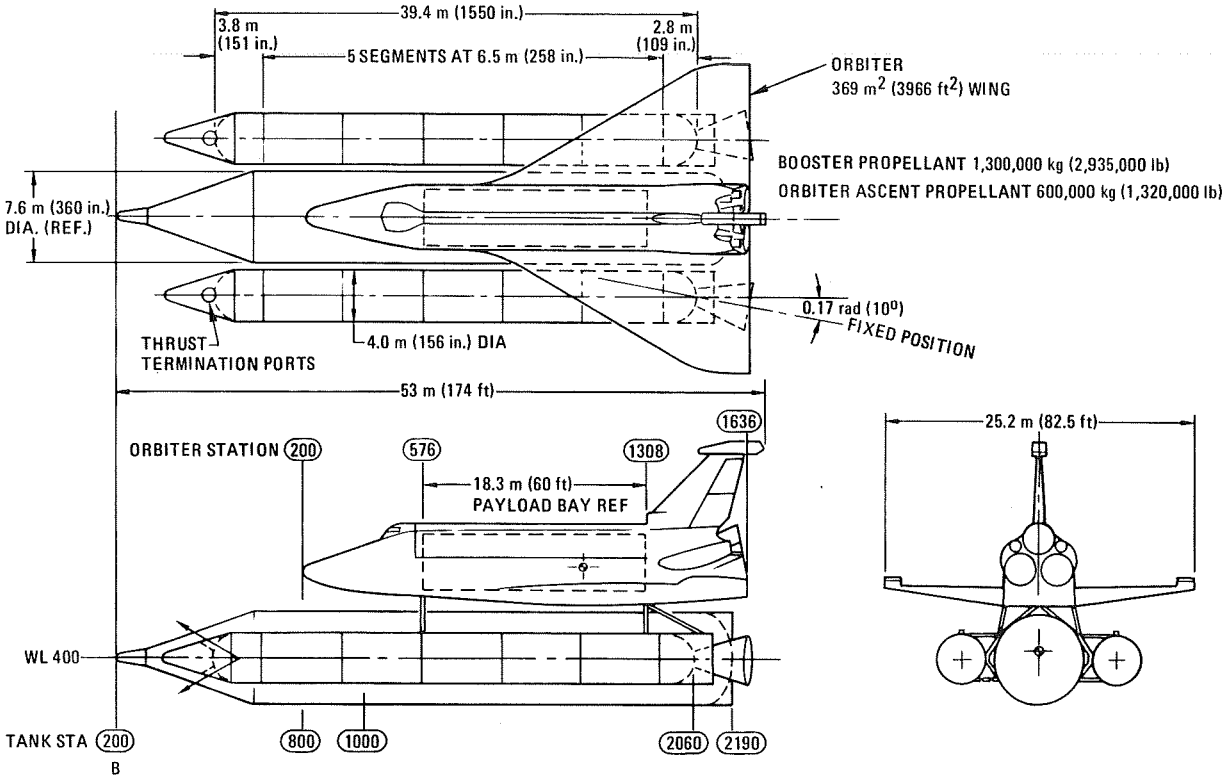

Figure 2. Solid Motor Vehicle

The orbiter external propellant tank contains two 7.62 M (25 ft) diameter tanks. The forward liquid oxygen tank has a volume of 462 M^3 (16,300 ft^3), and the aft liquid hydrogen tank volume is 1320 M^3 (46,500 ft^3).

The study mainly concentrated on using only the three main orbiter engines for vehicle control. This is certainly the desired approach from both cost and weight considerations. All three engines are gimballed for pitch and yaw control, but only the two engines that are symmetrically located relative to the vehicle's pitch plane are differentially gimballed in pitch for roll control.

Another control configuration for this vehicle uses thrust vector control of the solid motors in conjunction with the main orbiter engines. This study considered secondary injection TVC for the solid motors. Aerodynamic surfaces were not considered because of their ineffectiveness at the liftoff flight condition.

3 ANALYSIS PROCEDURE

This study constitutes a linear analysis of the influence of the launch vehicle vibration modes on overall vehicle stability. Nonlinearities and nonlinear effects are not included in the dynamic models, nor in the interpretations of the study results unless specifically stated to the contrary.

The first part of this section describes a conventional autopilot and the particular model that is used in this study. The major features of the dynamic models are discussed briefly in the second part. The third part contains a discussion of conventional autopilot design considerations with particular emphasis on parasitic mode stability. This part presents the background for the results discussed in the next two sections. The discussion in the third part and the results of the study are presented in terms of the root locus analysis method. A brief description of this technique is contained in Appendix E.

Conventional Autopilot

The word "conventional" refers to non-adaptive autopilots having proportional plus derivative feedback. These control systems are comprised of independent control channels, one each for the pitch, yaw, and roll control axes. A functional control channel for a conventional autopilot is shown schematically in Figure 3.

The primary feedback loop for this vehicle attitude control system is through the attitude sensor (displacement gyro or platform). The attitude sensor produces a signal proportional to the angular difference between the instantaneous vehicle attitude and the desired vehicle attitude. This error signal is then used to displace the thrust chambers and cause the vehicle to change attitude in a direction that nulls the error signal. Vehicle guidance steering is effected by changing the desired vehicle attitude.

To obtain the required rigid body stability and response characteristics, lead compensation is incorporated through a rate feedback loop. The signals proportional to the vehicle rotational rates are provided by the rate sensors, one for each control axis.

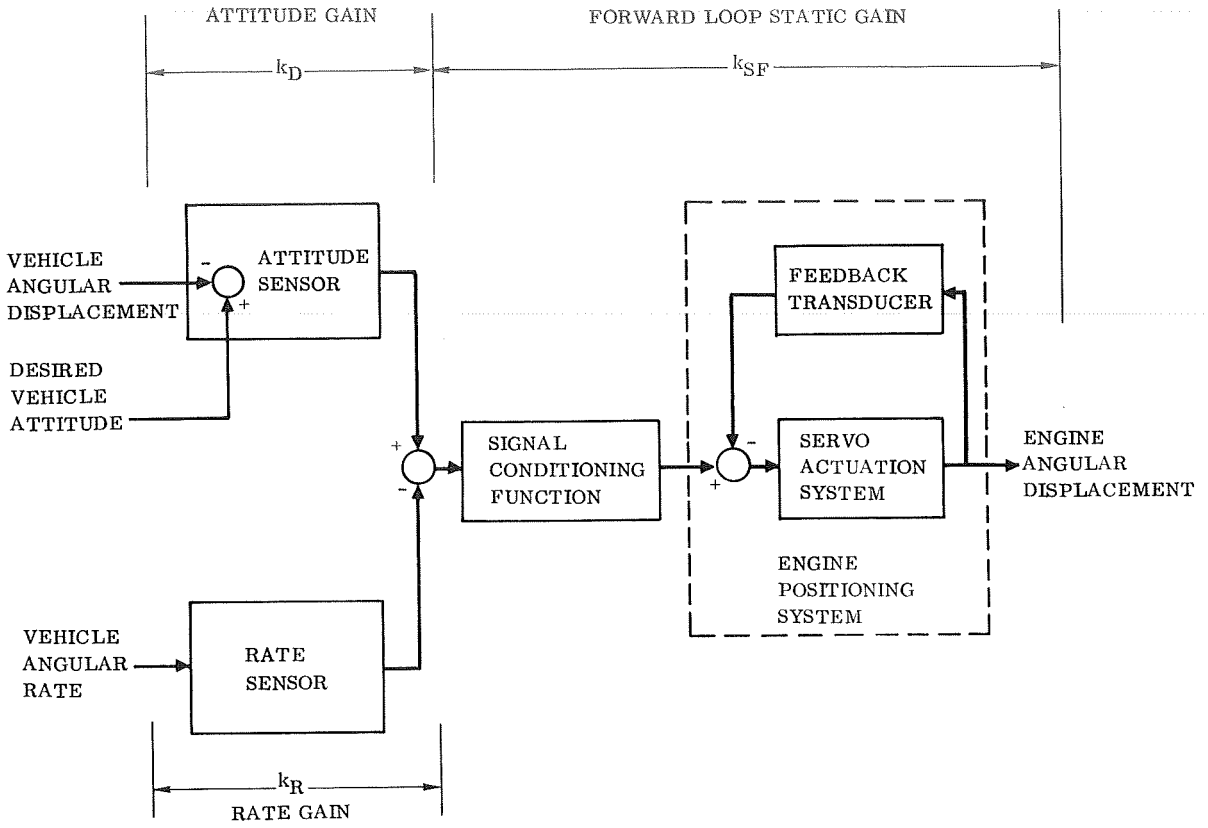

Figure 3. Conventional Autopilot Schematic

The total system error signal is the sum of the attitude reference error signal and the rate signal. This total error signal is sent through a conditioning function before being applied to the engine positioning system. The primary purpose of the conditioning function is to provide additional stability compensation, as may be required, to prevent the buildup of oscillations in the autopilot loop that would otherwise occur from the coupling of parasitic modes into the control system rate and attitude sensors. Another purpose is to provide a signal that is approximately proportional to the time integral of the attitude reference error signal. This integral signal maintains the attitude error signal at null in the presence of steady-state torques (i.e., eliminates the need for the vehicle to be "tilted" to compensate these steady-state torques). However, this function can be satisfactorily supplied by guidance in some instances. Part or all of this conditioning function could also be accomplished in each of the feedback loops forward of the sensor summing junction.

The conditioned error signal is then fed to the engine positioning system, a secondary position feedback control system. This system causes the actual angular displacement of the vehicle's control thrust chambers.

The schematic in Figure 3 can be evolved into the single channel feedback control system block diagram that is used in the stability analysis. This block diagram is shown in Figure 4. The relationship between the autopilot gains in the two diagrams is defined as follows.

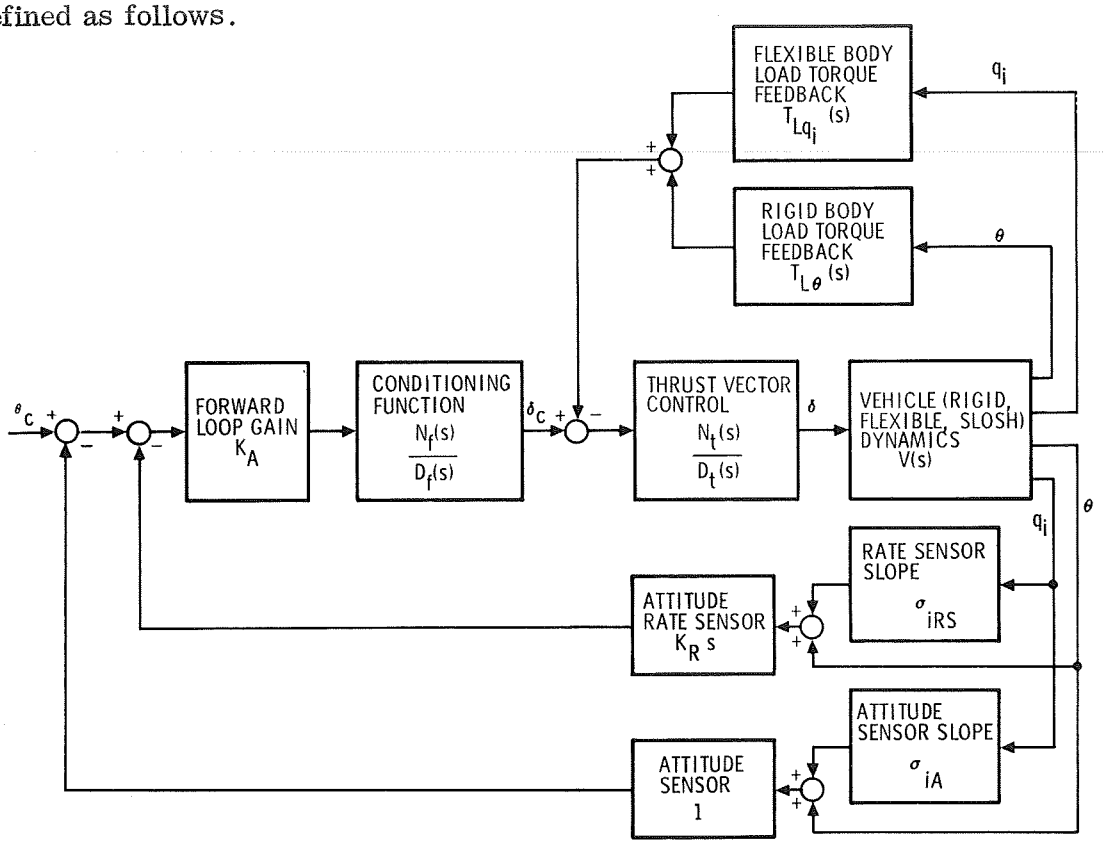

Figure 4. Attitude Control System Block Diagram

Forward loop gain (end-to-end attitude gain):

$$K_A = k_D\, k_{SF}\, \frac{\text{rad. engine displacement}}{\text{rad. attitude sensor input}}$$

End-to-end rate gain:

$$K_A\, K_R = k_R\, k_{SF}\, \frac{\text{rad. engine displacement}}{\frac{\text{rad}}{\text{sec}}\ \text{rate sensor input}}$$

K_R can now be determined in terms of the functional schematic gains as:

$$K_R = \frac{K_A\, K_R}{K_A} = \frac{k_R\, k_{SF}}{k_D\, k_{SF}} = \frac{k_R}{k_D}\ \text{sec}$$

Thus, K_R is the rate-to-attitude gain ratio. This technique for expressing the block diagram gains enables the system rate gain dependence to be handled as an equivalent lead filter.

The conditioning function contains stabilization filters whose principal function is to stabilize the higher frequency parasitic modes; viz., the elastic (bending) modes. A secondary function is to attenuate high frequency signals; this function aids in noise suppression. The integration function is not included for the purposes of this study, since it will have little effect on the parasitic modes.

The rate sensor (rate gyro) dynamic properties can be modeled by a quadratic lag function. The natural frequency for a typical rate gyro is 160 rad/sec with a damping ratio of greater than 0.4. These dynamic properties will have an effect on only the higher frequency elastic modes, and they have not been included in the autopilot model. However, if they prove to be significant, these effects can be considered in evaluating the analysis results. The attitude sensor dynamic properties are not significant in the range of frequencies considered in this study.

Analysis Models

This section discusses the general features of the mathematical models used in this analysis. A detailed description of each of these models and the complete equations of motion are contained in the appendices.

For stability studies, the dependent variables are small perturbational quantities. The measured variables can be considered to consist of two parts, a steady-state component that varies slowly as a function of time and a perturbational component that varies relatively rapidly at frequencies corresponding to the various modes of oscillation of the launch vehicle. These latter quantities are the subject of interest in dynamic stability studies.

Since the symmetry of these launch vehicles corresponds to that of an airplane, the equations of motion follow closely the standard development used for aircraft dynamic analysis. The longitudinal set of equations describes the motion in the plane of symmetry, and the lateral equations describe the motion out of this plane. In the stability analysis these two sets of equations are considered to be uncoupled from each other. The equations are linearized by neglecting the products of perturbation variables, using the small-angle approximation for trigonometric functions, and setting the Euler angle rates equal to the body rates.

Elastic vehicle model. - Since the vehicle elastic modes are orthogonal, coupling appears only through the external forces. In the elastic models the engine masses have been lumped into the mass of the thrust structure. Thus, the only engine inertia terms included in the equations of motion are those associated with the engine gimbal angle variable. For all of the elastic modes, the damping ratio used in the equations is a relatively conservative value of one-half per cent.

The distributed aerodynamic properties are not included in the bending mode generalized forces. The small value of dynamic pressure at liftoff indicates that these aerodynamic forces are negligible relative to the TVC system and engine inertia forces. Generally, the effect of the aerodynamic terms on the bending mode stability is to slightly increase the effective modal damping and decrease the mode frequency. However, they may be destabilizing to "interconnect" modes in a piggyback configuration at later flight times.

Two sets of modes were generated for each vehicle, reflecting the vehicle symmetry. The symmetric set portrays the elastic vehicle characteristics in the plane of symmetry, and the antisymmetric set describes these characteristics out of the plane of symmetry.

Propellant sloshing model. - The spring-mass and pendulum analogies are widely used to describe the dynamic characteristics of propellant sloshing. For present operational launch vehicles the "mechanical" parameters that are used in these models are derived from the solution of the hydrodynamic equations. This solution assumes that the tank is axisymmetric in shape, the vehicle center of mass lies on the tank centerline, and the vehicle acceleration vector is aligned with this centerline. It is these latter two assumptions which are not directly applicable to the space shuttle configurations.

A recent study (Ref. 1) investigated the effects of acceleration vector "tilt" relative to the tank centerline under one-g conditions. The results of this study indicate that the axisymmetric model parameters are valid in cylindrical tanks for "tilt" angles of approximately 0.087 rad (5 deg) and fluid levels with a greater than one height-to-diameter ratio. These conditions approximate the liftoff conditions for the shuttle vehicles.

Based upon these results and the relatively small center-of-mass offsets at liftoff, the axisymmetric propellant slosh models are considered to be adequate at this time of flight. The pendulum analogy is used in these stability analyses for the dual flyback vehicle booster propellant tanks and for the solid motor vehicle orbiter external tanks. Propellant sloshing is not considered in the dual flyback vehicle orbiter

propellant tanks because these tanks are "full" throughout the ascent flight phase (i.e., the slosh masses are negligible).

Only the first lateral slosh modes are considered in this study. This mode has the lowest frequency, the least inherent fluid damping, and the greatest effective mass of moving fluid. The masses associated with the second and higher slosh modes for these shuttle configuration tanks are only a few per cent of the first mode mass for all fluid levels except the near empty condition.

Thrust vector control system models. — Equivalent lumped parameter engines and actuators are used to generate the pitch and yaw control forces. These equivalent engines are located on the appropriate vehicle centerline. Roll control forces for the dual flyback vehicle are modeled by an equivalent force couple centered about the booster centerline. This force couple is generated by multiplying the total booster thrust by a derived moment arm such that the control moment is equivalent to that obtained from gimballing all twelve booster engines differentially in both pitch and yaw. Since roll control forces for the solid motor vehicle are obtained by differentially gimballing two orbiter engines in pitch, this model is straightforward.

A third-order actuator model is used in all three control channels. This model has a closed loop resonant frequency, at load, of 50 rad/sec and a damping ratio of three tenths. The servo resonant frequency is 70 radians per second and the servo loop gain is 13 sec^{-1}. These model parameters are based on the requirements that were generated in earlier space shuttle studies.

Conventional Autopilot Design Considerations

The control function of the flight control system provides acceptable stability and control throughout flight of the launch vehicle. In this respect, the terms stability and control take on different connotations. Control implies the ability of the vehicle to execute steering commands generated by guidance and programmed steering and, having executed these commands, to maintain the desired trajectory in the presence of external disturbances. Stability, on the other hand, relates to the stabilization of the "parasitic" modes. The "parasitic" modes, e.g., the propellant sloshing and the elastic modes, arise from the many resonances caused by the physical properties of the launch vehicle. The stability function of the control system is to prevent parasitic modal oscillations from passing through the control channel with amplification and phasing that would cause the oscillation to be sustained or to diverge. It is this stability function that is of primary concern in this study.

The autopilot gains, K_A and K_R, are primarily determined by the desired control mode parameters: rigid body frequency and damping ratio. The desired rigid body control response is dominated by the need for minimal (within practicable limits) dynamic overshoot in response to atmospheric disturbances. It is axiomatic in control theory that minimal response to disturbances is achieved with high gains and bandwidth in the feedback and compensation signal paths. Unfortunately, this is incompatible with the lightly damped structural modes and an acceptable compromise must be worked out.

The control mode response is considered in this study only for the purpose of obtaining "reasonable" autopilot gains with which to evaluate the stability of the parasitic modes. No effort is made to optimize this response. Since increasing gain, specifically the product of K_A and K_R, is generally destabilizing to these parasitic modes, the smallest acceptable values are of particular interest. For this purpose a rigid body response with a damped frequency of approximately 1 to 1.5 rad/sec and a damping ratio of between 0.3 and 0.4 is used as a guide. It should be kept in mind, though, that it may be necessary to increase these gains to obtain a "tighter" response during the higher dynamic pressure region of flight.

The principal concern during the liftoff flight condition is the stability of the higher-frequency parasitic modes associated with airframe flexibility. These modes of oscillation manifest themselves as a series of lightly damped poles and zeros in the transfer function representing vehicle dynamics.

The response of the launch vehicle at high frequencies is usually dominated by the lowest-frequency flexible modes as these have the least inherent damping, the greatest gain through the flight control system, and are the closest in frequency to the atmospheric disturbances that are the potential source of their excitation. Vehicle vibration in one or more of these modes contributes to the bending moment experienced by the vehicle and constitutes a significant contribution to the total vehicle loads, especially for the largest class of launch vehicles where the excitation is greatest. For these reasons the stabilization of these modes is usually achieved by ensuring that the phase of the parasitic signal picked up by the system sensors will not cause regenerative oscillations. In other words, the locus emanating from the elastic mode pole is forced to depart into the left-half plane. It is even possible to phase this signal such that the thrust vector deflection acts to stabilize the oscillation; the closed-loop flexible mode root will have greater damping than the open-loop pole, having a beneficial effect on the vehicle loads.

The higher-frequency flexible modes, by contrast, have greater inherent damping, contribute less to the vehicle loads, and have less gain through the flight control system loop. These modes are gain stabilized as opposed to the phase stabilization of the lower modes; the bending oscillations are decoupled from the flight control system by high

attenuation at these higher bending frequencies. For these modes the closed-loop root will always be in the left-half plane for all phase orientations. In addition, the precision of the modal data at the higher modal frequencies makes reliance on phase stabilization speculative; the uncertainties in the mathematical model are too great.

Those flexible modes in the range of the engine position servo resonance are a special case. There may be sufficient friction in the engine gimbal to ensure satisfactory stability. If not, then these modes must be examined closely with the possibility in mind of modifying the position servo transfer function itself to obtain the required degree of stability. In particular the load torques become quite important.

An important elastic mode stability consideration is the frequency of the so-called "tail-wags-dog" zero (TWD). This is the frequency at which the lateral force at the gimbal axis due to thrust forces is exactly balanced by the inertial force of thrust chamber motion. Below this frequency the thrust forces are dominant and above it the engine inertia forces are dominant.* The significance of this zero for elastic stability is that the locus departure angle from an elastic pole undergoes a 180-degree phase shift when the pole passes through this frequency. This makes phase stabilization of a mode whose open-loop pole frequency is very near the TWD zero highly impractical.

The gain and phase of an elastic mode locus is strongly dependent upon the modal slopes at the attitude and rate sensor locations. Therefore, the choice of sensor location will have considerable influence on the stability properties of the flight control system. This situation will be illustrated by considering only the first body bending mode. The pole-zero plot for this configuration is shown in Figure 5. The first diagram shows the effect of rate and attitude sensors (located at the same point) being slightly aft of the first mode antinode. For this position the modal slope at the sensor location will have the same sign as the slope at the engine gimbal point. In the second diagram the sensors are slightly forward of the antinode and the sensor modal slope has the opposite sign to the slope at the engine gimbal point. Root locus departure angles (the direction in which the root locus emanates from the bending pole) are shown assuming flat (zero phase shift) autopilot response. The aft location results in inherently stable operation for the bending root; vice versa for the forward location. Additional phase lag due to the engine position servo, sensor dynamics, and autopilot filtering (all desirable since phase lag implies attenuation of the high-frequency bending modes) will cause the direction of departure to rotate clockwise. This benefits the situation shown

*The frequency of the TWD zero can be determined approximately by using the expression

$$\omega_{TWD} = \sqrt{\frac{Tc}{M_R \ell_R}} \quad \frac{rad}{sec}$$

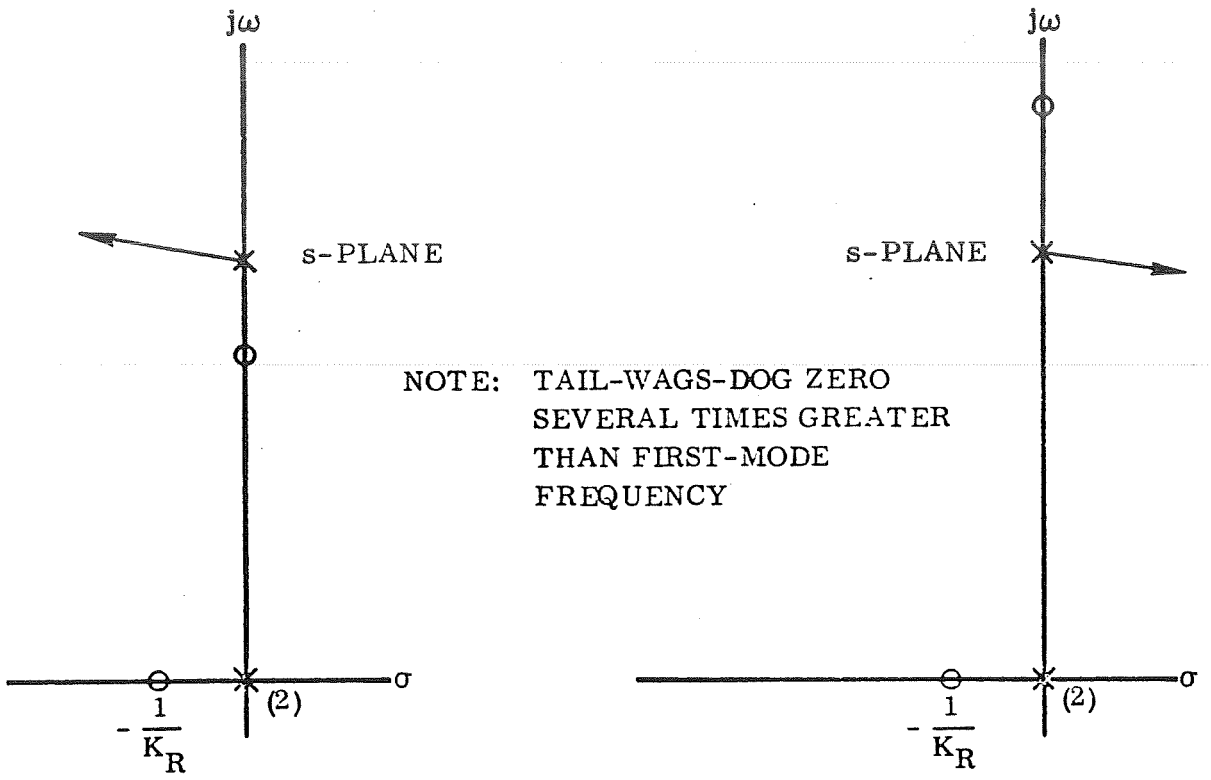

a. Rate and Position Sensors Aft of Antinode

b. Rate and Position Sensors Forward of Antinode

Figure 5. Change in Root Locus Departure Angles with Sensor Location, First Bending Mode

in the second diagram and deteriorates the first. Further, the modal frequency increases with flight time, meaning increasing amounts of phase lag at the bending frequency. A choice of configurations results. One can choose an aft location with minimal autopilot lag, in which case the critical flight time is toward the end of a particular stage of flight (the locus tends to depart upward, a marginal situation if there is some uncertainty in modal frequency). The other choice is a forward location with sufficient lag for stabilization at the beginning of a particular stage of flight (the locus departs more or less downward, increasing the modal stability as the flight progresses). The aft location implies minimal system lag and attenuation, good for the low (rigid body and propellant slosh) frequencies, bad for the high (higher bending) frequencies. The forward choice of sensor location implies the reverse. The higher-frequency modes may enjoy considerable stability margin and closed-loop modal damping while the rigid body and propellant slosh stability suffers. One may be forced into the complication of a simultaneous switch from one sensor location and filter configuration to another part way through a particular stage of flight. If the frequency of this mode is above the TWD frequency, then the two diagrams in Figure 5 must be reversed and the corresponding changes made to the discussion in this paragraph. Also, it is clear that the 180-degree phase shift upon passing through the antinode makes a sensor location too close to this antinode impractical.

A second and more general situation is to have the rate and attitude sensors at different locations on the vehicle. The location of the attitude sensor is usually dictated by physical considerations, particularly if it is the inertial platform of the launch vehicle attitude control system. However, the rate sensor is not subject to these same considerations, and its compactness permits moving it to numerous other locations on the vehicle.

Assuming essentially sinusoidal inputs, the rate sensor signal can be thought of as being $[K_R\ \omega_B\ (\sigma_{RS}/\sigma_A)]$ times as large as the attitude sensor signal (σ_{RS} and σ_A are modal slopes at the rate and attitude sensor locations and ω_B is the frequency of a particular elastic mode). Thus, the influence of the attitude sensor location on the system stability is generally, but not always, relatively small. Under these conditions the remarks in this section concerning sensor locations and locus departure angles apply primarily to the rate sensor. Therefore, the different sensor locations could become necessary if the modal slope at the attitude sensor location was not compatible with elastic mode stability considerations.

Another possibility is that of using two rate sensors, the so-called "gyro mixing" technique for stabilization of bending modes. This offers an additional degree of freedom to the control engineer as the two rate gains can be scheduled to hold a fixed equivalent gain, phase, or some combination of both at bending frequencies. This solution might also be feasible in those situations where it is physically inconvenient to locate a single gyro, for example in a location that suffers from high local levels of vibration. And finally, it may be possible to phase stabilize two body bending modes at once (e. g., 1st and 2nd body modes), which is generally beyond the capabilities of a single rate sensor at all flight times. Although this is not generally considered to be a conventional autopilot configuration, it is briefly considered in this study.

The choice of autopilot filter is made in concert with the choice of sensor location. The objective is to provide proper phase shift at the frequencies of the bending modes being phase stabilized while maximizing attenuation at high frequencies and minimizing the phase lag at low (below first mode) frequencies. What constitutes proper phase shift at bending frequencies depends on the phase margins desired, which in turn ultimately depends on modal accuracy and hardware tolerance assessments. Requirements for 30 degrees of phase margin and 6 db of gain margin have been used successfully on Atlas-type launch vehicles.

Generally, the stability of the propellant sloshing parasitic modes is not a major concern during the liftoff flight condition. Primarily, this is due to the small sloshing masses relative to the total vehicle mass (less than 10 percent) and the low value of vehicle total acceleration at this time of flight. The result is a very low level vehicle response to the forces and moments that are generated by the sloshing propellants.

Similar to the elastic modes, the propellant sloshing modes of oscillation manifest themselves as a series of lightly damped poles and zeros in the vehicle dynamic transfer function. Experience has shown that the coupling between these modes and the elastic modes is negligible if the frequency separation is a factor of 2 or greater. However, there is usually considerable coupling between some of the sloshing modes because of the standard practice of grouping, in pairs, circular cylindrical tanks of the same diameter. In this case the slosh pendulums will couple most strongly if they are located on opposite sides of the vehicle center of mass. This is the situation for the shuttle vehicles considered in this study.

Another condition which is applicable to these study vehicles is the disparity between the magnitude of the two sloshing masses. This results from the fact that the density of liquid hydrogen is approximately 1/16 that of liquid oxygen. Thus, the effect of liquid hydrogen sloshing on control system stability will be considerably less than the effect of liquid oxygen sloshing.

The pole-zero sequence along the imaginary axis determines the difficulty to be encountered in stabilizing the slosh modes. If the sequence with increasing frequency is zero, pole, zero, pole, the system is relatively easy to stabilize. In the absence of any compensation, closing a feedback path around the transfer function results in loci departing directly up the imaginary axis from the poles. With the net lead from the combination of autopilot filtering, rate feedback, and actuator lag, the loci depart upward into the left-half plane. This situation is illustrated in diagrams a. and b. of Figure 6.

If one of the dipoles in the pole-zero sequence is reversed the locus emanating from that pole will depart downward and into the right-half plane, creating a closed-loop sloshing instability. This situation is illustrated in diagram c. of Figure 6 . Such a dipole has what is termed an unstable configuration. Since such a dipole requires lag for stabilization (to rotate the locus into the left-half plane), while the remaining dipole is destabilized with increasing lag, the situation usually calls for antislosh baffles.

With the pole-zero sequence of dipoles in a stable configuration, autopilot lag tends to destabilize the system. Since the slosh frequencies generally increase with increasing flight time, due to increasing axial acceleration, the root locus departure angles from the poles representing the slosh modes tend to rotate clockwise into the right-half plane; flight control system lag increases at the higher frequencies. Aggravating this situation is the decreasing vehicle mass which increases vehicle sensitivity to sloshing. The result is a tendency for the sloshing stability problem to be at its worst toward the end of a particular stage of flight.

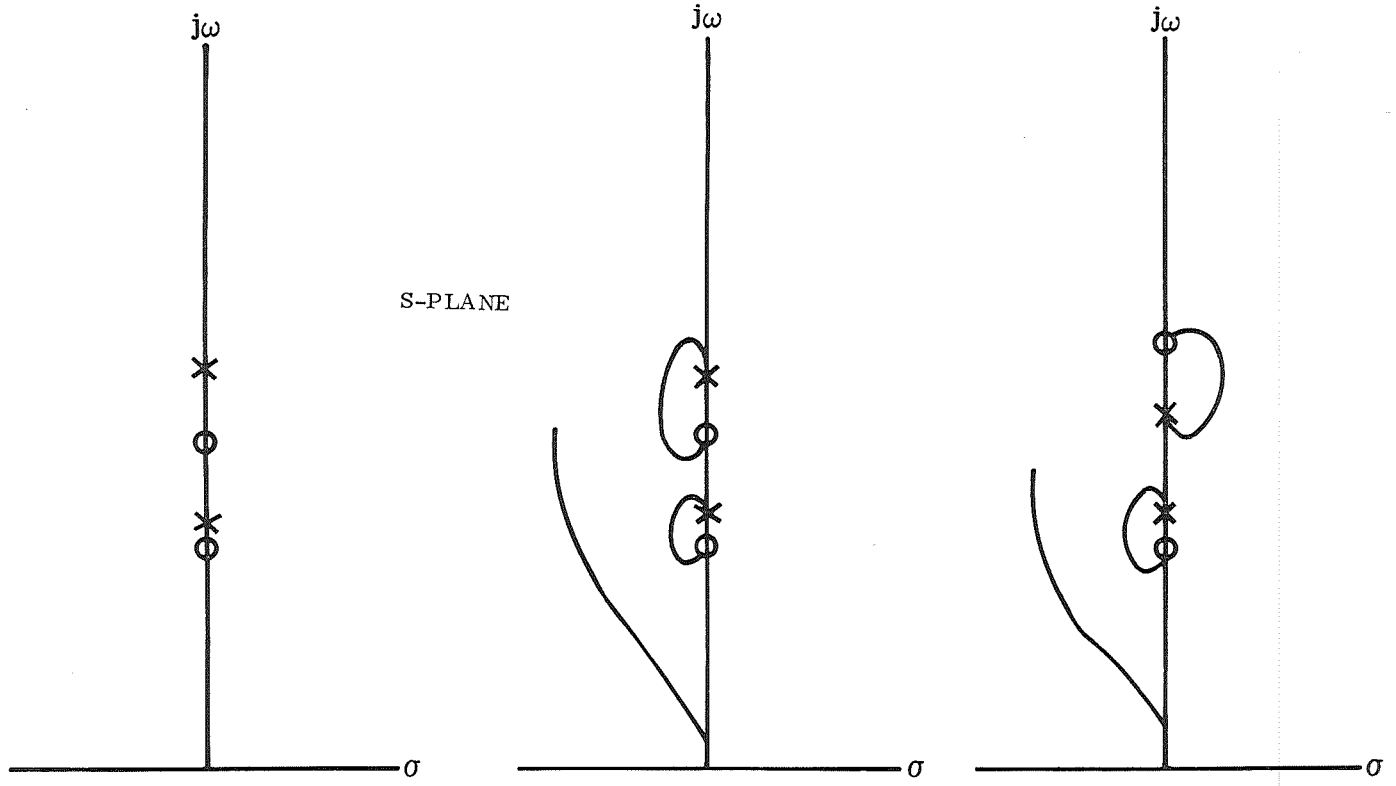

a. Stable Pole-Zero Configuration

b. Stable Pole-Zero Configuration With Conventional Autopilot

c. Unstable Pole-Zero Configuration with Conventional Autopilot

Figure 6. Stable and Unstable Slosh Pole-Zero Configurations for a Two Propellant Tank Vehicle

Up to this point the slosh damping has been ignored. In practice it is usually very small, particularly if the tank has a large free surface area and is "clean" internally, having no internal structural members. The approximation made is quite good unless baffles or other internal structures are added. In this case the poles associated with vehicle slosh modes having considerable motion in the baffled tank tend to move to the left. The damping is nonlinear, increasing with increasing fluid motion. Thus, some slosh activity is necessary to provide the damping. If one relies on baffling to stabilize an otherwise marginally stable sloshing mode, a slosh limit cycle is the result. Low fluid motion (low damping) leads to an unstable root, which causes a divergent response at the frequency of the unstable root. As the amplitude increases, so does the damping and the open-loop pole and closed-loop root move toward the left. The stable operating point is at some limit cycle amplitude where the damping is sufficient to place the closed-loop root on the imaginary axis. The reverse argument shows that an initially damped closed-loop root will move toward the $j\omega$ axis as the modal response amplitude dies down, reducing the damping. Clearly the amount of baffling determines the limit cycle amplitude. For this study slosh damping was assumed to be zero to obtain the maximum degree of sensitivity of the control system stability to these sloshing modes.

Slosh limit cycles also arise as a result of the nonlinear nature of electrohydraulic engine positioning servos. These arise out of the servo lag's dependence on the amplitude of engine motion and will result in stable or unstable limit cycle operating points.

This discussion serves to indicate the consequences of using one of the following means for stabilizing propellant sloshing:

a. Passive stabilization — Requires modification of the internal structure of the tank to increase the damping (baffles).

b. Active stabilization — Requires modification of the flight control system via addition of auxiliary loops (direct slosh pressure feedback or, more commonly, accelerometer feedback), or network shaping.

Either of these approaches carries its own advantages and disadvantages. Active compensation implies additional flight control system elements that must work to ensure mission success. Further, it is not always possible to synthesize such a system. On the other hand, there is little if any weight penalty. Passive means are more foolproof, but they carry a weight penalty. In either case, additional slosh modal damping mitigates inflight slosh loads that will be experienced, important since the frequencies are within the range of atmospheric disturbances.

4 DUAL FLYBACK VEHICLE ANALYSIS

This section contains the analysis results for the dual flyback vehicle. The first part surveys the rigid body stability and control characteristics to establish a set of baseline autopilot gains for the remainder of the discussion in this section. Part two looks at propellant sloshing mode stability at liftoff and near liftoff flight times. The next two parts analyze the elastic mode stability problem for symmetric and antisymmetric mode boundary conditions.

Some insight into the stability problem can be gained by examining the modal frequencies for the dual flyback vehicle and comparing them with frequencies of current operational vehicles. This frequency comparison is presented in Figure 7.

The obviously greater modal density of the dual flyback vehicle is primarily due to its unsymmetrical piggy-back arrangement. The two large vehicles are elastically coupled at two locations along their length. With this coupling arrangement, the combined vehicle contains modes which are dominated by one vehicle or the other, as well as modes which reflect the interaction of the two vehicles and the elastic linkage system. This is in contrast to the operational vehicles, whose stages are joined in tandem. With these vehicles the elastic properties of the individual vehicles and the interstage adapters tend to weld together to form a single composite vehicle.

A comparison between the dual flyback vehicle and the Atlas/Centaur vehicle illustrates this difference in the modal properties of the two types of vehicles. The first and second composite modes for the Atlas/Centaur vehicle exhibit the classic first and second body bending mode shapes. For the dual flyback vehicle the composite symmetric mode shapes (reference Appendix C) exhibit a booster first body bending mode on modes 2, 3 and 5; and modes 6, 7 and 9 contain a booster second body bending mode. Of course, the indicated booster mode is not dominant in all of these composite mode shapes, but it will be detected by the booster autopilot sensors and must be considered accordingly in the stability analysis.

The dual flyback vehicle mode shapes are also influenced by wing modes and vertical fin modes, which are not present on the other two configurations.

There is a frequency separation of approximately a factor of two between the propellant sloshing modes and the first elastic modes. This fact indicates that there is only a small degree of coupling between these highly tuned (lightly damped) modes of oscillation.

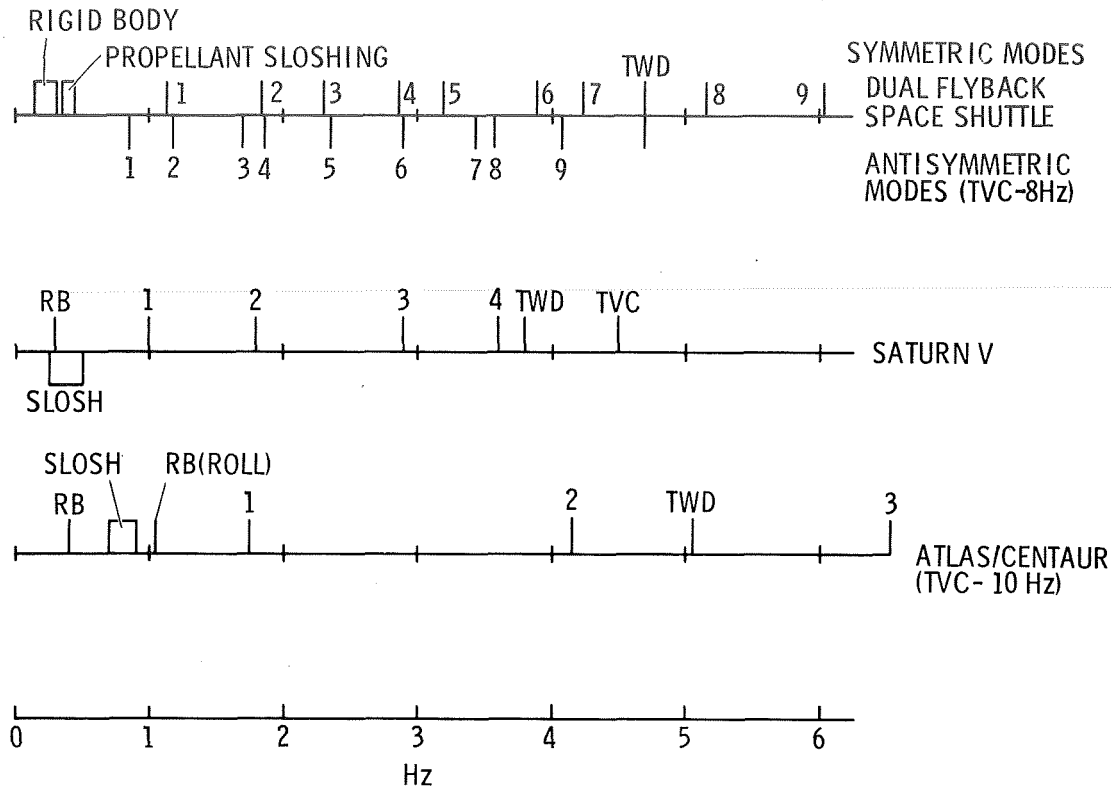

Figure 7. Modal Frequency Comparison

This analysis considers only autopilot sensors that are located on the booster vehicle. Since these sensors are required by the booster flyback capability they can also readily be used during the ascent flight phase.

Rigid Body Mode

The root locus diagrams for the rigid body modes in each of the three control planes are shown in Figure 8. For these diagrams the three control planes are considered uncoupled from each other (yaw/roll coupling effects will be discussed later). The damped frequency and damping ratio for autopilot gains of $K_A = 1.0$ and $K_R = 0.7$ are summarized below.

Response Parameter	Control Plane		
	Pitch	Yaw	Roll
Damped Frequency (rad/sec)	1.05	1.3	1.6
Damping Ratio	0.45	0.45	0.5

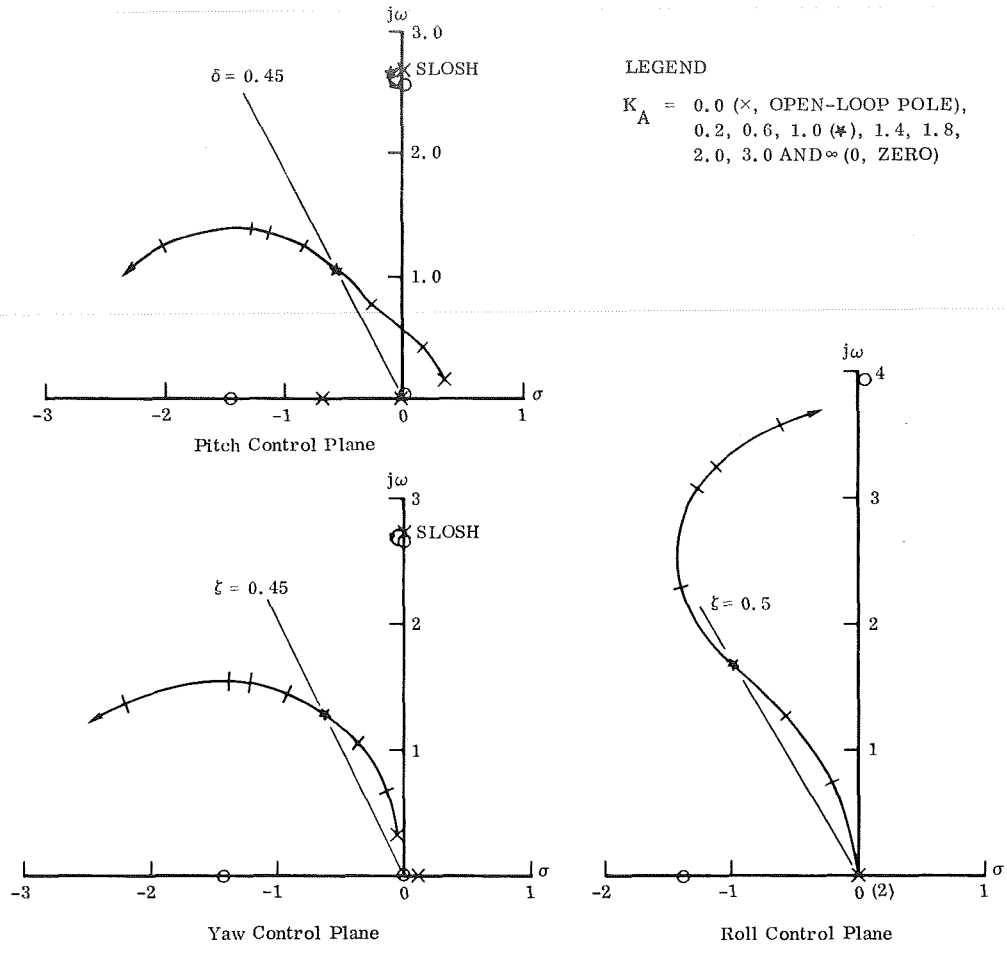

Figure 8. Rigid Body Modes

The damping ratios are somewhat larger than required for this time of flight, which indicates that the rate gain (K_R) could be reduced. This would result in a decrease in system phase lead (increase in lag) rotating the locus toward the right-half plane and decreasing the damping ratio. Lag compensation that may be required for elastic mode stability will produce the same type of effect. It is also apparent that the value of K_A can be less than 1.0 in the yaw and roll control planes.

Propellant Sloshing Mode Stability

Propellant sloshing stability is generally not a problem at liftoff. The sloshing masses are only a small percentage of the vehicle mass, and the vehicle acceleration is not much greater than 9.8 m/sec^2 (1 g). For the dual flyback vehicle, the oxidizer (LO_2) and fuel (LH_2) masses are 7% and 0.6% of the reduced vehicle mass (total mass less masses of slosh pendulums), and the vehicle acceleration is 13.2 m/sec^2 (1.35 g). These conditions are present at an approximate flight time of liftoff plus 10 sec; this time having been chosen to permit some buildup in sloshing masses and vehicle acceleration.

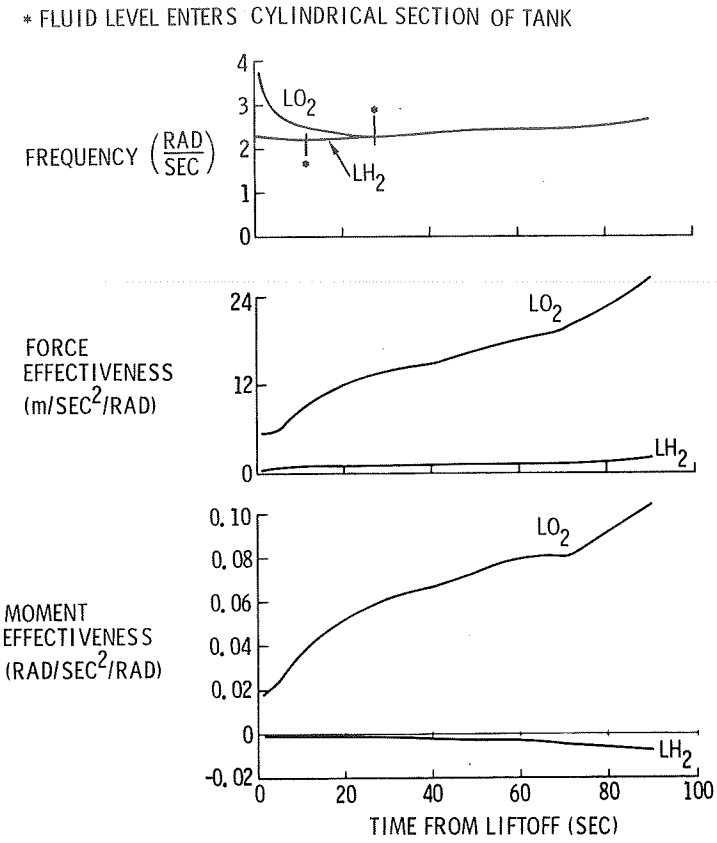

Figure 9. Key Sloshing Parameters

Figure 9 illustrates the changes which the key sloshing parameters undergo as a function of flight time. As long as one or both of the fluid levels is in the forward dome section of the tank (reference Appendix C) the propellant sloshing natural frequencies are different. This frequency separation, although small, tends to reduce the degree of slosh coupling during liftoff. The force effectiveness and moment effectiveness curves indicate that oxidizer sloshing will have a greater influence on system stability than fuel sloshing. The different signs of the two moment effectiveness curves means that the two sloshing pendulum hinge points are on opposite sides of the vehicle center of mass. This condition is favorable to slosh coupling when the two natural frequencies are the same.

Propellant sloshing stability at the study condition of liftoff + 10 sec is shown in Figure 10. These root locus diagrams are plotted in terms of damping ratio and frequency to illustrate the magnitude of tank damping that would be required to stabilize an unstable condition. The equations that were used to generate these loci assume zero natural tank damping.

The single-order actuator model used here is adequate for the range of frequencies being considered in this analysis. The two values of K_c reflect two different levels of effective system lag filtering that can be produced by the actuator, with $K_c = 5$ depicting the higher lag condition. This varying lag is primarily the result of actuator nonlinearities.

Both tanks exhibit pole above zero low residue loci. Although the hydrogen tank is unstable at a gain of $K_A = 1$ it is a very slowly divergent condition, which requires less than 0.1% damping to stabilize. This amount of damping is on the order of what is usually assumed for wall wiping.

The loci in Figure 11 portray a later flight condition, liftoff + 40 sec. Now, both fluid levels are in the cylindrical section of each tank and the sloshing natural

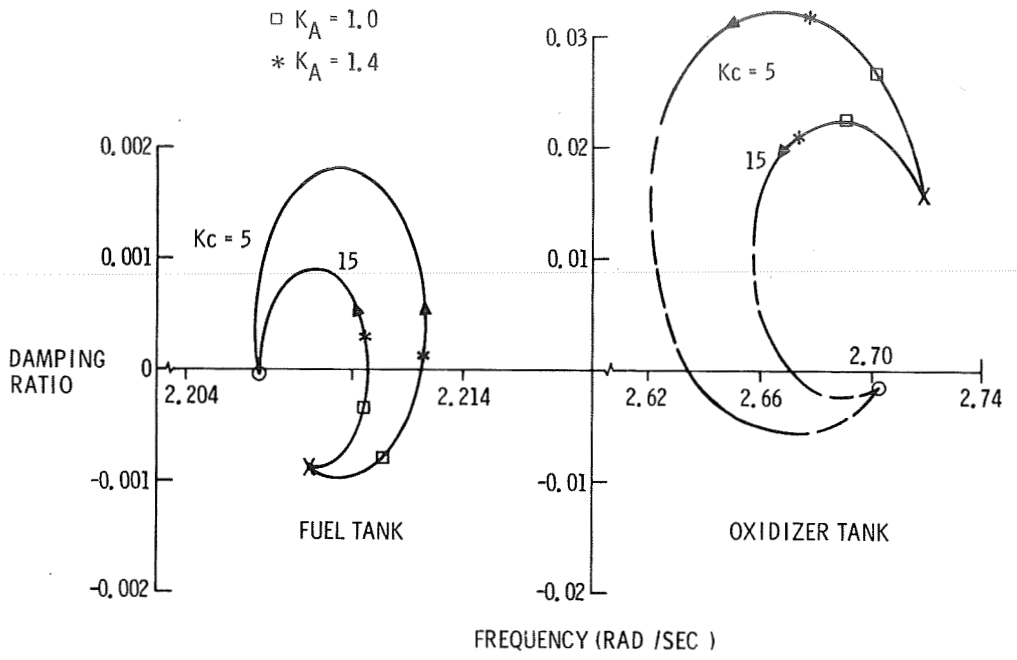

Figure 10. Propellant Sloshing — Liftoff +10 Sec

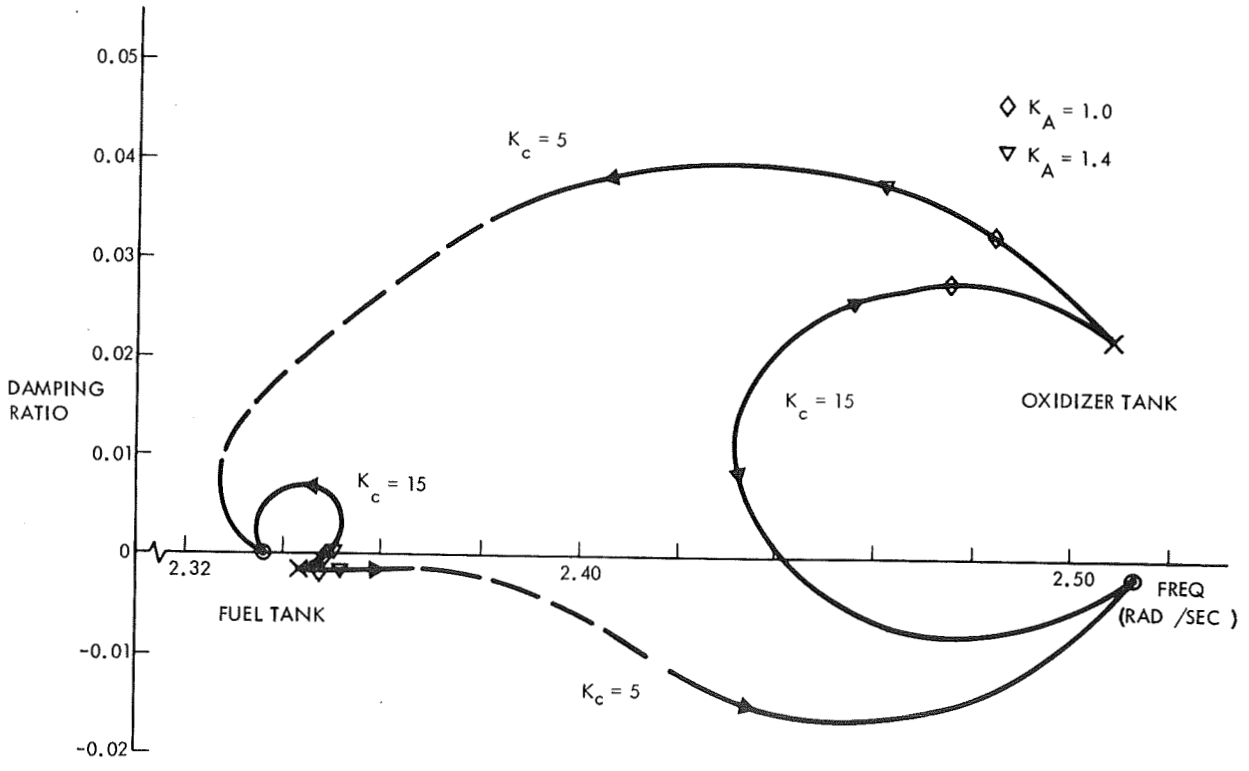

Figure 11. Propellant Sloshing — Liftoff +40 Sec

frequencies are equal. Although the stability characteristics at a gain of $K_A = 1$ are not appreciably different, the loci have taken a different form from that shown in Figure 10. The oxidizer pole has moved slightly below the zero, which indicates that an unstable configuration is developing. Also, this figure shows the start of extensive coupling between the two slosh modes. The indications are that propellant sloshing stability will become more critical for later flight times.

It can be concluded that propellant sloshing is not a stability problem at liftoff. Therefore, for the remainder of this study, only the oxidizer slosh mode is included in the system equations. The reason for including this mode is to determine if it couples in any significant manner with the elastic modes.

Symmetric Elastic Mode Stability

One of the most important considerations relative to elastic mode stability is the location of the autopilot sensors; in particular the rate sensor. For this vehicle the values of the modal slopes are such that the location of the attitude sensor has only a secondary effect on elastic stability. Therefore, it is placed forward in the nose of the booster, which is the most favorable location from the standpoint of operating environment. This analysis then examines the effects of rate sensor locations forward and aft of the principal first body-bending mode antinode. These sensor locations are illustrated in Figure 12 in relation to the elastic vehicle model.

For purposes of discussion in this report a distinction is made between the phrases "elastic mode" and "body mode". "Elastic mode" (or just "mode") refers in general to each of the composite vehicle modes, whereas the phrase "body mode" is used to identify a particular mode shape that is associated with a particular part of the total vehicle. For example, referring to the elastic mode shapes appearing in Appendix C (Figure C3) it is clear that elastic modes 2 and 3 both contain the first booster body mode shape, and elastic mode 9 contains the second booster body mode. Although this distinction is admittedly artificial, the reference to body modes more clearly describes the mode shape from the standpoint of the modal relationship between the autopilot sensor locations and the engine gimbal point.

In the table below the symmetric vehicle elastic modes are classified according to the body mode shape that is exhibited on the booster vehicle. Although elastic modes 1 and 4 exhibit elastic deflections, the modal slope has the same sign over the entire length of the booster.

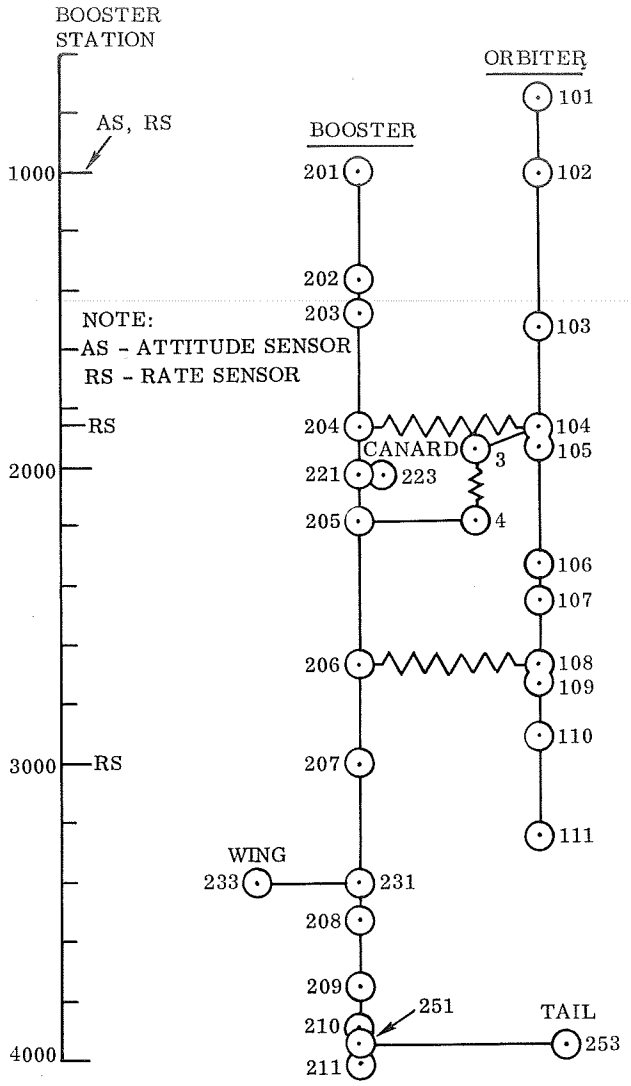

Figure 12. Autopilot Sensor Locations

Elastic Mode	Booster Body Mode	Comments
1	(Orbiter Mode)	Very small deflections
2	First	Principal first mode
3	First	
4		Large aft-end deflections
5	First	Very small deflections
6	Second	Predominantly a longitudinal mode
7	Second	
8	First	Very small deflections
9	Second	Principal second mode

For this vehicle, phase stabilizing the first body mode could require phase stabilization for the first five elastic modes. It is also possible that some of these first body modes can be gain stabilized, because they have a very small effective modal gain.

The elastic stability problem is initially analyzed with an uncompensated autopilot for two rate sensor locations: one forward of the first body mode antinode at model node 204, and one aft of this antinode at model node 207. These locations are considered to be sufficiently removed from the location of the antinode to preclude a first body mode slope sign reversal at either location during the ascent flight phase. The root locus diagram for the forward rate location is shown in Figure 13, and for the aft location in Figure 14.

In both of these figures the over-all stability picture is illustrated by the diagram on the left. The other diagrams are enlargements of specific areas of interest; namely, those areas which contain the loci of the individual elastic modes whose stability properties cannot be readily deduced from the overall diagram.

Figure 13 shows that modes 2 and 3 must be phase stabilized since the modal gains are large enough to preclude gain stabilization. The other lower frequency first body mode (mode 5) locus also departs toward the right-half plane, but it is stable for all reasonable values of autopilot gain (K_A). Any lag compensation which is introduced to stabilize modes 2 and 3 will certainly enhance the stability of mode 5. The mode 1 locus has a stable orientation because the modal slope at the forward rate sensor location has the same sign as that at the engine gimbal point.

Mode 4 is unstable for all values of autopilot gain. It also has a low modal gain because of the very small modal slopes at the autopilot sensor locations. The stability of this particular mode is discussed in greater detail later.

Modes 6, 7, 8 and 9 are gain stable with at least 6 dB gain margins (from $K_A = 1$) for all phase orientations. The gain attenuation introduced by autopilot lag compensation will increase the stability margins of these modes.

For the aft rate sensor location (Figure 14) all mode loci exhibit stable configurations. Mode 4 is stable, despite the fact that its open-loop pole is in the right-half plane, because of the increased modal slope at the rate sensor location.

It was pointed out earlier that a forward rate sensor location is most desirable from the standpoint of elastic mode stability toward the end of the ascent flight phase. With this in mind the forward rate sensor configuration is discussed in more detail.

Figure 15 illustrates the stability conditions for a rate sensor located at model node 201, the location of the attitude sensor. In comparing the loci in this figure with those in Figure 13 the principal differences are increased modal gains and some phase shifts. These differences are due to the larger modal slopes at the more forward rate sensor location, and they are more pronounced for the high frequency modes than for the lower frequency modes. The changes in the second body modes are particularly noticeable because the rate sensor location at model node 204 is very close to a second body mode antinode. However, the autopilot lag compensation required to phase stabilize modes 2 and 3 will result in a gain attenuation factor of 3 to 4 at these second body mode frequencies. This comparison also illustrates the general rule that increasing gains have a destabilizing influence on the elastic mode loci, in that a greater reliance must be placed on the more uncertain technique of phase stabilization, particularly for the higher frequency modes.

Returning to a rate sensor location at model node 204, Figure 16 describes the conditions obtained if the load torque feedback around the control actuator is removed (these terms are eliminated from the actuator equation). Comparing this figure with Figure 13 reveals that the load torque feedback effect is most pronounced at the higher frequencies, near the engine actuator frequency. Its dominant influence on the root

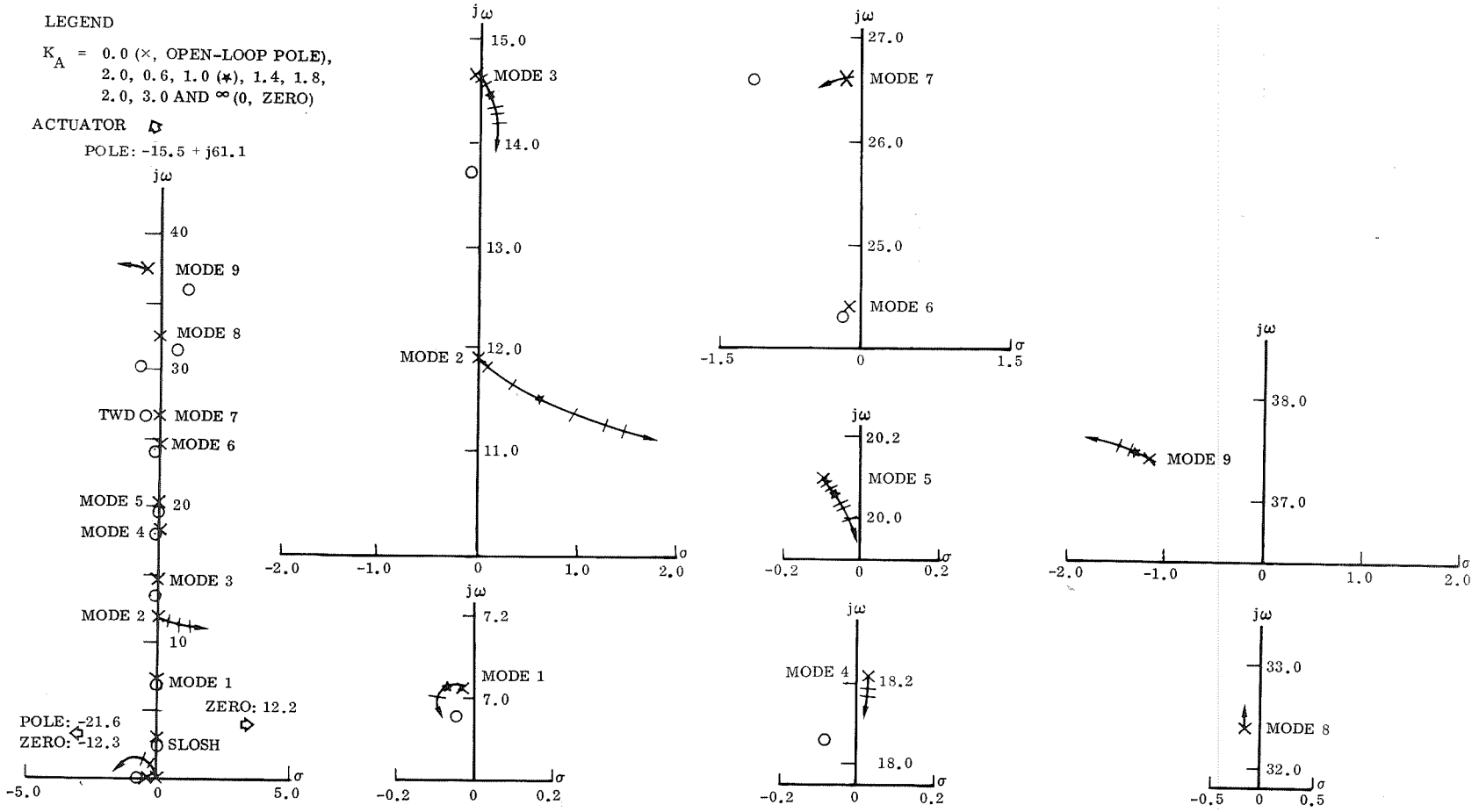

Figure 13. Forward Rate Sensor (Node 204), Uncompensated Autopilot

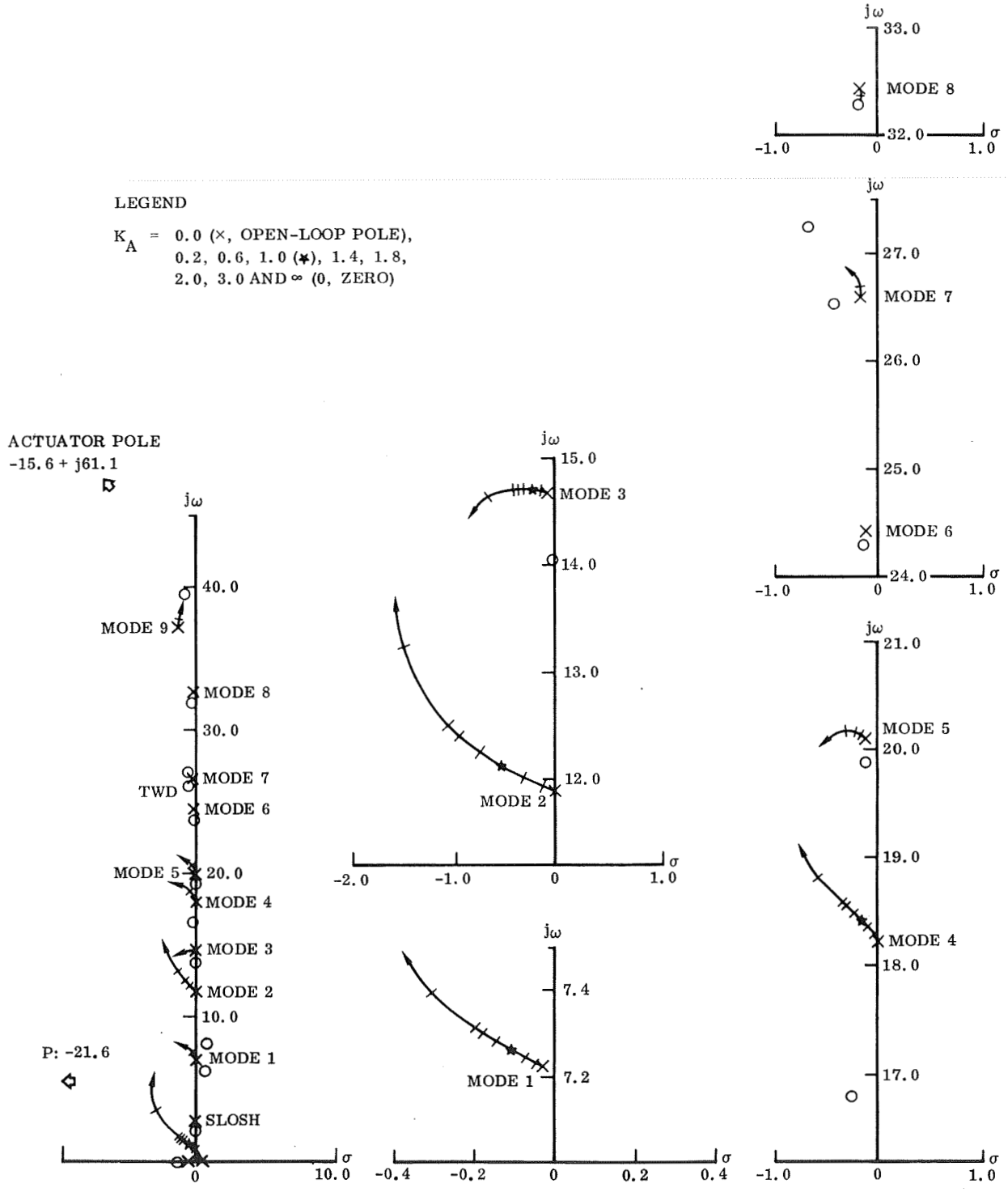

Figure 14. Aft Rate Sensor (Node 207), Uncompensated Autopilot

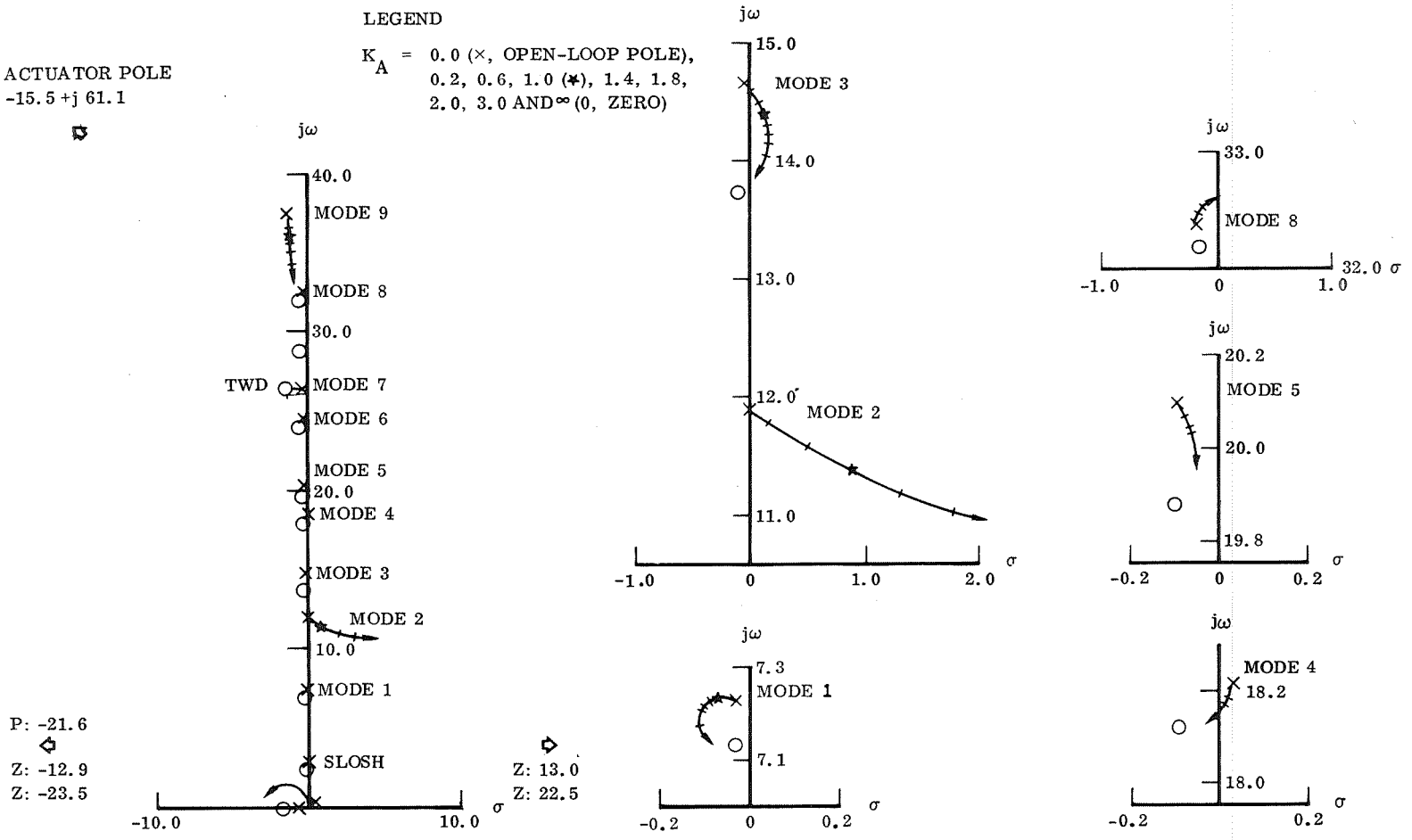

Figure 15 . Forward Rate Sensor (Node 201), Uncompensated Autopilot

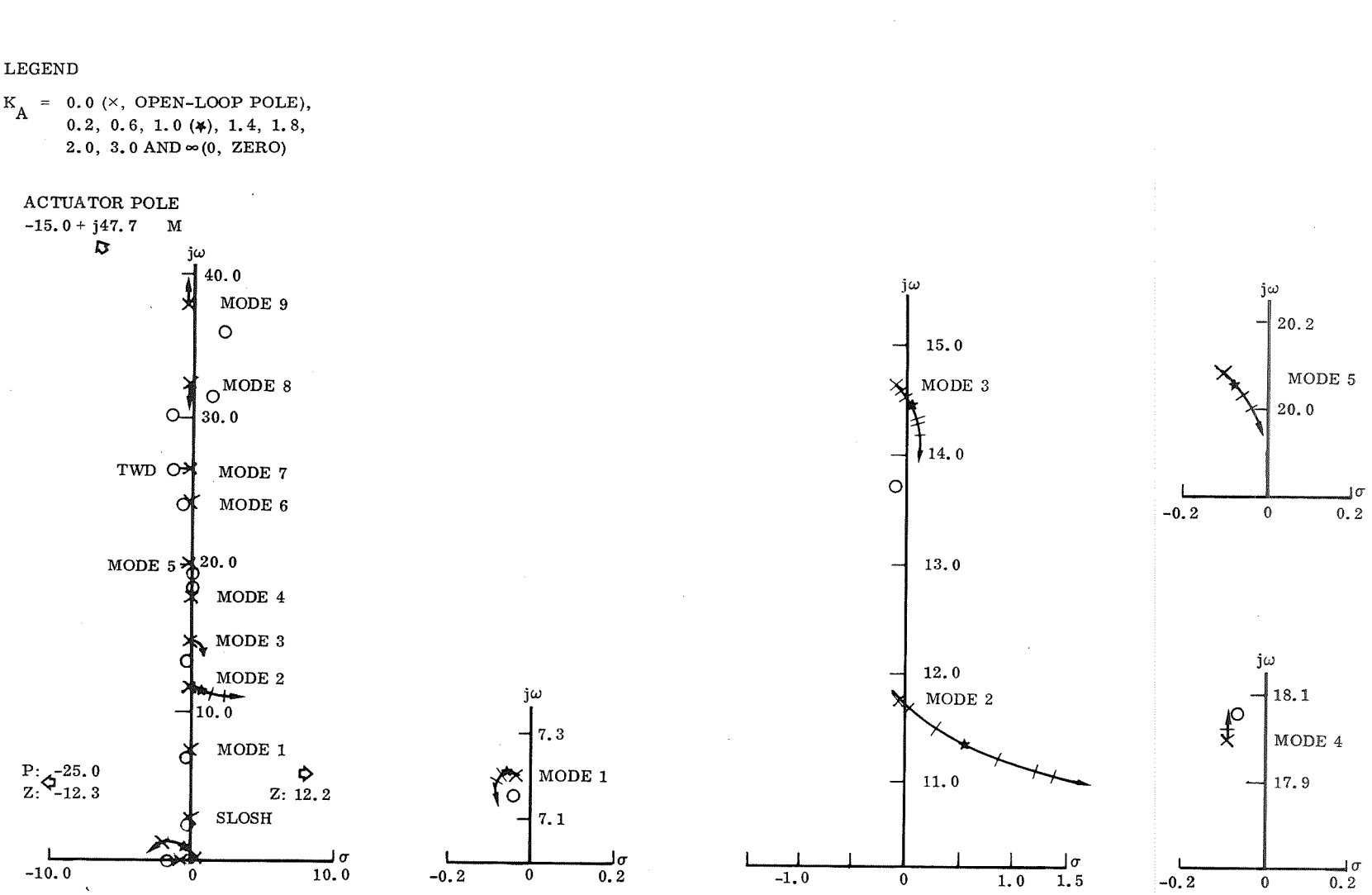

Figure 16. Forward Rate Sensor (Node 204), Uncompensated Autopilot, Actuator Load Torque Feedback Neglected

locus plot is to shift the location of the mode and actuator open-loop poles, in some instances toward increased stability and in others toward decreased stability. In particular, note the destabilizing effect that the load torque feedback has on mode 4.

This figure illustrates that the stability of mode 4 will be very much influenced by the effective spring rates for the actuator backup structure for each of the twelve engines and the friction terms and nonlinearities inherent in the engine actuator systems. Since none of these effects was included in this simplified linear analysis, this discussion only indicates a potential problem area that must be carefully considered in the design phase. Generally, the stability of this type of mode can be modified to some degree by the control the designer has over actuator system requirements and actuator backup structure spring rates.

If stability compensation is added to the autopilot for phase stabilizing modes 2 and 3 (model node 204 rate sensor location), the results are shown in Figure 17. The compensation consists of a forward loop quadratic lag filter with a natural frequency of 15 rad/sec and critical damping ($\zeta = 0.707$). Now all of the elastic mode loci (again, with the exception of mode 4) have stable closed-loop roots for the range of autopilot gains of interest.

Although mode 1 has adequate stability margins, the introduction of the filter has had a destabilizing influence on it. This mode is predominantly an orbiter mode, whose frequency changes very little with flight time. Therefore, as the frequencies of the other modes increase with flight time, the amount of autopilot lag filtering can be reduced with a resulting increase in the stability of this mode.

For this study it was practical to consider only briefly modal dispersions on frequency. The root locus plots for plus and minus ten per cent variations in elastic mode frequency are shown in Figures 18 and 19 using the compensated autopilot configuration. With some small adjustments to the filter natural frequency, adequate stability margins can be attained for all elastic modes, excluding mode 4. Certainly the conventional autopilot techniques are adequate to cope with these frequency dispersions.

If the stability of a mode with characteristics similar to those of mode 4 cannot be attained by careful actuator system design, a multiple rate sensor autopilot configuration may be required. This concept was very briefly examined by considering an autopilot with two rate sensors, one located forward of the first body mode antinode and one mounted aft of this antinode (model nodes 204 and 207). The influence of each sensor can be controlled by adjusting its rate gain. For this example the forward sensor has a rate gain (K_R) of 0.2 and the aft sensor a gain of 0.5. Thus, the effective rigid body gain is still 0.7. The root locus plot for this configuration is shown in Figure 20. Now, all elastic modes exhibit stable characteristics, including mode 4.

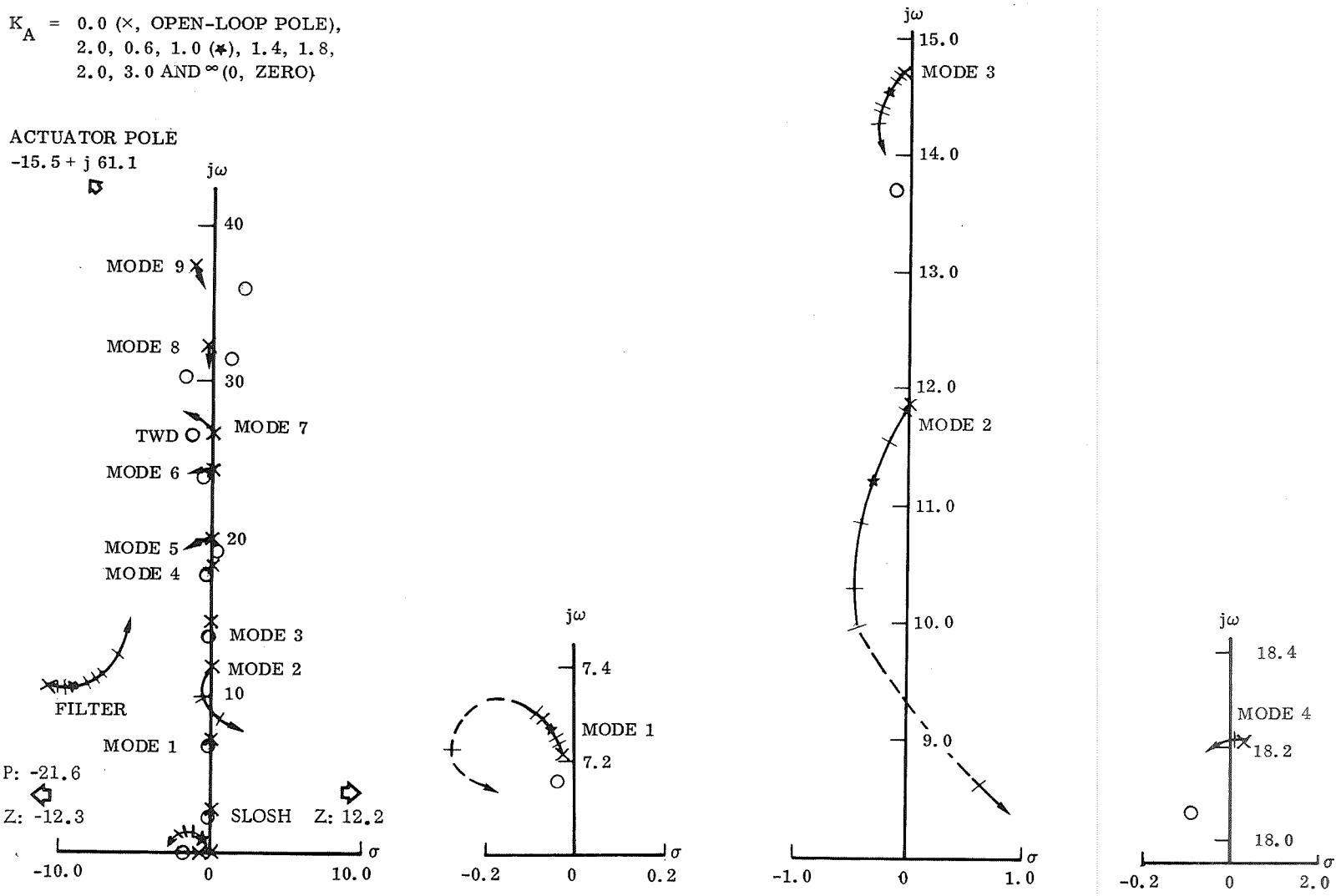

Figure 17. Forward Rate Sensor (Node 204), Compensated Autopilot

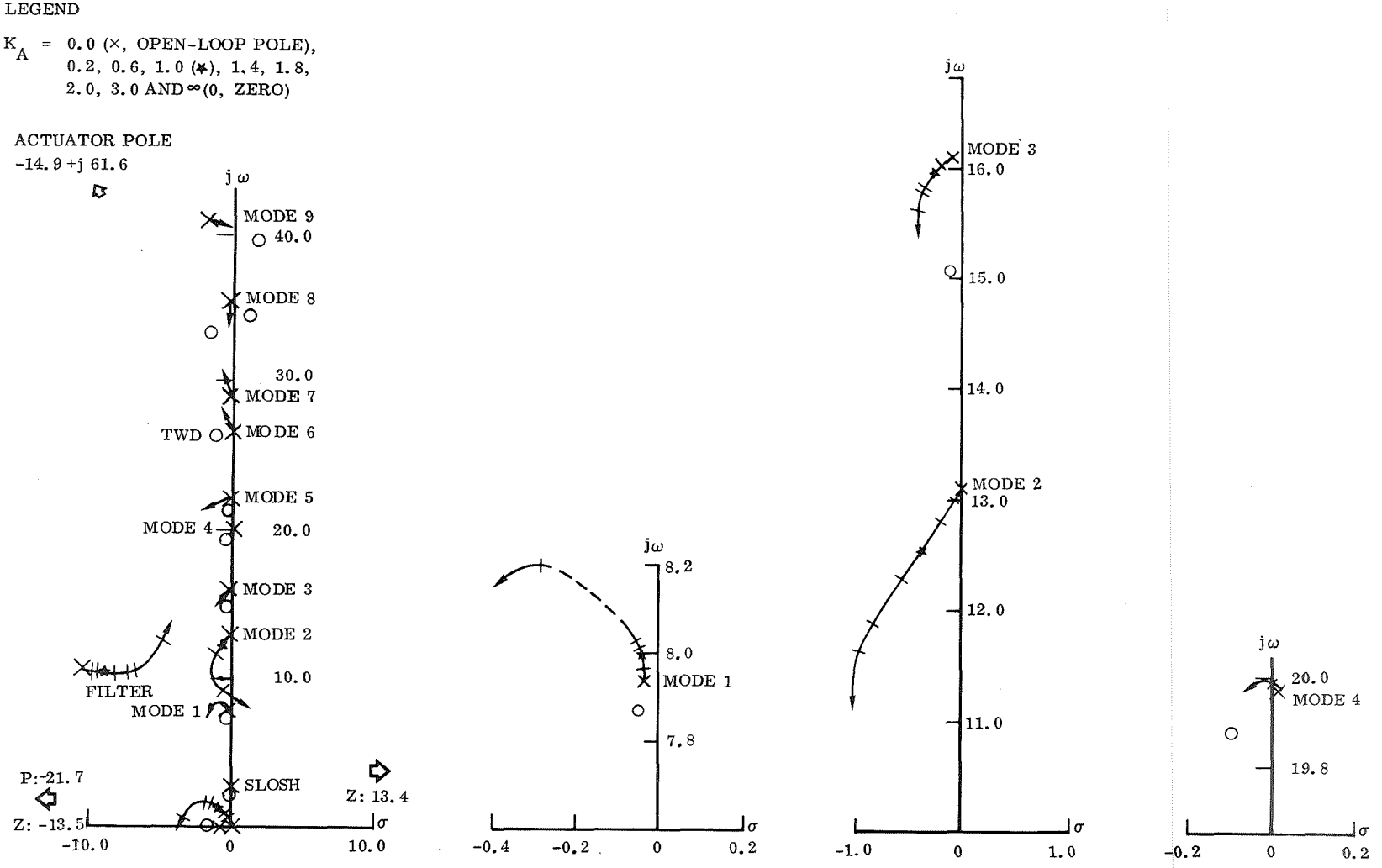

Figure 18. Forward Rate Sensor (Node 204), Compensated Autopilot, Elastic Mode Natural Frequencies Increased 10 Per Cent

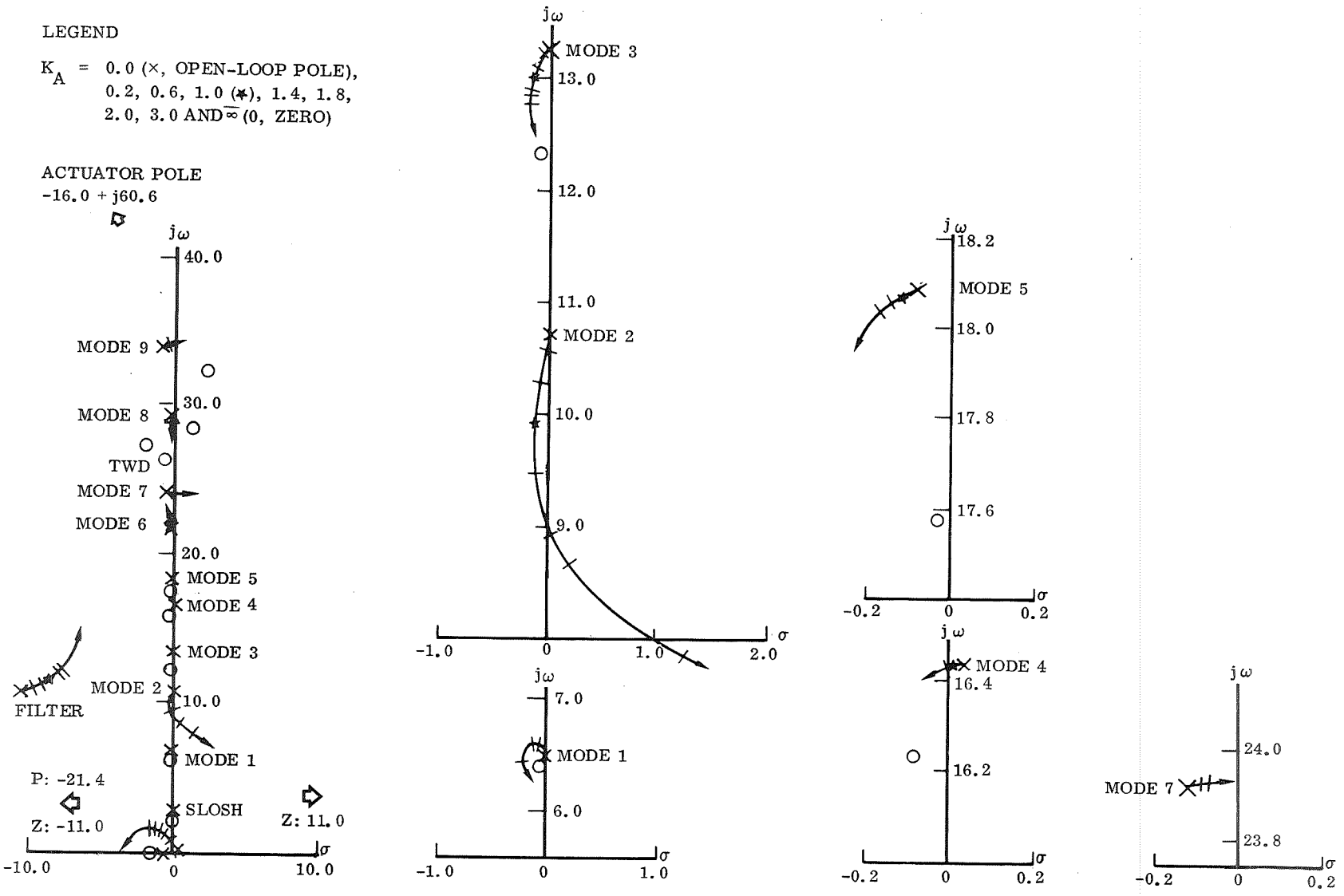

Figure 19. Forward Rate Sensor (Node 204), Compensated Autopilot, Elastic Mode Natural Frequencies Decreased 10 Per Cent

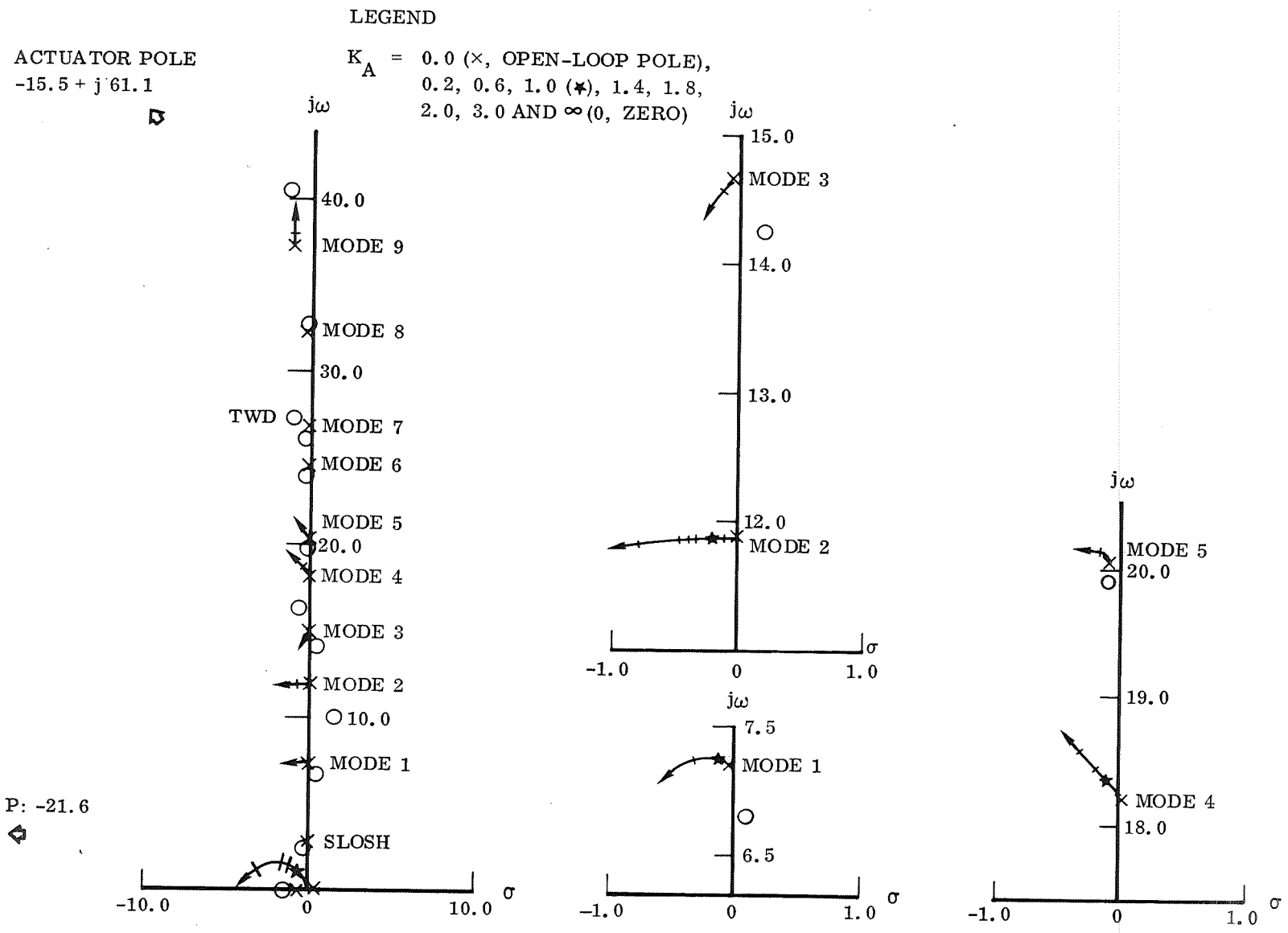

Figure 20. Forward (Node 204) and Aft (Node 207) Rate Sensors, Uncompensated Autopilot

In conclusion, this analysis has demonstrated the feasibility of using conventional autopilot techniques to provide the pitch control plane of the dual flyback vehicle with adequate stability and performance characteristics at the liftoff flight condition.

Antisymmetric Elastic Mode Stability

Antisymmetric elastic mode stability is analyzed in two phases. In the first phase a planar analysis is conducted for the yaw and the roll control planes separately. This initial planar approach permits greater visibility of the principal yaw and roll body mode stability properties by eliminating the effects of the vehicle dynamic model coupling terms. Then, in the second phase the coupled system is examined in terms of the results of these planar analyses.

In the table below the antisymmetric vehicle elastic modes are classified according to the body mode shape exhibited on the booster vehicle. The yaw and roll components are listed separately.

Elastic Mode	Booster Body Mode		Comments
	Yaw	Roll	
1	First		Predominantly a wing mode
2	First		"Scissor mode" between booster and orbiter
3	First		Principal first yaw mode
4	First		
5	First		
6	Second	First	Principal second yaw mode
7	Second		
8	Second		
9		First	Principal first roll mode

Unlike the symmetric modes, this set of modes does not contain a mode that is almost entirely composed of booster aft end deflection. This could be due to the different total vehicle elastic properties between the longitudinal and lateral planes. Another factor to consider is the difference in elastic models. The antisymmetric modes are obtained from a three-dimensional representation of the booster vehicle, whereas the symmetric modes use only a flexible beam model. This more detailed antisymmetric model may have a distributive effect on a "localized" mode shape.

Unless noted, the mode shape data (deflections and slopes) are expressed in terms of equivalent booster centerline parameters.

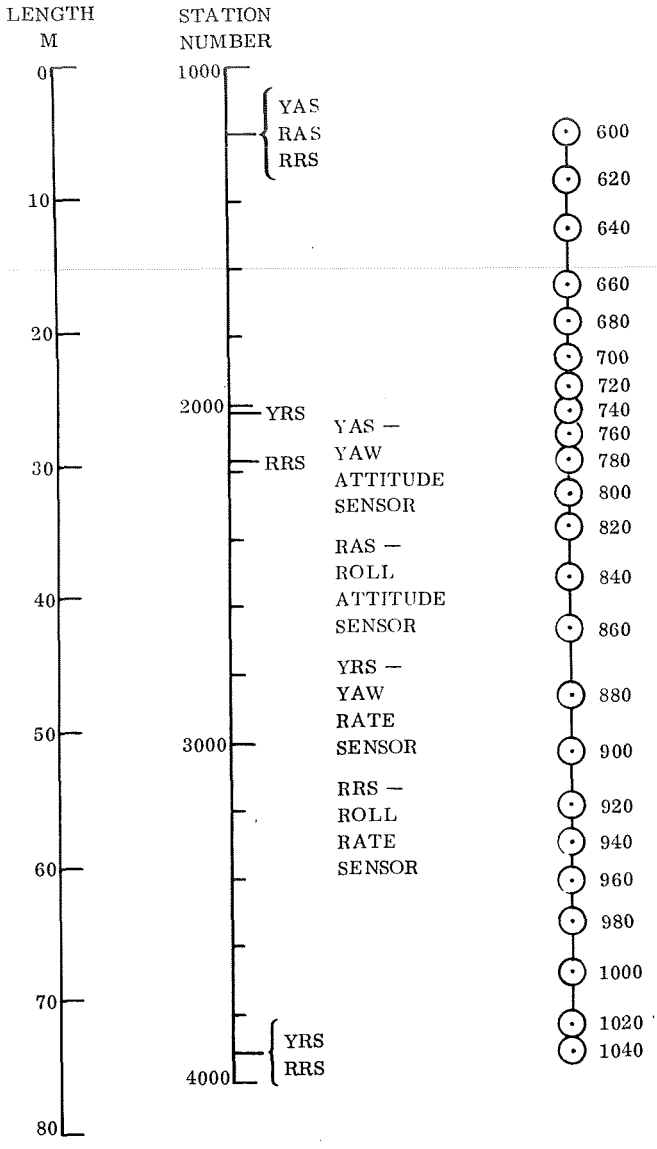

Figure 21. Autopilot Rate and Attitude Sensor Locations

The rate and attitude sensor locations examined here are illustrated in Figure 21 in relation to the elastic vehicle model.

Yaw Planar Analysis. – The root locus diagrams for rate sensor locations forward and aft of the first body mode antinode are shown in Figures 22 and 23. The forward location is at model node 740 and the aft location is at model node 1040 (the gimbal point). The only attitude sensor location considered is forward in the booster nose (model node 600).

Figure 22 shows that modes 2 and 3 are unstable (closed-loop roots in the right-half plane). Also, the modal gain is large enough that these two modes cannot be gain stabilized. Mode 1 is represented by a stable dipole configuration with a very small residue. In this configuration Mode 1 has a negligible influence on the stability properties of the other system modes.

Although the loci for modes 4, 5 and 6 depart toward the right-half plane, the closed-loop roots for $K_A = 1$ are in the left-half plane indicating stability. Also, modes 7, 8 and 9 are completely gain stable (i. e., these modes have at least a 6 dB gain margin for all phase orientations). Any lag compensation introduced to stabilize modes 2 and 3 will certainly increase the stability margins of modes 4 through 9. In this figure the second body mode loci depart toward the right-half plane. This condition is primarily due to the location of the rate sensor just aft of the second mode forward antinode. A more forward rate sensor location will result in these loci departing toward the left.

For the aft rate sensor location (Figure 23), all elastic mode loci exhibit stable configurations.

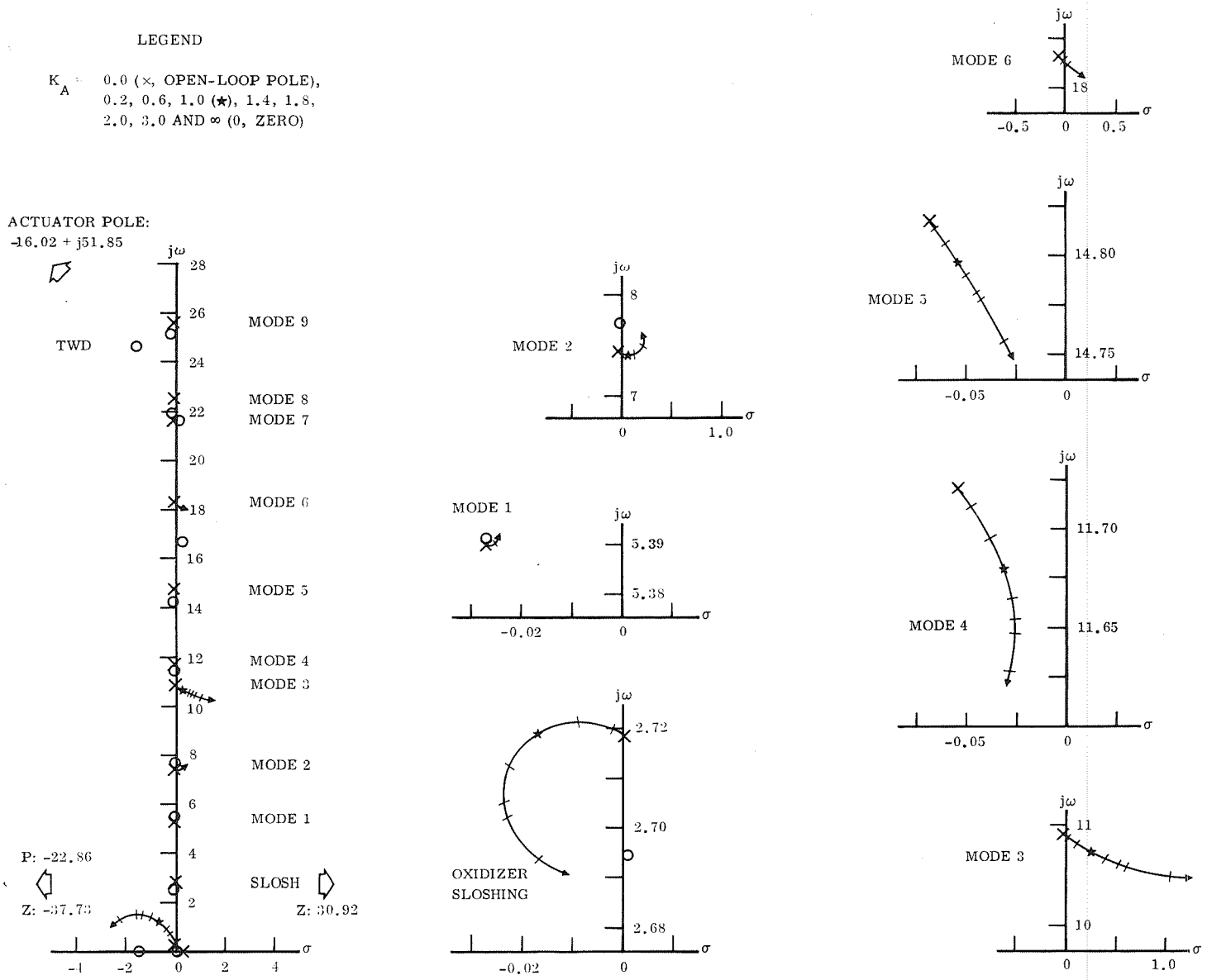

Figure 22. Planar Yaw Control, Forward Rate Sensor (Node 740)

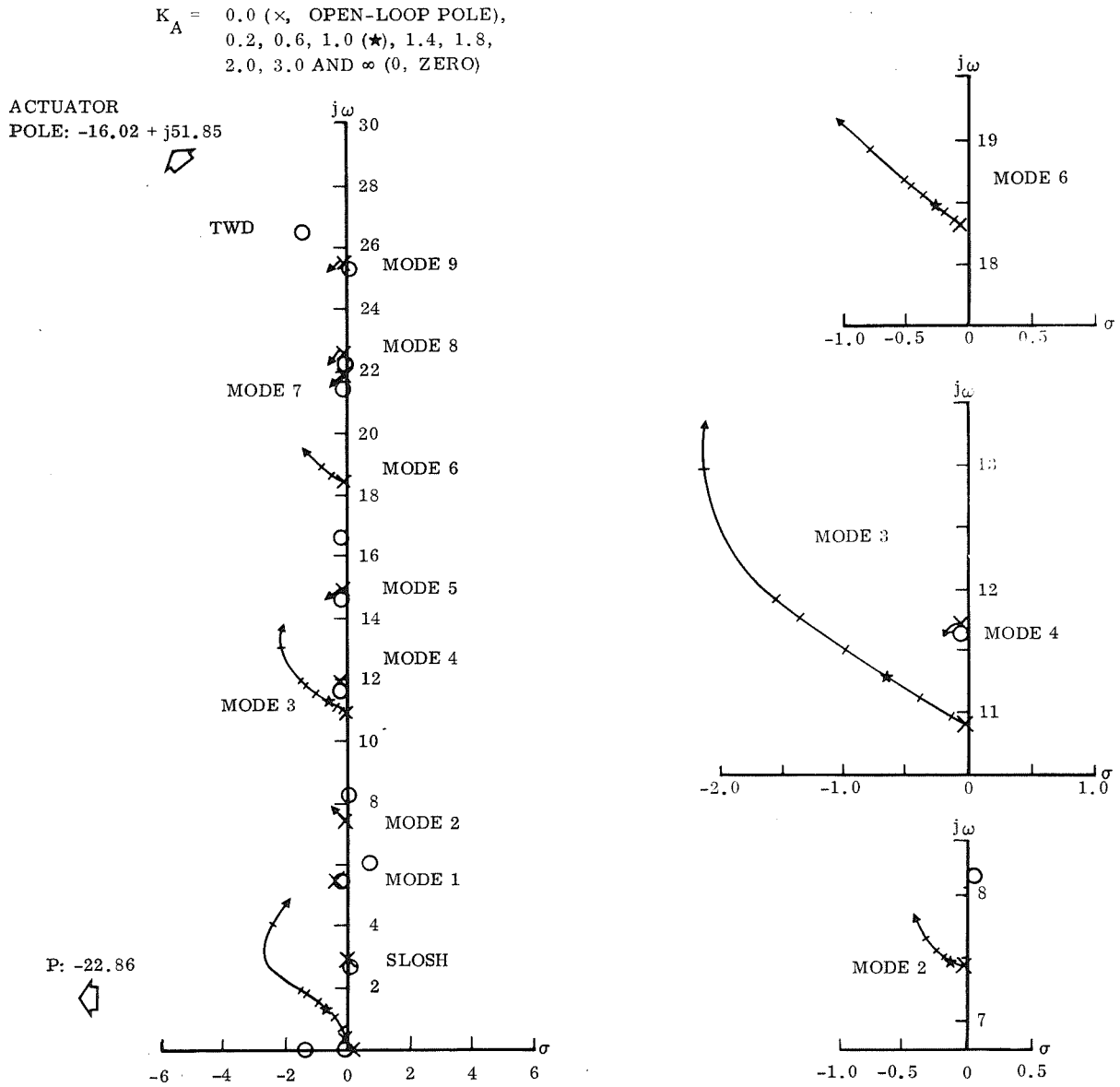

Figure 23. Planar Yaw Control, Aft Rate Sensor (Node 1040)

Returning to the forward rate sensor location (model node 740) Figure 24 illustrates the effect of adding autopilot compensation to provide phase stabilization for modes 2 and 3. The compensation consists of a forward loop quadratic lag filter with a natural frequency of 10 rad/sec and critical damping. Now, all of the elastic mode loci have stable closed-loop roots for a gain value of $K_A = 1$. Also, modes 5 through 9 are completely gain stable.

Although the introduction of this autopilot filter has a destabilizing influence on the propellant sloshing and rigid body modes, it does not produce unacceptable results. The propellant sloshing locus still retains its stable configuration (see Figure 22). At $K_A = 1.0$ the rigid body damping ratio has been reduced to 0.35 from 0.45, and the damped frequency has increased to 1.5 rad/sec from 1.3 rad/sec.

It is shown in the coupled system analysis that the coupling effects do not appreciably change the results obtained from this planar analysis. The differences that are noted in the coupled root loci are small from the standpoint of overall vehicle stability. Therefore, the effect of elastic mode frequency dispersions can be analyzed in this planar condition and the results, if significant, can be interpreted in terms of the coupled system.

Using the compensated forward rate sensor configuration, the root locus diagrams for a plus ten percent and a minus ten percent change in elastic mode natural frequencies are given in Figures 25 and 26. These figures illustrate that all loci still have stable closed-loop roots at a gain of $K_A = 1.0$. The somewhat marginal stability qualities exhibited by mode 2 for the decreased frequency conditions are easily improved by small adjustments to the autopilot compensation.

Roll Planar Analysis. – The root locus diagrams for forward and aft roll rate sensor locations are presented in Figures 27 and 28. The forward rate sensor location is in the booster nose at model node 600, and the aft location is at model node 1040 (the gimbal point). For both rate sensor locations, the roll attitude sensor is positioned in the booster nose.

In comparing these two figures, only modes 6 and 9 exhibit the approximately 180-degree phase shift associated with first body modes when the rate sensors are on opposite sides of the antinode. Although the other modes exhibit roll deflections, there is no sign change between the aft and forward sections of the vehicle. Hence, the loci representing these modes assume the inherently stable configuration characteristic of a first mode with an aft-mounted rate sensor.

For both rate sensor locations all elastic mode loci have stable closed-loop roots at $K_A = 1.0$. Also, in both figures the mode 9 locus exhibits the smallest stability margins. Although this mode could be classified as a higher frequency mode, it

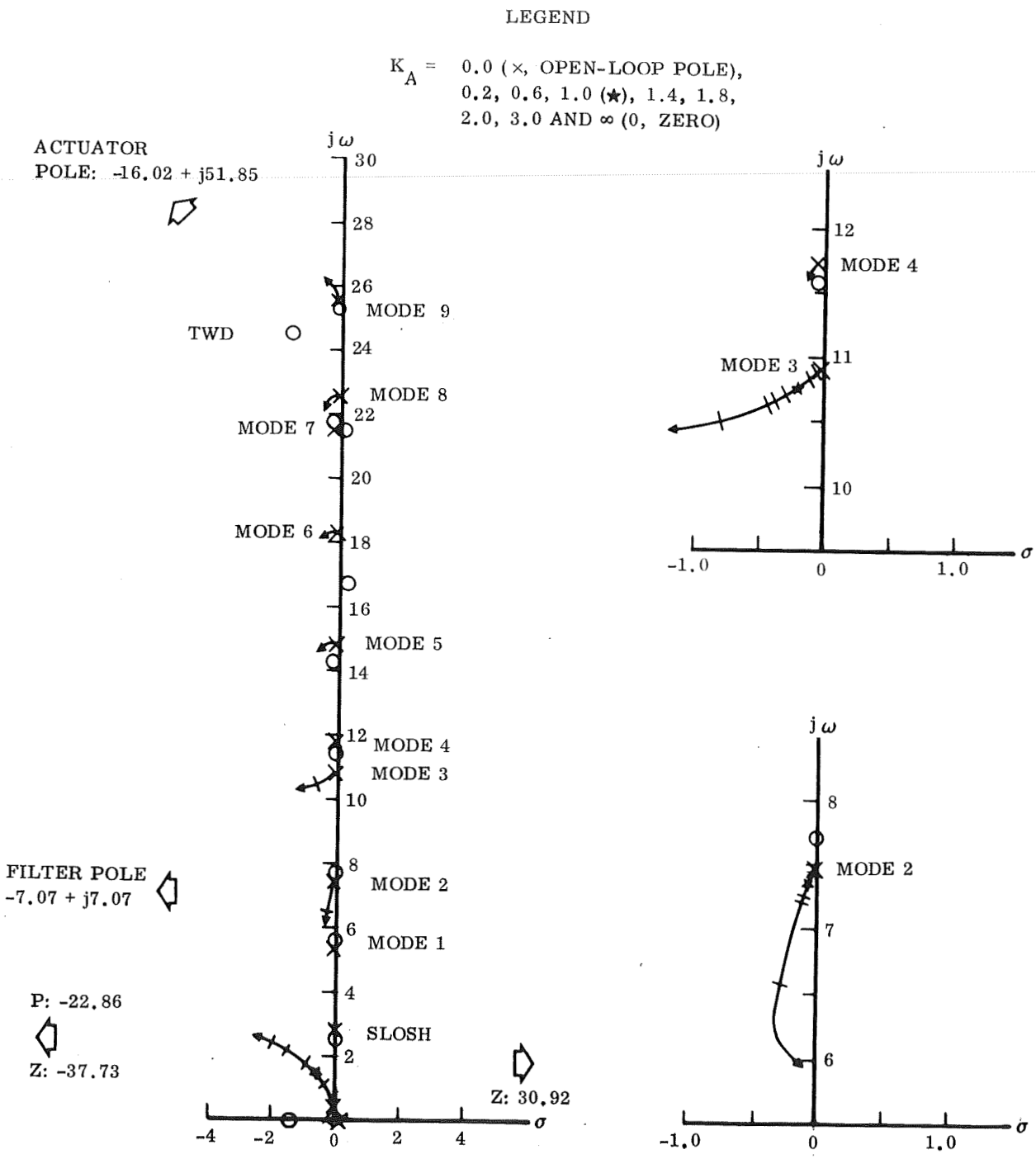

Figure 24. Planar Yaw Control, Forward Rate Sensor (Node 740), Compensated Autopilot

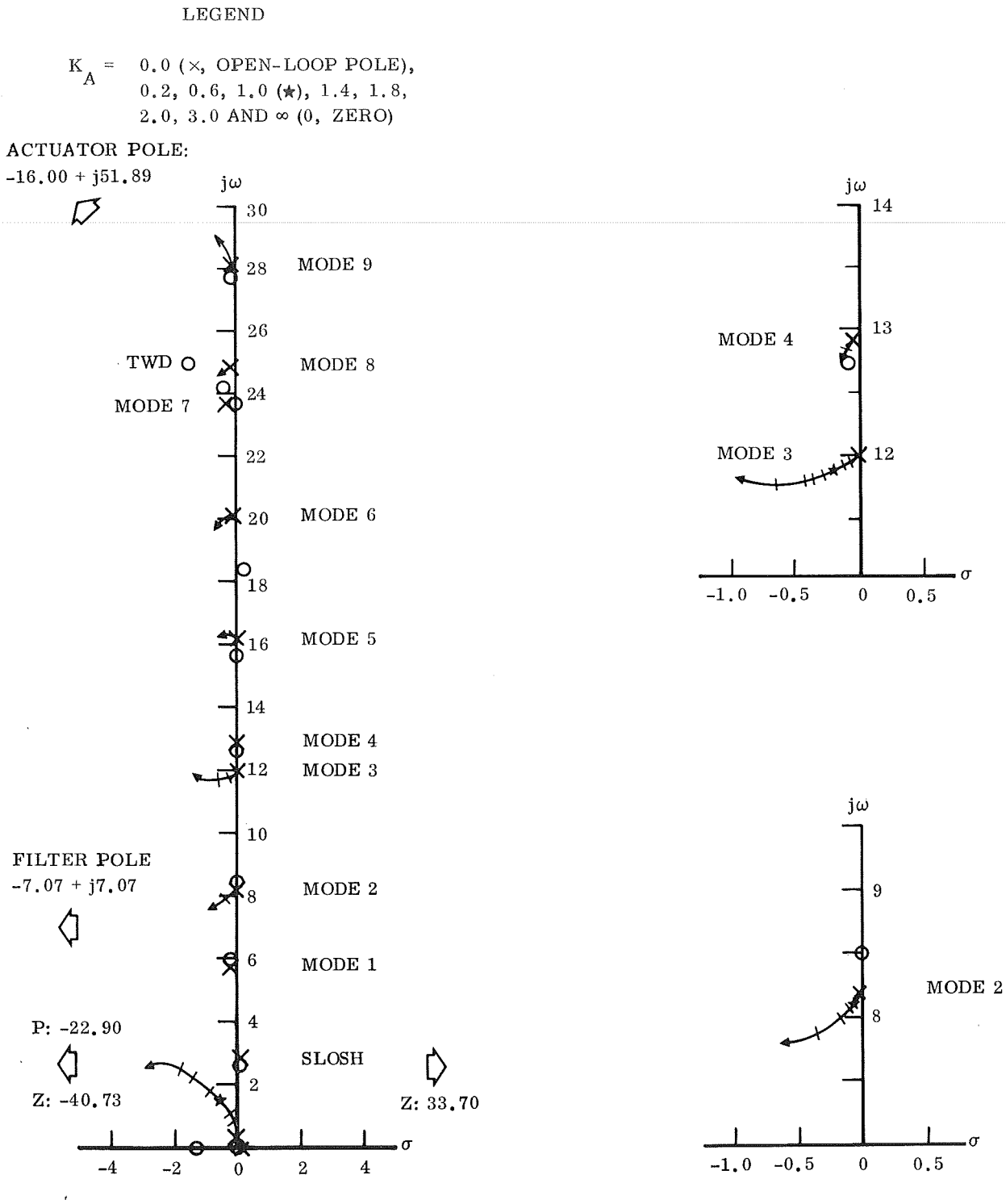

Figure 25. Planar Yaw Control, Forward Rate Sensor (Node 740), Compensated Autopilot, ω_{BEND} + 10%

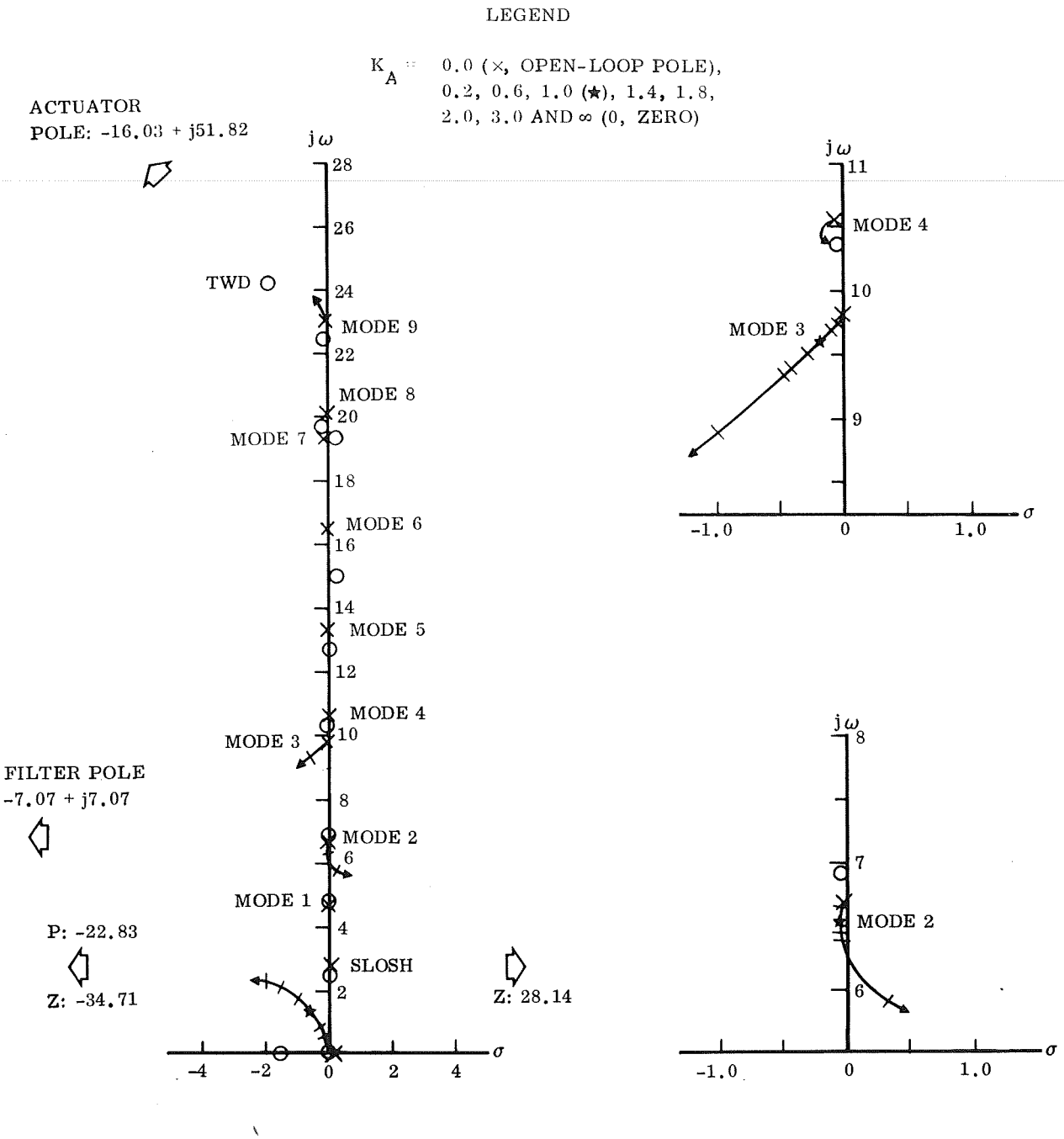

Figure 26. Planar Yaw Control, Forward Rate Sensor (Node 740), Compensated Autopilot, ω_{BEND} - 10%

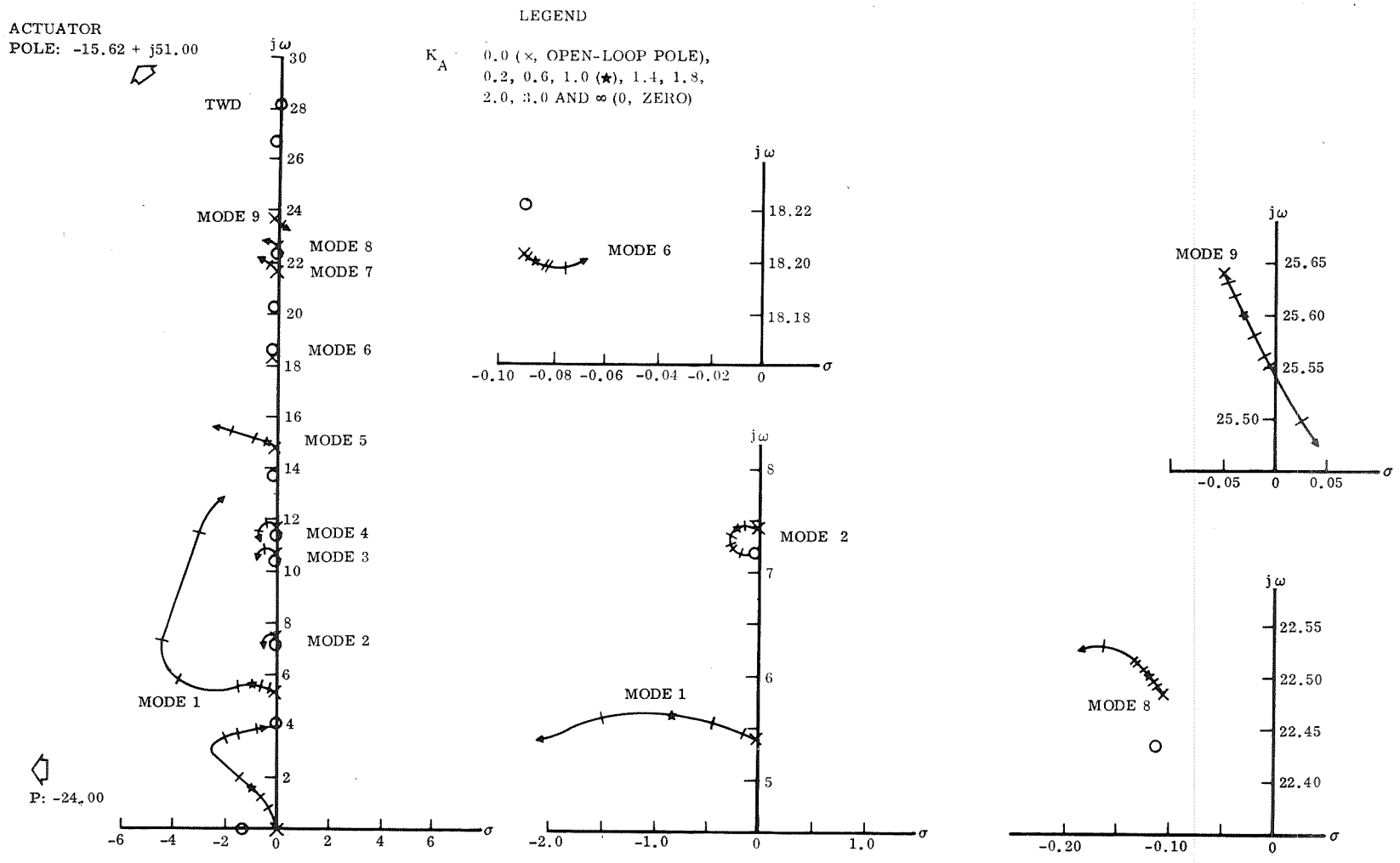

Figure 27. Planar Roll Control, Forward Rate Sensor (Node 600)

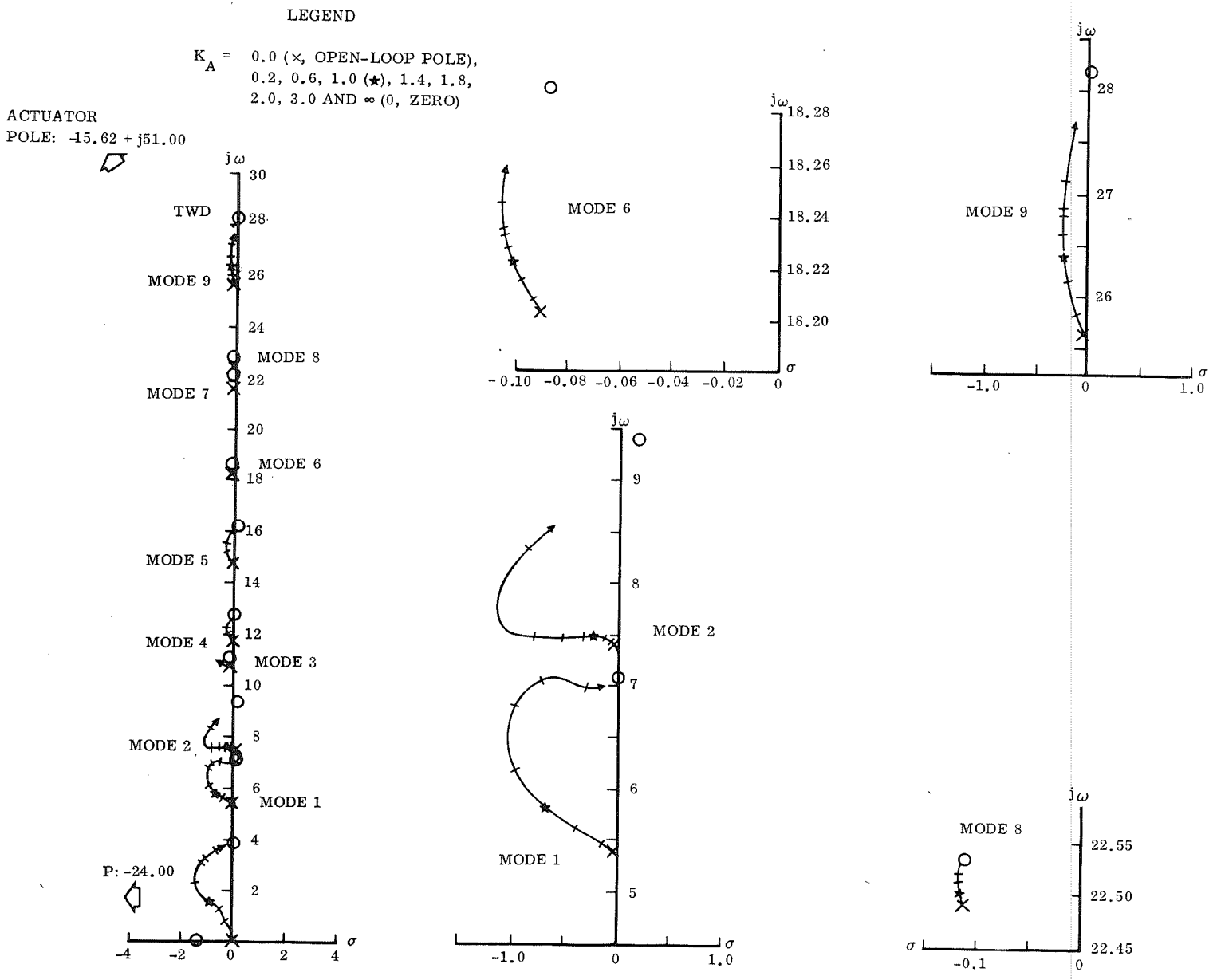

Figure 28. Planar Roll Control, Aft Rate Sensor (Node 1040)

represents the principal first body mode and has sufficiently high modal gains to require phase stabilization at this early flight time. The preferred orientation of this locus is attained with the forward rate sensor location because of the tendency of the locus to rotate clockwise with increasing modal frequency.

With this large complex and unsymmetrical structure, it might be anticipated that greater consideration should be given to local structural deformations in determining satisfactory autopilot sensor locations for this vehicle than has been the practice on other vehicles. It then follows that sufficiently detailed elastic models must be required to evaluate these effects. The use in this part of the study of a partial three-dimensional elastic model permits a brief evaluation of this situation, particularly as it pertains to the model.

For the mode shapes that were derived from this three-dimensional model, the roll characteristics have the largest differences between the equivalent centerline representation and the representation of each node around the periphery of the vehicle. These differences encompass both the magnitudes and the signs of the roll deflections.

The root locus diagram for the condition where the roll rate sensor is located at one of these peripheral nodes is shown in Figure 29. The particular node represented in this figure is on the underside of the vehicle, just aft of the canard at S. N. 2170 (model node 780-7). The roll modal data reveals that Figure 28 can be used for a comparison between this peripheral rate sensor location and a location that reflects an equivalent centerline position, particularly relative to loci departure angles.

The loci departure angles for several elastic modes have undergone an approximately 180-degree phase shift at the underside rate sensor location, and modes 2, 4, 6, 7 and 9 require some degree of phase stabilization. In particular, mode 4 at 11.7 rad/sec requires greater than 90 degrees of phase lead or phase lag. From the standpoint of conventional autopilot techniques, this is not a practical location for the roll rate sensor.

A review of the roll modal data at the model node located on the topside of the vehicle (at model node 780) reveals that these data are very similar to the equivalent centerline data. Thus, a rate sensor located at this topside node will have similar stability characteristics to those shown in Figure 28.

The effects of using the aft rate sensor configuration with dispersions in the elastic mode natural frequencies of plus and minus ten percent are shown in Figures 30 and 31. These figures illustrate that all loci still have stable closed-loop roots at a gain of $K_A = 1.0$.

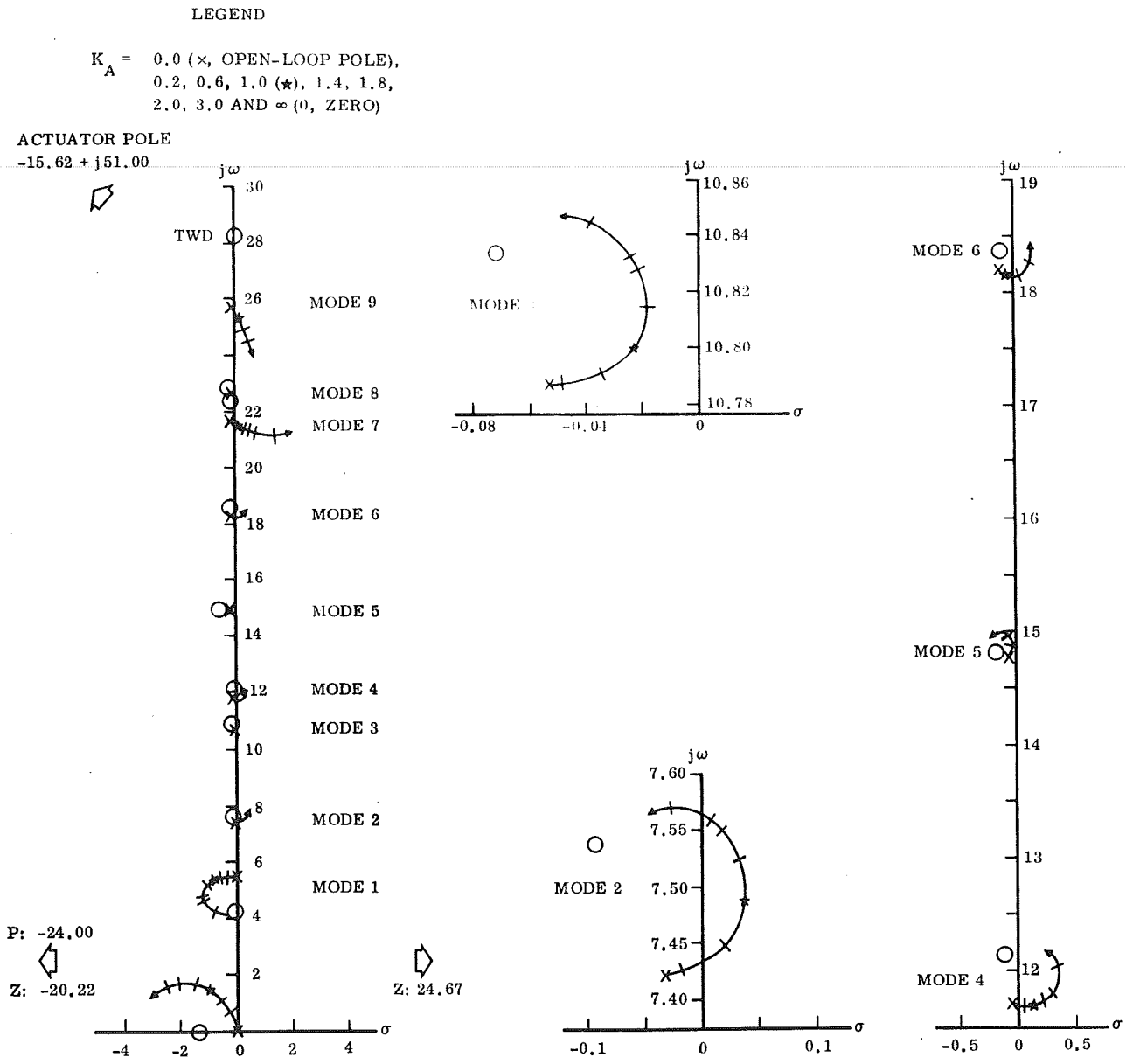

Figure 29. Planar Roll Control, Underside Rate Sensor (Node 780-7)

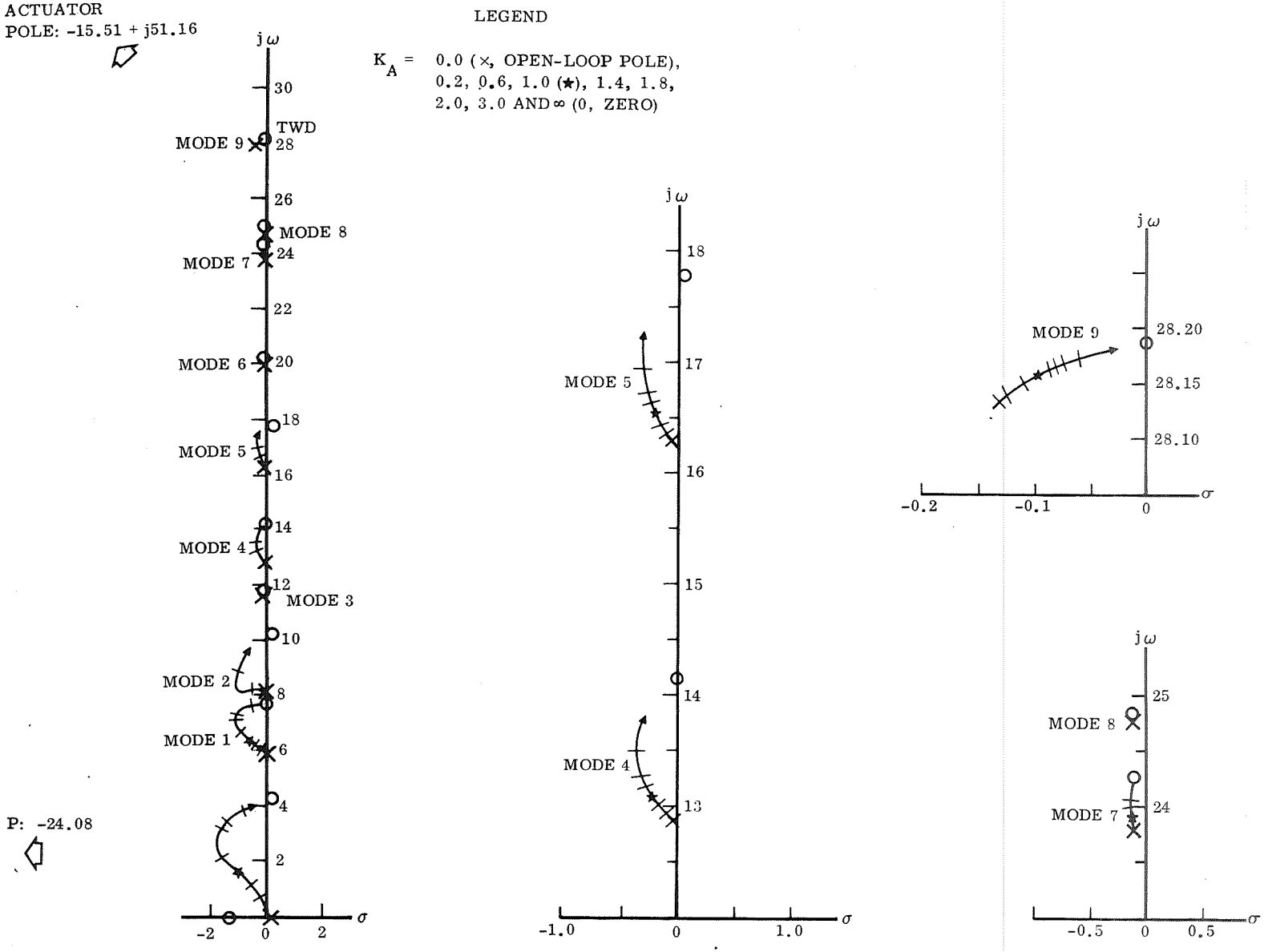

Figure 30. Planar Roll Control, Aft Rate Sensor (Node 1040), ω_{BEND} + 10%

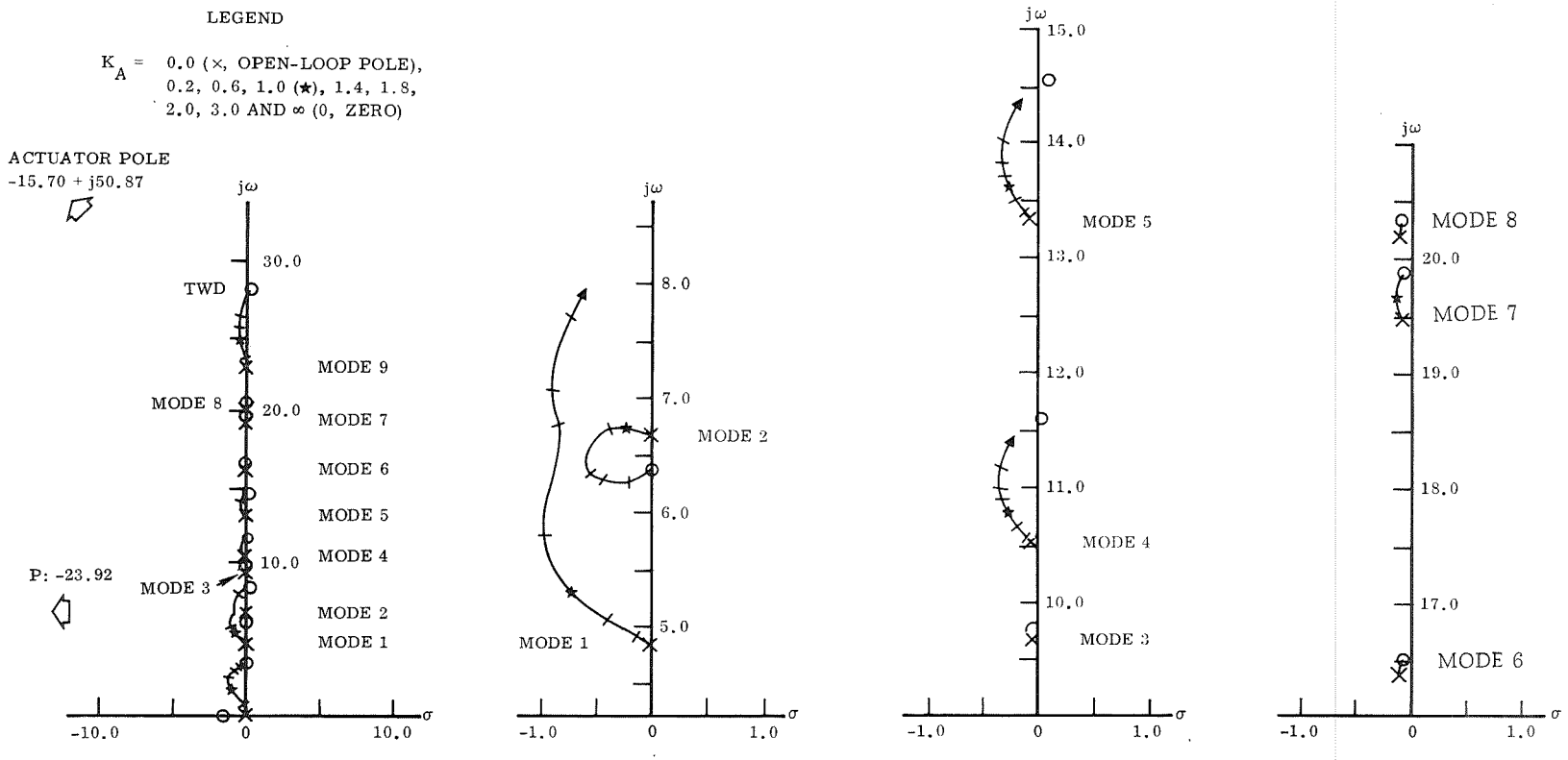

Figure 31. Planar Roll Control, Aft Rate Sensor (Node 1040), ω_{BEND} - 10%

Yaw/Roll Coupled Analysis. – With a multiloop multivariable control system, each response can be related to each input by a transfer function. The common denominator for all these transfer functions is the system characteristic equation. As with single variable systems, stability information can be obtained from the root locations of this equation.

A limitation of the root locus method is that only one varying parameter can be considered per locus. Therefore, to analyze the stability of this coupled yaw/roll system, the forward loop gain, K_A, in one of the control planes is fixed, and the locus is generated by varying the corresponding gain in the other control plane. For example, if K_A in the roll autopilot is fixed and K_A in the yaw autopilot is varied, then the resulting loci will describe the stability characteristics of the yaw control system in the presence of the roll-plane coupling effects. The two fixed values of gain used here are 0.0 (open loop) and 1.0 (assumed nominal operating point). The fixed value of 0.0 permits an evaluation of the coupling effects that are not due to the other control plane autopilot (i.e., intermodal coupling and coupling through the engine gimbal actuators).

For this analysis, the forward rate sensor configuration with autopilot stability compensation (lag filter with natural frequency of 10 rad/sec and critical damping) is used for yaw control, and the aft rate sensor configuration is used for roll control. Since the forward roll rate sensor configuration demonstrated satisfactory stability characteristics, it could be used in place of the aft rate sensor.

Figure 32 shows the stability characteristics for the yaw control system with the roll autopilot gain set equal to zero. The vehicle dynamic and load torque feedback coupling effects can be evaluated by comparing this figure with Figure 24. The rigid body locus is unchanged, and the propellant sloshing locus has retained its stable orientation. The mode 1 locus shows a large effective gain increase (compare with Figure 22), but the $K_A = 1$ point still has a greater than 6 dB gain margin. This wing mode appears to be interacting strongly in the region of the engine thrust structure. The other lower frequency mode loci exhibit only very small differences in the range of gain values that are of interest here.

The higher frequency modes in the vicinity of the tail-wags-dog zero exhibit significant differences, as indicated by the changes in the zero locations. However, these modes are still completely gain stable. Since the location of the TWD zero is now being influenced by both the yaw and roll actuator systems, it also has shifted relative to its planar location.

The stability characteristics for the roll control system with the yaw autopilot gain set to zero are illustrated in Figure 33. In a comparison with Figure 28 only very small differences are noted.

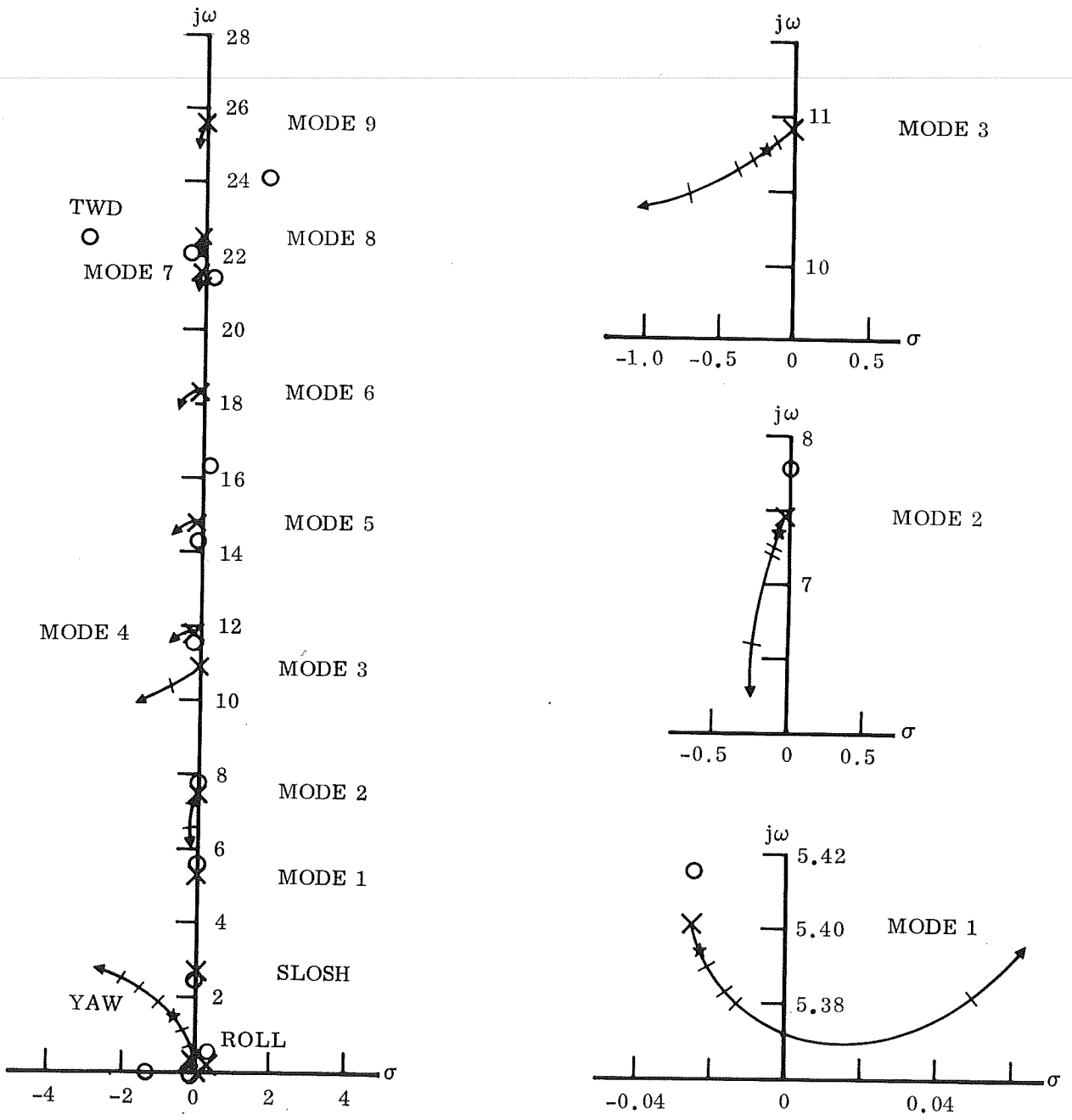

Figure 32. Coupled Yaw/Roll, Vary Yaw Autopilot Gain, Roll Gain = 0.0

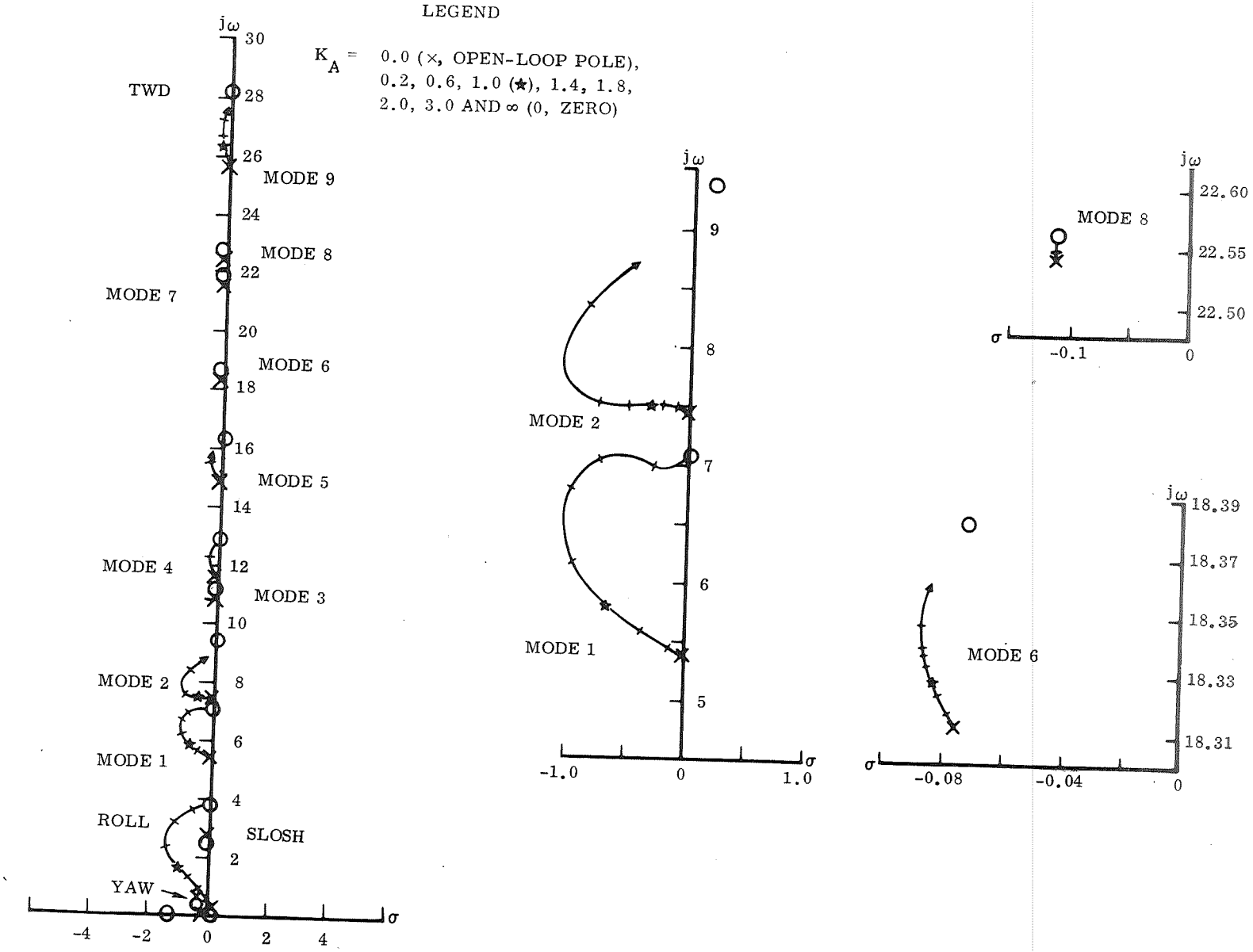

Figure 33. Coupled Yaw/Roll, Vary Roll Autopilot Gain, Yaw Gain = 0.0

The completely coupled system is illustrated in Figure 34 with a variable yaw autopilot forward loop gain and a fixed value of 1.0 (nominal operating point) for the roll autopilot gain. The loci in this figure have the general shape shown in Figure 32, and the open loop poles (the Xs) for the bending mode loci are located at the position of the closed-loop roots (K_A = 1.0 points) in Figure 33. Figure 34 shows that the loci for Modes 1, 4, 5, 6, 7, 8 and 9 are gain stable with at least 6 dB gain margin for all values of phase, and that Modes 2 and 3 are phase stable with phase margins greater than or equal to thirty degrees.

Figure 35 is the corresponding plot for a variable roll autopilot forward loop gain and a fixed value of 1.0 (nominal operating point) for the yaw autopilot gain. Here, the loci have the general shape shown in Figure 33, and the open-loop poles for the bending mode loci are located at the position of the closed-loop roots in Figure 32. All of the bending mode loci in Figure 35 are adequately stabilized with Modes 3, 6, and 8 gain stable for all phase orientations.

In conclusion, this analysis has demonstrated the feasibility of using conventional autopilot techniques to provide lateral (yaw/roll) control for the dual flyback vehicle with adequate stability and performance characteristics at the liftoff flight condition.

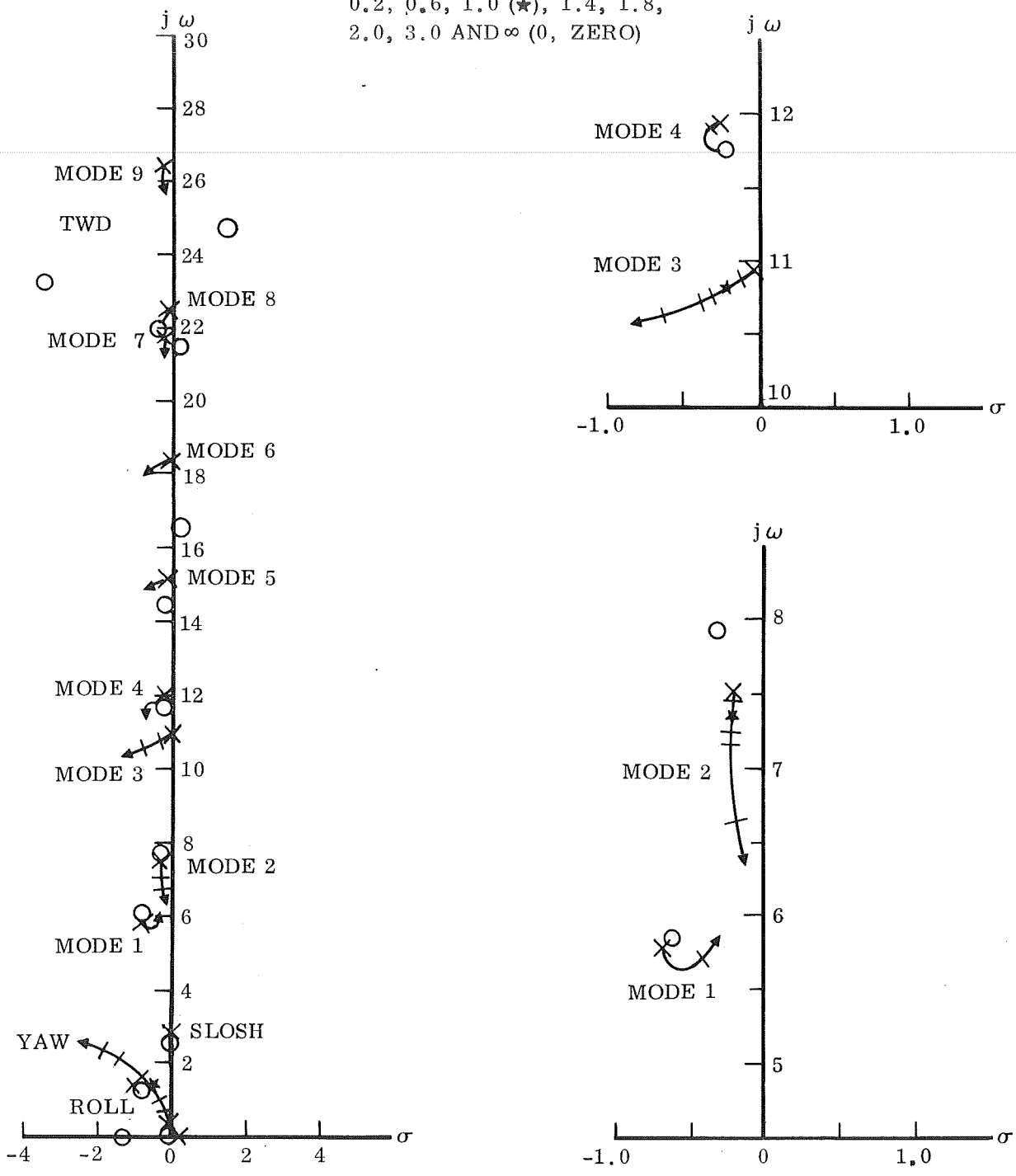

Figure 34. Coupled Yaw/Roll, Vary Yaw Autopilot Gain, Roll Gain = 1.0

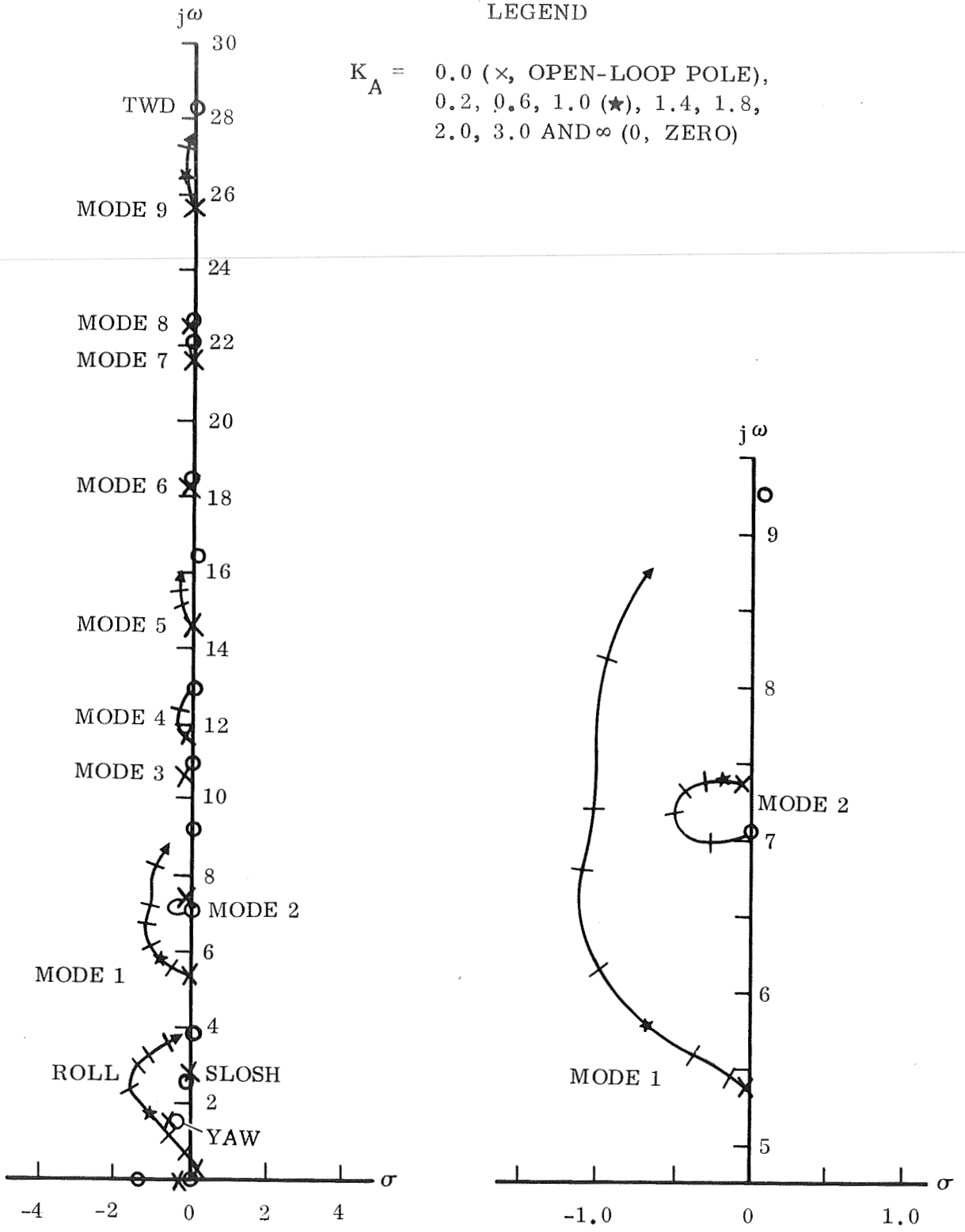

Figure 35. Coupled Yaw/Roll, Vary Roll Autopilot Gain, Yaw Gain = 1.0

5 SOLID MOTOR VEHICLE ANALYSIS

This section contains the analysis results for the solid motor vehicle. The first part surveys the rigid body stability and control characteristics to establish a set of baseline autopilot gains for reference in the remainder of this section. This part also discusses propellant sloshing mode stability. The last two parts analyze the elastic mode stability problem for symmetric and antisymmetric mode boundary conditions.

Figure 36 compares the solid motor vehicle modal frequencies with those for

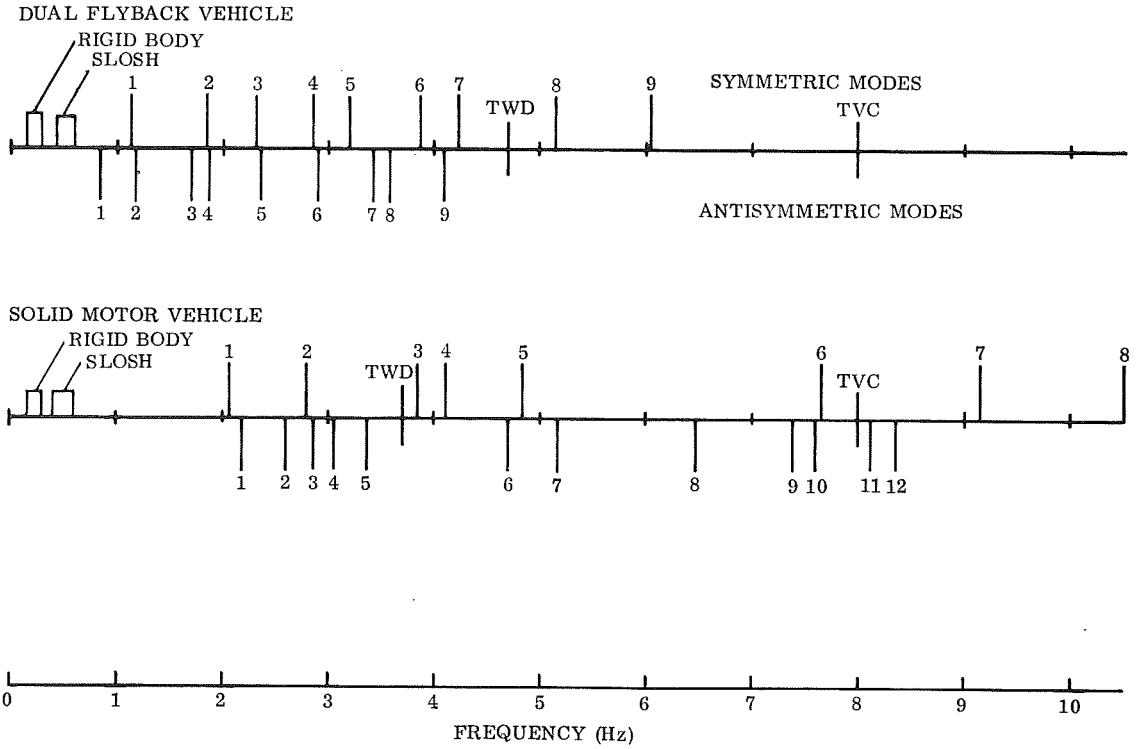

Figure 36. Modal Frequency Comparison

the dual flyback vehicle. The solid motor vehicle has higher first elastic mode frequencies and the resulting frequency separation of greater than a factor of two between the propellant sloshing modes and the lower elastic modes greatly minimizes the coupling potential between these modes.

The decrease in the tail-wags-dog frequency indicates that this singularity will have a greater influence in determining the stability characteristics of the solid motor vehicle first body modes than it did for the dual flyback vehicle.

Control forces for this vehicle can be obtained from three sources: the orbiter liquid propellant engines, the solid rocket motors, and the orbiter aerodynamic surfaces. Current shuttle concepts favor using thrust vector control on the orbiter engines with the possibility of using the orbiter aerodynamic surfaces if additional control forces are required during the high dynamic pressure region of flight. Thrust vector control on the solid motors is not considered a viable alternative at this time because of the cost and weight penalties that are associated with its implementation.

The baseline configuration for this study uses only thrust vector control of the three orbiter engines. Aerodynamic surfaces are not considered because of their relative ineffectiveness at the liftoff flight condition. Thrust vector control on the solid motors is briefly considered to demonstrate its effect on elastic mode stability.

Rigid Body and Propellant Sloshing Modes

There are two areas of concern relative to the magnitude of the control forces available on the solid motor vehicle during the atmospheric portion of flight. The first involves the control authority (gimbal angle capability) required to satisfactorily maintain the vehicle's desired heading. The second pertains directly to this study and involves the stability and performance characteristics of the vehicle control mode.

Some insight into the second area at the liftoff flight condition can be obtained by examining the control moment effectiveness ratios (control thrust times control moment arm divided by moment of inertia) for each of the control planes:

	Solid Motor Vehicle		
Control Plane	Orbiter TVC Only	Orbiter TVC + Solid Motor TVC	Dual Flyback Vehicle
Pitch	0.31	1.6	1.8
Yaw	0.27	1.4	1.8
Roll	0.11	2.4	3.0

If the orbiter engines and the solid motors are both used for control, the solid motor vehicle ratios are comparable to those for the dual flyback vehicle. However, if only the orbiter engines are considered, the ratios are considerably less than those for the other two configurations. This implies that the "baseline" solid motor

vehicle (orbiter TVC only) will require higher autopilot gains to obtain satisfactory control mode response characteristics.

The control mode gains can be determined from the pitch, yaw and roll control mode root loci shown in Figure 37. For a minimum response with a damping ratio not less than 0.3 and a damped natural frequency of approximately 1 rad/sec, the autopilot forward loop gains are: pitch = 4.0, yaw = 4.0, and roll = 10.0. The autopilot rate gain (K_R) for each control channel is 0.7.

Propellant sloshing will have a negligible effect on the overall vehicle stability characteristics at the liftoff flight condition. The oxidizer and fuel sloshing masses are only 0.9% and 0.3% of the vehicle mass. The tank levels that correspond to this time of flight are shown in Figure D1 in Appendix D. It has already been shown in Figure 36 that the lowest elastic mode frequencies are approximately a factor of three removed from the sloshing natural frequencies, indicating a negligible coupling potential between these very lightly damped modes.

The sloshing natural frequencies are illustrated in Figure 38 as a function of flight time. The two sloshing modes have different natural frequencies because the oxidizer fluid level is in the conical section of the tank during these early flight times. This frequency separation and the relatively small fuel sloshing mass will tend to further minimize the coupling potential between these sloshing modes.

Based upon these facts and the results of the dual flyback vehicle analyses it is assumed that propellant sloshing effects can be neglected at this time of flight. In order to evaluate this assumption and detect any potential surprises the vehicle model used in this section includes the oxidizer sloshing mode.

Symmetric Elastic Mode Stability

From the standpoint of stability and control, the solid motor space shuttle configuration represents a major design departure from present operational vehicles, and even from the dual flyback vehicle. Four large bodies, three of which have quite different structural properties are coupled together in a parallel arrangement. This produces a situation where there can be a large amount of interaction between the individual elements of the vehicle through the connecting linkage systems.

Some indication of this interaction can be obtained by examining the elastic mode shapes contained in Appendix D (Figure D3). The body bending mode shapes are summarized in the following table.

LEGEND

K_A = 0.0 (×, POLE), 0.2, 0.6, 1.0, 2.0, 3.0, 4.0 (✱), 5.0, 6.0, 8.0, 10.0, ∞(0, ZERO)

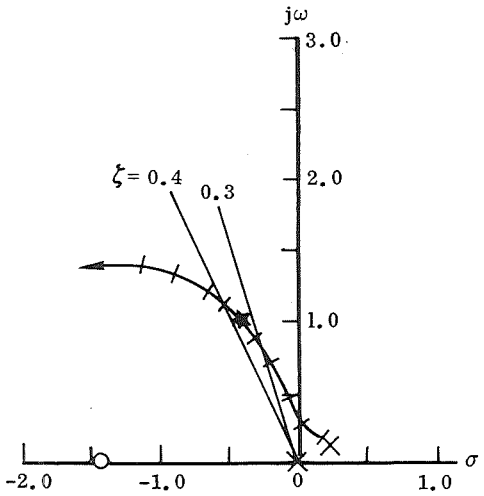

(a) Pitch Control Mode

LEGEND

K_A = 0.0 (×, POLE), 0.2, 0.6, 1.0, 2.0, 4.0 (✱), 5.0, 6.0, 8.0, 10.0, 12.0, ∞(0, ZERO)

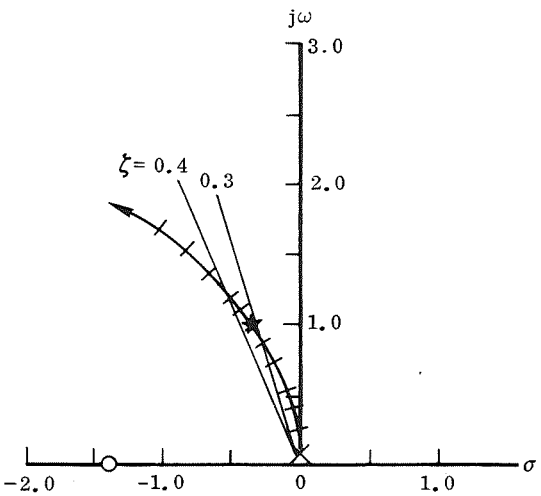

(b) Yaw Control Mode

LEGEND

K_A = 0.0 (×, POLE), 0.2, 1.0, 2.0, 4.0, 6.0, 8.0, 10.0 (✱), 15.0, 20.0, 25.0, 30.0, ∞(0, ZERO)

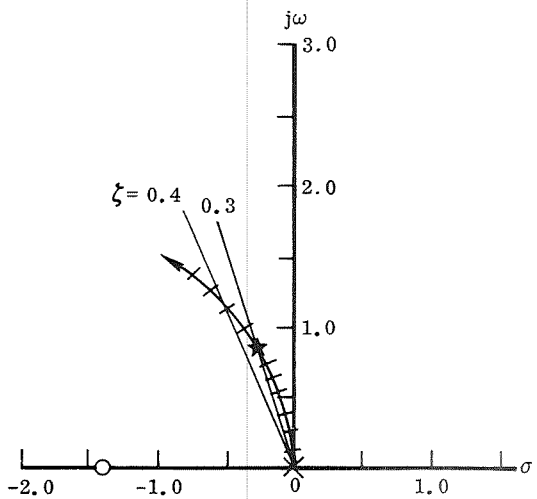

(c) Roll Control Mode

Figure 37. Rigid Body Root Loci

Elastic Mode	Body Mode			Comments
	Orbiter	Tank	SRM	
1			"Bridge"	Orbiter pitching and plunging on links
2				Orbiter pitching motion on links
3	First		First	Dominant orbiter mode
4	First	First	First	Orbiter opposing tank and dominant SRM mode
5				Large orbiter forward end deflections
6	Second			Dominant orbiter forward end
7	Second	First	Second	Dominant SRM mode
8	Second	First		Dominant tank mode

Only those body modes that exhibit all of the classical properties of the indicated mode shape are listed. In the first elastic mode the SRM element mode shape represents the classic first mode for an elastic body that is pinned at both ends.

There is an important difference between the orbiter mode shape in elastic mode 5 and the orbiter first body mode shapes in elastic modes 3 and 4. In mode 5 the sign relationship between the modal slope along the length of the element and the modal deflection at the engine gimbal point is the opposite of the corresponding relationship for a first body mode. If the autopilot sensors are mounted on the orbiter, this sign difference will appear in a root locus diagram as a 180 degree phase shift between the locus departure angles from the mode 4 and 5 open loop poles. Considering the small frequency separation between these two modes, this condition will complicate the elastic mode stability problem, particularly if one or both of these modes is dependent on some form of phase stabilization.

Although the preferred location for the autopilot sensors is on the orbiter, the stability complications that developed indicated that it might be more advantageous to locate these sensors on the tank or the SRM. The sensor locations examined in this analysis are indicated in Figure 39.

The root locus diagrams for orbiter rate sensor locations forward and aft of the first body mode antinode are shown in Figures 40 and 41. The forward location is at model node 4 and the aft location is at model node 7. For both cases the attitude sensor is located in the orbiter nose (model node 1).

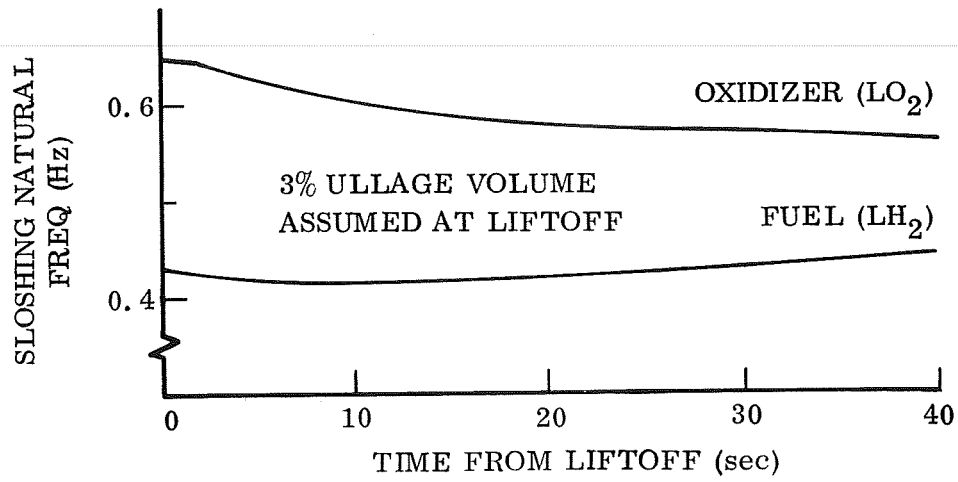

Figure 38. Solid Motor Vehicle Propellant Sloshing Natural Frequencies

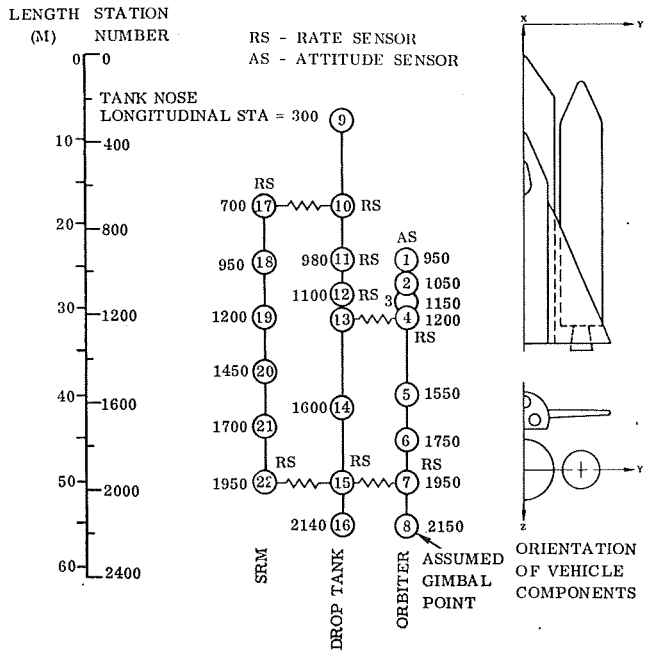

Figure 39. Autopilot Sensor Locations

The stability consequences of the high autopilot forward loop gain are clearly evident in Figure 40. The high modal gain forces the closed-loop roots to be significantly displaced from the open-loop poles. This makes modal phasing particularly critical, even for the higher frequency modes. Theoretically, the modal gain attenuation required to stabilize this configuration (approximately -17 dB) could be obtained by locating the rate sensor very close to the first body mode antinode. However, the uncertainties inherent in the location of an antinode for all flight times and the existence of two first body mode antinodes (one for each first mode) eliminates this solution from practical consideration.

The location of the tail-wags-dog zero at approximately 19 rad/sec has placed this singularity below the orbiter first body mode natural frequencies, but above the two lowest frequency elastic modes. As a result of this location the loci emanating from the first body mode open loop poles are departing upward, instead of the downward orientation that is customarily associated with a forward rate sensor configuration.

The highly unstable condition at the nominal operating gain precludes the use of conventional autopilot techniques to stabilize this configuration. Adequate gain attenuation cannot be practically obtained and phase compensation is limited by the opposing nature of the mode 4 and mode 5 loci and the small frequency separation between these modes.

For the aft rate sensor location (Figure 41) the effect of the high autopilot forward loop gain is evidenced by the nearness of the nominal operating gain to the terminal zero. However, except for the locus from the mode 3 open-loop pole, all elastic mode loci are completely inside the left-half plane.

Although modes 2 and 3 have similar modal parameters relative to the rate sensor location and the engine gimbal point, the presence of the TWD zero has resulted in an approximately 180 degree difference in their locus departure angles, and an unstable system.

The small frequency separation between these two modes makes phase stabilization extremely difficult. An example of this is shown in Figure 42 where a single lag filter with a 0.008 second time constant has been added to the autopilot forward loop. Although this filter contributes only ten degrees of phase lag at 24 rad/sec it is sufficient to cause the loci to "swap" zeros. Now, any additional phase lag will increase the system instability by producing a clockwise rotation of the mode 2 locus.

The effects of modal frequency uncertainties in this unstable region are simulated by varying the natural frequency of mode 2 by minus 2 rad/sec and by plus 2.9 rad/sec.

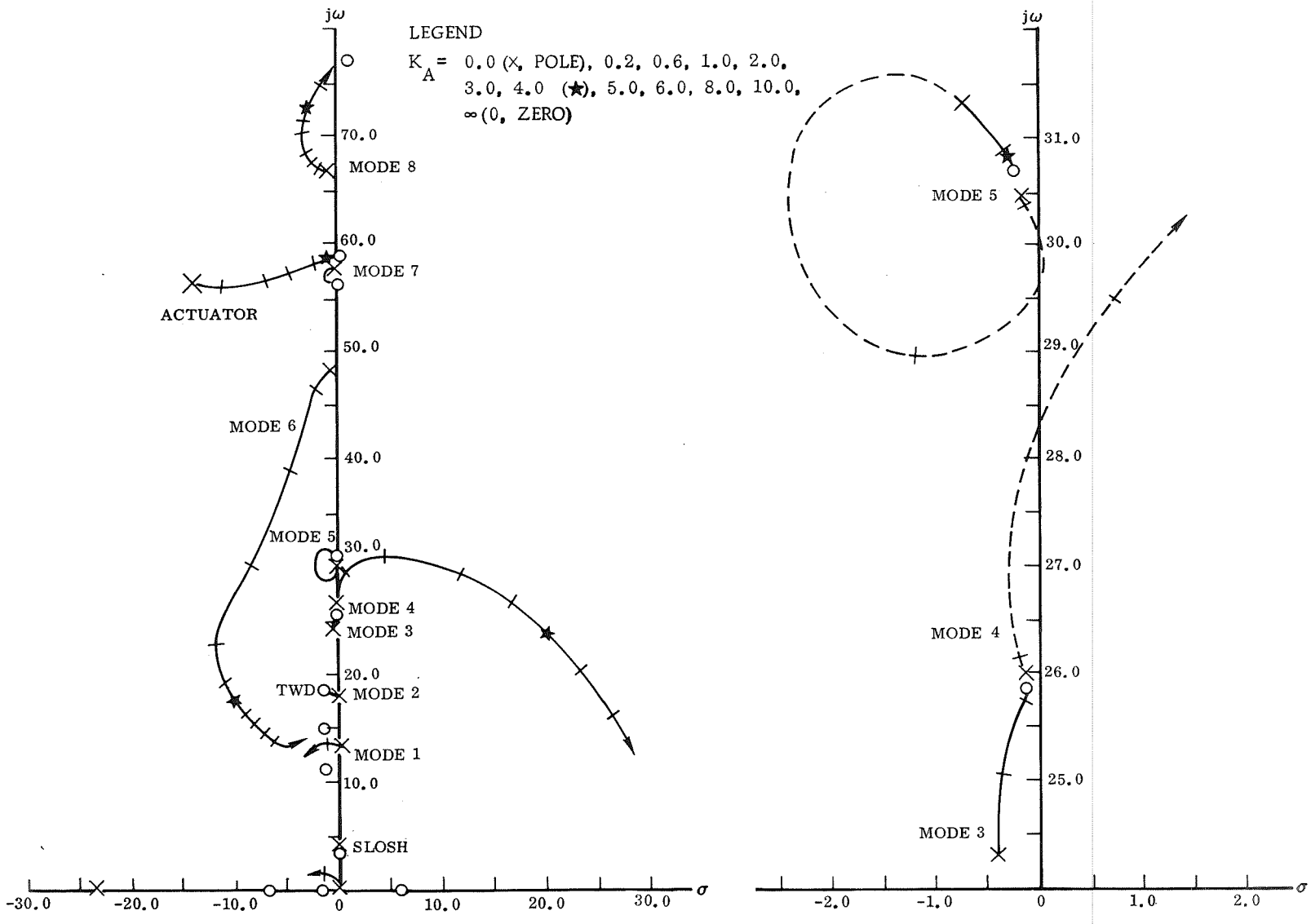

Figure 40. Forward Rate Sensor on Orbiter (Node 4)

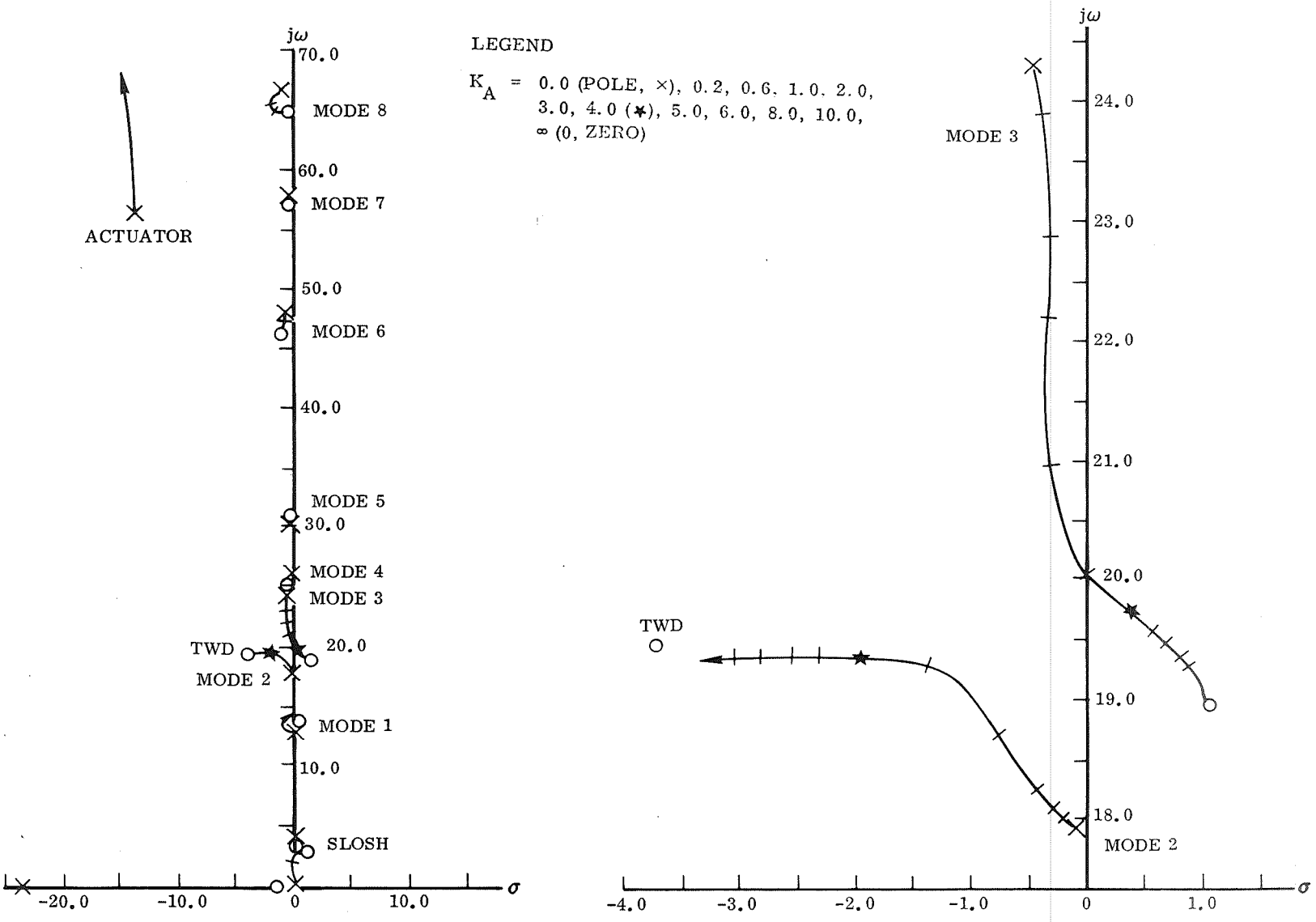

Figure 41. Aft Rate Sensor on Orbiter (Node 7)

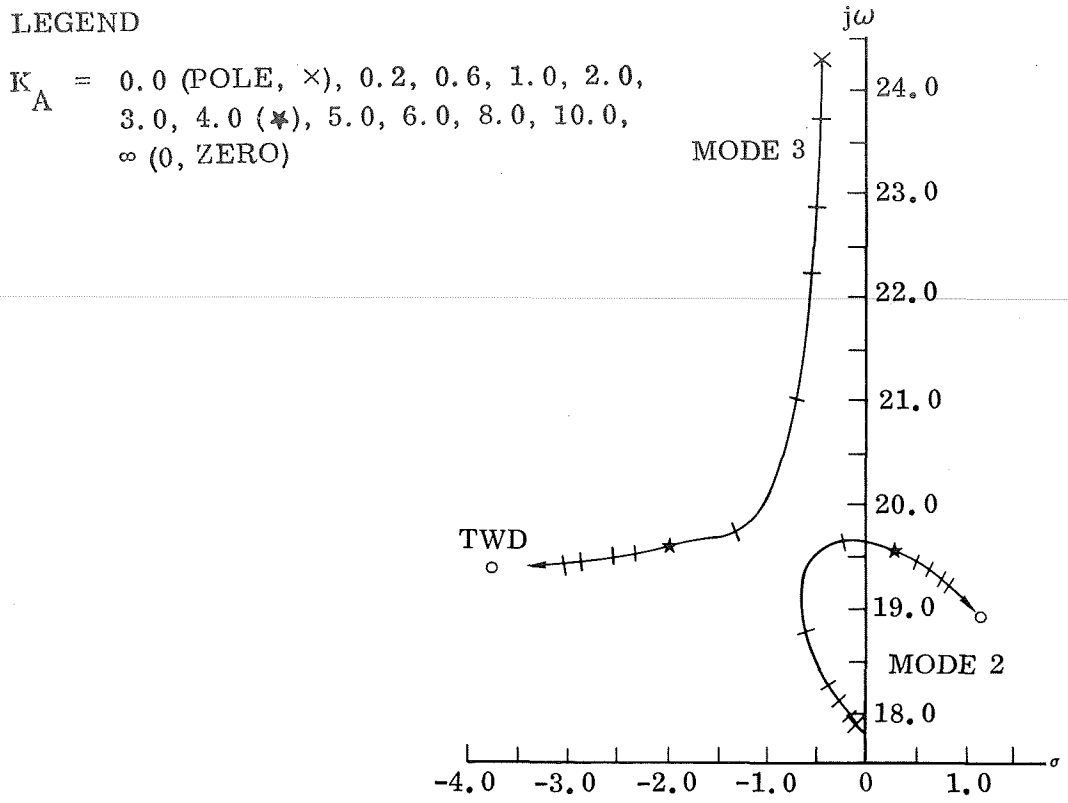

Figure 42. Aft Rate Sensor on Orbiter (Node 7), Compensated Autopilot

The root locus diagrams for these two conditions, along with the one for the "nominal" value of frequency, are shown in Figure 43.

Increasing the frequency separation between the mode 2 open-loop pole and the TWD zero increases the system stability. In both cases the system is now more amenable to conventional autopilot stability compensation, but the high gain still makes the attainable degree of stability marginal.

Thus far conventional autopilot techniques have been considered for a configuration which has the autopilot sensors mounted on the orbiter and uses only orbiter engine TVC. The high modal gains and the closeness of the elastic mode frequencies limits the ability of these techniques to provide adequate stability compensation for this configuration.

Although the two rate sensor concept is not, strictly speaking, a conventional autopilot technique, the extra degree of freedom that it provides the controls designer could be very useful for this vehicle. Figure 44 shows the results for a two rate sensor configuration where the rate gain for the forward rate sensor at node 4 is 0.2

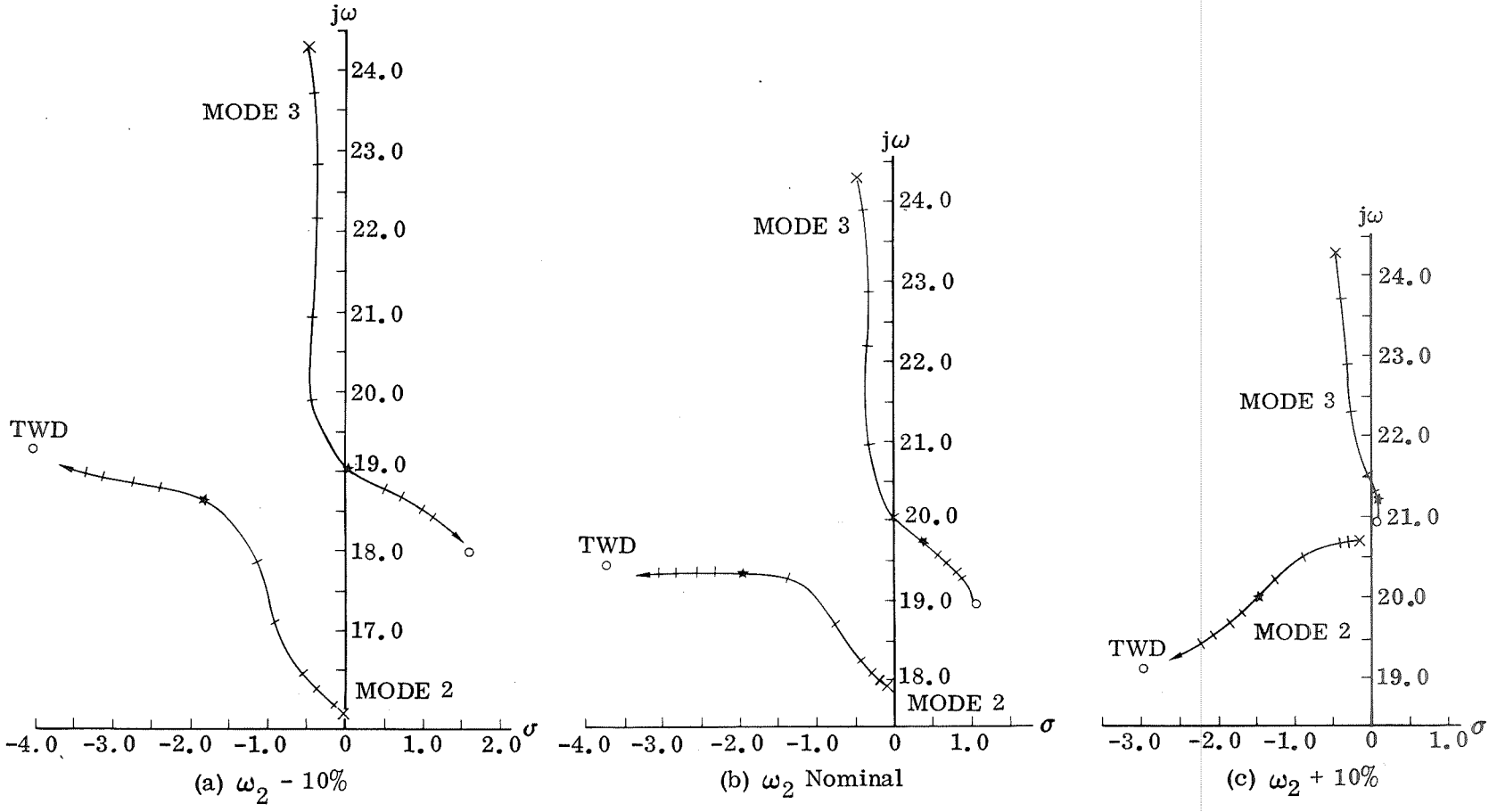

Figure 43. Aft Rate Sensor on Orbiter (Node 7), Vary Mode 2 Natural Frequency

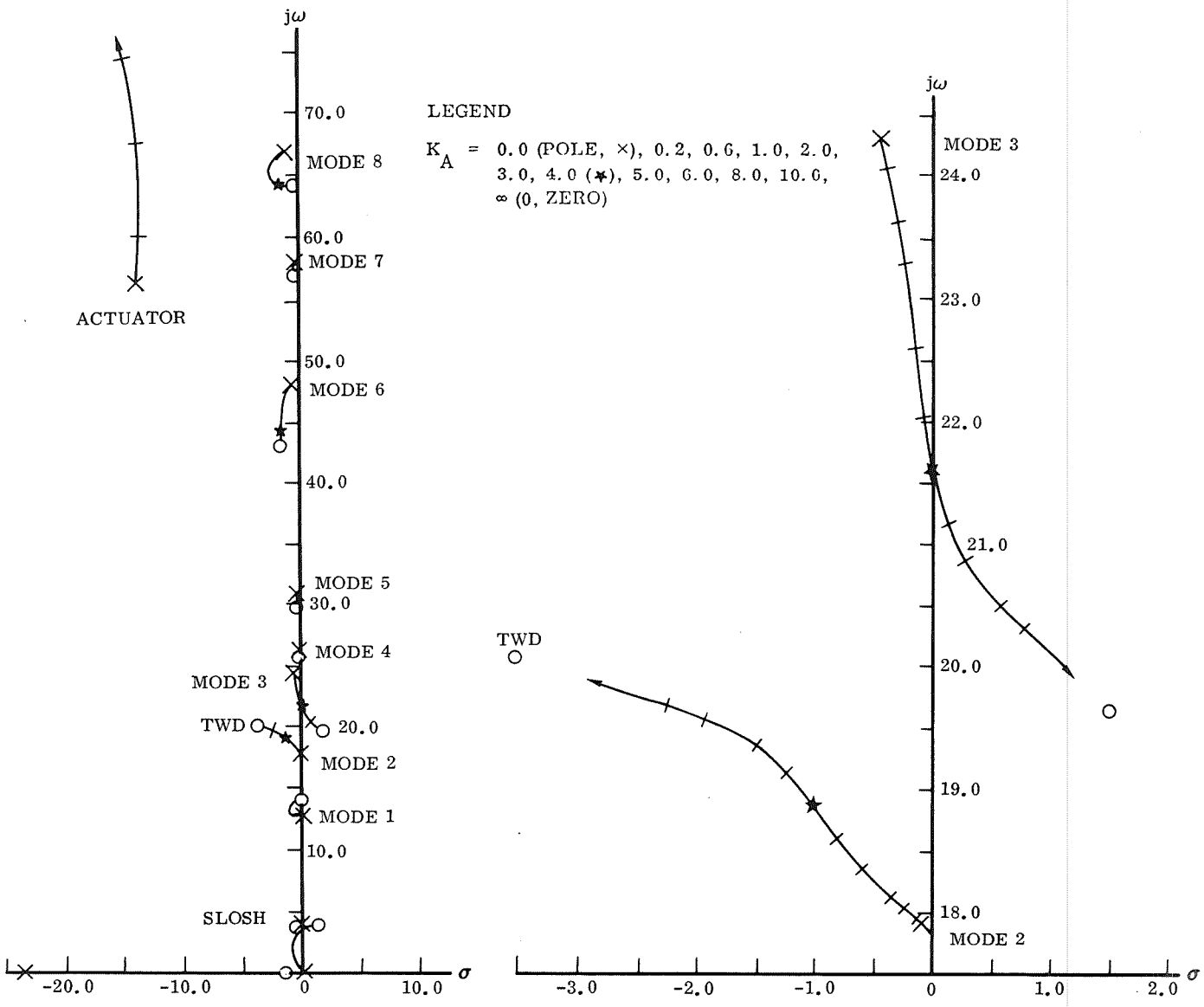

Figure 44. Two Rate Sensors on Orbiter, Forward at Node 4 and Aft at Node 7

and 0.5 for the aft rate sensor at node 7. The autopilot attitude sensor is located in the orbiter nose at node 1.

The rate gains are weighted in favor of the aft rate sensor because of the highly unstable condition produced by the forward rate sensor. The result is that the loci near the TWD zero are oriented in much the same way as they are for the aft rate sensor configuration (see Figure 41). However, the two rate sensor configuration produces a noticeable stability improvement by introducing some modal gain attentuation into the mode 2 and mode 3 loci. A small amount of lag filtering can now be used to shift the mode 3 closed-loop root into the left-half plane.

Although system stability can be attained with this autopilot configuration, the gain and phase margins are not adequate, particularly for the modes near the TWD zero. The root loci orientations in this region are sensitive to the modal parameters and large stability margins are required to compensate for modal uncertainties.

To round-out this symmetric mode analysis two other control configurations will be briefly analyzed. The first will consider mounting the autopilot sensors, principally the rate sensor, on the other vehicle elements (the external tank and the SRM). The second configuration will add SRM TVC to the orbiter TVC.

Figure 45 (a) shows the root locus diagram for a rate sensor mounted on the tank near the orbiter forward linkage system (node 12) and an attitude sensor located in the orbiter nose (node 1). All modes exhibit stable characteristics with the exception of mode 3 (orbiter first body mode) and mode 8 (tank first body mode).

When the two autopilot sensors are located on different vehicle components it is possible that the attitude signal may dominate the rate signal. It is easy to verify from the mode shape in Figure D3 of Appendix D that this is the situation for mode 3. This also suggests that this mode could be stabilized by filtering only the attitude signal, particularly if the stability of the neighboring modes is not dependent on this signal.

Figure 45 (b) illustrates the effect of placing a critically damped quadratic lag filter, with a natural frequency of 10 rad/sec, in the attitude signal path. Mode 3 has been stabilized without destabilizing any of the surrounding modes, although the orientation of some of them (e.g., mode 6)has been significantly altered. This leaves only the first tank mode in an unstable configuration. Because of the high modal gains this mode must be phase stabilized by introducing approximately ninety degrees of phase lag into the autopilot forward loop. This large amount of phase lag will make the modes at 30 and 25 rad/sec marginally stable.

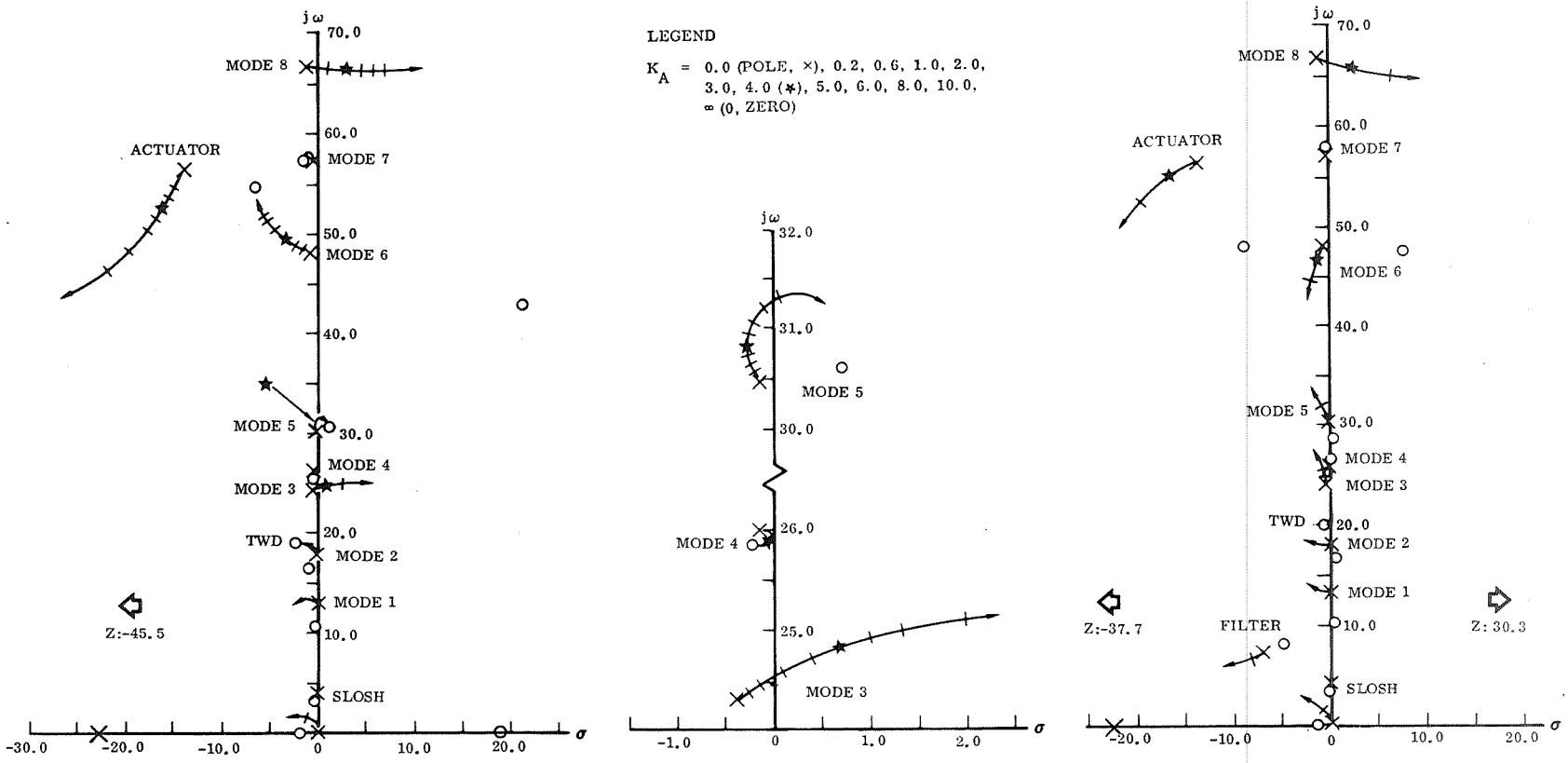

(a) Uncompensated Autopilot

(b) Compensated Autopilot

Figure 45. Rate Sensor Near Mid Tank (Node 12), Attitude Sensor In Orbiter Nose (Node 1)

The high signal attenuation factor introduced by the quadratic lag filter in the attitude sensor feedback path minimizes the influence of this sensor on the stability of modes above 20 rad/sec. This condition produces approximately the same results obtained if the attitude sensor is placed at the same location as the rate sensor.

Although the rate sensor position in Figure 45 is near the middle of the tank element, it is aft of the tank first body mode antinode. A sensor position near the orbiter aft linkage system (node 15) was also analyzed with results very similar to those for the mid-tank position. The only difference of any consequence to the system stability is the mode 8 gain increase for the aft sensor location. This modal gain increase increases the phase compensation required for stability, making this aft sensor location less desirable than the mid-tank position.

Locating the rate and attitude sensors on the tank near the SRM forward linkage system (node 10) produces the results shown in Figure 46. Now the rate sensor is forward of the first tank mode antinode and mode 8 departs into the left-half plane. All loci exhibit stable configurations except mode 4. Unfortunately, modes 3 and 4 are in a basically unstable configuration. Introducing the lag compensation required to stabilize mode 4 will cause the two loci to "swap" zeros, with the result that the system will still be unstable.

Locating the rate sensor on the forward end of the SRM (node 17) and the attitude sensor in the orbiter nose produces the root loci configuration shown in Figure 47. Modes 1, 3 and 7 exhibit unstable orientations and filtering the attitude sensor signal does not alter this situation. All three modes must be phase stabilized, but the conflicting phase stabilization requirements between adjacent modes rules out this approach.

The root locus diagram for the rate sensor on the aft end of the SRM (node 22) and the attitude sensor in the orbiter nose is shown in Figure 48(a). Modes 2, 3, 4 and 7 exhibit unstable orientations. If the attitude sensor is moved to the rate sensor location on the SRM (Figure 48(b)) only modes 2 and 7 are still unstable. However, any phase compensation introduced to stabilize these modes will destabilize either mode 3 or mode 4.

One of the major difficulties in attempting to solve the elastic mode stability problem for this vehicle is the destabilizing influence of high modal gains. These high gains, for the most part, are a result of the relatively high autopilot forward loop gain required to achieve satisfactory control-mode stability and response characteristics. To decrease this gain, it is necessary to increase the magnitude of the control forces.

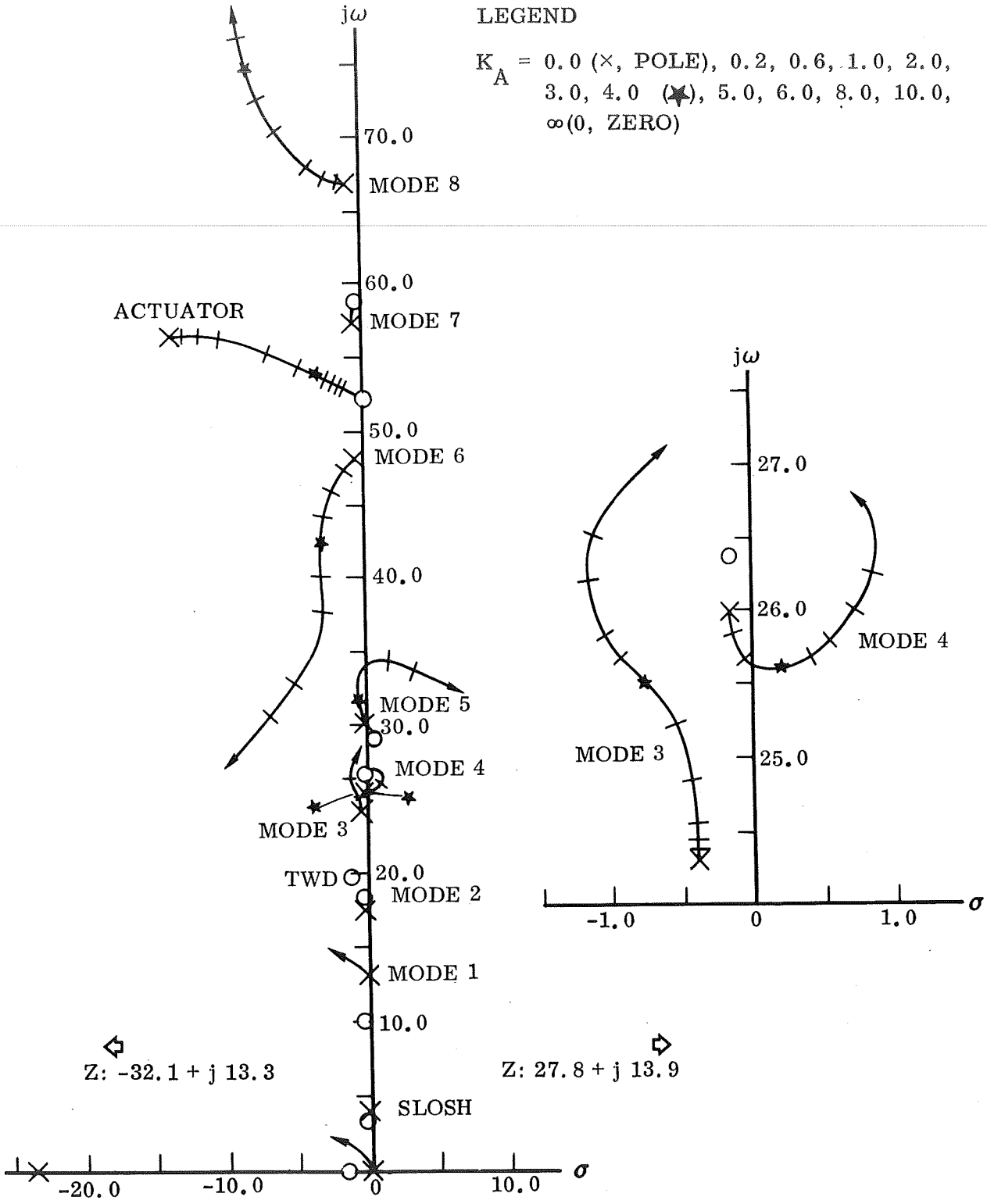

Figure 46. Forward Rate and Attitude Sensors on Tank at Node 10

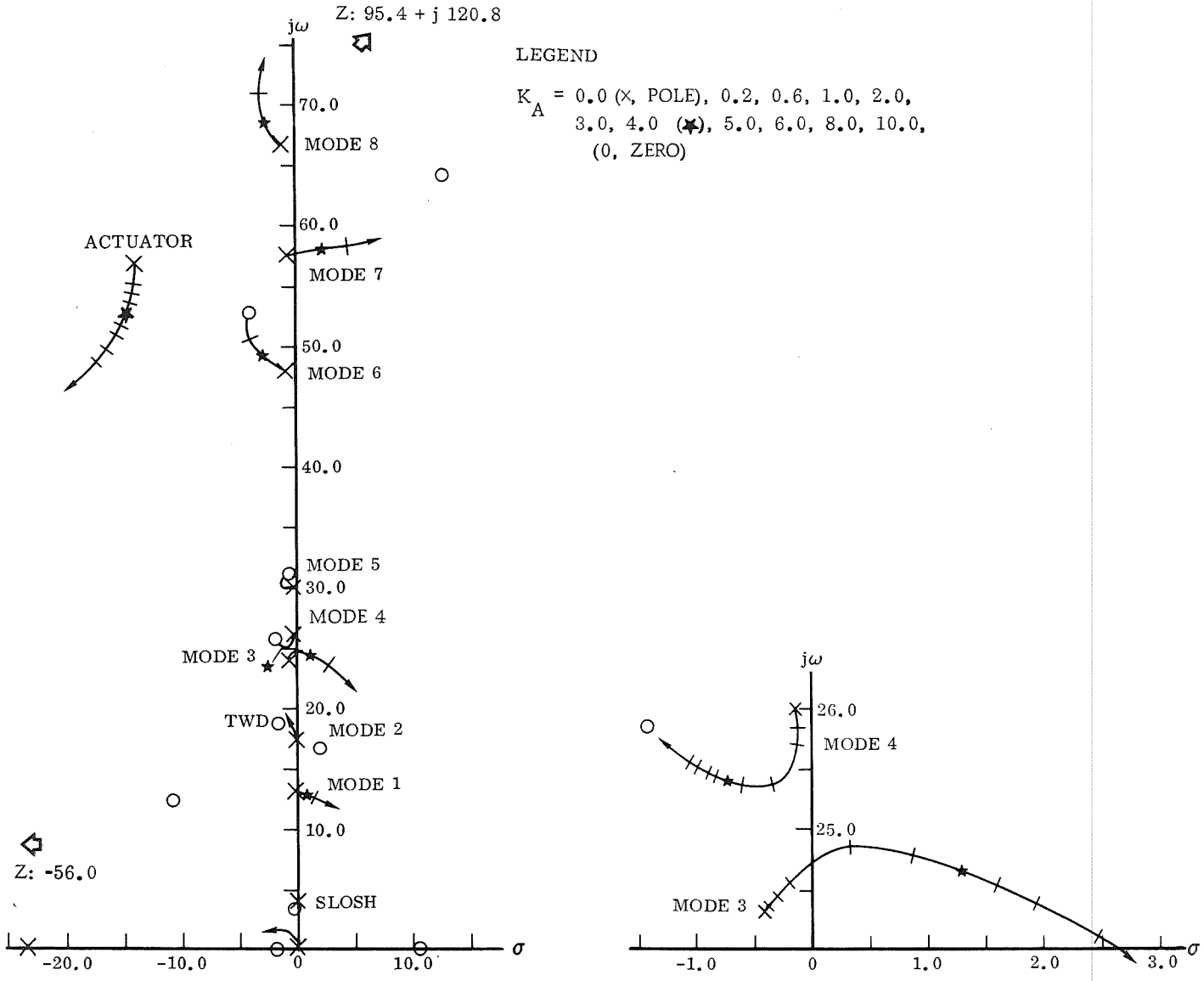

Figure 47. Rate Sensor Forward on SRM (Node 17), Attitude Sensor in Orbiter Nose (Node 1)

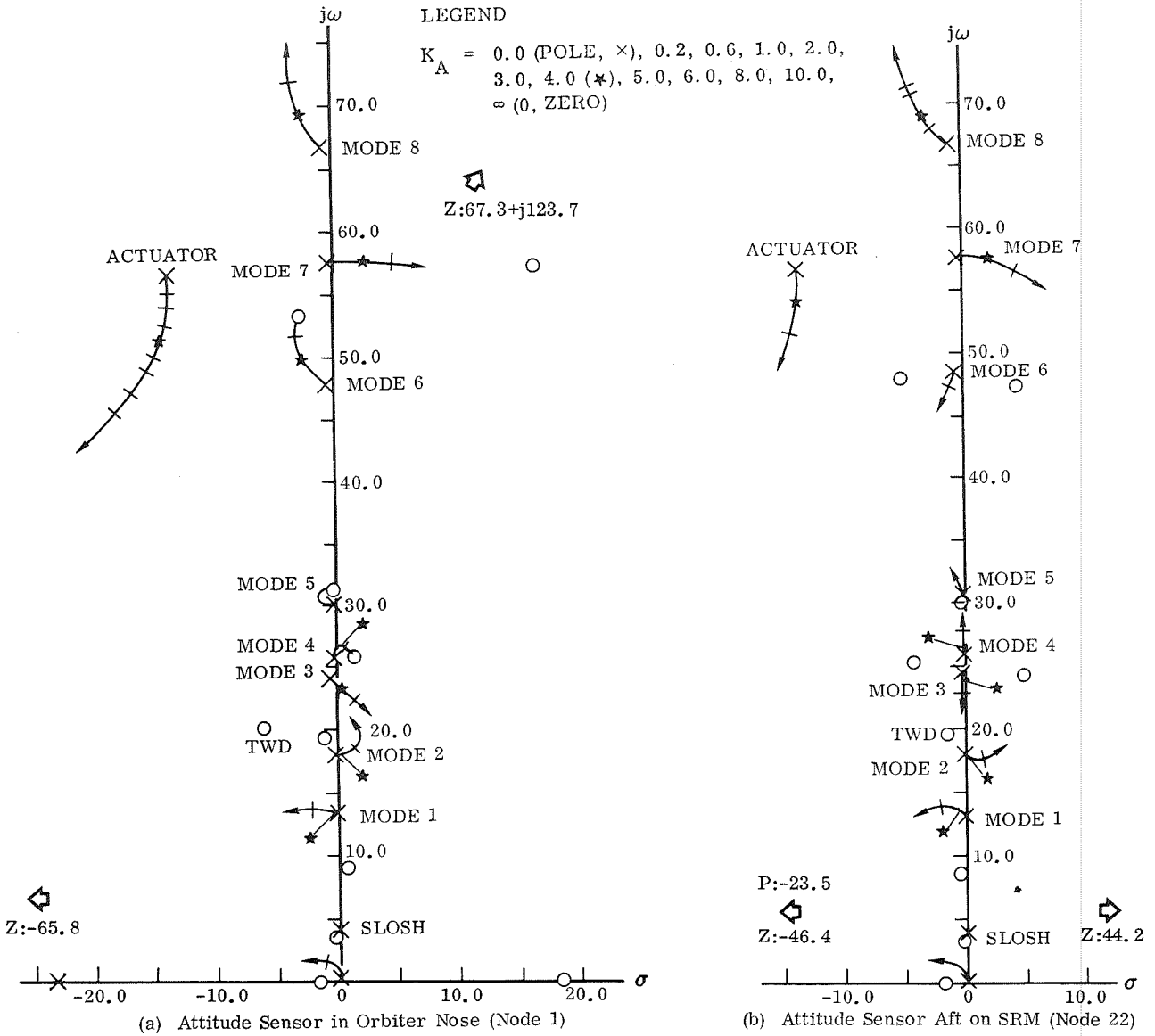

Figure 48. Rate Sensor Aft on SRM (Node 22)

To a first-order approximation, the effect of a control force increase on elastic mode stability generally can be evaluated with the nominal control thrust root locus diagrams. Simply shift the closed-loop root along the same elastic-mode locus to the new value of autopilot forward-loop gain (K_A) determined from the control mode response requirements. This approximate technique is particularly applicable when already active controllers are being considered; such as an increase in the thrust of the orbiter engines.

For this vehicle increased control thrust can be obtained by adding a TVC system to the solid rocket motors. Since this concept involves the addition of a different actuator system and new force application point on the vehicle, the SRM TVC system is incorporated into the dynamic equations. A secondary injection system is modeled as a single-order lag with a time constant of 0.062 sec. For the purposes of this study, the vehicle mass properties are not adjusted to reflect the added system, and the engine command signal applied to the orbiter gimbal system is also used for the SRM TVC system.

Figure 49 shows the root locus diagram for autopilot sensors located on the orbiter (aft rate sensor at model node 7 and forward attitude sensor at model node 1). The enlargement of the control mode locus reveals that the minimum response characteristics can be obtained with an autopilot forward loop gain (K_A) of 0.6, as opposed to the gain of 4.0 without SRM TVC. All of the elastic mode closed-loop roots (K_A = 0.6 points) have assumed stable orientations with the exception of the slightly unstable mode 2. This instability reflects the complications that are introducted by the TWD zero from the orbiter engine gimbal system. These complications will be present for all practical values of gain.

A comparison between Figure 49 and Figure 41 reveals that the reduced autopilot gain has improved the overall system stability and enhanced the potential for being able to provide adequate stability compensation. Of course, it has not eliminated all of the stability problems associated with this vehicle.

This comparison also illustrates that significant changes occur in some locus orientations. Thus, the approximate method of estimating gain reduction effects can only be used to obtain a rough first-order approximation. Even with this limitation, it can be seen in Figure 40 that a reduction in gain to K_A = 0.6 will result in a significant improvement in the system stability of this forward rate sensor configuration.

This symmetric elastic mode stability analysis serves to delineate the difficulties associated with using conventional autopilot techniques to provide system stability for this study vehicle configuration. The feasibility of using these techniques for this vehicle is not resolved by this analysis. The best results obtained with

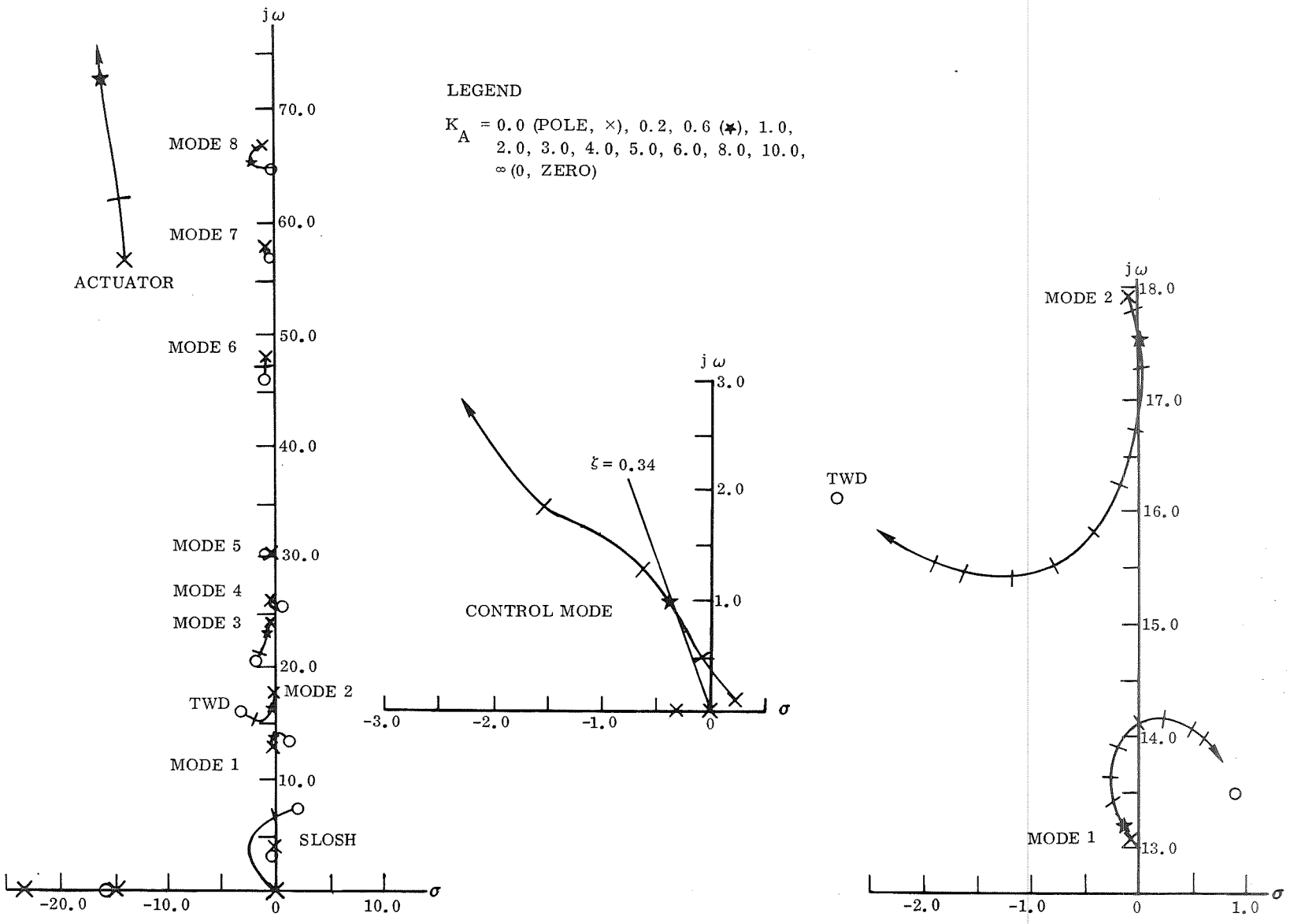

Figure 49. Solid Motor TVC with Autopilot Sensors Located on Orbiter (Rate Aft at Node 7 and Attitude Forward at Node 1)

a single rate sensor configuration were very marginal. Although the two-rate sensor configuration could provide positive system stability, it did not provide really satisfactory margins of stability.

Antisymmetric Elastic Mode Stability

As described in Section 3, the antisymmetric elastic mode stability is analyzed in two phases. The first phase consists of a planar analysis of both the roll and the yaw control planes separately. This planar analysis is artificial in the sense that the modal data consists of the yaw and roll components from the coupled antisymmetric modal data. Then the second phase analyzes the complete coupled system.

In the table below the antisymmetric elastic modes are described in relation to the body modes that appear on each of the three different vehicle elements. The yaw and roll components of each elastic mode are listed separately.

	Lateral (Yaw) Projection Body Mode			Roll Projection Body Mode			
Elastic Mode	Orbiter	Tank	SRM	Orbiter	Tank	SRM	Comment
1					First	First	
2			First		First	First	
3			First				
4		First					
5		First	First				
6		First	First	First	Second		Dominant coupled tank/ SRM first yaw mode.
7		First	First	First			Dominant orbiter first roll mode.
8		First	First	Second	Second		Dominant tank first yaw mode.
9	First	First	First	Second			Dominant orbiter roll mode.
10	First	First	First	Second			Dominant orbiter first yaw mode.
11	First	First		Second			
12			Second				

For the first seven elastic modes the orbiter lateral bending appears essentially as a rigid body interacting with the other vehicle elements through its interconnecting linkage system. Finally in mode 8 some significant lateral elastic motion appears

that is in opposition to the dominant tank first-yaw mode. The shape and construction of the orbiter vehicle produces a much stiffer structure in yaw than in pitch. This is reflected in the high natural frequency of the orbiter first yaw body mode at 7.4 Hz, as compared to the first pitch body mode frequency at 3.8 Hz.

The autopilot rate and attitude sensor locations used in this study are shown in Figure 50 relative to the vehicle elastic model.

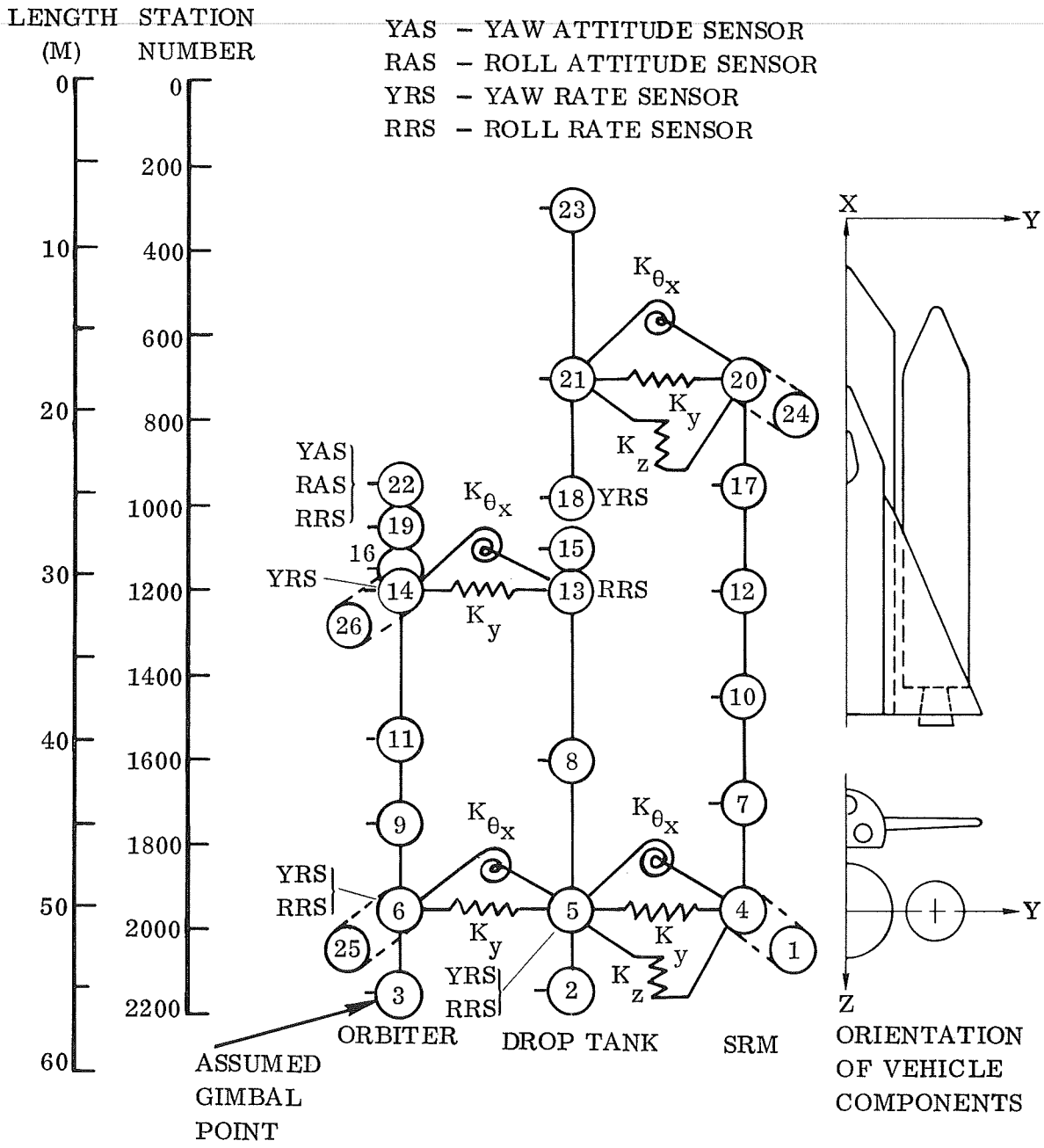

Figure 50. Autopilot Sensor Locations

Yaw Planar Analysis. – The root locus diagrams for rate sensor locations forward and aft of the first orbiter body mode antinode are shown in Figures 51 and 52. The forward location is at model node 14 and the aft location is at model node 6. The only attitude sensor location considered at this time is forward in the orbiter nose (model node 22). Several alternate locations, both on the orbiter and on the tank, were examined briefly.

Figure 51 shows that mode 10 is unstable. This is the dominant orbiter first yaw mode, and the modal gain is large enough to preclude gain stabilization. Several modes (1, 2, 7, 8, 9, 11 and 12) have very small residues and are completely gain stable. Modes 3, 4, 5 and 6 depart somewhat into the left-half plane and are stable for all gains. Filtering to affect mode 10 (at 45 rad/sec) could cause problems with mode 5 (at 21.2 rad/sec) and mode 6 (at 26 rad/sec).

Mode 10, with its open-loop pole at 45 rad/sec poses a severe problem because of the proximity of the engine actuator pole at 58.5 rad/sec. Any filtering to attempt to rotate the locus of mode 10 counter clockwise will result in "loci swapping"; i. e., the actuator locus becoming unstable and following a path similar to the mode 10 locus as shown. A possible solution would be to move the actuator pole by redesign of the actuator system. This would require analysis of even higher frequency modes (assuming the actuator poles were pushed higher by redesign) to ensure that the trouble caused by actuator poles in close proximity to modal poles is not simply shifted to a new area of the s-plane.

For the aft rate sensor location (Figure 52) all elastic mode loci exhibit stable configurations. Several modes do not have significant stability margins, but for this time of flight there are no problems.

In order to complete the planar study, and to develop alternate sensor locations should the need arise when yaw and roll are realistically coupled, some combinations of sensors located on the orbiter and the tank were briefly investigated. One considered a combination of attitude sensor mounted forward on the orbiter (model node 22) and the rate sensor mounted forward of the first mode antinode on the tank (model node 18). The result was somewhat similar to the results for both sensors mounted forward on the orbiter (Figure 51). Here the orbiter first body mode (mode 10) again departs directly toward the right-half plane, but additionally modes 3, 5 and 8 also depart primarily to the right. The conclusion is that this sensor location combination has no advantages over the forward location on the orbiter.

Another sensor location combination that was investigated had both rate and attitude sensors located forward on the tank at model node 18. Here modes 3 and 4 depart to the right but have relatively small residues and could be gain stabilized.

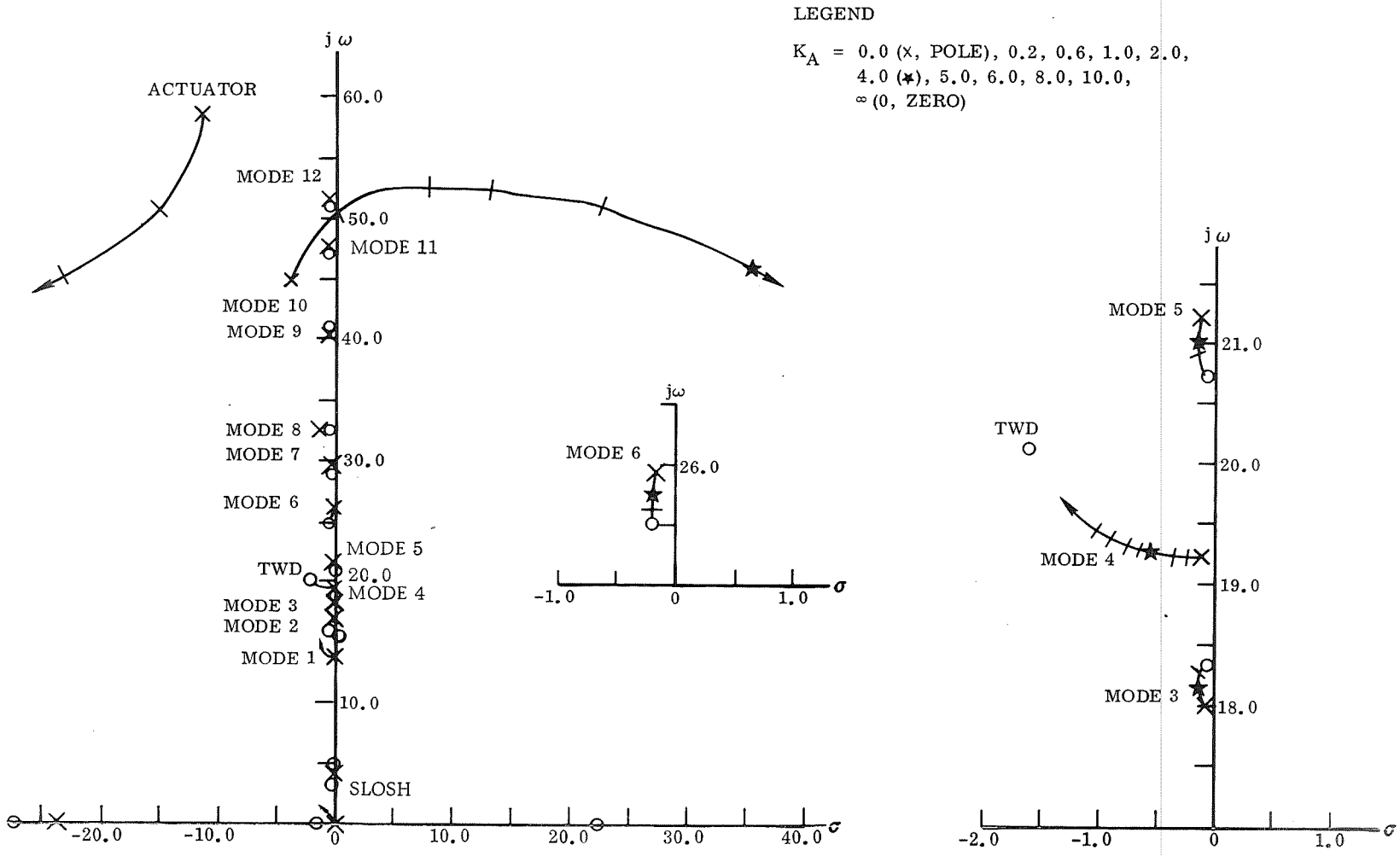

Figure 51. Yaw Forward Rate Sensor (Node 14) and Forward Attitude Sensor (Node 22) on Orbiter

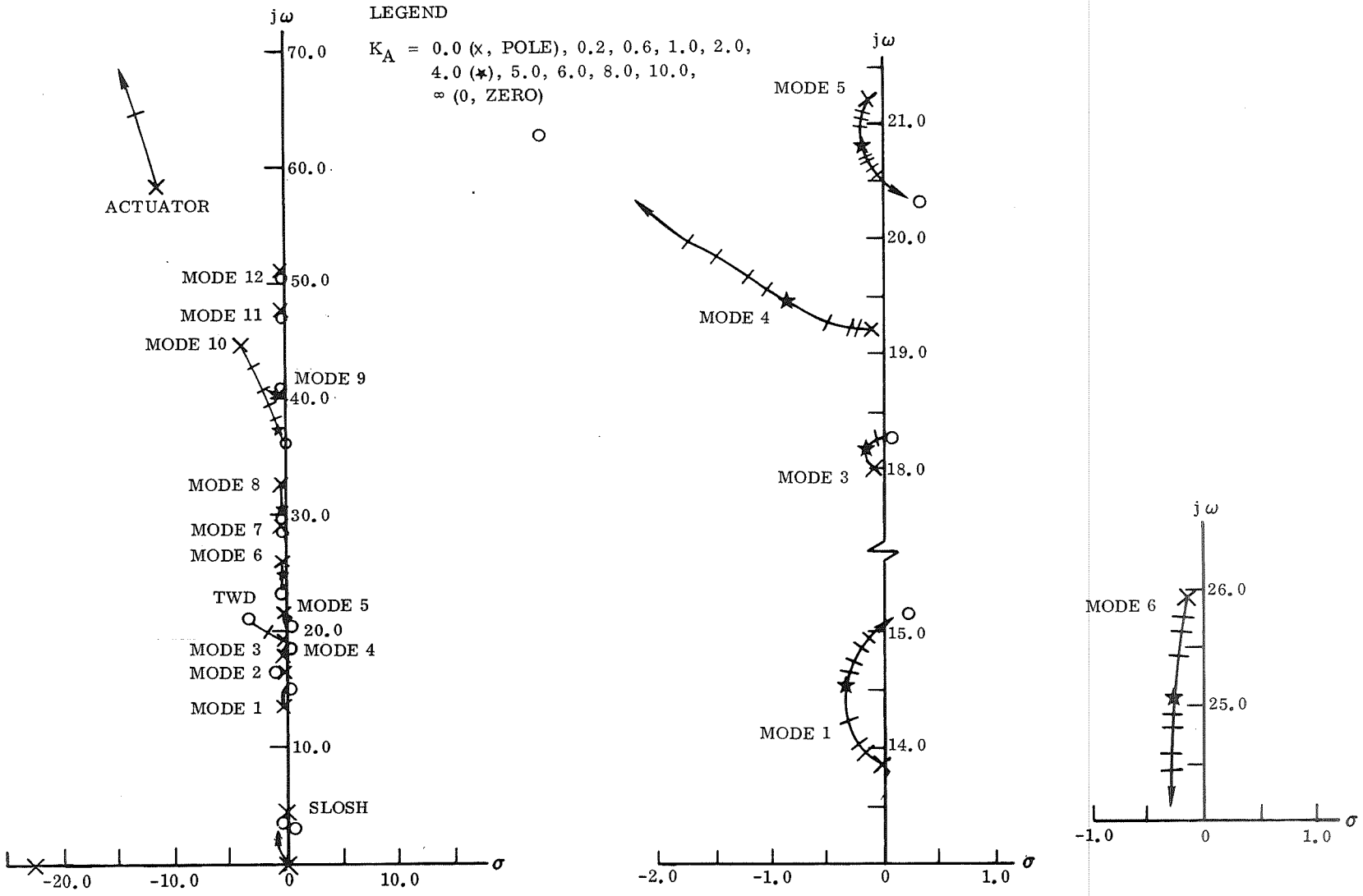

Figure 52. Yaw Aft Rate Sensor (Node 6) and Forward Attitude Sensor (Node 22) on Orbiter

Modes 6 and 8, however, depart directly toward each other and have such large modal amplitudes that gain stabilizing them would be difficult. Any phase shift introduced to improve the stability of mode 6 will cause mode 5 to "swap" and depart into the right-half plane. Thus, this configuration also provides no apparent benefits.

When the rate sensor was located aft on the tank (model node 5), and the attitude sensor mounted forward on the orbiter (model node 22), mode 10 presented the same problem as before; i. e. , the locus departs directly into the right-half plane with large modal gain. In addition the first, sixth, and seventh modes also depart somewhat to the right although they have smaller modal gains.

Figure 53 shows the effects of locating both sensors aft on the orbiter (model node 6). This configuration has results similar to those of Figure 52. Although the margins are not large, at the required operating gains, all modes are stable without further compensation.

Thus, using an aft rate sensor with either a forward or aft attitude sensor will provide a planar yaw (artificially decoupled) channel that is stable for the first twelve modes but does not have acceptable stability margins.

Roll Planar Analysis. — The root locus diagrams for planar control of the roll channel are presented in Figure 54 for a forward rate sensor location (model node 22) and in Figure 55 for an aft rate sensor location (model node 6). The attitude sensor location for both of these cases is at model node 22 in the orbiter nose.

In comparing these two figures, mode 7 shows the classic 180-degree phase shift associated with first body modes when the rate sensors are on opposite ends of the vehicle. Mode 9 shows a large modal amplitude with the rate sensor forward as compared to the small modal amplitude with the rate sensor aft. Mode seven in the aft rate sensor case is unstable at the closed-loop gain required for control. However, the aft sensor case appears more amenable to filtering because, in the forward rate sensor case, modes 7 and 9 depart directly toward each other, and the large modal amplitude associated with each will result in "loci swapping" as filtering is introduced to rotate the loci. With the aft sensor this does not occur, and Figure 56 shows the results of adding a quadratic lag filter to the aft rate sensor case. The filter has $\zeta = 0.7$ and $\omega_n = 117$ rad/sec. This stabilizes the mode 7 locus to neutral stability but causes the locus associated with the actuator to rotate clockwise, causing the closed-loop operating point to lie in the right-half plane. Some further changes to the engine actuator system would be required to stabilize this configuration.

Both attitude and rate sensors are located aft (model node 5 on the tank) as a possible alternate location (Figure 57). This is a satisfactory location, although modes 5 and 11 depart substantially to the right. The modal amplitudes for all modes are small, and at the gains required for closed-loop control all are slightly stable.

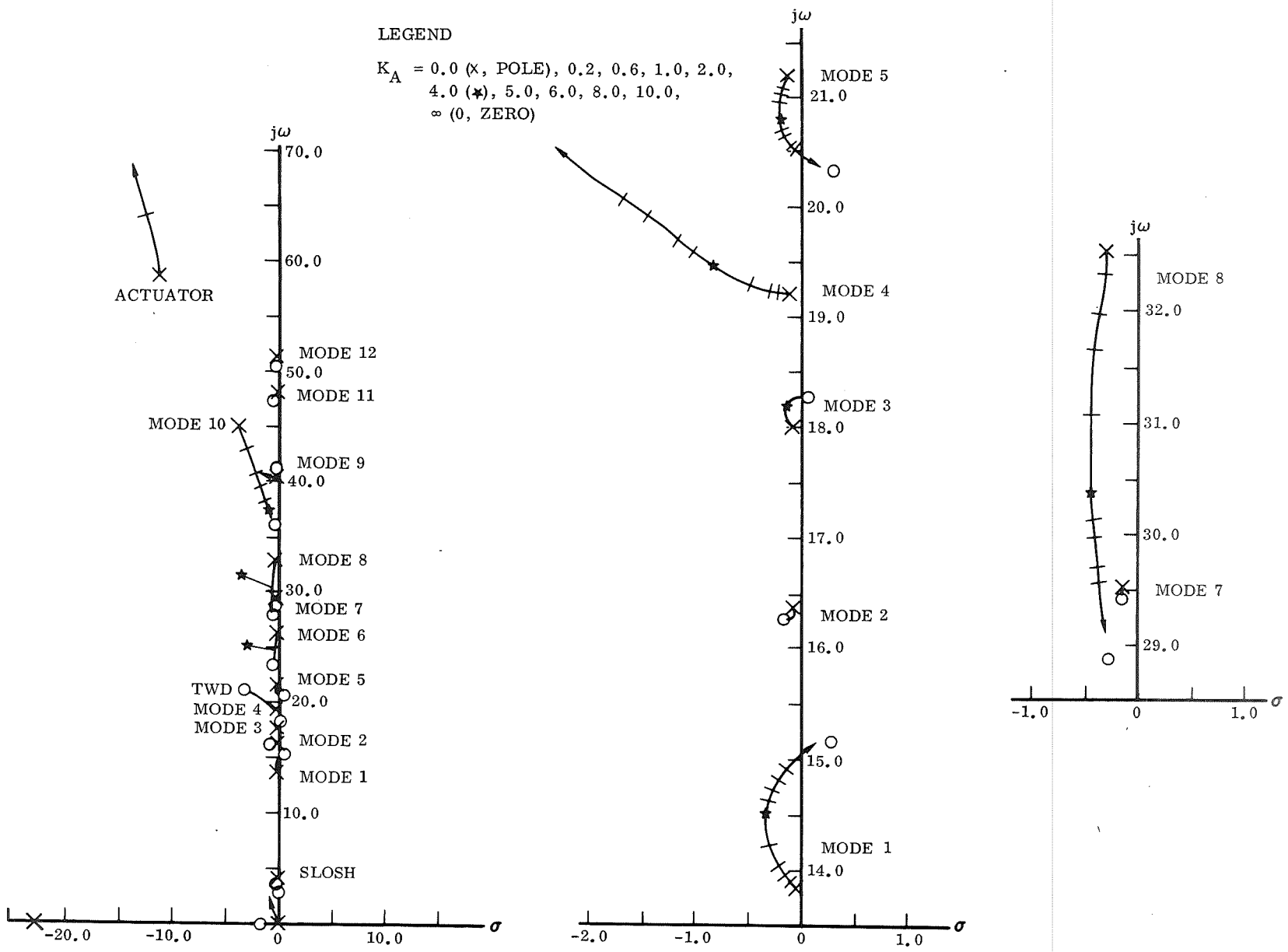

Figure 53. Yaw Rate and Attitude Sensors Aft on Orbiter (Node 6)

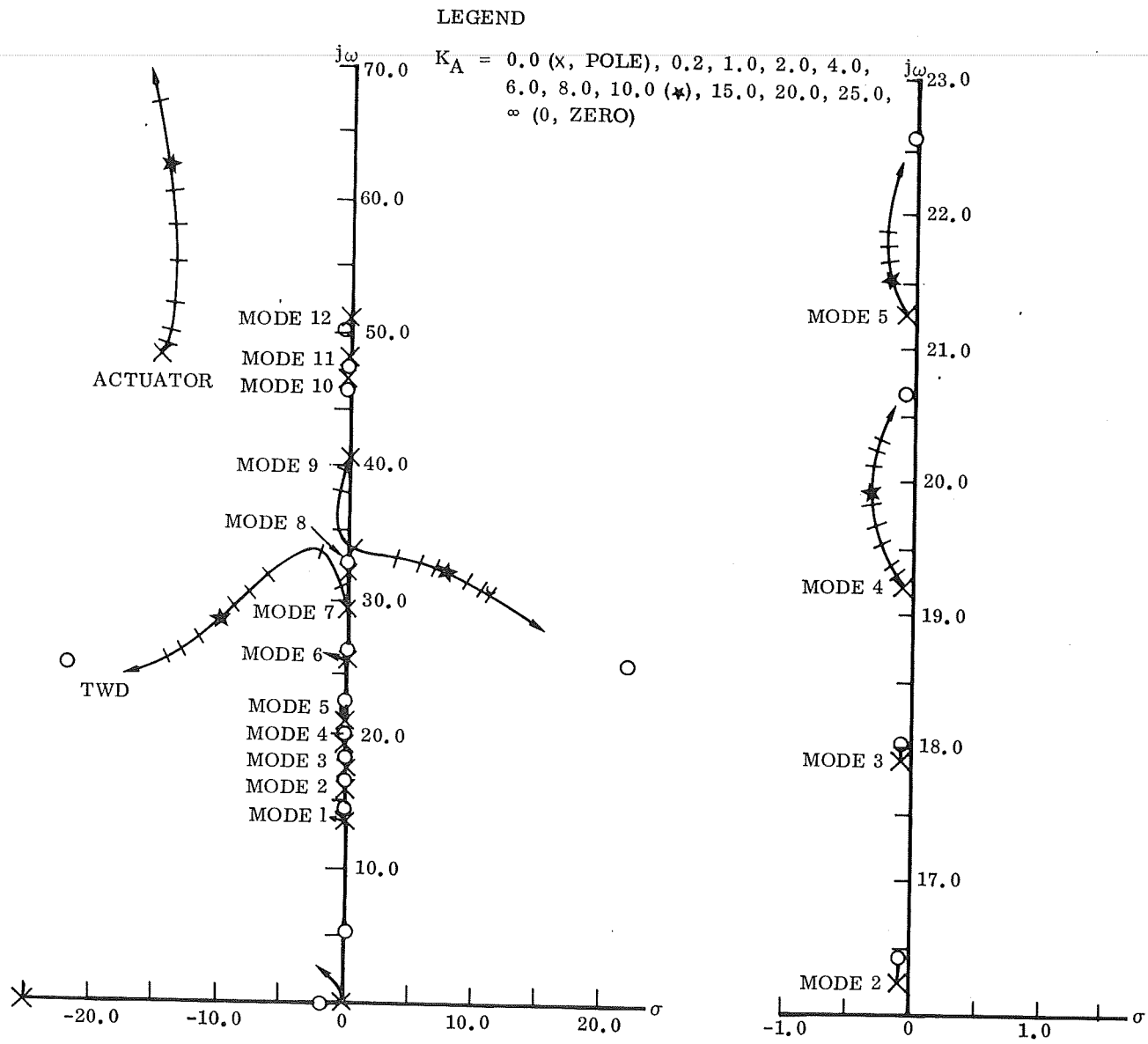

Figure 54. Roll Rate and Attitude Sensors Forward on Orbiter (Node 22)

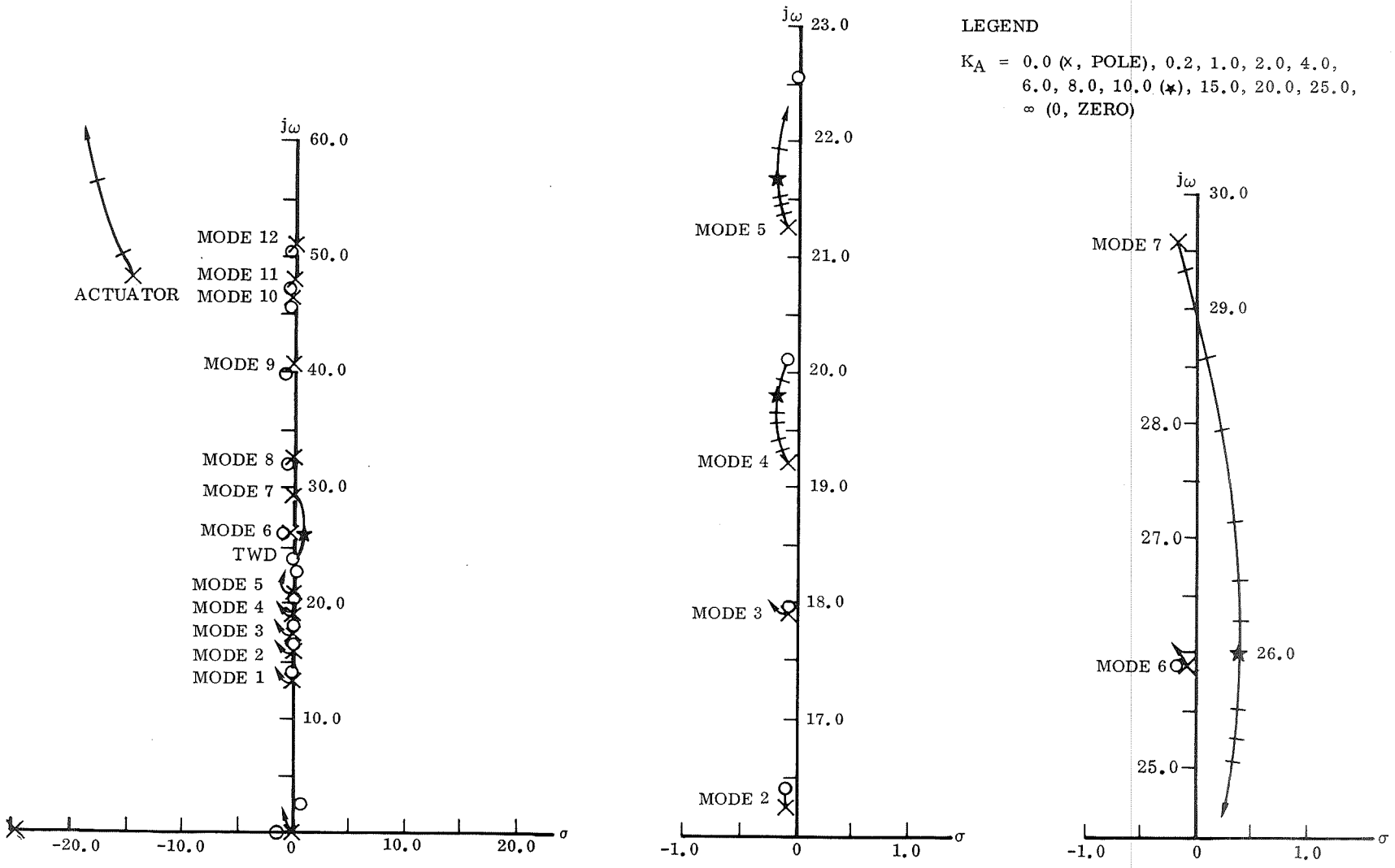

Figure 55. Roll Rate Sensor Aft (Node 6) and Attitude Sensor Forward (Node 22) on Orbiter

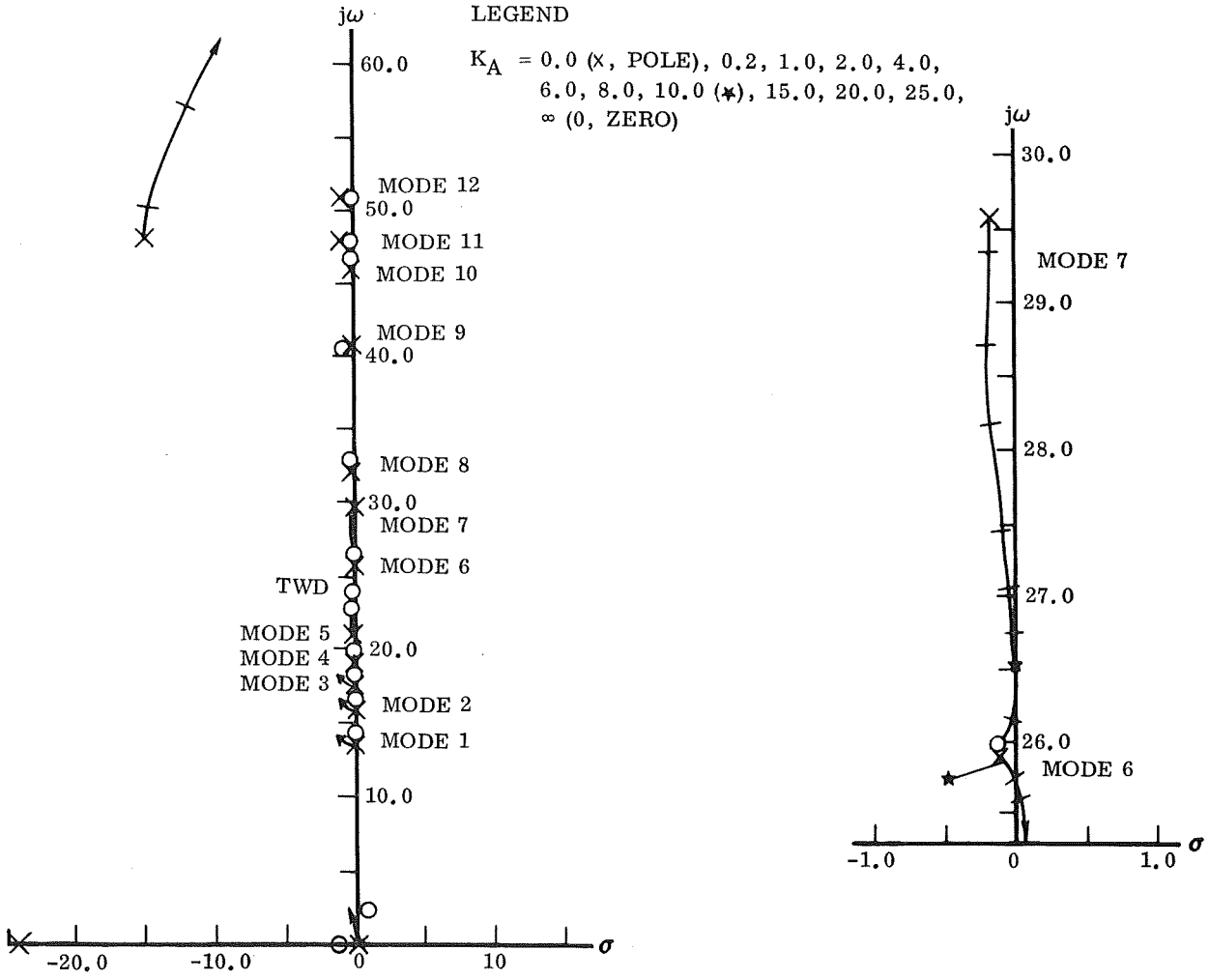

Figure 56. Roll Rate Sensor Aft (Node 6) and Attitude Sensor Forward (Node 22) on Orbiter, Autopilot Compensation Included

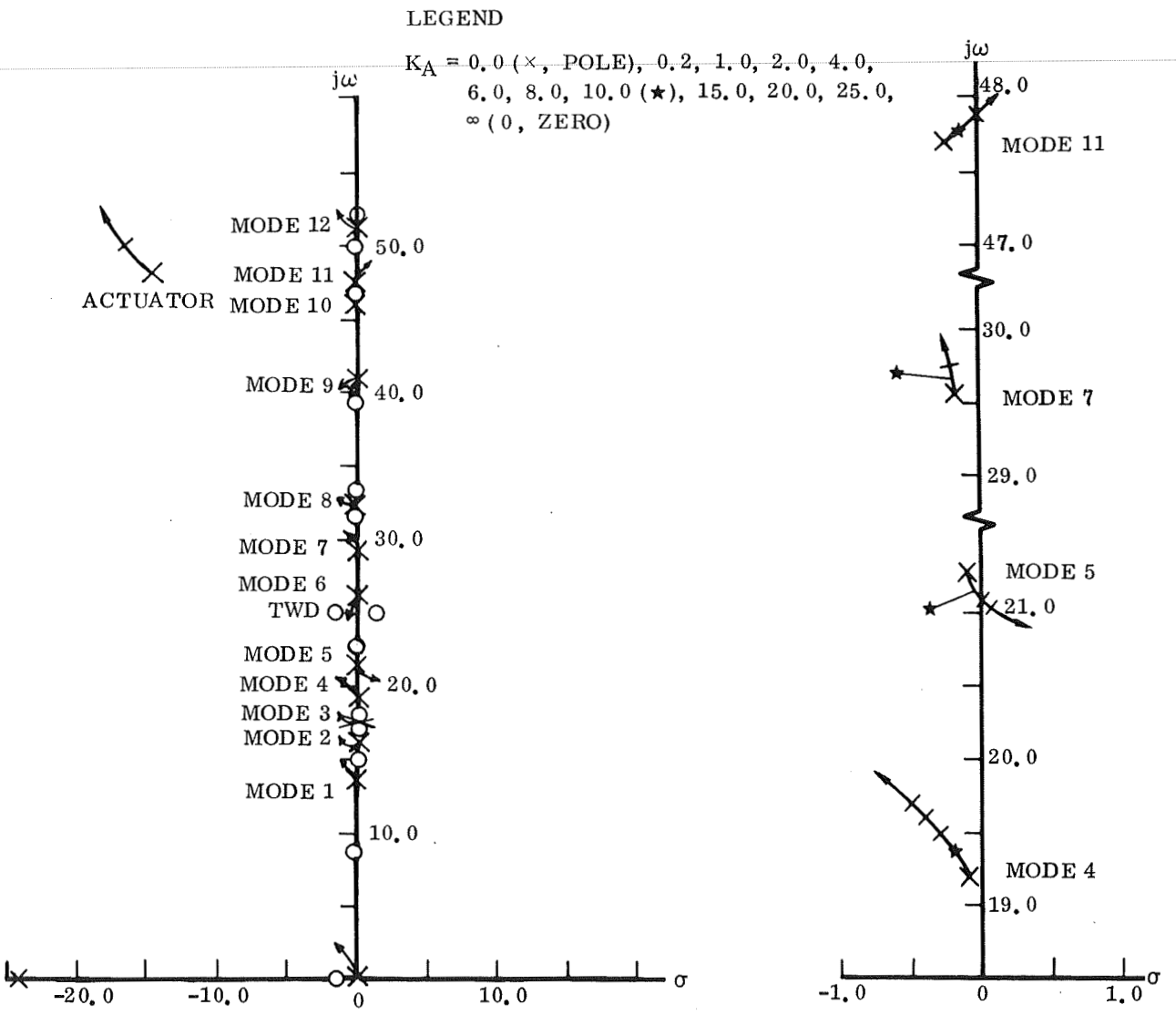

Figure 57. Roll Attitude and Rate Sensors Aft on Tank (Node 5)

Another alternate combination that was investigated had the rate sensor aft on the tank (model node 5) and the attitude sensor aft on the orbiter (model node 6). This configuration had results similar to those obtained with both sensors aft on the tank. The mode 7 response is more pronounced but departs to the left. Modes 5 and 11 continue to depart to the right but again have operating points slightly in the left-half plane.

A forward attitude sensor (model node 22) on the orbiter and an aft rate sensor (model node 5) on the tank has a pronounced mode 7 response departing directly into the right-half plane. Modes 5 and 11 have results similar to the other cases where the rate sensor was tank mounted.

Finally, a case was considered in which both sensors were forward mounted, with the attitude sensor at model node 22 on the orbiter and the rate sensor at model node 13 on the tank. Modes 5 and 7 depart directly toward the right-half plane, and mode 7 is unstable at the required closed-loop gain.

In the roll planar analysis, an aft rate sensor and an aft attitude sensor proved more satisfactory than the other conditions analyzed; however, none provided really satisfactory stability margins.

Yaw/Roll Coupled Analysis. – The analysis for coupled yaw/roll for this configuration follows substantially the same technique as that employed for the dual flyback configuration.

For an initial investigation, the roll and yaw forward attitude sensors were located at model node 22 on the orbiter and the aft rate sensors were located at model node 6 on the orbiter. This combination is considered as the most desirable from an equipment location point of view. Figure 58 shows the root locus diagram for this configuration with the roll gain (K_{AR}) fixed at 10 and the yaw gain (K_{AY}) varied. The effect is to move one mode loci completely into the right-half plane (at ω = 26 rad/sec) and to have the closed-loop operating point of another (ω = 18 rad/sec) in the right-half plane. This is not a satisfactory sensor location autopilot gain combination.

The second configuration investigated combined the aft yaw rate sensor (model node 6) with the forward yaw attitude sensor (model node 22) on the orbiter and aft roll rate (model node 5) with aft roll attitude (model node 5) on the tank. Figure 59 shows the results of fixing K_{AR} = 10 and varying K_{AY}. In this case the mode with poles at ω= 19 rad/sec has its operating point in the right-half plane, and the mode with poles at ω = 28.6 rad/sec has its operating point on the jω axis.

In order to pinpoint just what was causing this coupled instability, K_{AR} was set equal to zero and K_{AY} varied. This removes the coupling through the roll autopilot.

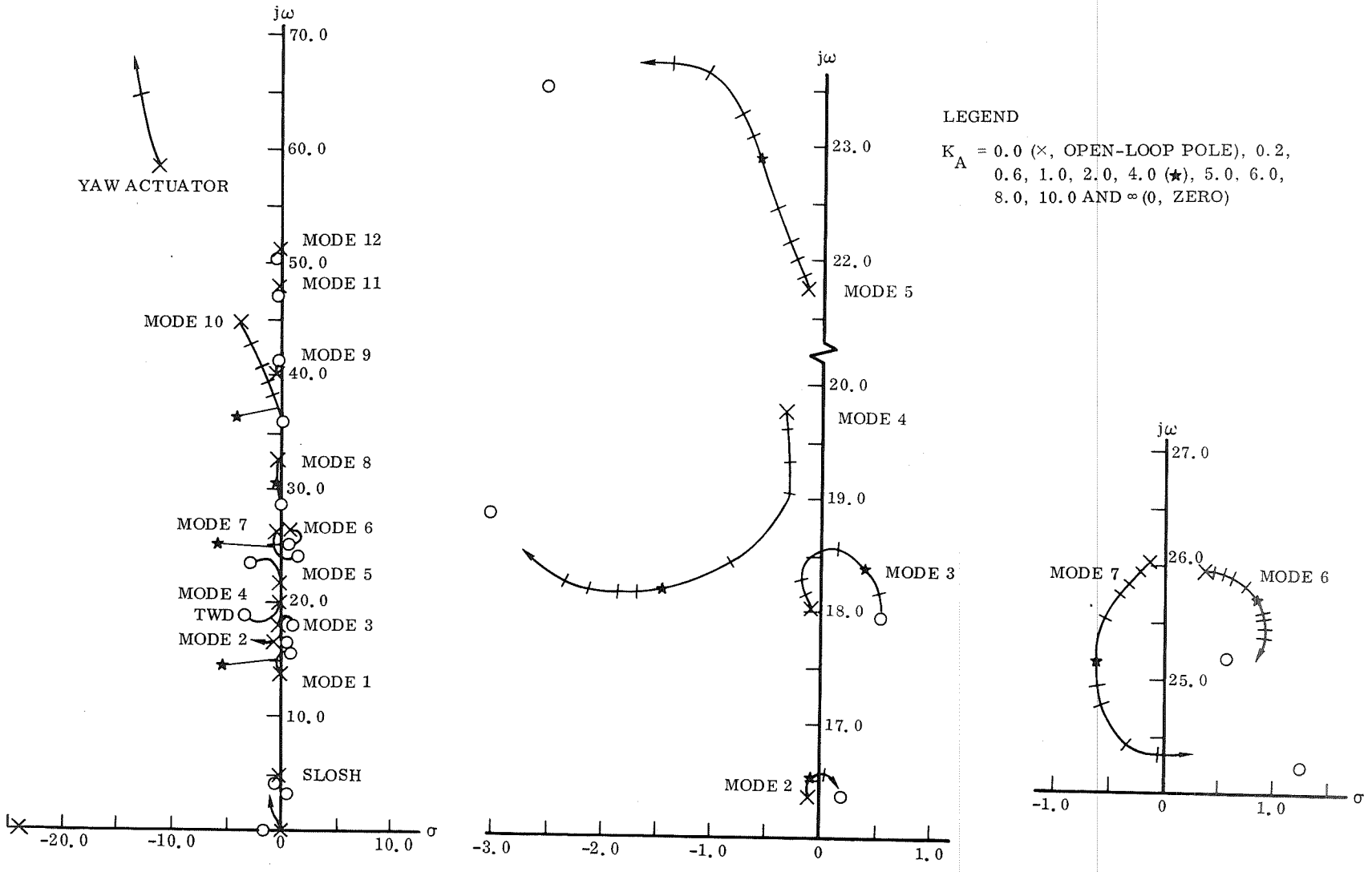

Figure 58. Coupled Yaw/Roll, Aft Orbiter Rate Sensors, Fixed Roll Gain and Vary Yaw Gain

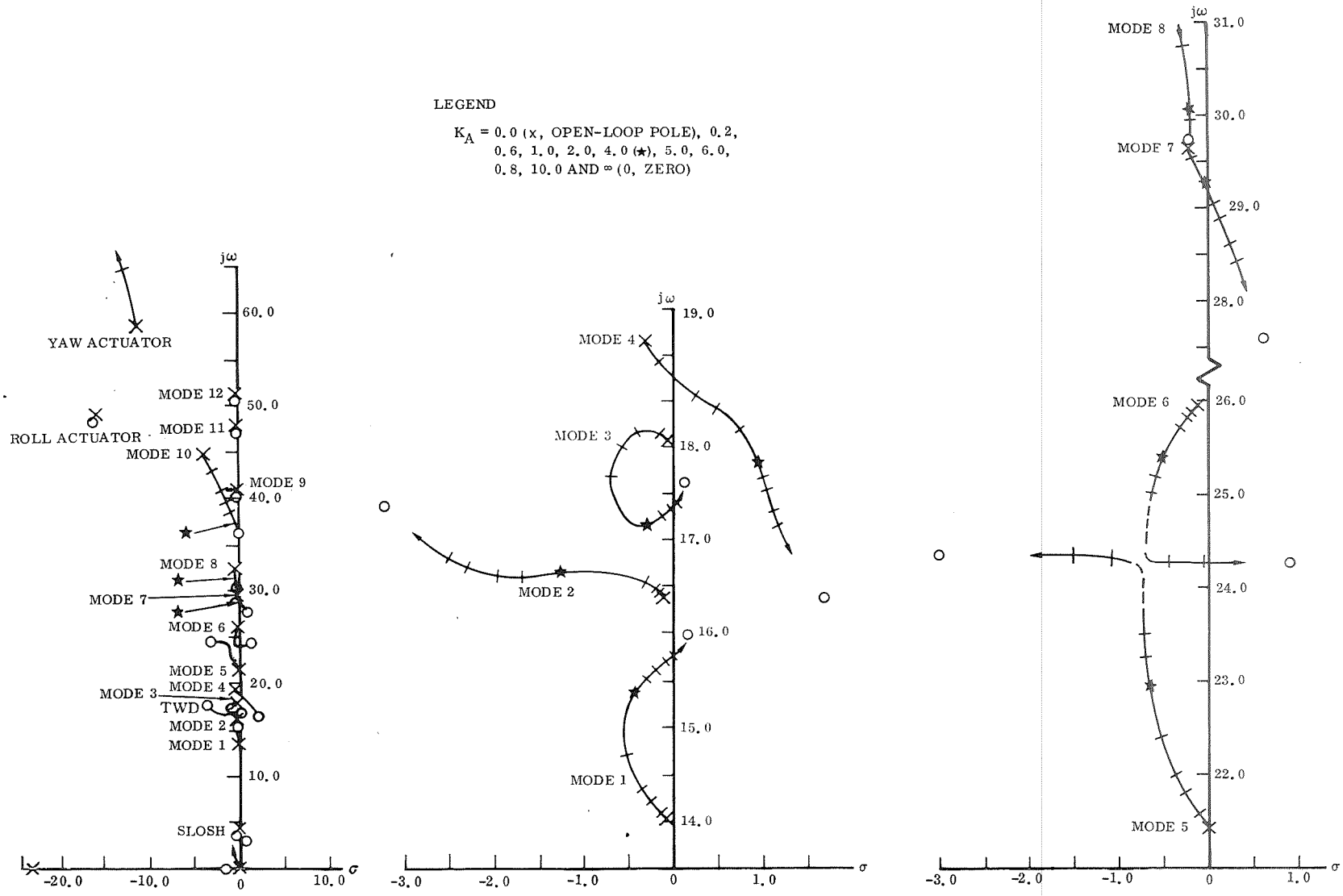

Figure 59. Coupled Yaw/Roll, Aft Rate Sensors (Yaw on Orbiter and Roll on Tank), Fixed Roll Gain, Vary Yaw Gain

The result is shown in Figure 60 and is very similar to that seen in Figure 59, but considerably different from the planar results shown in Figure 52. This would indicate that the problem is coupling through the yaw attitude control system. To ascertain this, K_{AY} was set equal to zero and K_{AR} varied. Figure 61 shows the results, which are similar to the corresponding planar analysis results (Figure 57). This verifies that the problem is yaw autopilot coupling. Since the yaw gain is primarily set at a high level due to the rigid-body restriction, there appears to be little chance of stabilizing this configuration with conventional autopilot techniques.

No indications of whether a satisfactory system could be obtained with SRM TVC or with multiple sensor systems were obtained, since these configurations were not investigated.

The marginal stability conditions illustrated in the planar analyses, the complexity of this coupled system, and the simplified nature of the elastic model indicated that further analysis at this coupled level was not warranted at this time. The results of this brief yaw/roll coupled analysis indicated that modal coupling through the attitude control system is a very important consideration for this solid motor vehicle.

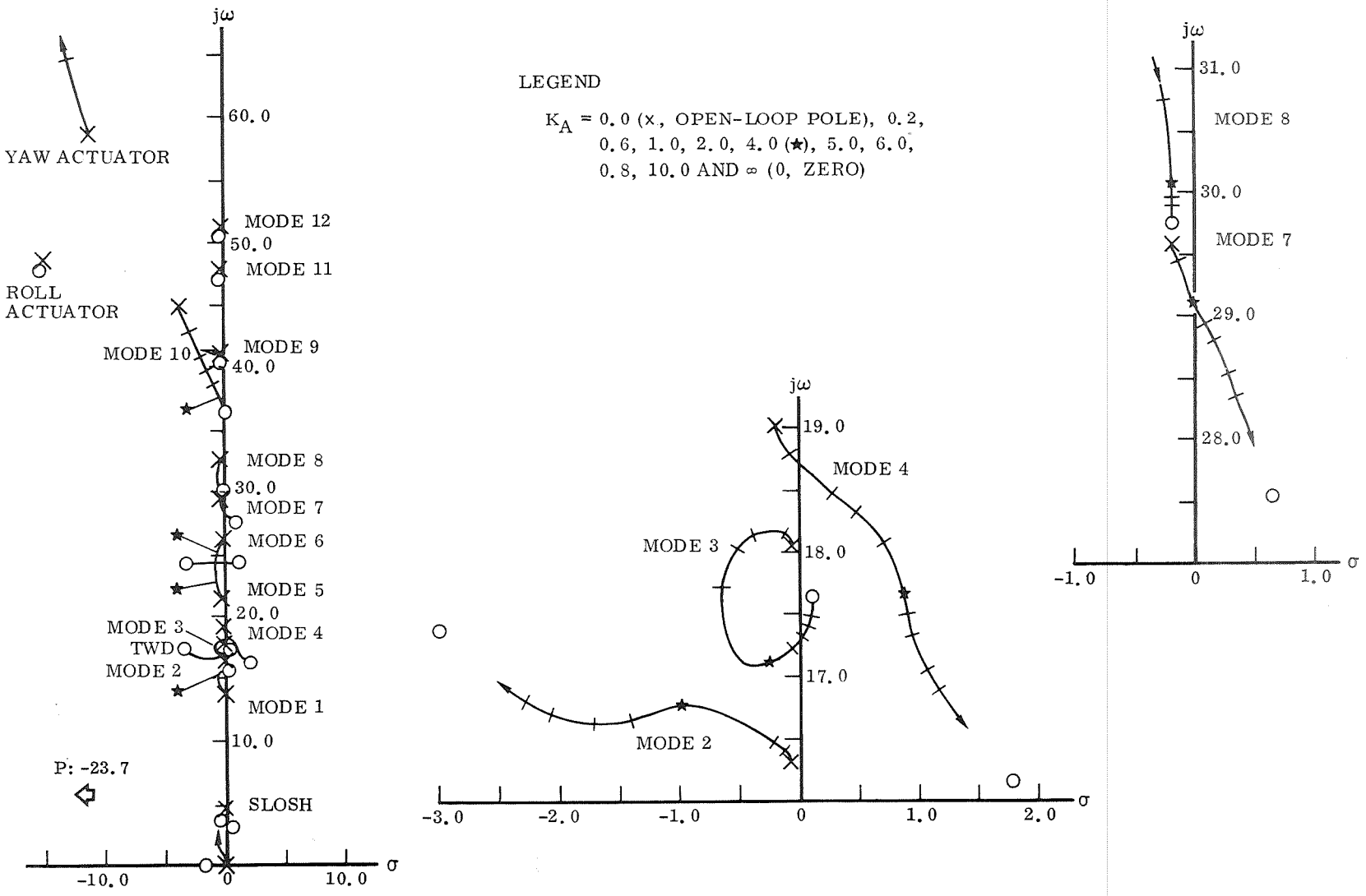

Figure 60. Coupled Yaw/Roll, Aft Yaw Rate Sensor on Orbiter, Roll Gain Set to Zero, Yaw Gain Varied

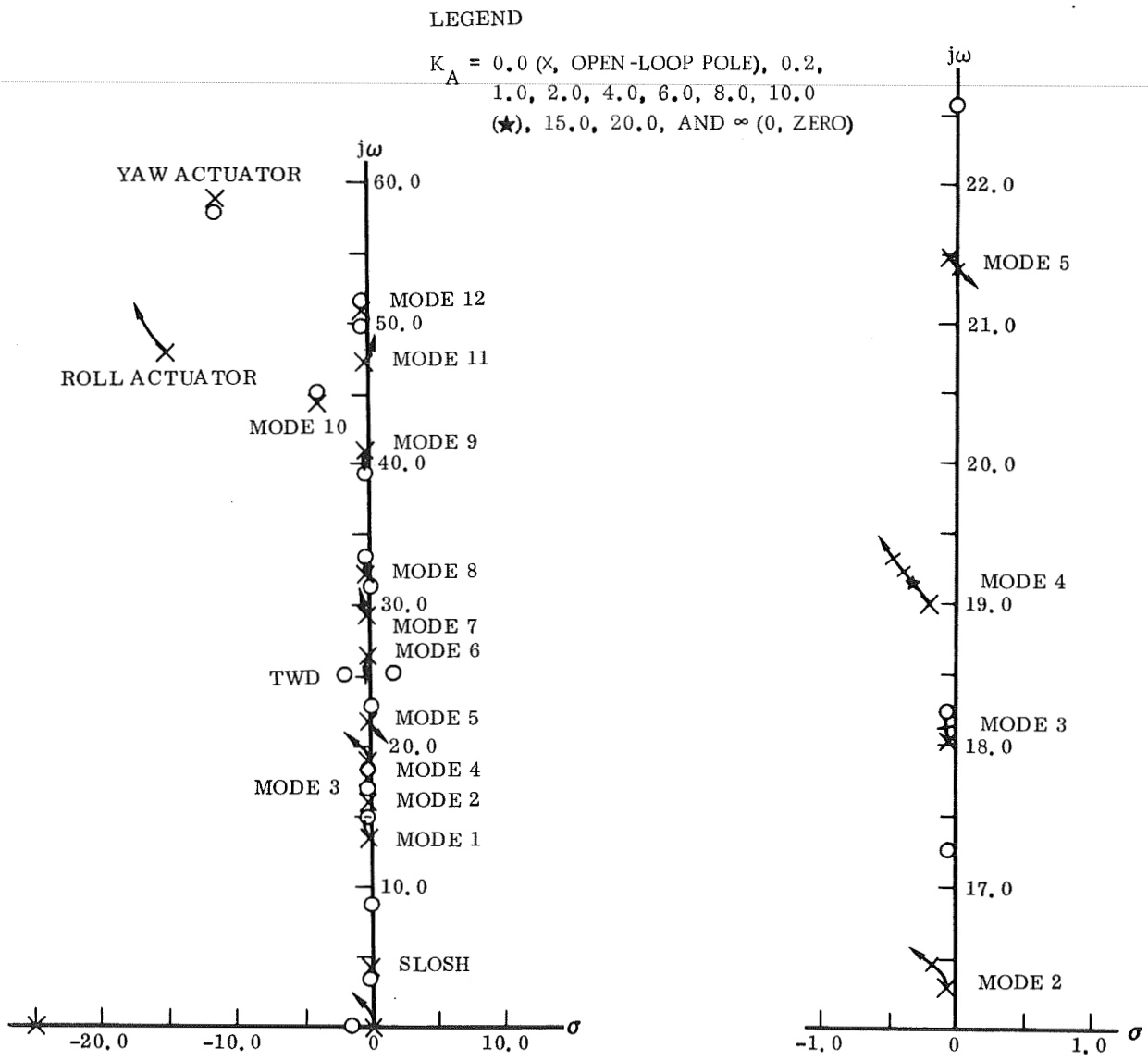

Figure 61. Coupled Yaw/Roll, Aft Roll Sensors on Tank, Yaw Gain Set to Zero, Roll Gain Varied

6 CONCLUSIONS

Dual Flyback Vehicle

The results of this study indicate that conventional autopilot techniques can be used to stabilize the vibration modes at the liftoff flight condition. Furthermore, use of the forward rate sensor configuration appears feasible in both the pitch and yaw autopilot control planes. This particular configuration has the greatest potential for later flight times when, if the elastic modes follow conventional patterns, the stability margins increase as modal frequencies increase.

Propellant sloshing did not become an important stability consideration at this time of flight. No coupling is indicated between these modes and the lower frequency elastic modes.

Elastic coupling between the orbiter and the booster does not appear to appreciably affect the total vehicle elastic mode stability. This is probably due in large part to the fact that the orbiter weight is only 20 percent of the booster weight at liftoff. Thus at later flight times, when the vehicle weights are more comparable, significant changes in the elastic coupling between the two vehicles could occur. This observation and the omission of aeroelastic effects means that the results of this study cannot be extrapolated with any degree of confidence beyond the liftoff flight condition.

Solid Motor Vehicle

Due to the preliminary nature of the modal data available and the extreme sensitivity of control system stability to these data, the results of this study are inconclusive in determining whether or not conventional autopilot techniques can be used to adequately stabilize the vehicle.

Although positive elastic mode stability is attained for the symmetric mode case, the margins of stability are small. For the antisymmetric mode case significant elastic mode coupling is evidenced for the yaw/roll coupled system. This coupling produces unstable modes, which are not amenable to conventional stabilization techniques. Propellant sloshing is not an important stability factor at liftoff.

Three important interrelated considerations that complicate the elastic mode stability of this vehicle are the high modal gain, the location of the "tail-wags-dog" zero, and the high degree of elastic coupling between the vehicle elements through the links that join these elements together. The high modal gain is due in large part to

the relatively high autopilot forward-loop gain required to obtain satisfactory control mode performance characteristics. This high autopilot gain is, in turn, due to the low control thrust (considering the size of the vehicle) provided by the orbiter engines.

The "tail-wags-dog" zero is located in the frequency range of the lower frequency body modes. The phase shift introduced by this singularity not only complicates the stability problem for the liftoff condition, but it will also introduce extraordinary considerations as the modal frequencies change with increasing flight times.

The combination of the high modal gain and the "tail-wags-dog" zero location accentuates the importance of the elastic mode frequency density, increases the potential coupling through the attitude control system, and increases the sensitivity of the system stability problem to variations in the modal parameters.

Based on these approximate mode shapes, and the preceding comments conventional, single-rate-sensor stabilization does not appear feasible if only the orbiter engines are used for control. However, a brief investigation of adding solid motor TVC (secondary injection) indicates that improved stability properties can be attained with this increase in control thrust. Another brief study of a two rate sensor autopilot configuration indicates that the vehicle stability properties can be improved by employing a multiple sensor autopilot configuration.

7 RECOMMENDATIONS

The complexity of the stability problem for the solid motor vehicle and the choice of this concept for continued development indicate that studies of vehicle vibration mode stability should be continued. These studies should be expanded to include other critical flight times (e.g. maximum dynamic pressure, solid motor burnout, etc.). They should also include alternate autopilot configurations, such as multiple sensors and adaptive techniques.

The brief investigation of multiple sensors showed sufficient improvement that further study of this concept is definitely warranted. The use of multiple sensors for redundancy has been considered in earlier space shuttle studies, although all sensors were at the same location. This concept should now be broadened to a study of multiple sensors at various locations to satisfy both redundancy and elastic mode stability requirements.

The structural complexity of this solid motor vehicle concept and the sensitivity of the vehicle stability to its elastic properties indicate that further elastic model development should be pursued in parallel with the stability studies.

Langley Research Center
National Aeronautics and Space Administration
Hampton, Virginia, November 24, 1972

APPENDIX A

LIST OF SYMBOLS

Symbols	Definition
g	Gravity constant
I_R	Engine gimballed moment of inertia about gimbal point
I_{xx}	Vehicle roll moment of inertia about center of mass
I_{yy}	Vehicle pitch moment of inertia about center of mass
I_{zz}	Vehicle yaw moment of inertia about center of mass
I_{xz}	Vehicle x-z plane product of inertia about center of mass
K_A	Autopilot forward loop gain
K_C	Actuator servo loop gain
K_o	Actuator load torque feedback gain
K_R	Autopilot rate-to-attitude gain ratio
k_D	Attitude sensor gain
k_R	Rate sensor gain
k_{SF}	Autopilot forward loop static gain
L_P	Sloshing pendulum length
L_β	Aerodynamic roll moment coefficient due to perturbation of β
ℓ_c	Distance from vehicle center of mass to liquid control engine gimbal point along X body axis
ℓ_{cs}	Distance from vehicle center of mass to solid engine thrust application point along X body axis

ℓ_{Ez}	Distance from vehicle centerline to liquid control engine gimbal point along Z body axis
ℓ_{Ey}	Distance from vehicle centerline to solid engine thrust application point along Y body axis
ℓ_P	Sloshing pendulum moment arm
ℓ_R	Distance from gimbal point to engine center of mass
ℓ_{RE}	Equivalent roll control moment arm
M_E	Engine gimballed mass
M_P	Propellant sloshing mass
M_R	Vehicle reduced mass ($M_T - \Sigma M_P$)
M_T	Vehicle total mass
M_u	Aerodynamic pitch moment coefficient due to perturbation of u
M_w	Aerodynamic pitch moment coefficient due to perturbation of w
η_i	Generalized mass of i^{th} elastic mode
Q_o	Vehicle steady-state pitch rate
N_β	Aerodynamic yaw moment coefficient due to perturbation of β
s	Laplace variable (complex frequency)
T (or T_c)	Liquid engine control thrust
T_{RAT}	Ratio of equivalent roll control thrust to total liquid engine control thrust
T_S	Solid engine thrust
U_o	Vehicle steady-state forward velocity

$\dot{U}_o$	Vehicle steady-state forward acceleration
V_T	Magnitude of vehicle velocity vector
W_o	Vehicle steady-state plunging velocity
X_u	Aerodynamic longitudinal force coefficient due to perturbation of u
X_w	Aerodynamic longitudinal force coefficient due to perturbation of w
Y_β	Aerodynamic side force coefficient due to perturbation of β
Z_u	Aerodynamic plunging force coefficient due to perturbation of u
Z_w	Aerodynamic plunging force coefficient due to perturbation of w
z_{cg}	Distance from vehicle centerline to vehicle center of mass along Z axis
δ_{op}	Steady-state thrust vector angular deflection in pitch
δ_{oy}	Steady-state thrust vector angular deflection in yaw
ζ_{cn}	Actuator servo damping ratio
ζ_d	Actuator system closed loop damping ratio
θ_o	Steady-state pitch angle relative to launch pad
ρ	Density of liquid propellants
σ_{PA}, σ_{yA}	Elastic mode slopes at attitude sensor locations in pitch and yaw control planes
σ_{RA}	Elastic mode roll deflection at roll attitude sensor location
σ_{PRS}, σ_{yRS}	Elastic mode slopes at rate sensor locations in pitch and yaw control planes
σ_{RRS}	Elastic mode roll deflection at roll rate sensor location

σ_{zT}, σ_{yT}	Elastic mode slopes at thrust application point in XZ and XY planes
σ_{xT}	Elastic mode roll deflection at thrust application point
Φ_{zP}, Φ_{yP}	Elastic mode deflection at propellant sloshing hinge point parallel to vehicle Z and Y axes
Φ_{zT}, Φ_{yT}, Φ_{xT}	Elastic mode deflection at thrust application point parallel to vehicle Z, Y and X axes
ω_B, ω_P	Elastic and propellant sloshing natural frequencies
ω_C	Actuator servo resonant frequency
ω_{TWD}	Frequency of tail-wags-dog zero

APPENDIX B

ANALYSIS MODELS AND PERTURBATION EQUATIONS

This appendix summarizes the analysis models and presents the perturbation equations that are used in this analysis. It also briefly describes the solution technique that is used to calculate the roots of the characteristic equation.

The definition of the vehicle coordinate system is shown in Figure B1. The origin of the coordinate axes is located at the vehicle center of mass.

RIGID BODY EQUATIONS

Translation Equations

$$su + Q_o w + W_o s\theta = \frac{\Delta F_x}{M_T}$$

$$s\beta - \frac{W_o}{U_o} s\phi + s\psi = \frac{\Delta F_y}{U_o M_R}$$

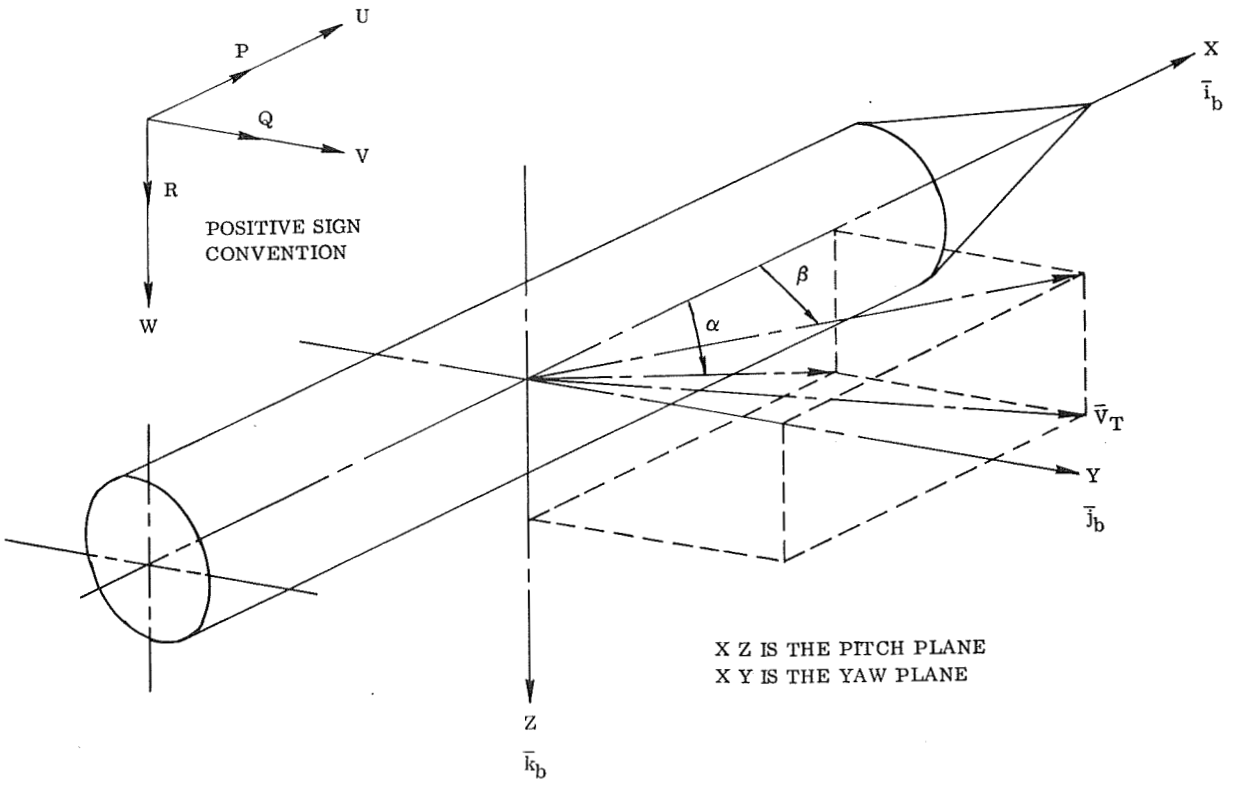

Figure B1. Vehicle Coordinate System

$$sw - Q_o u - U_o s\theta = \frac{\Delta F_z}{M_R}$$

$\Delta F = \Sigma$ (thrust forces) $+ \Sigma$ (gravity forces)

$+ \Sigma$ (aerodynamic forces) $+ \Sigma$ (engine inertia forces) $+ \Sigma$ (slosh forces)

Rotation Equations

$$s^2 \phi - \frac{I_{xz}}{I_{xx}} (s^2 \psi + Q_o s\phi) + \frac{I_{zz} - I_{yy}}{I_{xx}} Q_o s\psi = \frac{\Delta L_x}{I_{xx}}$$

$$s^2 \theta = \frac{\Delta L_y}{I_{yy}}$$

$$s^2 \psi - \frac{I_{xz}}{I_{zz}} (s^2 \phi - Q_o s\psi) + \frac{I_{yy} - I_{xx}}{I_{zz}} Q_o s\phi = \frac{\Delta L_z}{I_{zz}}$$

$\Delta L = \Sigma$ (thrust torques) $+ \Sigma$ (aerodynamic torques) $+ \Sigma$ (engine inertia torques) $+ \Sigma$ (slosh torques)

The engine inertia forces and torques used in these equations are only those due to engine gimbal angles.

In the above equations:

$U = U_o + u$ $\quad P = P_o + p$ $\quad p = \dot{\phi}$ $\quad \beta \approx \frac{v}{U_o}$

$W = W_o + w$ $\quad Q = Q_o + q$ $\quad q = \dot{\theta}$

$V = V_o + v$ $\quad R = R_o + r$ $\quad r = \dot{\psi}$

PROPELLANT SLOSHING EQUATIONS

The propellant sloshing dynamics are illustrated in Figure B2.

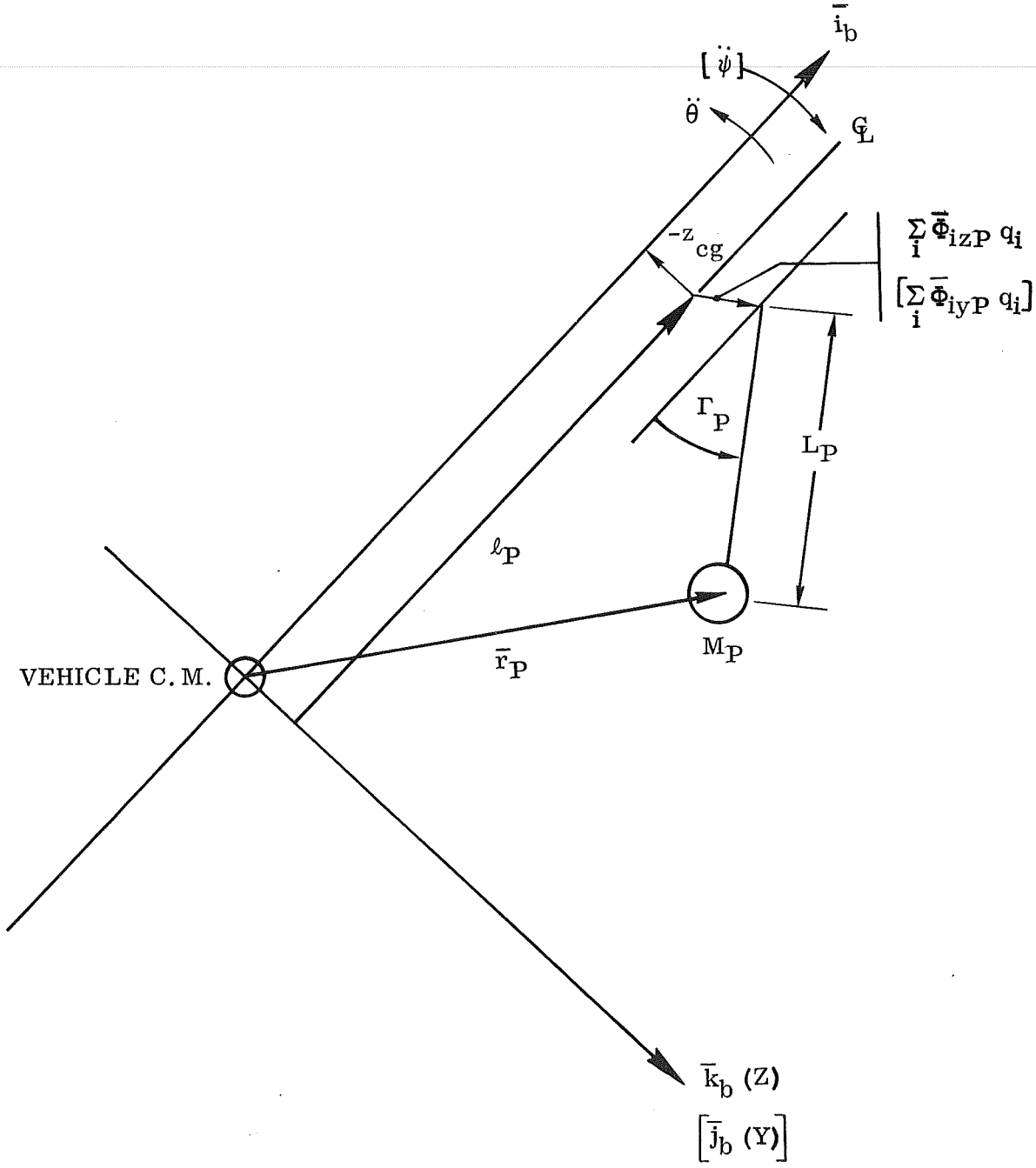

Figure B2. Propellant Sloshing Dynamics (Pendulum Analogy)

Longitudinal Equation

$$(s^2 + 2\zeta_{pk}\omega_{pk}s + \omega_{pk}^2)\,\Gamma_{pk} = -\frac{1}{L_{pk}}\,s\,w$$

$$+\left(\frac{\ell_{pk} - L_{pk}}{L_{pk}}\,s^2 + \frac{U_o}{L_{pk}}\,s\right)\theta - \sum_i \frac{1}{L_{pk}}\,\Phi_{izpk}\,s^2\,q_i$$

Lateral Equation

$$(s^2 + 2\zeta_{pk}\omega_{pk}s + \omega_{pk}^2)\,\Gamma_{pk} = -\frac{U_o}{L_{pk}}\,s\,\beta$$

$$-\left(\frac{\ell_{pk} - L_{pk}}{L_{pk}}\,s^2 + \frac{U_o}{L_{pk}}\,s\right)\psi - \sum_i \frac{1}{L_{pk}}\,\Phi_{iypk}\,s^2\,q_i$$

In these equations $\omega_{pk}^2 = \frac{\dot{U}_o}{L_{pk}}$ and $k = 1, 2, \ldots, m$

ELASTIC VEHICLE EQUATIONS

$$(s^2 + 2\zeta_{Bi}\omega_{Bi}s + \omega_{Bi}^2)\,q_i = \frac{Q_i}{\mathcal{M}_i}$$

$$Q_i = \Sigma(\text{thrust forces}) \cdot \Phi_{Ti}$$

$$+ \Sigma\,(\text{engine inertia forces}) \cdot \Phi_{Ei}$$

$$+ \Sigma\,(\text{sloshing forces}) \cdot \Phi_{Pi}$$

$$+ \Sigma\,(\text{engine inertia torques}) \cdot \sigma_{Ti}$$

where $\sigma_i = \frac{\partial \Phi_i}{\partial X}$ and $i = 1, 2, \ldots, n$

The engine inertia forces and torques used in these equations are only those due to engine gimbal angles. The modal displacements and slopes, Φ_i and σ_i, are obtained from orthogonal normal modes.

GRAVITY PERTURBATION FORCES

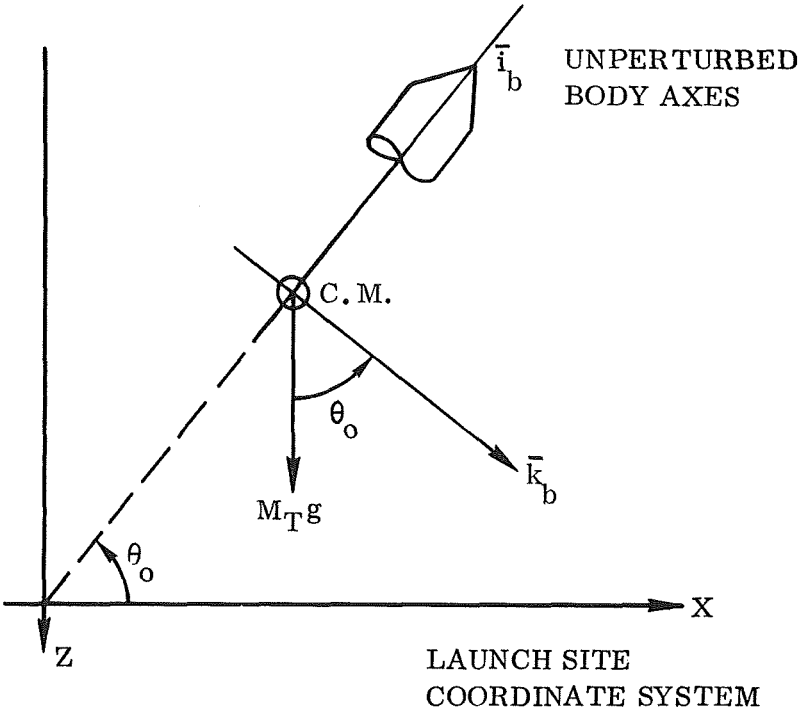

$$F_{gx} = - M_T g (\cos \theta_o) \theta$$

$$F_{gy} = M_T g [(\sin \theta_o) \psi + (\cos \theta_o) \phi]$$

$$F_{gz} = - M_T g (\sin \theta_o) \theta$$

Since the center of the body axis coordinate system is located at the vehicle center-of-mass the gravity torques equal zero.

AERODYNAMIC PERTURBATION ACCELERATION COEFFICIENTS

The aerodynamic forces and moments are expressed as dimensionalized coefficients (1/sec) for the body variable rates (u, w, $\dot{\theta}$, etc.).

Translation Equations

$$\frac{F_{xa}}{M_T} = X_u\, u + X_w\, w$$

$$\frac{F_{ya}}{U_o M_R} = (Y_{\dot{\beta}}\, s + Y_\beta)\, \beta + Y_p\, s\phi + Y_r\, s\, \psi$$

$$\frac{F_{za}}{M_R} = Z_u\, u + (Z_{\dot{w}}\, s + Z_w)\, w + Z_\theta\, s\theta$$

Rotation Equations

$$\frac{L_{xa}}{I_{xx}} = L_\beta \beta + L_{pa}\, s\phi + L_r\, s\, \psi$$

$$\frac{L_{ya}}{I_{yy}} = M_u\, u + (M_{\dot{w}}\, s + M_w)\, w + M_\theta\, s\theta$$

$$\frac{L_{za}}{I_{zz}} = (N_{\dot{\beta}}\, s + N_\beta)\, \beta + N_p\, s\phi + N_r\, s\, \psi$$

ENGINE INERTIA PERTURBATION FORCES AND TORQUES

Figures B3, B4, and B5 illustrate the engine gimballing dynamic models and parameter definitions.

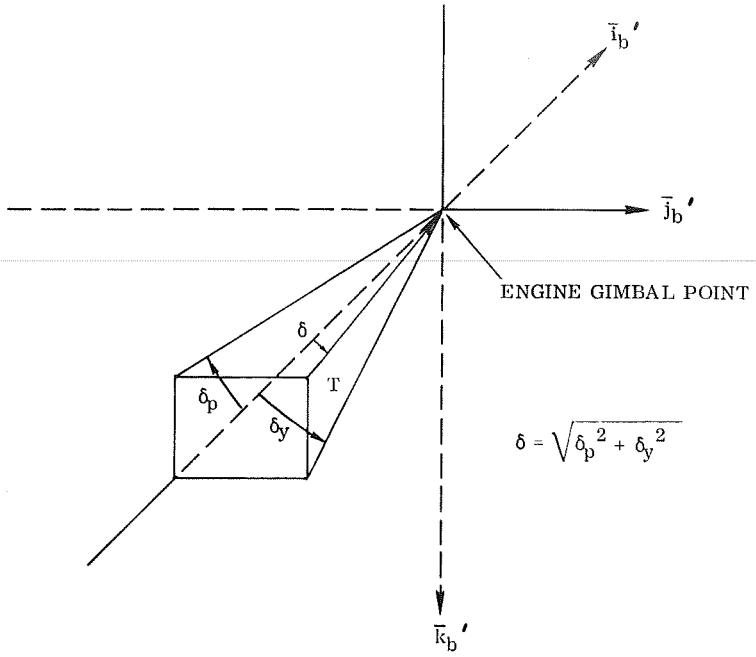

(a) Pitch and Yaw Control

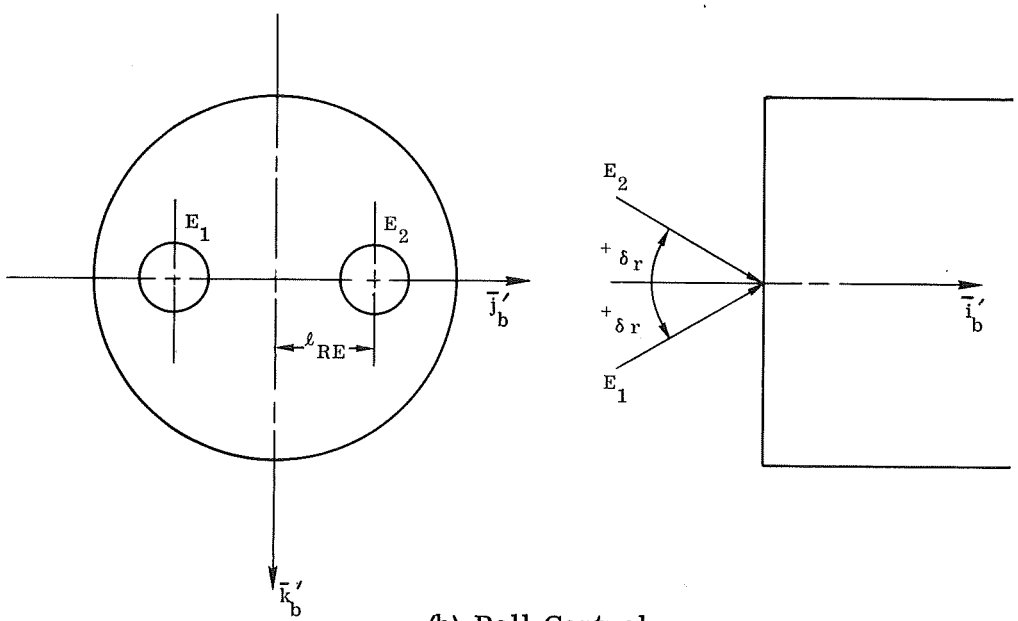

(b) Roll Control

Figure B3. Engine Gimbal System

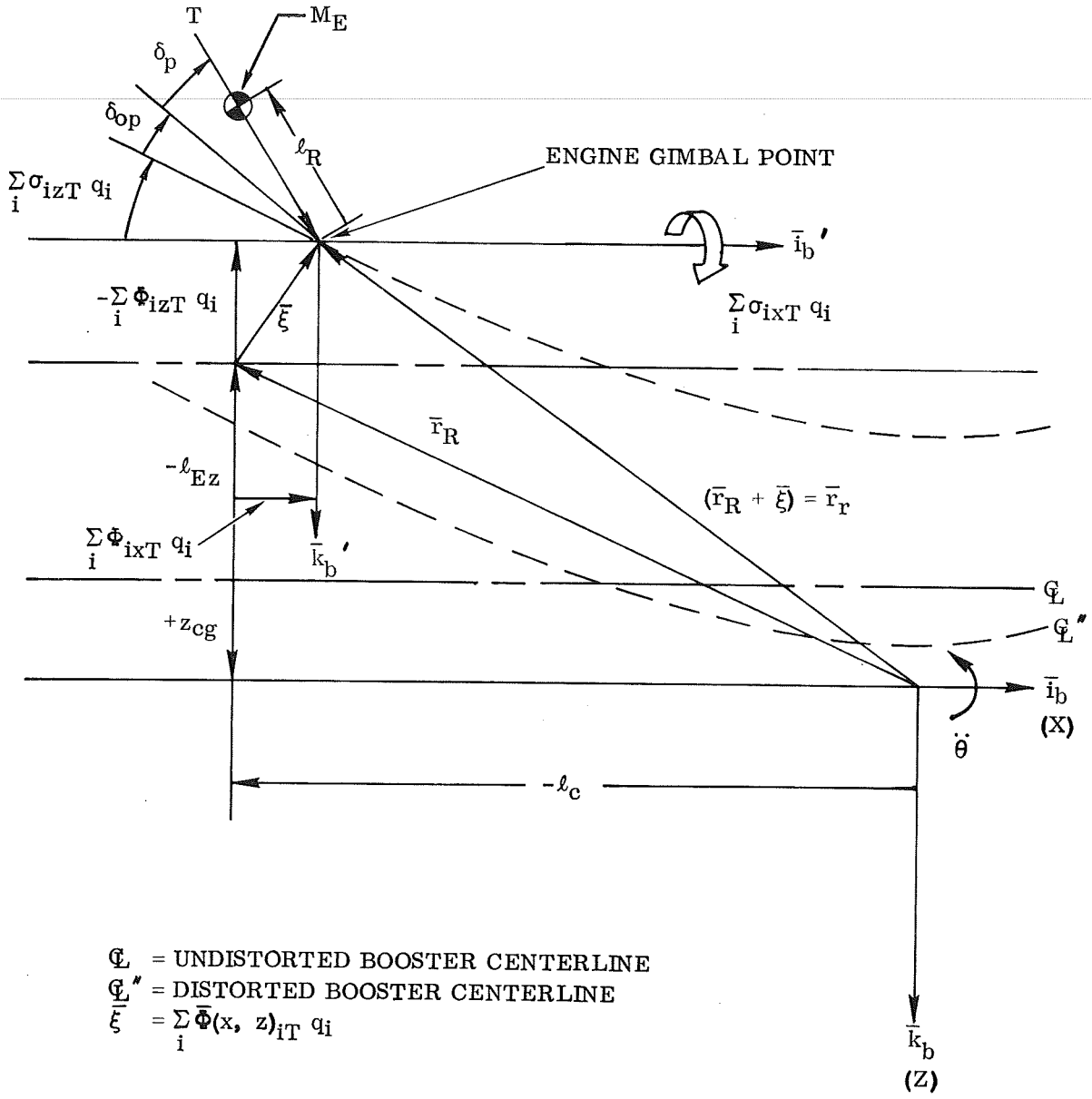

℄ = UNDISTORTED BOOSTER CENTERLINE
℄″ = DISTORTED BOOSTER CENTERLINE
$\bar{\xi} = \sum_i \bar{\Phi}(x, z)_{iT}\, q_i$

Figure B4. Longitudinal (Pitch Plane) Rocket Engine Dynamics

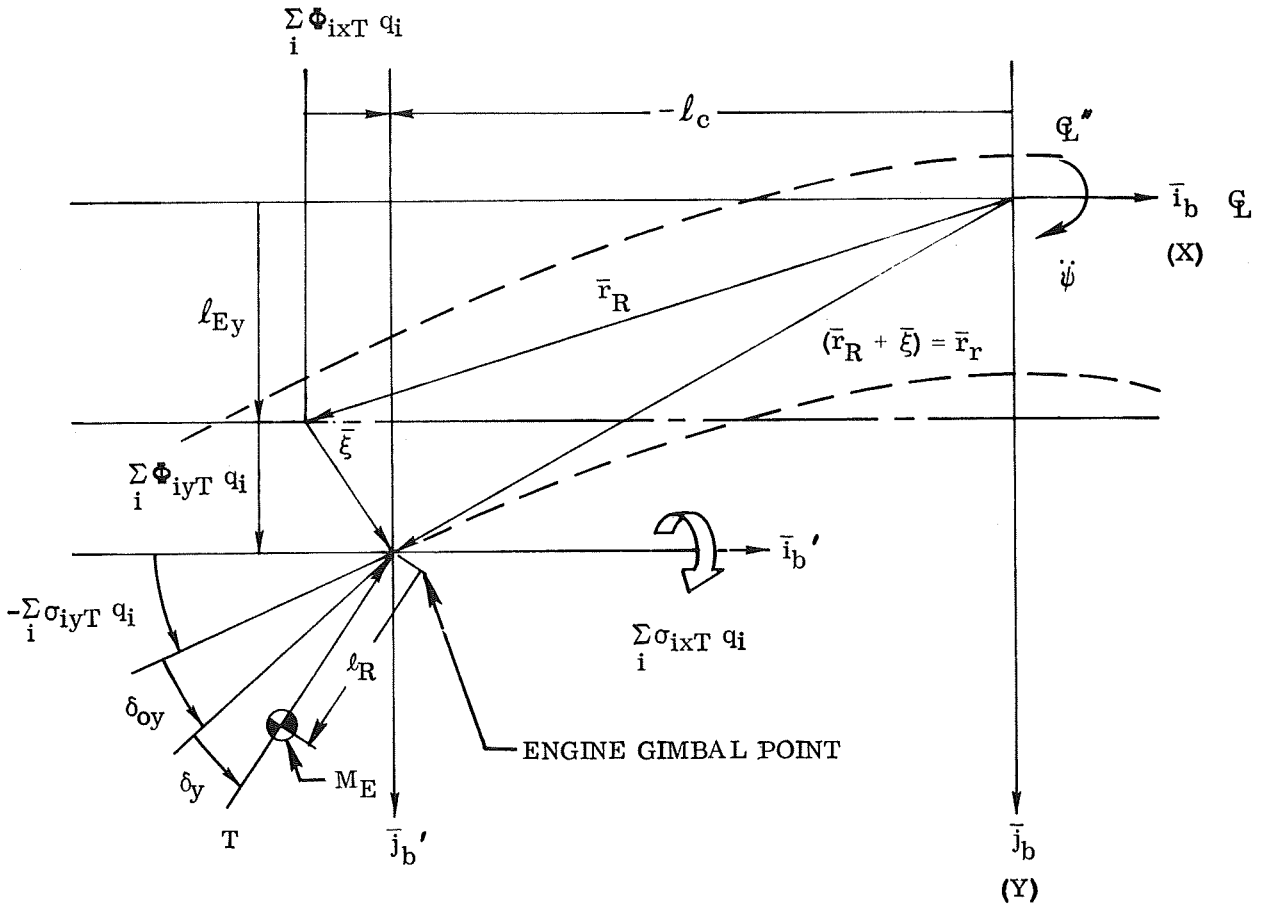

$\mathcal{L}$ = UNDISTORTED BOOSTER CENTERLINE
$\mathcal{L}''$ = DISTORTED BOOSTER CENTERLINE
$\bar{\xi} = \sum_i \Phi(x, y)_{iT}\, q_i$

Figure B5. Lateral (Yaw/Roll Plane) Rocket Engine Dynamics

The engine inertia forces and torques acting on the vehicle at the gimbal point are as follows:

$$F_{Ex} = - M_E su - [M_E (\ell_{Ez} - z_{cg}) - M_E \ell_R \delta_{op}] s^2 \theta$$

$$- \sum_i [M_E \ell_R \delta_{op} \sigma_{izT} + M_E \Phi_{ixT}] s^2 q_i$$

$$- M_E \ell_R \delta_{op} s^2 \delta_p$$

$$F_{Ey} = - M_E U_o s\beta + M_E (\ell_{Ez} - z_{cg} - \ell_R \delta_{op}) s^2 \phi$$

$$+ [- M_E (\ell_c - \ell_R) s^2 - M_E U_o s + M_E \dot{U}_o] \psi$$

$$+ \sum_i [- M_E \Phi_{iyT} + M_E \ell_R \sigma_{iyT} - M_E \ell_R \delta_{op} \sigma_{ixT}] s^2 q_i$$

$$- M_E \ell_R s^2 \delta_y$$

$$F_{Ez} = - M_E s w + [M_E (\ell_c - \ell_R) s^2 + M_E U_o s$$

$$- M_E \dot{U}_o] \theta + \sum_i [- M_E \Phi_{izT} + M_E \ell_R \sigma_{izT}] s^2 q_i$$

$$+ M_E \ell_R s^2 \delta_p$$

$$L_{Ex} = - M_E U_o \ell_R \delta_{op} s\beta + [- I_R + M_E \ell_R \delta_{op} (\ell_{Ez} - z_{cg})] s^2 \phi$$

$$+ [- M_E \ell_R \ell_c \delta_{op} s^2 - M_E \ell_R U_o \delta_{op} s + M_E \ell_R \dot{U}_o \delta_{op}] \psi$$

$$+ \sum_i [- M_E \ell_R \delta_{op} \Phi_{iyT} - I_R \sigma_{ixT}] s^2 q_i$$

$$+ T_{RAT} M_E \ell_R \ell_{RE} s^2 \delta_r$$

$$L_{Ey} = M_E \ell_R \delta_{op} s u - M_E \ell_R s w + [M_E \ell_R \delta_{op} (\ell_{Ez} - z_{cg})$$

$$+ M_E \ell_R \ell_c - I_R] s^2 \theta + \sum_i \{ [- M_E \ell_R \Phi_{izT}$$

$$+ I_R \sigma_{izT} + M_E \ell_R \delta_{op} \Phi_{ixT}] s^2$$

$$+ M_E \ell_R U_o \sigma_{izT} s + M_E \ell_R \dot{U}_o \sigma_{izT} \} q_i$$

$$+ (I_R s^2 + M_E \ell_R U_o s + M_E \ell_R \dot{U}_o) \delta_p$$

$$L_{Ez} = M_E U_o \ell_R s\beta + [- M_E \ell_R (\ell_{Ez} - z_{cg}) s^2$$

$$+ M_E \ell_R \delta_{op} U_o s - M_E \ell_R \delta_{op} \dot{U}_o] \phi$$

$$+ (M_E \ell_R \ell_c - I_R) s^2 \psi + \sum_i \{ [M_E \ell_R \Phi_{iyT}$$

$$-I_R \sigma_{iyT}] s^2 + [-M_E \ell_R U_o \sigma_{iyT} + M_E \ell_R \delta_{op} U_o \sigma_{ixT}] s$$

$$+ [-M_E \ell_R \dot{U}_o \sigma_{iyT} + M_E \ell_R \dot{U}_o \delta_{op} \sigma_{ixT}] \} q_i$$

$$+ [I_R s^2 + M_E \ell_R U_o s + M_E \ell_R \dot{U}_o] \delta_y$$

The total engine inertia torques acting on the vehicle are obtained from the following expressions:

$$L_{Rx} = L_{Ex} - (\ell_{Ez} - z_{cg}) F_{Ey}$$

$$L_{Ry} = L_{Ey} + (\ell_{Ez} - z_{cg}) F_{Ex} - \ell_c F_{Ez} - \sum_i M_E \dot{U}_o \Phi_{izT} q_i$$

$$L_{Rz} = L_{Ez} + \ell_c F_{Ey}$$

THRUST PERTURBATION FORCES AND TORQUES

The thrust forces and torques are obtained from Figures B3, B4, and B5.

$$F_{Tx} = -\sum_i T\,\delta_{op}\,\sigma_{izT}\,q_i - T\,\delta_{op}\,\delta_p$$

$$F_{Ty} = \sum_i (T\,\sigma_{iyT} - T\,\delta_{op}\,\sigma_{ixT} + T_s\,\sigma_{iyTs})\,q_i - T\,\delta_y$$

$$F_{Tz} = \sum_i (T\,\sigma_{izT} + T_s\,\sigma_{izTs})\,q_i + T\,\delta_p$$

$$L_{Tx} = \sum_i [T\,\delta_{op}\,\Phi_{iyT} - T\,(\ell_{Ez} - z_{cg})\,\sigma_{iyT} + T\,(\ell_{Ez} - z_{cg})\,\delta_{op}\,\sigma_{ixT} + T_s\,\delta_{oy}\,\Phi_{izTs} + T_s\,\ell_{Ey}\,\sigma_{izTs} + T_s\,z_{cg}\,\sigma_{iyTs} - T_s\,\ell_{Ey}\,\delta_{oy}\,\sigma_{ixTs}]\,q_i + T\,(\ell_{Ez} - z_{cg})\,\delta_y + T_{RAT}T\,\ell_{RE}\,\delta_r$$

$$L_{Ty} = \sum_i [T\,\Phi_{izT} - T\,\delta_{op}\,(\ell_{Ez} - z_{cg})\,\sigma_{izT} - T\,\ell_c\,\sigma_{izT} - T\,\delta_{op}\,\Phi_{ixT} + T_s\,\Phi_{izTs} - T_s\,\ell_c\,\sigma_{izTs}]\,q_i + [T\,\delta_{op}\,(z_{cg} - \ell_{Ez}) - T\,\ell_c]\,\delta_p$$

$$L_{Tz} = \sum_i [- T \Phi_{iyT} + T \ell_c \sigma_{iyT} - T \ell_c \delta_{op} \sigma_{ixT}$$

$$- T_s \Phi_{iyTs} + T_s (\ell_c - \ell_{Ey} \delta_{oy}) \sigma_{iyTs}] q_i$$

$$- T \ell_c \delta_y$$

PROPELLANT SLOSHING PERTURBATION FORCES AND TORQUES

The propellant sloshing forces and torques are obtained from Figure B2.

$$F_{Sx} = 0$$

$$F_{Sy} = \dot{U}_o \sum_k M_{pk} \Gamma_{pk}$$

$$F_{Sz} = \dot{U}_o \sum_k M_{pk} \Gamma_{pk}$$

$$L_{Sx} = \dot{U}_o \sum_k M_{pk} z_{cg} \Gamma_{pk}$$

$$L_{Sy} = - \dot{U}_o \sum_k M_{pk} \ell_{pk} \Gamma_{pk}$$

$$L_{Sz} = \dot{U}_o \sum_k M_{pk} \ell_{pk} \Gamma_{pk}$$

ACTUATOR PERTURBATION EQUATIONS

The same third-order linear actuator model is used in all three control planes. Figure B6 illustrates this model and presents the parameter values used in this study. The log magnitude and phase diagrams for this particular set of parameters are given in Figure B7.

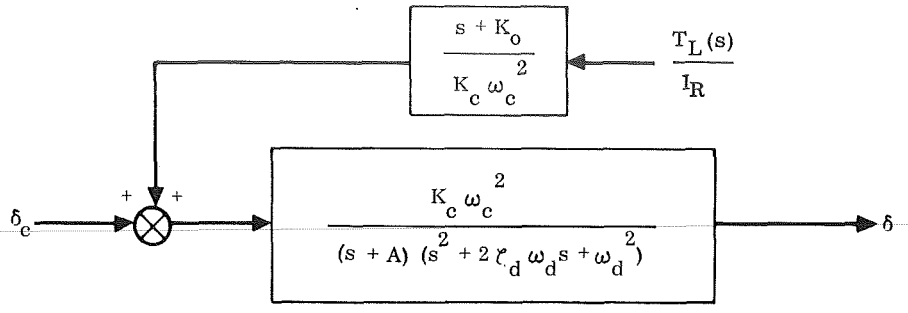

ω_d = 50 Rad./Sec. (Closed-Loop Resonant Frequency, at Load)

$\zeta_d \geq$ 0.3 (By Design)

A = 25 $(1/2\,\omega_d)$

ω_c = 70 Rad/Sec (Servo Resonant Frequency)

K_c = 12.8 Sec^{-1} (Servo Loop Gain)

K_o = 55 Sec^{-1} $(2\zeta_d \omega_d + A)$

Figure B6. Actuator Dynamic Model

The perturbation equation is:

$$(s^3 + 2\zeta_{cn}\omega_{cn}s^2 + \omega_{cn}^2 s + K_c\omega_c^2)\,\delta$$

$$= K_c\omega_c^2\,\delta_c + (s + K_o)\frac{1}{I_R}T_L(s)$$

where: $2\zeta_{cn}\omega_{cn} = 2\zeta_d\omega_d + A$

$$\omega_{cn}^2 = \omega_d^2 + 2\zeta_d\omega_d A$$

$$K_c\omega_c^2 = A\omega_d^2$$

An alternate actuator model uses only a single-order lag: $(s + K_c)\,\delta = K_c\,\delta_c$. This model is adequate for low frequency modes, such as rigid body and, sometimes, propellant sloshing.

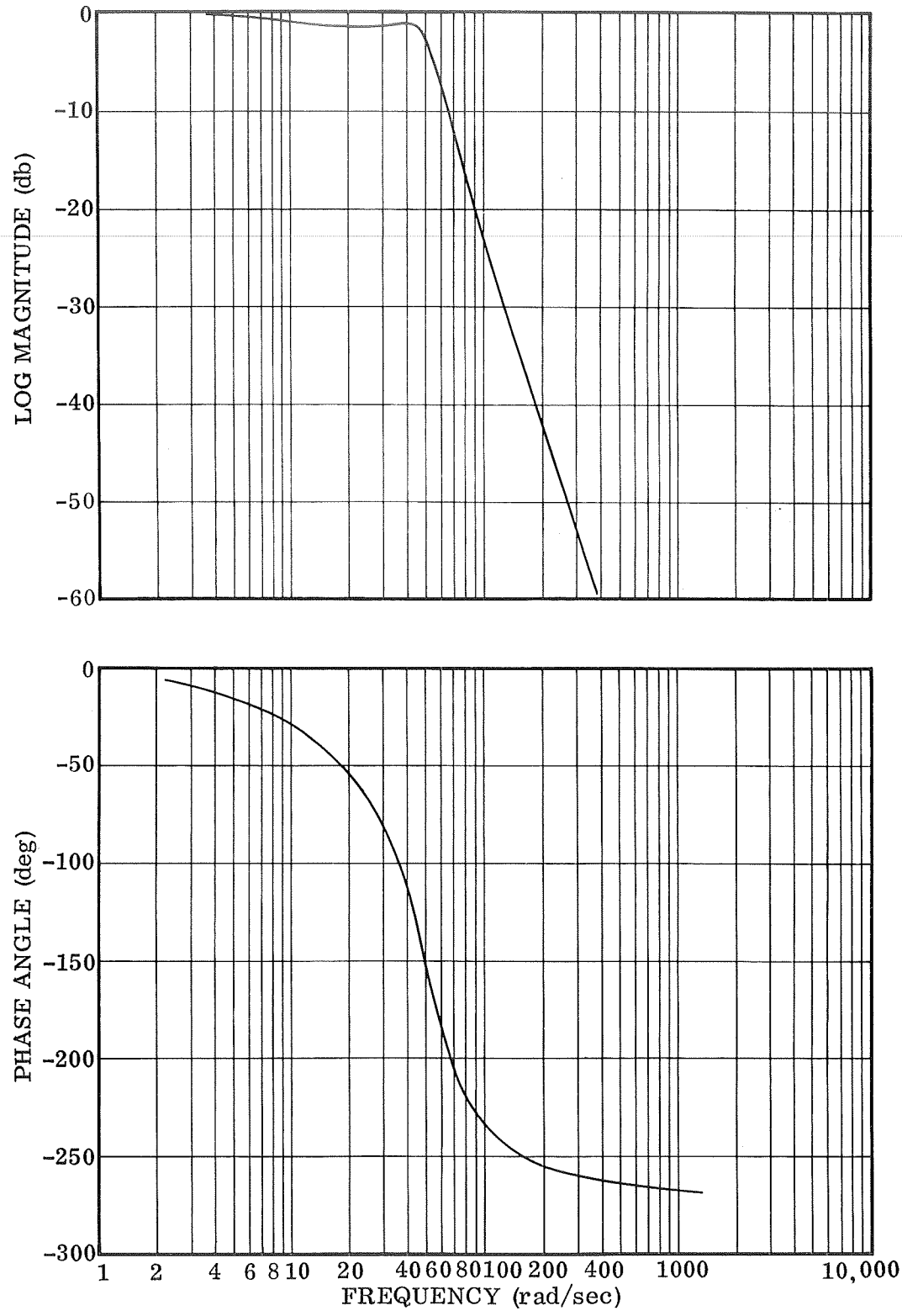

Figure B7. Actuator Model Log Magnitude and Phase Diagrams

The load torque feedback for each control plane is given below.

Roll Control Plane

$$T_{LR} = \sum_i M_E \ell_R \ell_{RE} \sigma_{ixT} s^2 q_i$$

Pitch Control Plane

$$T_{LP} = - M_E \ell_R \delta_{op} s u + M_E \ell_R s w$$

$$+ [I_R - M_E \ell_R \ell_c - M_E \ell_R \delta_{op} (\ell_{Ez} - z_{cg})] s^2 \theta$$

$$+ \sum_i (M_E \ell_R \Phi_{izT} - I_R \sigma_{izT} - M_E \ell_R \delta_{op} \Phi_{ixT}) s^2 q_i$$

Yaw Control Plane

$$T_{LY} = - M_E \ell_R U_o s \beta + M_E \ell_R (\ell_{Ez} - z_{cg}) s^2 \phi$$

$$-(M_E \ell_R \ell_c - I_R) s^2 \psi$$

$$+ \sum_i (- M_E \ell_R \Phi_{iyT} + I_R \sigma_{iyT}) s^2 q_i$$

CONVENTIONAL AUTOPILOT

The equations that describe the conventional autopilot are based on the block diagram shown in Figure B8. Although the following equations were written specifically for the pitch control channel, these equations are also applicable to the other two control channels when the appropriate changes are made to the perturbation variables.

Rate Sensor

$$\frac{1}{K_R} [F_1 (s)] \theta_{RS} = s \theta \overset{(*)}{-} \sum_i \sigma_{iRS} s q_i$$

(*) For the yaw and roll control channels this sign is + based on the sign conventions shown in Figures B4 and B5.

Attitude Sensor

$$[F_2(s)]\theta_A = \theta \overset{(*)}{-} \sum_i \sigma_{iA} q_i$$

(*) For the yaw and roll control channels this sign is + based on the sign conventions shown in Figures B4 and B5.

Actuator Command

$$[F_3(s)]\delta_c = -K_A\theta_{RS} - K_A\theta_A$$

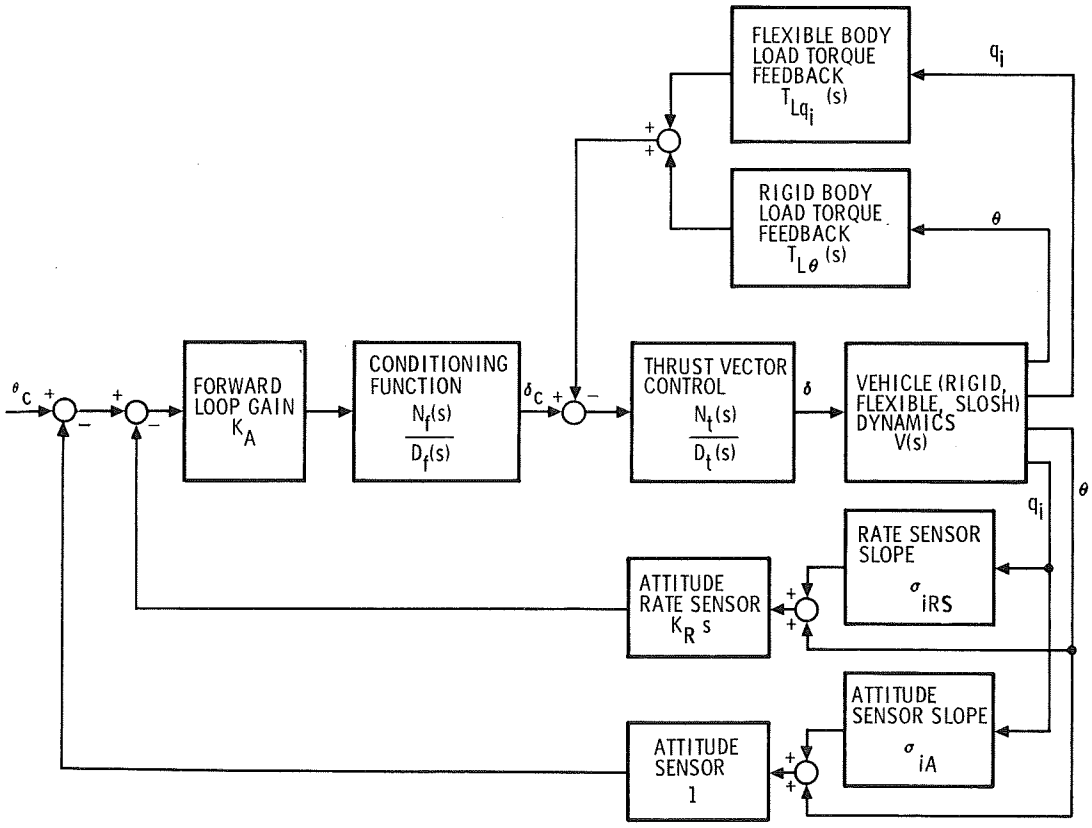

Figure B8. Attitude Control System Block Diagram

In the preceding equations, $F_1(s)$, $F_2(s)$ and $F_3(s)$ indicate capability for the addition of compensation filters.

SOLID MOTOR THRUST CONTROL

Secondary injection is considered for solid motor thrust control in the symmetric mode case (longitudinal equations). To incorporate this control function into the system equations requires the following additions to the longitudinal equations.

w Equation

$$F_{z\delta TS} = T_S \delta_{PS}$$

θ Equation

$$L_{y\delta TS} = - T_S \ell_{cS} \delta_{PS}$$

q_i Equation

$$Q_{i\delta TS} = T_S \Phi_{izTS} \delta_{PS}$$

The TVC system is approximated by:

$$(s + K_c) \delta_{PS} = K_c \delta_{CP}$$

where $K_c = 15 \text{ sec}^{-1}$ ($\tau = 0.0067$ sec)

The command for the TVC system is the same as that sent to the liquid propellant gimballed engines.

COMPLETE SYSTEM EQUATIONS

The complete system equations, as they are used in this study, are presented here. Terms which were demonstrated to have a negligible effect on the analysis results have been eliminated. The primary reason for this simplification is to reduce the complexity and cost of obtaining the roots to the characteristic equation.

These equations can be represented in a matrix format. The roots of the characteristic equation are determined by finding the eigenvalues of the determinant on the left-hand side. The root loci are then obtained by plotting these roots, for different values of autopilot gain, on the complex plane and connecting the points in the direction of increasing gain values from 0 (open-loop pole) to ∞ (zero).

LONGITUDINAL EQUATIONS

$\dot{u}$ Equation

$$(s - X_u)\, u + (Q_o - X_w)\, w + \left(-\frac{M_E \ell_R \delta_{op}}{M_T} s^2 + W_o s + g \cos\theta_o\right)\theta$$

$$+ \sum_i \left[\left(\frac{M_E \ell_R \delta_{op}}{M_T} \sigma_{izT}\right) s^2 + \left(\frac{T \delta_{op}}{M_T}\right)\sigma_{izT}\right] q_i + \left(\frac{M_E \ell_R \delta_{op}}{M_T} s^2 + \frac{T \delta_{op}}{M_T}\right)\delta_p = 0$$

$\dot{w}$ Equation

$$(-Q_o + Z_u)\, u + (s - Z_w)\, w + (-U_o s + g \sin\theta_o)\,\theta$$

$$- \frac{\dot{U}_o}{M_R} \sum_k M_{pk} \Gamma_{pk} + \sum_i \left(-\frac{T}{M_R}\sigma_{izT} - \frac{T_S}{M_R}\sigma_{izTS}\right) q_i$$

$$+ \left(-\frac{M_E \ell_R}{M_R} s^2 - \frac{T}{M_R}\right)\delta_p = 0$$

$\ddot{\theta}$ Equation

$$\left(-\frac{M_E \ell_R \delta_{op}}{I_{yy}} s - M_u\right) u - M_w w + \left[1 - 2\frac{M_E \ell_R \delta_{op}\left(\ell_{Ez} - z_{cg}\right)}{I_{yy}}\right] s^2 \theta$$

$$+ \frac{\dot{U}_o}{I_{yy}} \sum_k M_{pk} \ell_{pk} \Gamma_{pk} + \sum_i \left\{\left[\frac{M_E \ell_R \delta_{op}\left(\ell_{Ez} - z_{cg}\right)}{I_{yy}}\sigma_{izT} - \frac{M_E \ell_R \delta_{op}}{I_{yy}}\Phi_{ixT}\right] s^2\right.$$

$$+\left[-\frac{T}{I_{yy}}\Phi_{izT}+\left(\frac{T\,\ell_c}{I_{yy}}+\frac{T\,\delta_{op}\,(\ell_{Ez}-z_{cg})}{I_{yy}}\right)\sigma_{izT}+\frac{T\,\delta_{op}}{I_{yy}}\Phi_{ixT}\right.$$

$$\left.-\frac{T_S}{I_{yy}}\Phi_{izTS}+\frac{T_S\,\ell_{cS}}{I_{yy}}\sigma_{izTS}\right]\Bigg\}q_i+\Bigg\{\left[\frac{M_E\,\ell_c\,\ell_R}{I_{yy}}-\frac{I_R}{I_{yy}}+\frac{M_E\,\ell_R\,\delta_{op}\,(\ell_{Ez}-z_{cg})}{I_{yy}}\right]s^2$$

$$-\frac{M_E\,\ell_R\,U_o}{I_{yy}}\,s+\left[\frac{T\,\ell_c}{I_{yy}}+\frac{T\,\delta_{op}\left(\ell_{Ez}-z_{cg}\right)}{I_{yy}}-\frac{M_E\,\ell_R\,\dot{U}_o}{I_{yy}}\right]\Bigg\}\delta_p=0$$

$\ddot{\Gamma}_{pk}$ Equation (Propellant Sloshing)

$$\frac{1}{L_{pk}}\,s\,w+\left(-\frac{\ell_{pk}-L_{pk}}{L_{pk}}\,s^2-\frac{U_o}{L_{pk}}\,s\right)\theta+(s^2+2\,\zeta_{pk}\,\omega_{pk}\,s+\omega_{pk}^{\,2})\,\Gamma_{pk}$$

$$+\sum_i\frac{1}{L_{pk}}\Phi_{izpk}\,s^2\,q_i=0$$

$$\text{where }\omega_{pk}^{\,2}=\frac{\dot{U}_o}{L_{pk}}\quad\text{and } k=1,\,2,\,\ldots,m$$

$\ddot{q}_i$ Equation (Elastic Body)

$$M_E\,\ell_R\,\delta_{op}\,\sigma_{izT}\,s\,u+[M_E\,\ell_R\,\delta_{op}\,(\ell_{Ez}-z_{cg})\,\sigma_{izT}-M_E\,\ell_R\,\delta_{op}\,\Phi_{ixT}]\,s^2\,\theta$$

$$-\dot{U}_o\sum_k M_{pk}\,\Phi_{izpk}\,\Gamma_{pk}+\mu_i\,(s^2+2\,\zeta_{Bi}\,\omega_{Bi}\,s+\omega_{Bi}^{\,2})\,q_i$$

$$+\sum_{j=1}^{n}\{[(M_E\,\ell_R\,\delta_{op}\,\Phi_{ixT})\,\sigma_{jzT}+(M_E\,\ell_R\,\delta_{op}\,\sigma_{izT})\,\Phi_{jxT}]\,s^2$$

$$+[(-T\,\Phi_{izT}+T\,\delta_{op}\,\Phi_{ixT})\,\sigma_{jzT}-(T_S\,\Phi_{izTS})\,\sigma_{jzTS}]\}\,q_j$$

$$+[(-M_E\,\ell_R\,\Phi_{izT}+I_R\,\sigma_{izT}+M_E\,\ell_R\,\delta_{op}\,\Phi_{ixT})\,s^2+M_E\,\ell_R\,U_o\,\sigma_{izT}\,s$$

$$+ (- T \Phi_{izT} + M_E \ell_R \dot{U}_o \sigma_{izT} + T \delta_{op} \Phi_{ixT})] \delta_p = 0$$

$\ddot{\delta}_p$ Equation

$$\frac{M_E \ell_R \delta_{op}}{I_R} (s^2 + K_o s) u - \frac{M_E \ell_R}{I_R} (s^2 + K_o s) w + \left[\frac{M_E \ell_R \ell_c}{I_R} - 1 \right.$$

$$\left. + \frac{M_E \ell_R \delta_{op} (\ell_{Ez} - z_{cg})}{I_R} \right] (s^3 + K_o s^2) \theta + \sum_i \left[- \frac{M_E \ell_R}{I_R} \Phi_{izT} + \sigma_{izT} \right.$$

$$\left. + \frac{M_E \ell_R \delta_{op}}{I_R} \Phi_{ixT} \right] (s^3 + K_o s^2) q_i + (s^3 + 2 \zeta_{cn} \omega_{cn} s^2 + \omega_{cn}^2 s + K_c \omega_c^2) \delta_p$$

$$- K_c \omega_c^2 \delta_{cp} = 0$$

PITCH AUTOPILOT EQUATIONS

Rate Sensor

$$\frac{1}{K_{RP}} \left(\frac{1}{\omega_{F1}^2} s^2 + \frac{2 \zeta_{F1}}{\omega_{F1}} s + 1 \right) \theta_{RS} - s \theta + \sum_i \sigma_{iPRS} s q_i = 0$$

Attitude Sensor

$$\left(\frac{1}{\omega_{F2}^2} s^2 + \frac{2 \zeta_{F2}}{\omega_{F2}} s + 1 \right) \theta_A - \theta + \sum_i \sigma_{iPA} q_i = 0$$

Actuator Command

$$\left(\frac{1}{\omega_{F3}^2} s^2 + \frac{2 \zeta_{F3}}{\omega_{F3}} s + 1 \right) \delta_{cp} + K_p \theta_{RS} + K_p \theta_A = 0$$

LATERAL EQUATIONS

$\dot{\beta}$ Equation

$$\left(\frac{V_T}{U_o}s - \frac{Y_\beta}{U_o}\right)\beta + \left(\frac{M_E \ell_R \delta_{op}}{M_R U_o}s^2 - \frac{W_o}{U_o}s - \frac{g}{U_o}\cos\theta_o\right)\phi + \left(s - \frac{g}{U_o}\sin\theta_o\right)\psi$$

$$- \frac{\dot{U}_o}{M_R U_o}\sum_k M_{pk}\Gamma_{pk} + \sum_i \left[\frac{M_E \ell_R \delta_{op}}{M_R U_o}\sigma_{ixT}s^2 + \left(-\frac{T_S}{M_R U_o}\sigma_{iyTS} - \frac{T}{M_R U_o}\sigma_{iyT} + \frac{T\,\delta_{op}}{M_R U_o}\sigma_{ixT}\right)\right] q_i + \left(\frac{M_E \ell_R}{M_R U_o}s^2 + \frac{T}{M_R U_o}\right)\delta_y = 0$$

$\ddot{\phi}$ Equation

$$\left(\frac{M_E \ell_R U_o \delta_{op}}{I_{xx}}s - L_\beta\right)\beta + \left\{\left[1 - 2\frac{M_E \ell_R \delta_{op}(\ell_{Ez} - z_{cg})}{I_{xx}}\right]s^2 - \frac{Q_o I_{xz}}{I_{xx}}s\right\}\phi$$

$$+ \left[\left(\frac{M_E \ell_R \ell_c \delta_{op}}{I_{xx}} - \frac{I_{xz}}{I_{xx}}\right)s^2 + \left(\frac{M_E \ell_R U_o \delta_{op}}{I_{xx}} + Q_o\frac{I_{zz} - I_{yy}}{I_{xx}}\right)s - \frac{M_E \ell_R \delta_{op}\dot{U}_o}{I_{xx}}\right]\psi$$

$$- \frac{\dot{U}_o}{I_{xx}}\sum_k M_{pk} z_{cg}\Gamma_{pk} + \sum_i \left\{\left[\frac{M_E \ell_R \delta_{op}}{I_{xx}}\Phi_{iyT} - \frac{M_E \ell_R \delta_{op}(\ell_{Ez} - z_{cg})}{I_{xx}}\sigma_{ixT}\right]s^2\right.$$

$$+ \left[-\frac{T_S \delta_{oy}}{I_{xx}}\Phi_{izTS} - \frac{T_S \ell_{Ey}}{I_{xx}}\sigma_{izTS} - \frac{T_S z_{cg}}{I_{xx}}\sigma_{iyTS} + \frac{T_S \ell_{Ey}\delta_{oy}}{I_{xx}}\sigma_{ixTS} - \frac{T\,\delta_{op}}{I_{xx}}\Phi_{iyT}\right.$$

$$\left.\left. + \frac{T(\ell_{Ez} - z_{cg})}{I_{xx}}\sigma_{iyT} - \frac{T\,\delta_{op}(\ell_{Ez} - z_{cg})}{I_{xx}}\sigma_{ixT}\right]\right\} q_i + \left[-\frac{M_E \ell_R (\ell_{Ez} - z_{cg})}{I_{xx}}s^2\right.$$

$$\left. - \frac{T(\ell_{Ez} - z_{cg})}{I_{xx}}\right]\delta_y + T_{RAT}\left[-\frac{M_E \ell_R \ell_{RE}}{I_{xx}}s^2 - \frac{T\,\ell_{RE}}{I_{xx}}\right]\delta_r = 0$$

$\ddot{\psi}$ Equation

$$- N_\beta \beta + \left[\left(\frac{M_E \ell_c \ell_R \delta_{op}}{I_{zz}} - \frac{I_{xz}}{I_{zz}}\right) s^2 + \left(Q_o \frac{I_{yy} - I_{xx}}{I_{zz}} - \frac{M_E \ell_R \delta_{op} U_o}{I_{zz}}\right) s + \frac{M_E \ell_R \delta_{op} \dot{U}_o}{I_{zz}}\right] \phi + \left[s^2 + \frac{Q_o I_{xz}}{I_{zz}} s\right] \psi - \frac{\dot{U}_o}{I_{zz}} \sum_k M_{pk} \ell_{pk} \Gamma_{pk}$$

$$+ \sum_i \left\{ \frac{M_E \ell_c \ell_R \delta_{op}}{I_{zz}} \sigma_{ixT} s^2 - \frac{M_E \ell_R \delta_{op} U_o}{I_{zz}} \sigma_{ixT} s + \left[\frac{T_S}{I_{zz}} \Phi_{iyTS} + \left(-\frac{T_S \ell_c}{I_{zz}} + \frac{T_S \ell_{Ey} \delta_{oy}}{I_{zz}}\right)\sigma_{iyTS} + \frac{T}{I_{zz}} \Phi_{iyT} - \frac{T \ell_c}{I_{zz}} \sigma_{iyT} + \left(\frac{T \ell_c \delta_{op}}{I_{zz}} - \frac{M_E \ell_R \delta_{op} \dot{U}_o}{I_{zz}}\right)\sigma_{ixT}\right] \right\} q_i + \left[\left(\frac{M_E \ell_c \ell_R}{I_{zz}} - \frac{I_R}{I_{zz}}\right) s^2 - \frac{M_E \ell_R U_o}{I_{zz}} s + \left(\frac{T \ell_c}{I_{zz}} - \frac{M_E \ell_R \dot{U}_o}{I_{zz}}\right)\right] \delta_y = 0$$

$\ddot{\Gamma}_{pk}$ Equation (Propellant Sloshing)

$$\frac{U_o}{L_{pk}} s \beta + \left(\frac{\ell_{pk} - L_{pk}}{L_{pk}} s^2 + \frac{U_o}{L_{pk}} s\right) \psi + \left(s^2 + 2 \zeta_{pk} \omega_{pk} s + \omega_{pk}^2\right) \Gamma_{pk}$$

$$+ \sum_i \frac{1}{L_{pk}} \Phi_{iypk} s^2 q_i = 0$$

where $\omega_{pk}^2 = \frac{\dot{U}_o}{L_{pk}}$ and $k = 1, 2, \ldots, m$

$\ddot{q}_i$ Equation (Elastic Body)

$$M_E \ell_R U_o \delta_{op} \sigma_{ixT} s \beta + \{ [M_E \ell_R \delta_{op} \Phi_{iyT} - M_E \ell_R \delta_{op} (\ell_{Ez} - z_{cg}) \sigma_{ixT}] s^2$$

$$- M_E \ell_R U_o \delta_{op} \sigma_{iyT} s + M_E \ell_R \delta_{op} \dot{U}_o \sigma_{iyT} \} \phi + (M_E \ell_R \ell_c \delta_{op} \sigma_{ixT} s^2$$

$$+ M_E \ell_R U_o \delta_{op} \sigma_{ixT} s - M_E \ell_R \delta_{op} \dot{U}_o \sigma_{ixT}) \psi - \dot{U}_o \sum_k M_{pk} \Phi_{iypk} \Gamma_{pk}$$

$$+ \mu_i (s^2 + 2 \zeta_i \omega_i s + \omega_i^2) q_i$$

$$+ \sum_{j=1}^{n} \Big[[(M_E \ell_R \delta_{op} \sigma_{ixT}) \Phi_{jyT} + (M_E \ell_R \delta_{op} \Phi_{iyT}) \sigma_{jxT}] s^2 - (M_E \ell_R U_o \delta_{op} \sigma_{iyT}) \sigma_{jxT} s$$

$$+ \{ - (T \delta_{op} \sigma_{ixT}) \Phi_{jyT} + [- T \Phi_{iyT} + T (\ell_{Ez} - z_{cg}) \sigma_{ixT}] \sigma_{jyT} + [T \delta_{op} \Phi_{iyT}$$

$$- M_E \ell_R \dot{U}_o \delta_{op} \sigma_{iyT} - T \delta_{op} (\ell_{Ez} - z_{cg}) \sigma_{ixT}] \sigma_{jxT} - (T_S \sigma_{oy} \sigma_{ixTS}) \Phi_{jzTS}$$

$$+ (- T_S \Phi_{izTS} - T_S \ell_{Ey} \sigma_{ixTS}) \sigma_{jzTS} + (- T_S \Phi_{iyTS} - T_S z_{cg} \sigma_{ixTS}) \sigma_{jyTS}$$

$$+ (T_S \ell_{Ey} \delta_{oy} \sigma_{ixTS}) \sigma_{jxTS} \} \Big] q_j$$

$$+ \{ (M_E \ell_R \Phi_{iyT} - I_R \sigma_{iyT}) s^2 - M_E \ell_R U_o \sigma_{iyT} s + [T \Phi_{iyT}$$

$$- M_E \ell_R \dot{U}_o \sigma_{iyT} - T (\ell_{Ez} - z_{cg}) \sigma_{ixT}] \} \delta_y + T_{RAT} (- M_E \ell_R \ell_{RE} \sigma_{ixT} s^2$$

$$- T \ell_{RE} \sigma_{ixT}) \delta_r = 0$$

$\ddot{\delta}_y$ Equation

$$\frac{M_E \ell_R U_o}{I_R} (s^2 + K_o s) \beta - \frac{M_E \ell_R (\ell_{Ez} - z_{cg})}{I_R} (s^3 + K_o s^2) \phi$$

$$+\left(\frac{M_E \ell_R \ell_c}{I_R} - 1\right)\left(s^3 + K_o s^2\right)\psi + \sum_i \left[\left(\frac{M_E \ell_R}{I_R}\Phi_{iyT} - \sigma_{iyT}\right)\left(s^3 + K_o s^2\right)\right] q_i$$

$$+\left(s^3 + 2\zeta_{cn}\omega_{cn} s^2 + \omega_{cn}^2 s + K_c \omega_c^2\right)\delta_y - K_c \omega_c^2 \delta_{cy} = 0$$

$\ddot{\delta}_r$ Equation

$$-\sum_i \left[\frac{M_E \ell_R \ell_{RE}}{I_R}\sigma_{ixT}\left(s^3 + K_o s^2\right)\right] q_i + \left(s^3 + 2\zeta_{cn}\omega_{cn} s^2 + \omega_{cn}^2 s\right.$$

$$\left. + K_c \omega_c^2\right)\delta_r - K_c \omega_c^2 \delta_{cr} = 0$$

YAW AUTOPILOT EQUATIONS

Rate Sensor

$$\frac{1}{K_{Ry}}\left(\frac{1}{\omega_{F1}^2} s^2 + \frac{2\zeta_{F1}}{\omega_{F1}} s + 1\right)\psi_{RS} - s\psi - \sum_i \sigma_{iyRS}\, s\, q_i = 0$$

Attitude Sensor

$$\left(\frac{1}{\omega_{F2}^2} s^2 + \frac{2\zeta_{F2}}{\omega_{F2}} s + 1\right)\psi_A - \psi - \sum_i \sigma_{iyA}\, q_i = 0$$

Actuator Command

$$\left(\frac{1}{\omega_{F3}^2} s^2 + \frac{2\zeta_{F3}}{\omega_{F3}} s + 1\right)\delta_{cy} + K_y \psi_{RS} + K_y \psi_A = 0$$

ROLL AUTOPILOT EQUATIONS

Rate and Attitude Sensors

$$\phi_S - \phi - K_{RR}\, s\, \phi - \sum_i \sigma_{iRA}\, q_i - K_{RR} \sum_i \sigma_{iRRS}\, s\, q_i = 0$$

Actuator Command

$$\left(\frac{1}{\omega_{F4}^2}\, s^2 + \frac{2\zeta_{F4}}{\omega_{F4}}\, s + 1 \right) \delta_{cr} + K_R\, \phi_S = 0$$

APPENDIX C

DUAL FLYBACK VEHICLE DATA

This appendix contains a tabulation of the dual flyback vehicle data used in this study. It also contains illustrations of the propellant sloshing tank geometries, the specific elastic vehicle models, and the elastic mode shapes.

Essentially all of these data were generated during the Space Shuttle Phase B and follow-on studies. The customary (English) system of units was used to develop the data.

The definition of symbols is contained in Appendix A.

The propellant sloshing parameters were generated by a version of the digital computer program described in Reference 2.

The symmetric configuration uses a flexible beam model, whereas the anti-symmetric configuration uses a detailed three dimensional model for the booster vehicle. Both configurations use a simplified eleven-node flexible beam model for the orbiter vehicle. The mode shapes were generated by the NASTRAN computer program. Further discussion of these models and of the NASTRAN computer program is contained in Reference 3.

TABLE C1. — VEHICLE MASS PROPERTIES

Parameter	Value (Liftoff + 10 seconds)	
T (12 engines)	2.94×10^7 N	(6.61×10^6 lb)
M_E (12 engines)	4.48×10^4 kg	(3070 slugs)
M_R	2.06×10^6 kg	(1.412×10^5 slugs)
M_T	2.21×10^6 kg	(1.515×10^5 slugs)
I_R (12 engines)	5.86×10^4 kg-m^2	(4.32×10^4 slug - ft^2)
I_{xx}	4.53×10^7 kg-m^2	(3.34×10^7 slug - ft^2)
I_{yy}	7.32×10^8 kg-m^2	(5.40×10^8 slug - ft^2)
I_{zz}	7.16×10^8 kg-m^2	(5.28×10^8 slug - ft^2)
I_{xz}	-1.970×10^7 kg-m^2	(-1.453×10^7 slug - ft^2)
ℓ_c	-44.5 m	(-146 ft)
ℓ_{Ez}	0 m	(0 ft)
ℓ_R	0.826 m	(2.71 ft)
ℓ_{RE}	4.61 m	(15.14 ft)
z_{cg}	-1.22 m	(-4 ft)
δ_{op}	-0.07 rad	(-4 deg)
T_{RAT}	2	

TABLE C2. — STEADY-STATE TRAJECTORY DATA

Parameter	Value (Liftoff + 10 Seconds)	
g	9.81 m/sec^2	(32.17 ft/sec^2)
Q_o	-0.0035 rad/sec	(-0.2 deg/sec)
U_o	31.09 m/sec	(102 ft/sec)
$\dot{U}_o$	13.14 m/sec^2	(43.1 ft/sec^2)
V_T	31.09 m/sec	(102 ft/sec)
W_o	1.86 m/sec	(6.1 ft/sec)
Θ_o	1.51 rad	(86.8 deg)
MACH	0.09	
Altitude	151.8 m	(498 ft)
Dynamic Press.	574.6 N/m^2	(12 lb/ft^2)

TABLE C3. — TOTAL VEHICLE AERODYNAMIC DATA

Parameter	Value (Liftoff + 10 seconds)	
X_u	-0.0006 1/sec	
X_w	0.00012 1/sec	
Z_u	0.0041 1/sec	
Z_w	0.144 1/sec	
M_u	$-0.000256 \frac{1}{\text{m-sec}}$	$\left(-0.000078 \frac{1}{\text{ft-sec}}\right)$
M_w	$0.00699 \frac{1}{\text{m-sec}}$	$\left(0.00213 \frac{1}{\text{ft-sec}}\right)$
Y_β	-0.430 m/sec^2	(-1.41 ft/sec^2)
L_β	-0.057 1/sec^2	
N_β	0.044 1/sec^2	

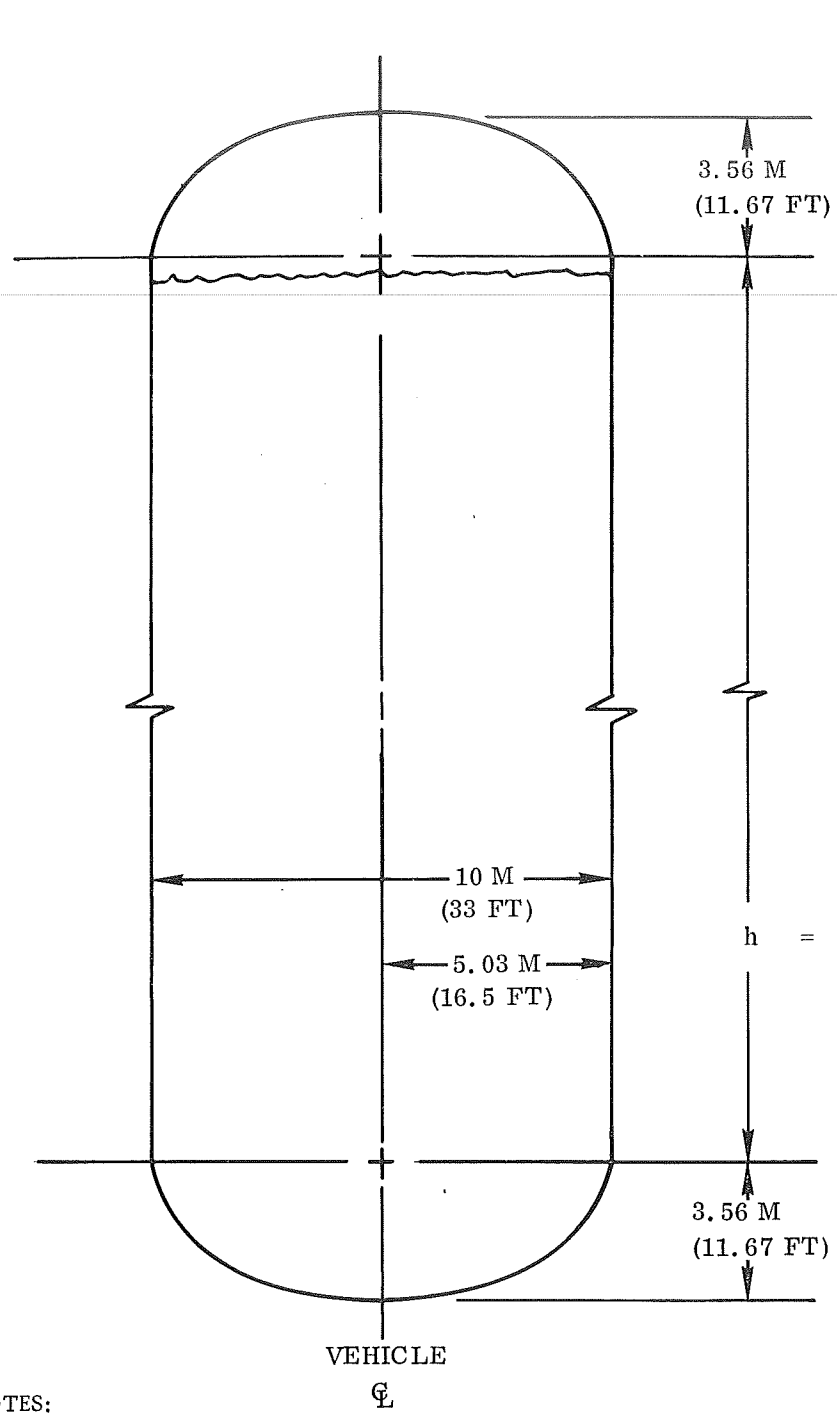

NOTES:

(1) ALL BULKHEADS ARE ELLIPTICAL SURFACES, MAJOR RADIUS = $\sqrt{2}$ × MINOR RADIUS.

(2) QUIESCENT FLUID LEVEL USED IN STUDY (~~~).

Figure C1. Main Propellant Tank Geometry

TABLE C4. — PROPELLANT SLOSHING DATA

Propellant Tank	Parameter	Value	
Oxidizer (LO_2)	M_P	1.51×10^5 kg	(10 350.0 slugs)
	L_P	1.98 m	(6.5 ft)
	ℓ_P	15.67 m	(51.4 ft)
	ω_P	2.58 rad/sec	(0.411 Hz)
	ρ	1136 kg/m^3	(70.9 lb/ft^3)
Fuel (LH_2)	M_P	12 565. kg	(861.0 slugs)
	L_P	2.71 m	(8.9 ft)
	ℓ_P	-4.30 m	(-14.1 ft)
	ω_P	2.2 rad/sec	(0.350 Hz)
	ρ	70.16 kg/m^3	(4.38 lb/ft^3)

TABLE C5. — AUTOPILOT AND ACTUATOR DATA

Parameter	Value
K_c	12.8 1/sec
K_o	55 1/sec
ω_c	70 rad/sec
ω_{cn}	57 rad/sec
ζ_{cn}	0.48 (N.D.)
K_R	0.7 sec
K_A	variable

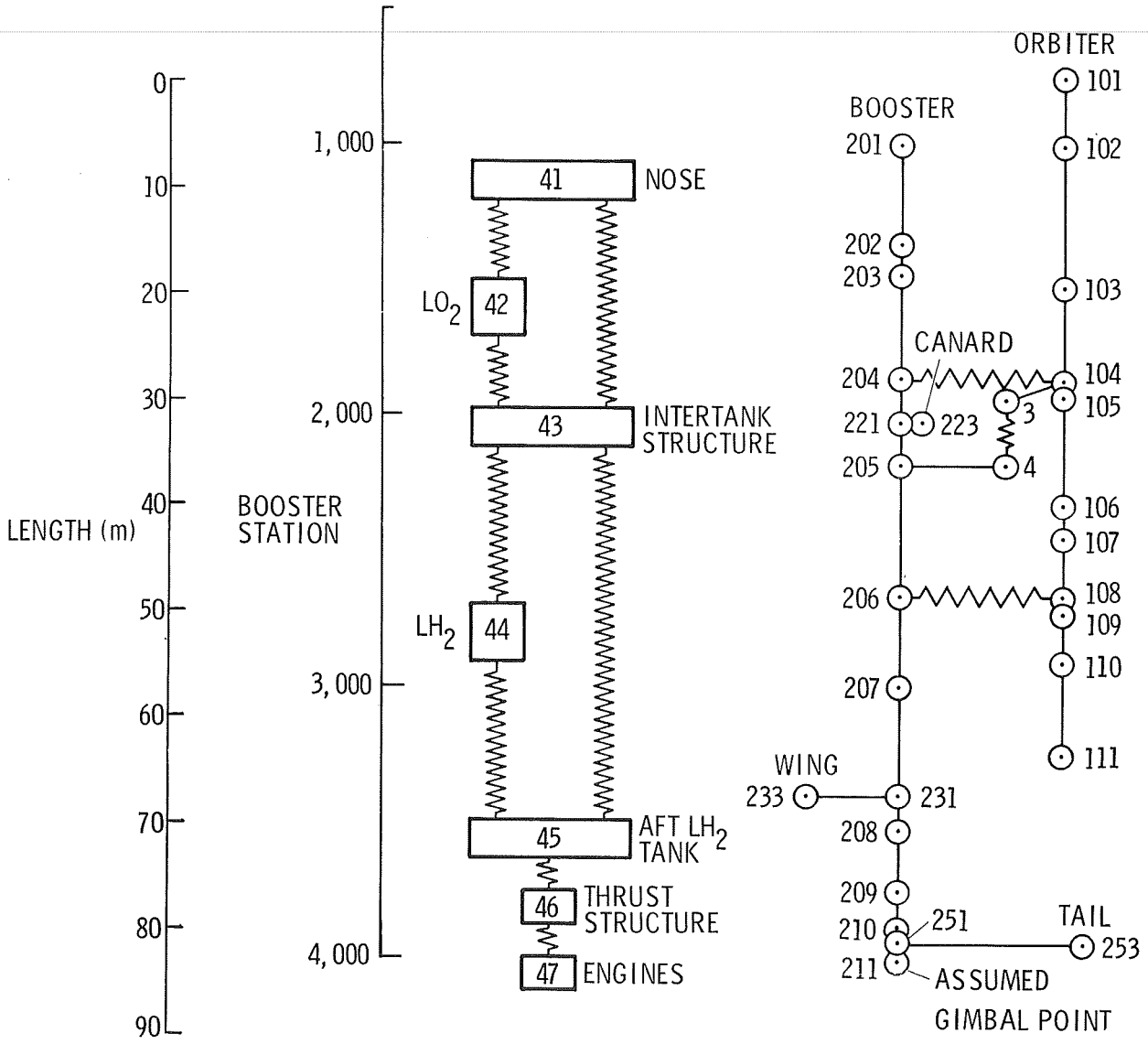

Figure C2. Elastic Model Schematic (Symmetric Boundary Conditions)

TABLE C6. — ELASTIC VEHICLE MODAL DATA
(SYMMETRIC BOUNDARY CONDITIONS)

Mode Number	$\mathcal{M}$ kg (slugs)	ω rad/sec (Hz)	Φ_{xT} $\frac{m}{m} \times 10^3$	Φ_{zT} $\frac{m}{m} \times 10^2$	Φ_{zP} $\frac{m}{m} \times 10^3$	σ_{zT} rad/m $\times 10^4$ (rad/ft $\times 10^4$)
1	350.3 (24)	7.2 (1.15)	1.893	-1.055	2.841	3.97 (1.21)
2	350.3 (24)	11.6 (1.85)	-1.939	2.631	11.70	-14.76 (-4.50)
3	350.3 (24)	14.6 (2.32)	-2.769	-1.234	-9.128	8.24 (2.51)
4	350.3 (24)	17.9 (2.85)	-0.1641	3.046	-0.798	-14.21 (-4.33)
5	350.3 (24)	20.1 (3.20)	-0.029	-0.7294	1.303	7.94 (2.42)
6	350.3 (24)	24.4 (3.88)	-16.87	0.1503	-1.59	-1.76 (-0.536)
7	350.3 (24)	26.6 (4.24)	2.635	0.9535	-7.501	-7.71 (-2.35)
8	350.3 (24)	32.4 (5.16)	0.426	0.2033	0.977	-2.87 (-0.874)
9	350.3 (24)	37.9 (6.03)	1.655	-3.03	4.309	37.96 (11.57)

TABLE C7. — PITCH CONTROL PLANE AUTOPILOT SENSOR ELASTIC MODAL DATA (SYMMETRIC BOUNDARY CONDITIONS)

Mode Number	σ_{PRS} or σ_{PA} - $\frac{rad}{m} \times 10^4 \left(\frac{rad}{ft} \times 10^4\right)$		
	Model Node 201 S.N. 1000	Model Node 204 S.N. 1860	Model Node 207 S.N. 3000
1	0.745 (0.227)	0.341 (0.104)	2.920 (0.890)
2	17.06 (5.20)	12.47 (3.80)	-8.924 (-2.72)
3	-15.36 (-4.68)	-9.646 (-2.94)	4.593 (1.40)
4	-1.125 (-0.343)	-0.3806 (-0.116)	-4.068 (-1.24)
5	-3.281 (-1.00)	-4.528 (-1.38)	3.773 (1.15)
6	-4.26 (-1.30)	-1.345 (-0.410)	0.219 (0.0667)
7	-24.84 (-7.57)	-7.973 (-2.43)	0.951 (0.290)
8	7.678 (2.34)	3.806 (1.16)	-1.207 (-0.368)
9	20.11 (6.13)	-0.5906 (-0.180)	-1.955 (-0.596)

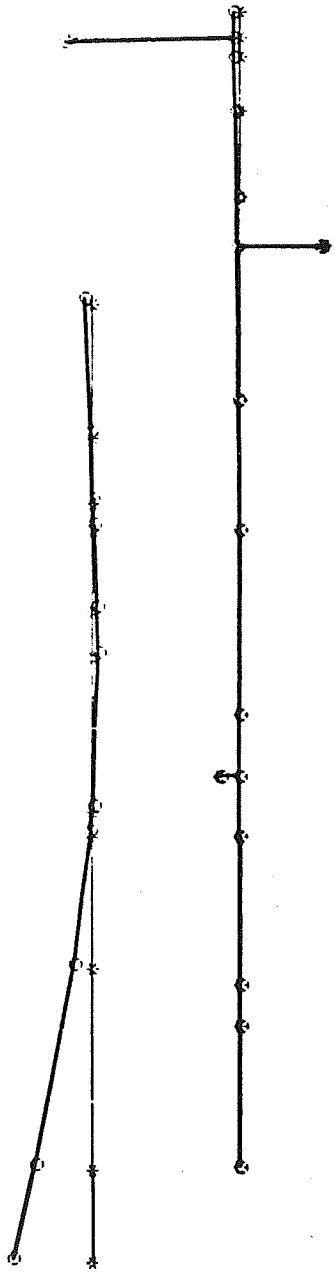

MODE 1 ORBITER FIRST MODE ω = 7.18 RAD/SEC (1.15 Hz)

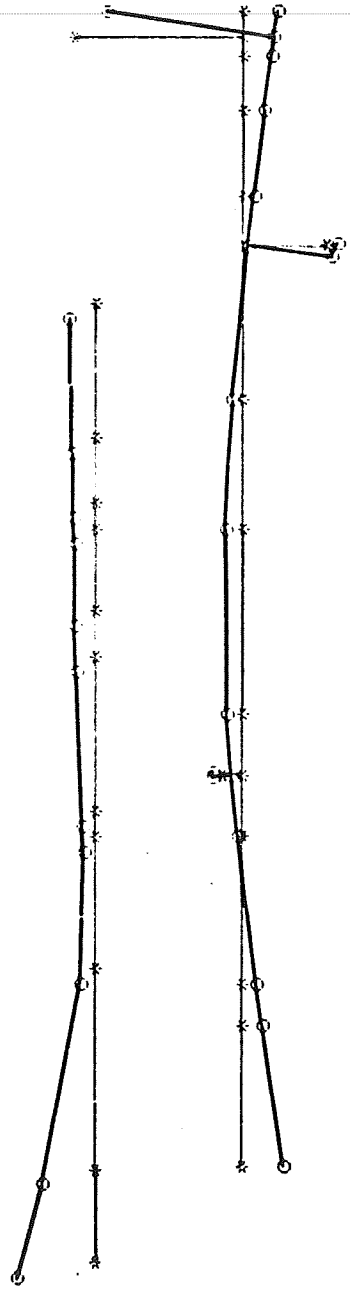

MODE 2 FIRST BOOSTER BODY MODE ω = 11.6 RAD/SEC (1.85 Hz)

Figure C3. Elastic Mode Shapes (Symmetric Boundary Conditions)

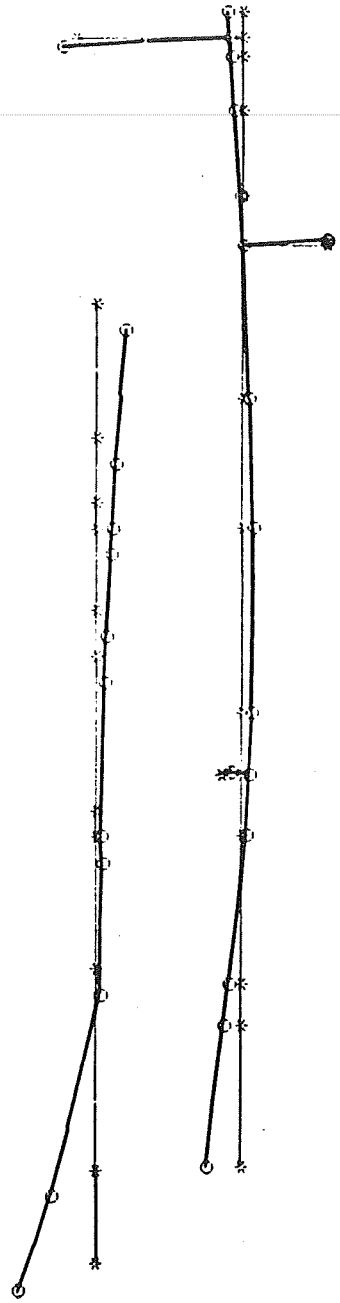

MODE 3 BOOSTER/ORBITER COUPLED MODE ω = 14.6 RAD/SEC (2.32 Hz)

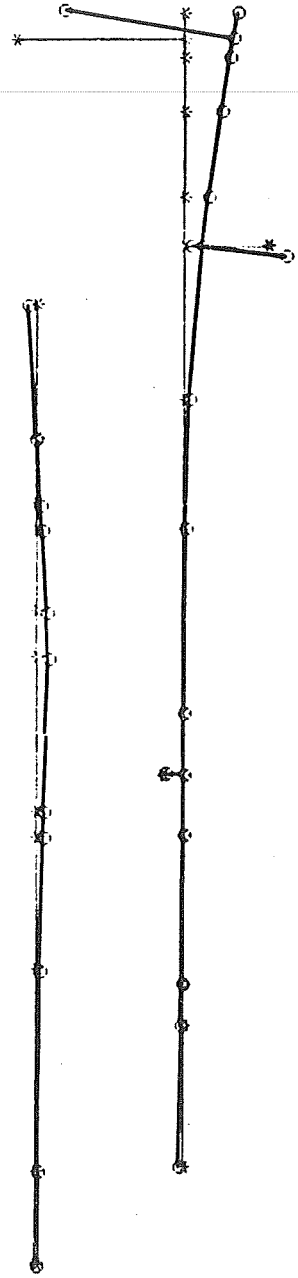

MODE 4 THRUST STRUCTURE MODE ω = 17.9 RAD/SEC (2.85 Hz)

Figure C3. — Continued

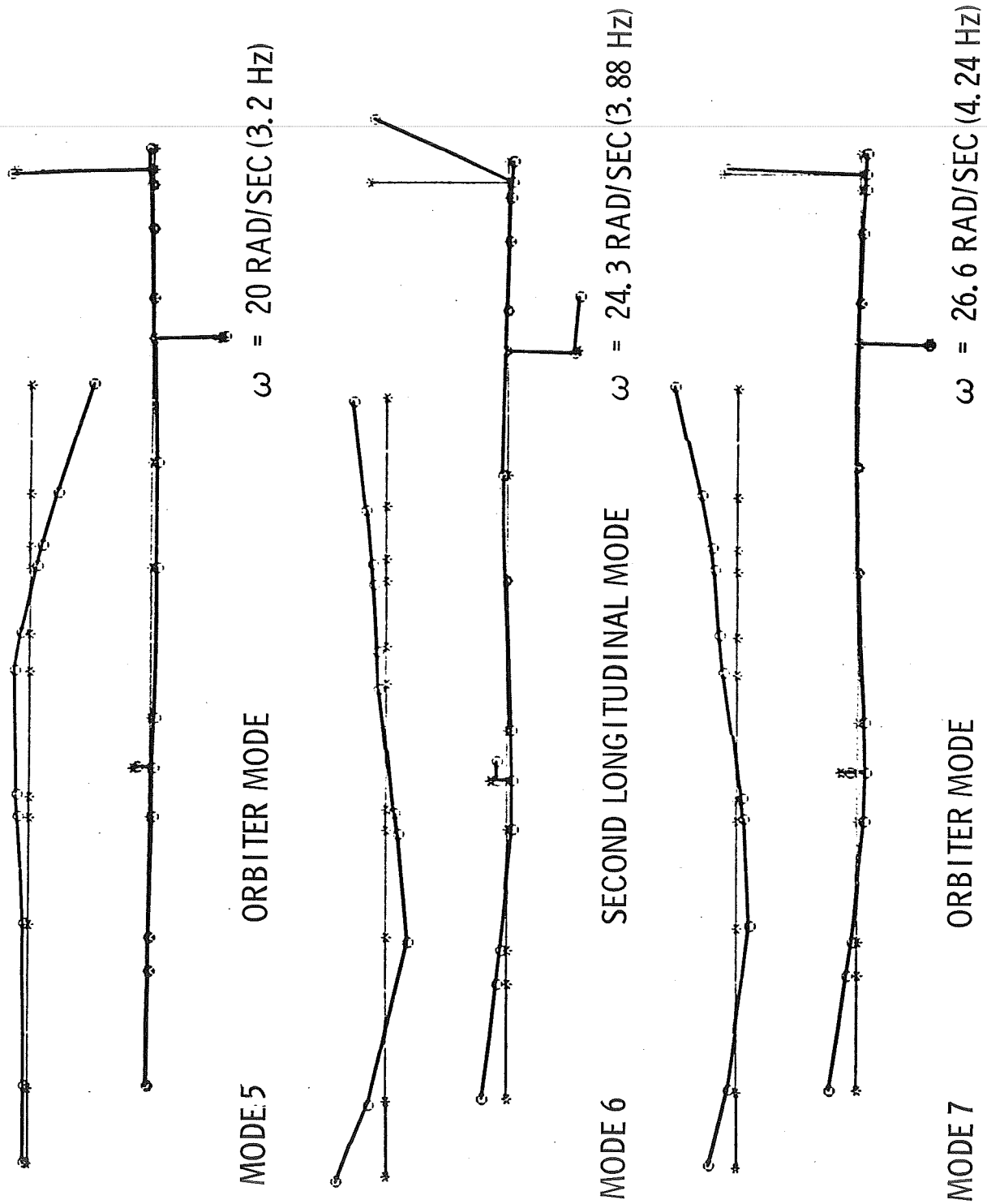

Figure C3. — Continued

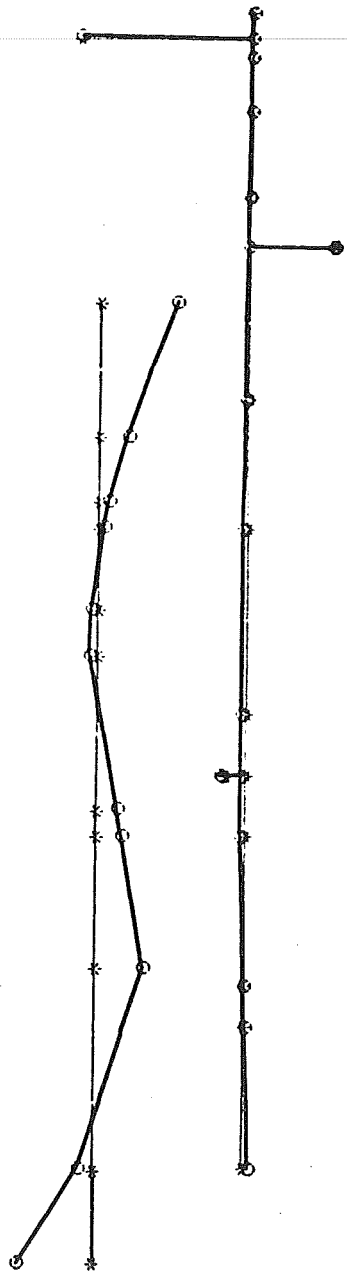

MODE 8 ORBITER SECOND MODE ω = 32.4 RAD/SEC (5.16 Hz)

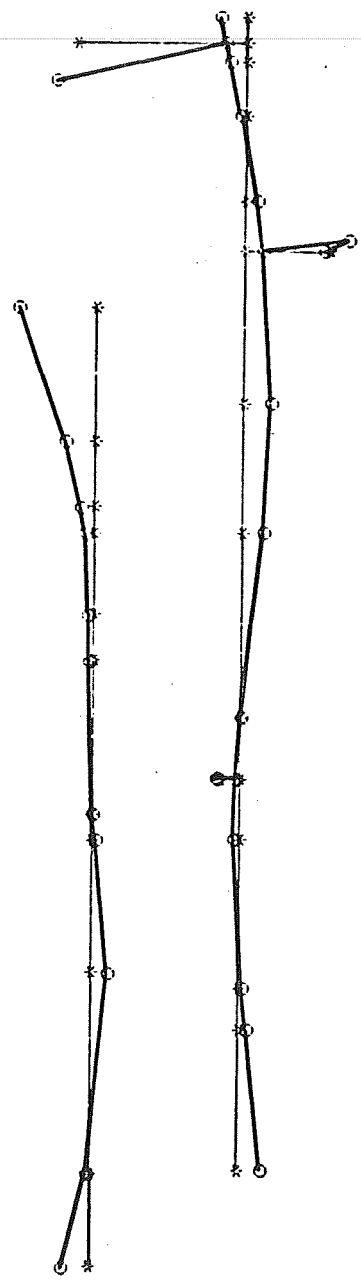

MODE 9 SECOND BOOSTER BODY MODE ω = 37.9 RAD/SEC (6.03 Hz)

Figure C3. — Concluded

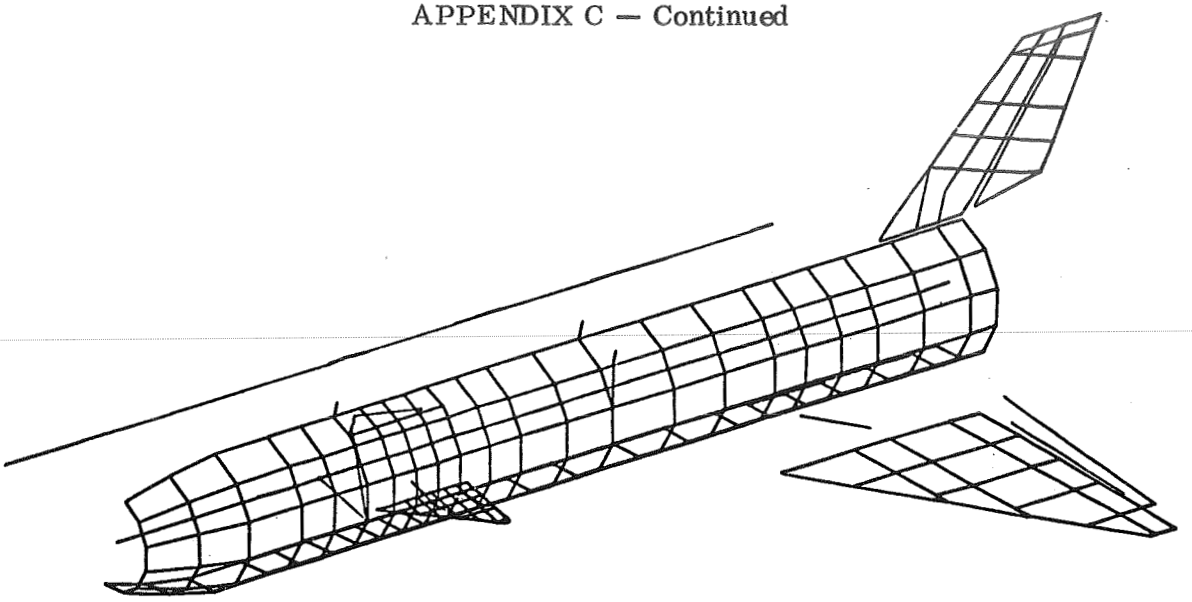

(a) Three Dimension Booster With Orbiter Flexible Beam Model

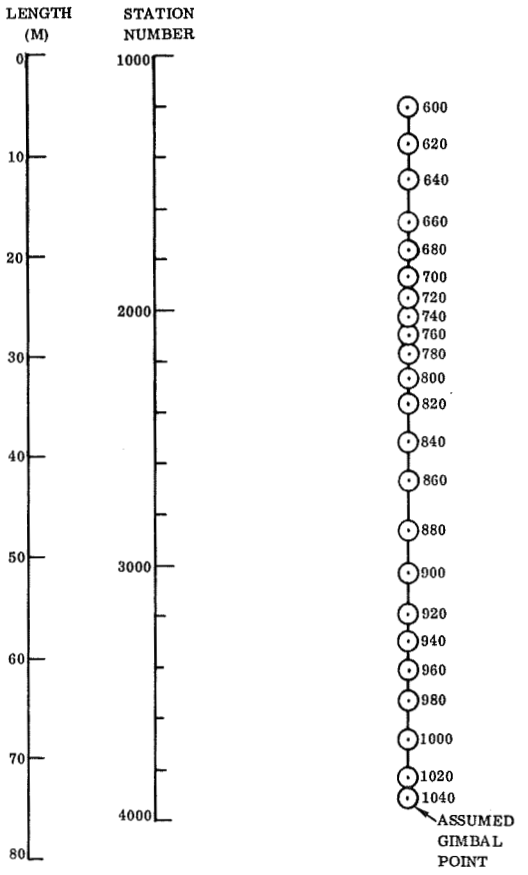

(b) Booster Centerline Representation

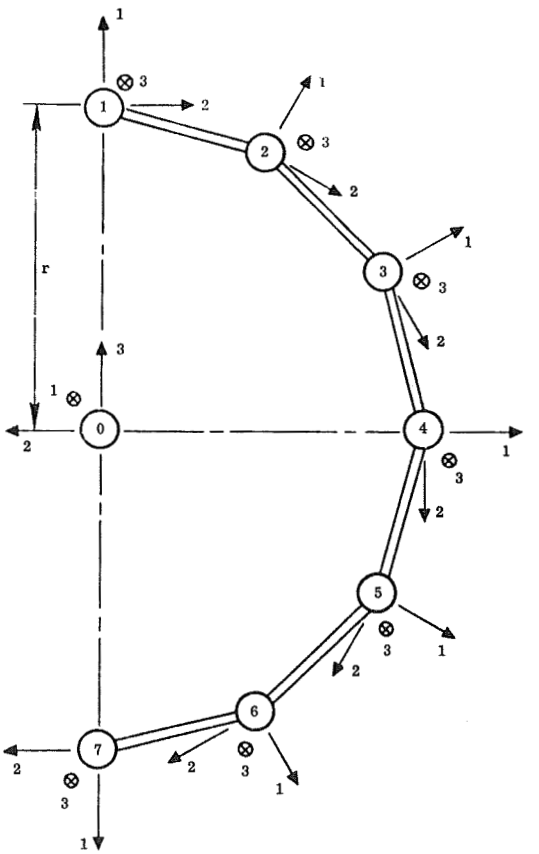

(c) Fuselage Model Cross Section

Figure C4. Elastic Model Schematics (Antisymmetric Boundary Conditions)

TABLE C8. — ELASTIC VEHICLE MODAL DATA (ANTISYMMETRIC BOUNDARY CONDITIONS)

Mode Number	m kg (slugs)	ω rad/sec (Hz)	Φ_{yT} $\frac{m}{m} \times 10^3$	Φ_{yP} $\frac{m}{m} \times 10^3$	σ_{xT} rad/m $\times 10^4$ (rad/ft $\times 10^4$)	σ_{yT} rad/m $\times 10^4$ (rad/ft $\times 10^4$)
1	350.3 (24)	5.4 (0.86)	0.4114	1.63	-21.52 (-6.56)	-0.275 (-0.0837)
2	350.3 (24)	7.4 (1.2)	-11.59	-6.79	10.70 (3.26)	4.03 (1.228)
3	350.3 (24)	10.8 (1.7)	22.25	2.82	3.81 (1.162)	-13.35 (-4.07)
4	350.3 (24)	11.7 (1.9)	-8.327	-8.99	-17.16 (-5.23)	6.39 (1.948)
5	350.3 (24)	14.8 (2.4)	-8.692	-3.22	-19.19 (-5.85)	3.895 (1.187)
6	350.3 (24)	18.2 (2.9)	16.72	-4.29	6.12 (1.867)	-14.8 (-4.51)
7	350.3 (24)	21.6 (3.4)	-4.084	-3.06	23.39 (7.13)	4.666 (1.422)
8	350.3 (24)	22.5 (3.6)	9.437	2.04	-5.73 (-1.747)	-9.269 (-2.825)
9	350.3 (24)	25.6 (4.1)	-6.216	0.935	-72.5 (-22.1)	7.185 (2.19)

TABLE C9. — YAW AND ROLL CONTROL PLANE AUTOPILOT SENSOR ELASTIC MODAL DATA (ANTISYMMETRIC BOUNDARY CONDITIONS)

Mode Number	σ_{yRS} or σ_{yA} - $\frac{rad}{m} \times 10^4$ $\left(\frac{rad}{ft} \times 10^4\right)$			σ_{RRS} or σ_{RA} - $\frac{rad}{m} \times 10^4$ $\left(\frac{rad}{ft} \times 10^4\right)$		
	Model Node 600 S.N. 1200	Model Node 740 S.N. 2024	Model Node 1040 S.N. 3913	Model Node 600 S.N. 1200	Model Node 780-7 S.N. 2170	Model Node 1040 S.N. 3913
1	0.820 (0.25)	0.689 (0.21)	-0.2746 (-0.0837)	-22.869 (-6.97)	-23.394 (-7.13)	-21.523 (-6.56)
2	-3.747 (-1.142)	-2.310 (-0.704)	4.029 (1.228)	9.974 (3.04)	-6.677 (-2.035)	10.696 (3.26)
3	7.333 (2.235)	5.732 (1.747)	-13.354 (-4.07)	17.520 (5.34)	-6.447 (-1.965)	3.812 (1.162)
4	-9.548 (-2.91)	-4.666 (-1.422)	6.391 (1.948)	-5.135 (-1.565)	8.317 (2.535)	-17.160 (-5.23)
5	-4.928 (-1.502)	-1.850 (-0.564)	3.894 (1.187)	-16.372 (-4.99)	0.643 (0.196)	-19.194 (-5.85)
6	-1.522 (-0.464)	2.205 (0.672)	-14.797 (-4.51)	-0.825 (-0.2515)	-12.238 (-3.73)	6.126 (1.867)
7	3.314 (1.01)	0.0103 (0.00313)	4.666 (1.422)	7.596 (2.315)	-23.459 (-7.15)	23.394 (7.13)
8	-1.276 (-0.389)	1.060 (0.323)	-9.269 (-2.825)	-4.593 (-1.4)	6.202 (1.89)	-5.732 (-1.747)
9	0.217 (0.0661)	-1.261 (-0.3845)	7.185 (2.19)	2.992 (0.912)	21.917 (6.68)	-72.510 (-22.1)

(a) Three-Dimensional View of First Body Mode

Figure C5. – Lateral and Torsional Elastic Mode Shapes
(Antisymmetric Boundary Conditions)

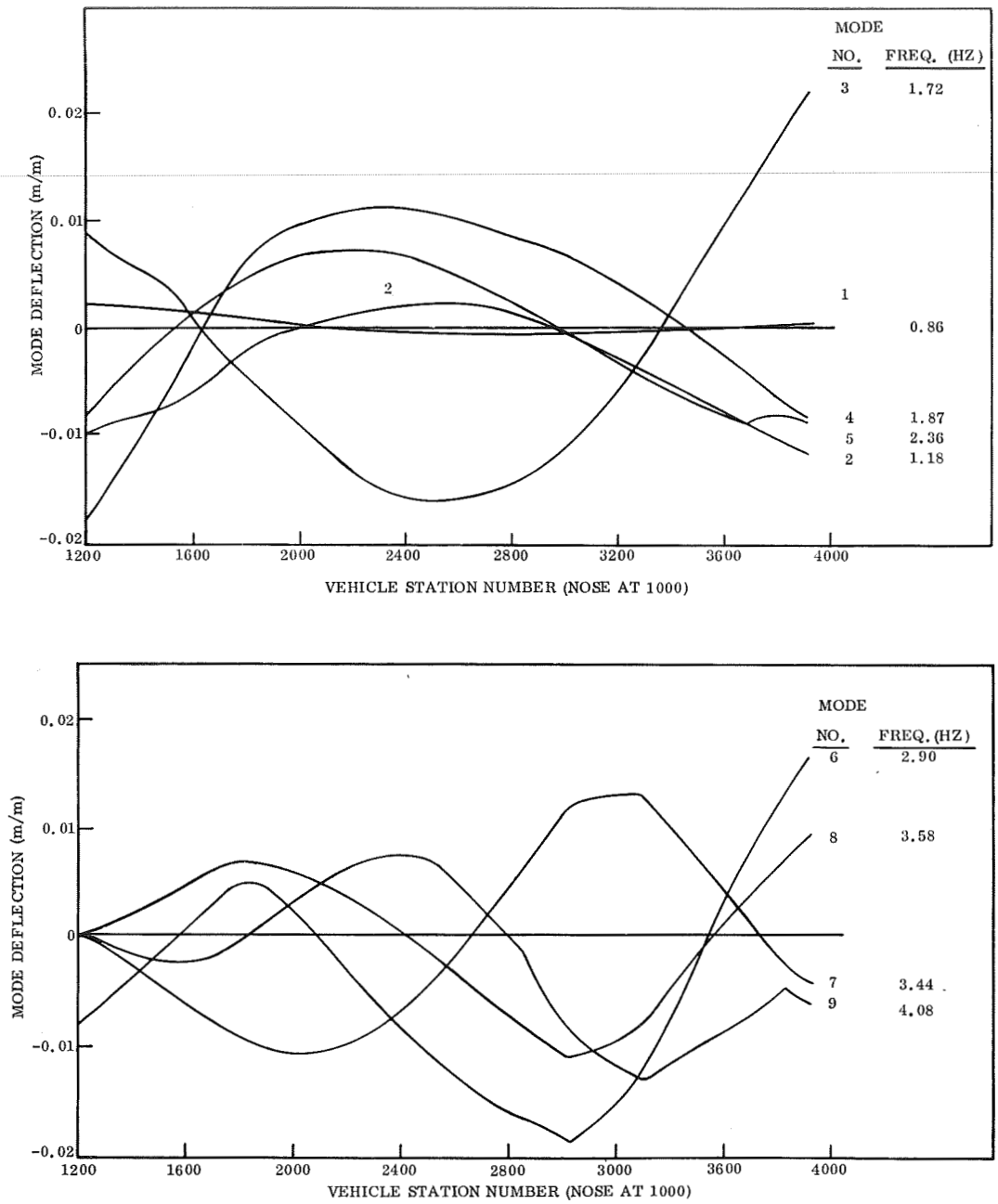

(b) Lateral Component of Equivalent Booster Centerline Elastic Mode Shapes

Figure C5. – Continued

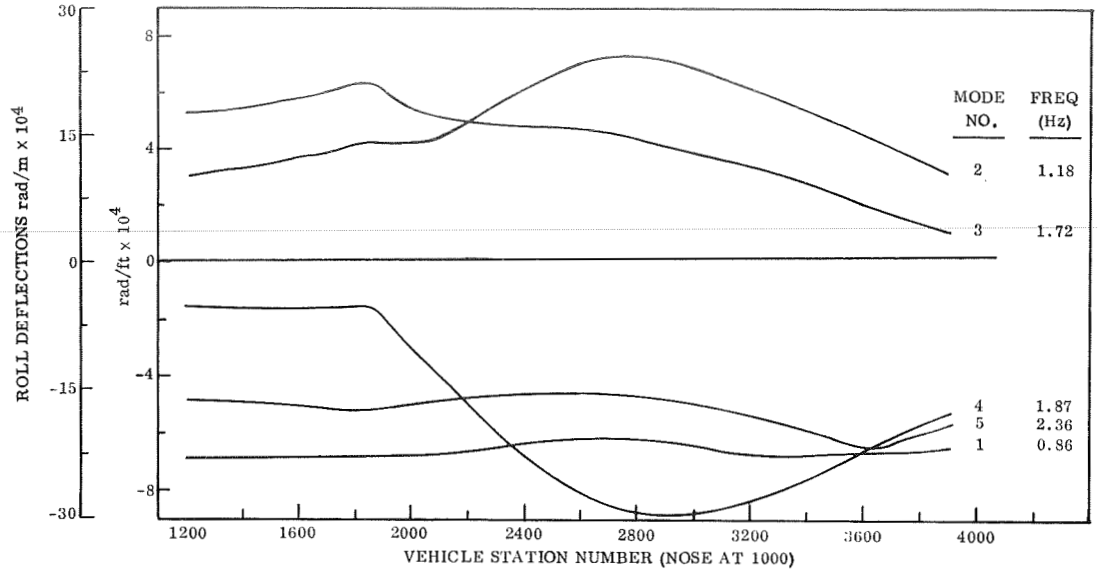

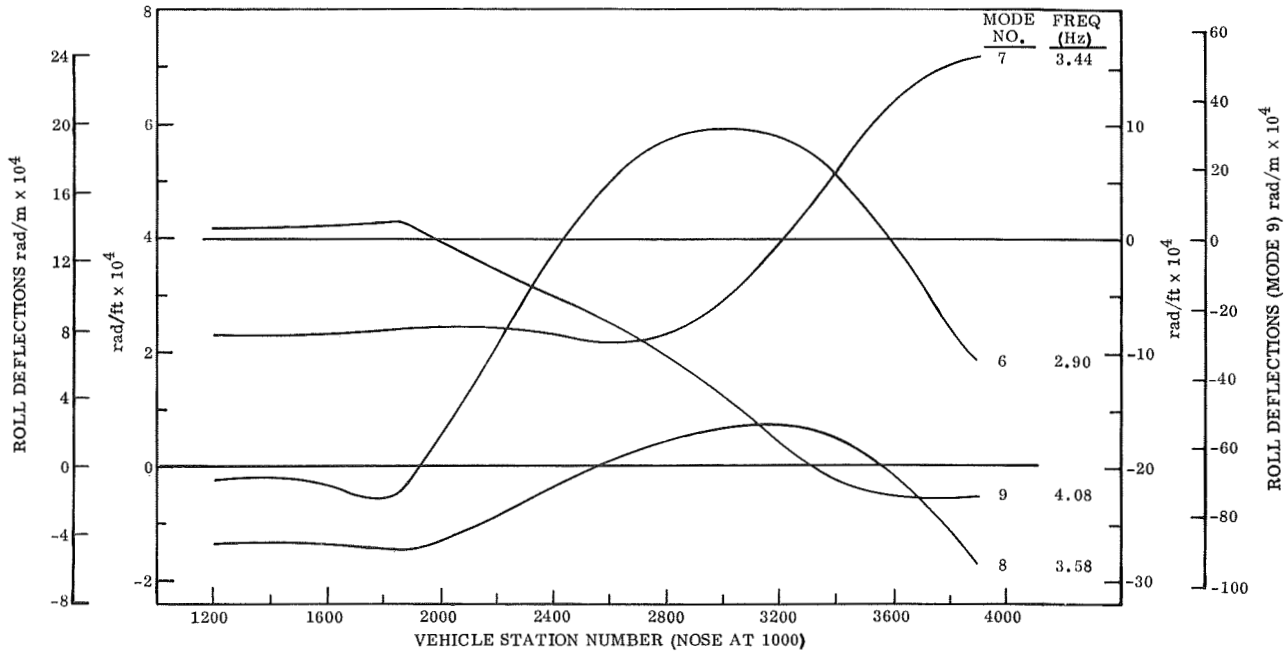

(c) Roll Component of Equivalent Booster Centerline Elastic Mode Shapes

Figure C5. – Concluded

APPENDIX D

SOLID MOTOR VEHICLE DATA

This appendix contains a tabulation of the solid motor vehicle data that was used in this study. It also contains illustrations of the propellant sloshing tank geometries, the specific elastic vehicle models, and the elastic mode shapes.

Essentially all of these data were generated during the Space Shuttle Phase B and follow-on studies. Therefore the data were developed using the customary (English) system of units.

The definition of symbols is contained in Appendix A.

The propellant sloshing parameters were generated by a version of the digital computer program described in Reference 2.

The symmetric configuration uses a flexible beam model constrained to pitch-plane motion. The antisymmetric configuration also uses a flexible beam model, but this model has all of the antisymmetric degrees of freedom. The antisymmetric mode shapes were generated by the NASTRAN computer program.

TABLE D1. – VEHICLE MASS PROPERTIES

Parameter	Value (Liftoff + 10 seconds)	
T (3 orbiter engines)	4.893×10^6 N	(1.1×10^6 lb)
T_S	2.5×10^7 N	(5.62×10^6 lb)
M_E (3 orbiter engines)	10 200 kg	(699 slugs)
M_R	2.10×10^6 kg	(1.44×10^5 slugs)
M_T	2.13×10^6 kg	(1.46×10^5 slugs)
I_R (3 orbiter engines)	25 260 kg-m^2	(18 630 slug-ft^2)
I_{xx}	6.73×10^7 kg-m^2	(4.96×10^7 slug-ft^2)
I_{yy}	3.63×10^8 kg-m^2	(2.68×10^8 slug-ft^2)
I_{zz}	4.12×10^8 kg-m^2	(3.04×10^8 slug-ft^2)
I_{xz}	1.40×10^7 kg-m^2	(1.03×10^7 slug-ft^2)
ℓ_c	-23.0 m	(-75.6 ft)
ℓ_{cS}	-23.0 m	(-75.6 ft)
ℓ_{Ey}	6.34 m	(20.8 ft)
ℓ_{Ez}	-7.25 m	(-23.8 ft)
ℓ_R	0.94 m	(3.08 ft)
ℓ_{RE}	1.39 m	(4.56 ft)
z_{cg}	-0.49 m	(-1.6 ft)
δ_{op}	0.09 rad	($\approx$ 5 deg)
δ_{oy}	0.18 rad	($\approx$ 10 deg)
T_{RAT}	2/3	

TABLE D2. — STEADY-STATE TRAJECTORY DATA

Parameter	Value (Liftoff + 10 seconds)	
g	9.81 m/sec^2	(32.17 ft/sec^2)
Q_o	-0.0089 rad/sec	(-0.51 deg/sec)
U_o	44.81 m/sec	(147 ft/sec)
$\dot{U}_o$	14.021 m/sec^2	(46 ft/sec^2)
V_T	44.81 m/sec	(147 ft/sec)
W_o	3.92 m/sec	(12.85 ft/sec)
θ_o	1.57 rad	(90 deg)
Mach Number	0.13	
Altitude	272.8 m	(895 ft)
Dynamic Pressure	1245 N/m^2	(26 lb/ft^2)

TABLE D3. – TOTAL VEHICLE AERODYNAMIC DATA

Parameter	Value (Liftoff + 10 seconds)	
X_u	-0.000702 1/sec	
X_w	-0.0010 1/sec	
Z_u	-0.0024 1/sec	
Z_w	0.12 1/sec	
M_u	0.000128 1/m-sec	(0.000039 1/ft-sec)
M_w	0.0021 1/m-sec	(0.00064 1/ft-sec)
Y_β	-47.55 m/sec^2	(-156 ft/sec^2)
L_β	-0.0673 1/sec^2	
N_β	-0.028 1/sec^2	

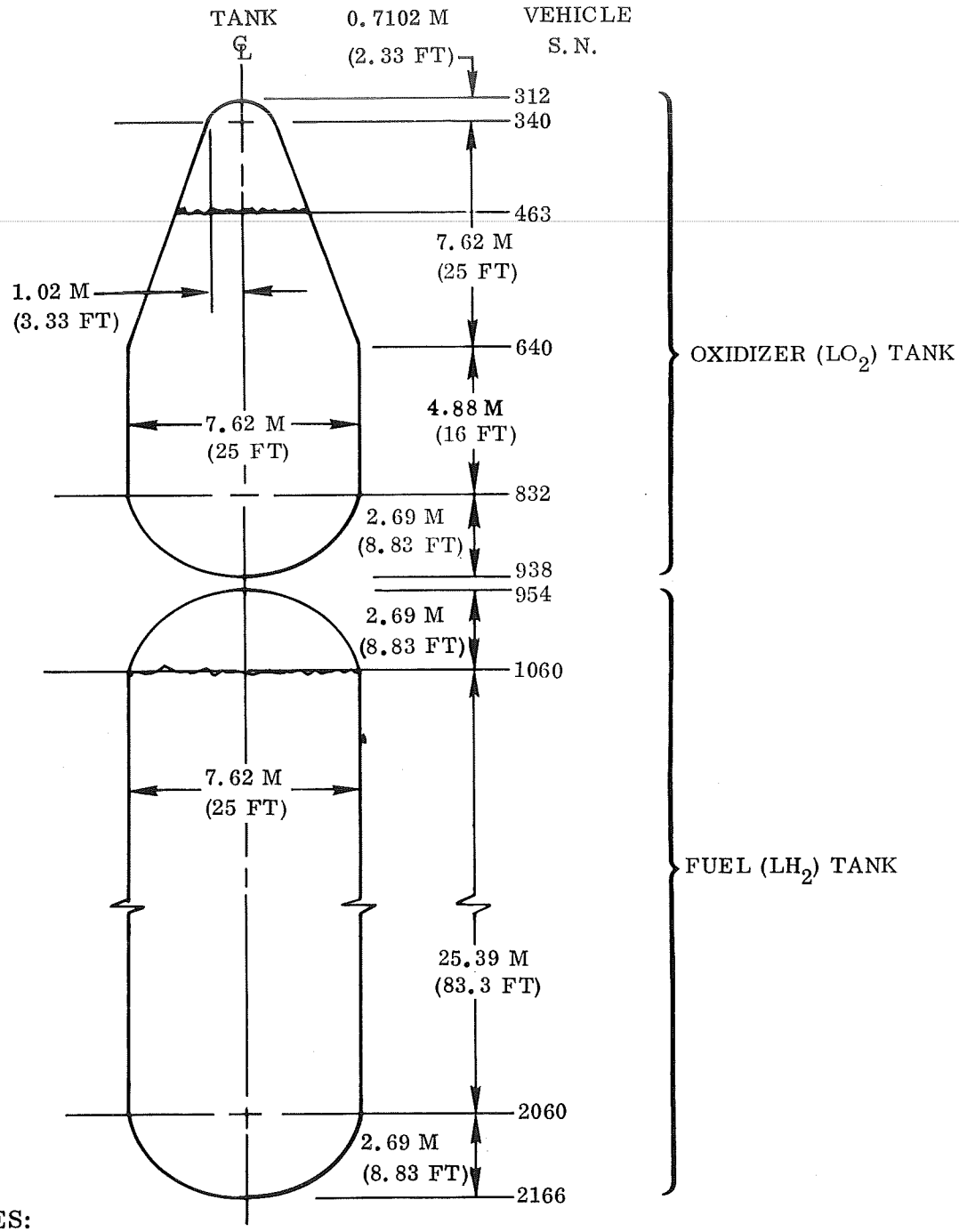

NOTES:

1. ALL BULKHEADS ARE ELLIPTICAL SURFACES, MAJOR RADIUS = $\sqrt{2}$ x MINOR RADIUS
2. QUIESCENT FLUID LEVEL USED IN STUDY (~~~~)

Figure D1. Main Propellant Tank Geometry

TABLE D4. – PROPELLANT SLOSHING DATA

Propellant Tank	Parameter	Value	
Oxidizer (LO_2)	M_P	18 607 kg	(1275 slugs)
	L_P	1.01 m	(3.3 ft)
	ℓ_P	16.6 m	(54.5 ft)
	ω_P	3.75 rad/sec	(0.6 Hz)
	ρ	1135.7 kg/m^3	(70.9 lb/ft^3)
Fuel (LH_2)	M_P	5560 kg	(381 slugs)
	L_P	2.06 m	(6.75 ft)
	ℓ_P	1.93 m	(6.33 ft)
	ω_P	2.47 rad/sec	(0.39 Hz)
	ρ	70.16 kg/m^3	(4.38 lb/ft^3)

TABLE D5. – AUTOPILOT AND ACTUATOR DATA

Parameter	Value
K_c	12.8 1/sec
K_o	55 1/sec
ω_c	70 rad/sec
ω_{cn}	57 rad/sec
ζ_{cn}	0.48
K_R	0.7 sec
K_A	variable

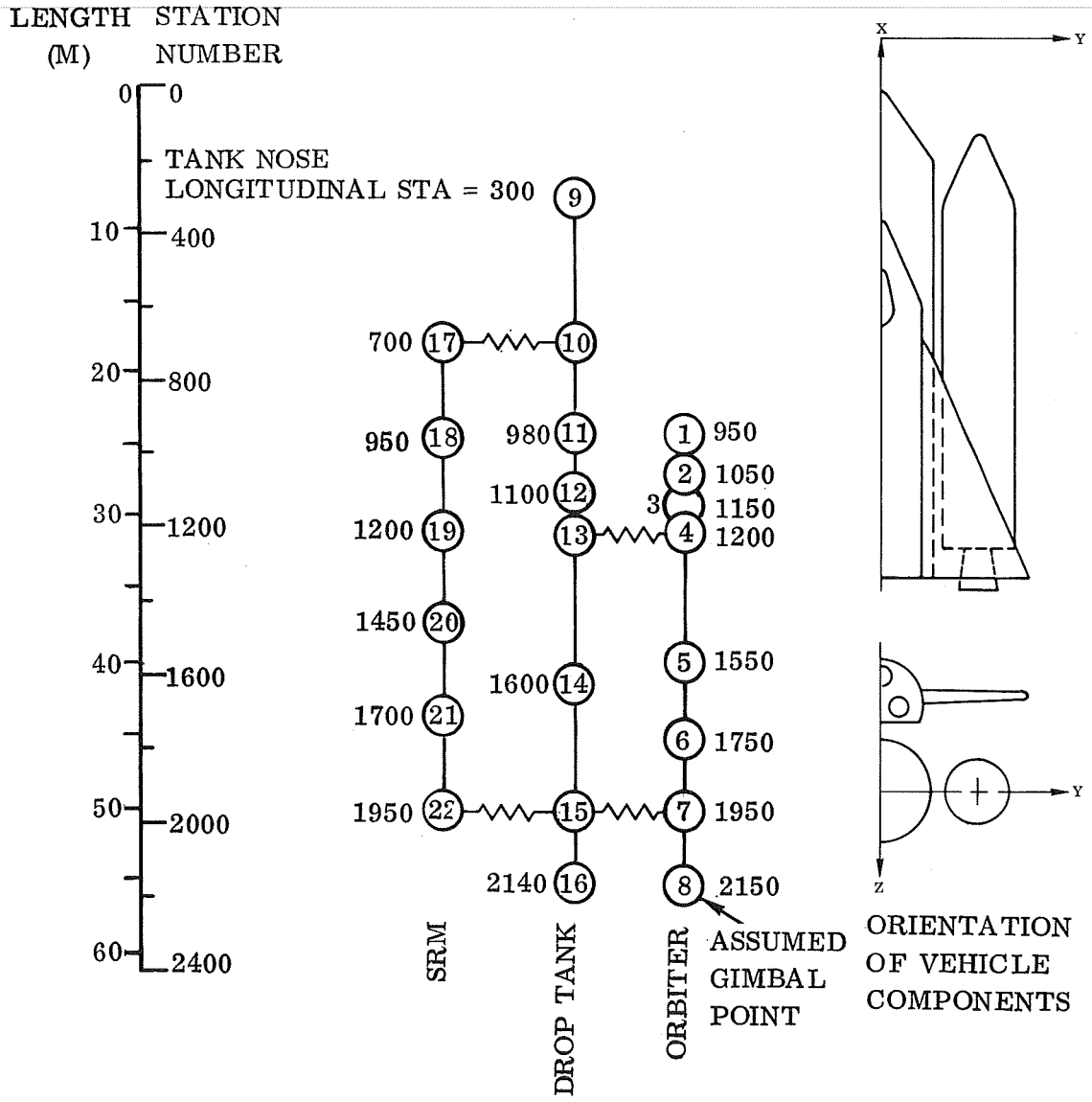

Figure D2. Elastic Model Schematic (Pitch Plane Boundary Conditions)

TABLE D6. – ELASTIC VEHICLE MODAL DATA (PITCH PLANE BOUNDARY CONDITIONS)

Mode Number	$\mathfrak{M}$ kg (slugs)	ω rad/sec (Hz)	Φ_{zT} $\frac{m}{m}$	Φ_{zP} $\frac{m}{m}$	σ_{zT} rad/m$\times 10^2$ (rad/ft $\times 10^2$)	Φ_{zTS} $\frac{m}{m}$	σ_{zTS} rad/m$\times 10^2$ (rad/ft$\times 10^2$)
1	226 940 (15 550)	13.05 (2.08)	-1.00	-0.110	3.320 (1.012)	-0.0836	4.315 (1.315)
2	57 208 (3 920)	17.6 (2.8)	-1.00	0.104	7.907 (2.41)	0.172	-1.624 (-0.495)
3	42 177 (2 890)	24.17 (3.85)	-0.634	-0.165	15.257 (4.65)	-0.0824	1.047 (0.319)
4	125 800 (8 620)	25.9 (4.12)	-0.308	0.00783	6.217 (1.895)	0.312	-5.807 (-1.77)
5	24 211 (1 659)	30.45 (4.85)	0.0926	0.491	0.2464 (0.0751)	0.0289	0.2411 (0.0735)
6	4 437 (304)	48.14 (7.66)	0.0405	-0.0788	-2.031 (-0.619)	-0.00276	-0.0682 (-0.0208)
7	809 970 (55 500)	57.5 (9.15)	0.185	-0.642	-5.036 (-1.535)	-0.621	28.184 (8.59)
8	23 350 (1 600)	66.0 (10.5)	0.138	-0.335	-4.065 (-1.239)	0.0549	-1.125 (-0.343)

TABLE D7. — PITCH CONTROL PLANE AUTOPILOT SENSOR ELASTIC MODAL DATA (PITCH PLANE BOUNDARY CONDITIONS)

σ_{PRS} or σ_{PA} — $\frac{rad}{m} \times 10^2$ $\left(\frac{rad}{ft} \times 10^2\right)$

Mode Number	Model Node 1 S. N. 950 on Orbiter	Model Node 4 S. N. 1200 on Orbiter	Model Node 7 S. N. 1950 on Orbiter	Model Node 10 S. N. 700 on Tank	Model Node 11 S. N. 980 on Tank	Model Node 12 S. N. 1100 on Tank	Model Node 15 S. N. 1950 on Tank	Model Node 17 S. N. 1700 on SRM	Model Node 22 S. N. 1950 on SRM
1	2.041 (0.622)	2.343 (0.714)	2.674 (0.815)	1.55 (0.473)	1.234 (0.376)	0.8777 (0.2675)	-0.1890 (-0.0576)	-3.553 (-1.083)	4.288 (1.317)
2	3.156 (0.962)	2.690 (0.820)	6.710 (2.045)	-0.063 (-0.0191)	0.0983 (0.02995)	0.2854 (0.0847)	0.804 (0.245)	0.3868 (0.1179)	-1.621 (-0.494)
3	-18.83 (-5.74)	-16.143 (-4.92)	13.813 (4.21)	-1.109 (-0.338)	-0.902 (-0.275)	-0.682 (-0.208)	0.1965 (0.0599)	-0.9203 (-0.2805)	1.047 (0.319)
4	-13.42 (-4.09)	-10.171 (-3.10)	5.437 (1.657)	1.33 (0.405)	0.7038 (0.2145)	0.0122 (0.00373)	-1.900 (-0.579)	6.109 (1.862)	-5.807 (-1.77)
5	-13.35 (-4.07)	-8.809 (-2.685)	0.574 (0.175)	3.39 (1.033)	2.720 (0.829)	1.998 (0.609)	-0.4885 (-0.1489)	-0.1965 (-0.0599)	0.2411 (0.0735)
6	-17.85 (-5.44)	-6.956 (-2.12)	-1.673 (-0.510)	-0.684 (-0.2085)	-0.468 (-0.1428)	-0.2218 (-0.0676)	0.0573 (0.01747)	-0.1240 (-0.0378)	-0.0682 (-0.0208)
7	-16.83 (-5.13)	-6.496 (-1.98)	-2.704 (-0.824)	-4.948 (-1.508)	-2.454 (-0.748)	0.1686 (0.0514)	5.922 (1.805)	29.070 (8.86)	28.217 (8.60)
8	-6.50 (-1.98)	-2.979 (-0.908)	-1.772 (-0.540)	-2.950 (-0.899)	-0.856 (-0.261)	1.312 (0.400)	4.922 (1.50)	-0.827 (-0.252)	-1.125 (-0.343)

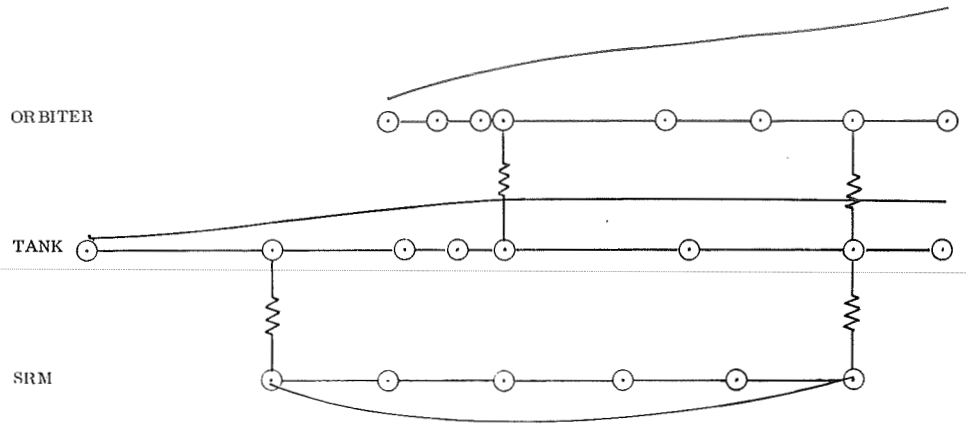

Mode 1, ω = 13.05 rad/sec (2.08 Hz)

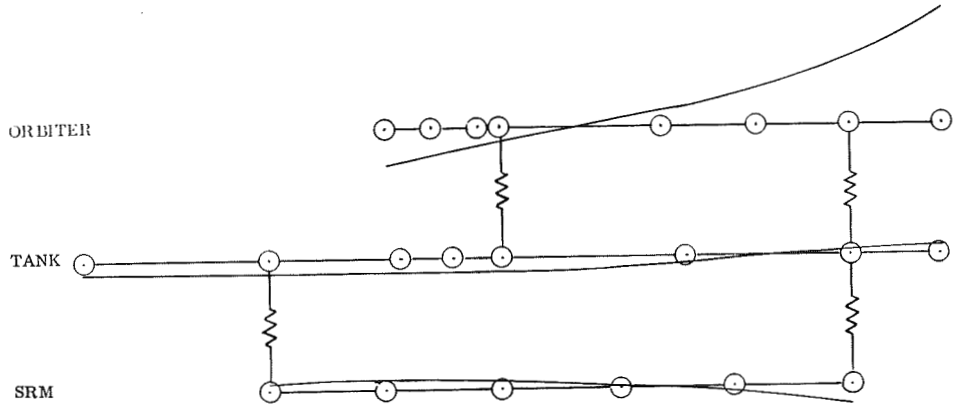

Mode 2, ω = 17.6 rad/sec (2.8 Hz)

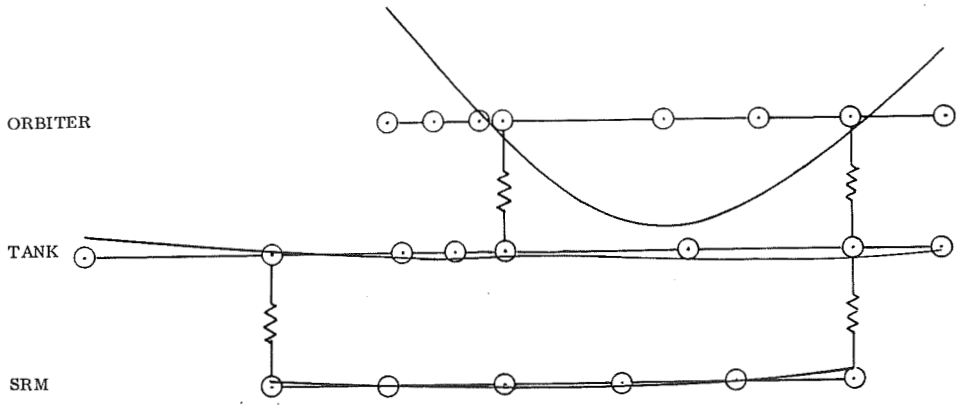

Mode 3, ω = 24.17 rad/sec (3.85 Hz)

Figure D3. —Elastic Mode Shapes (Pitch Plane Boundary Conditions)

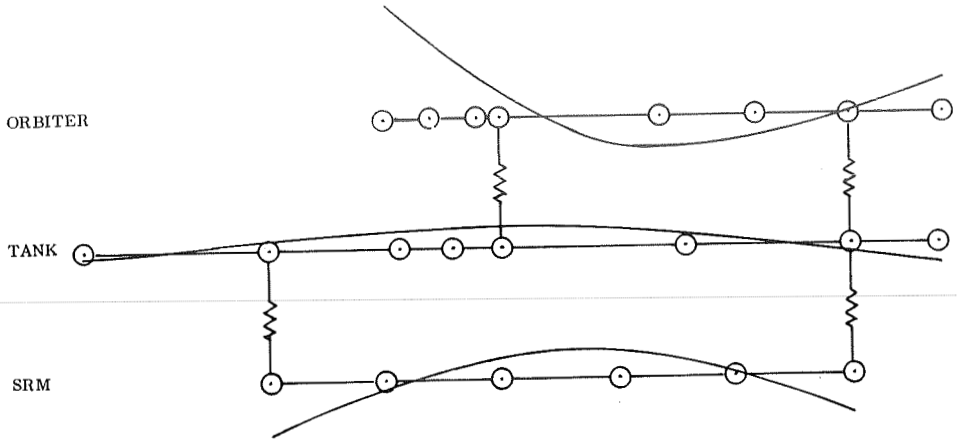

Mode 4, ω = 25.9 rad/sec (4.12 Hz)

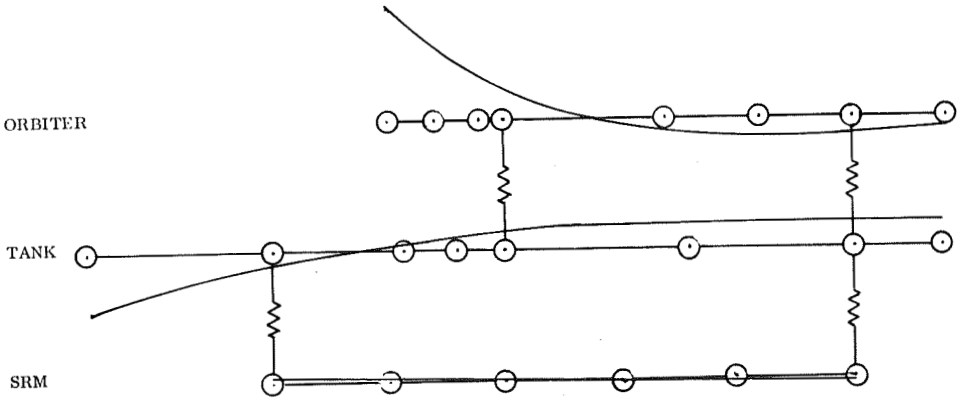

Mode 5, ω = 30.45 rad/sec (4.85 Hz)

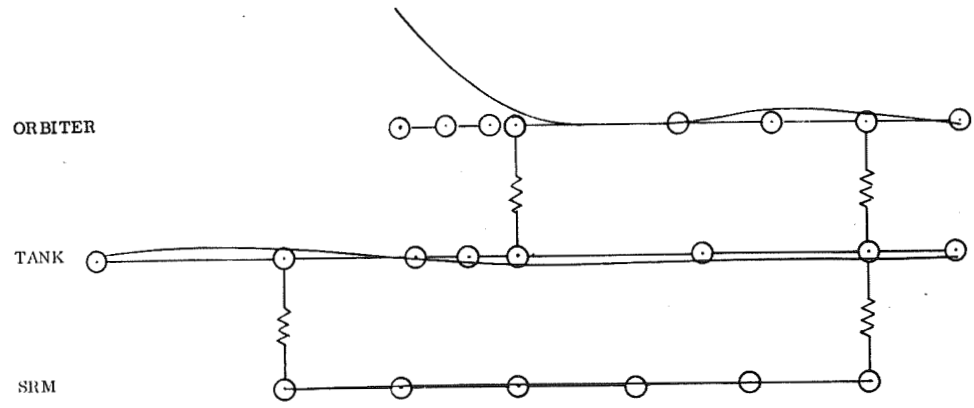

Mode 6, ω = 48.14 rad/sec (7.66 Hz)

Figure D3. – Continued

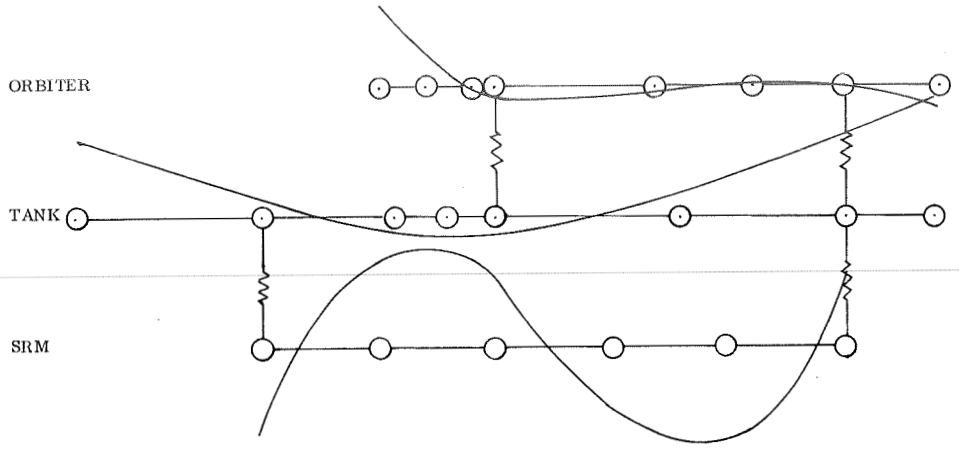

Mode 7, ω = 57.5 rad/sec (9.15 Hz)

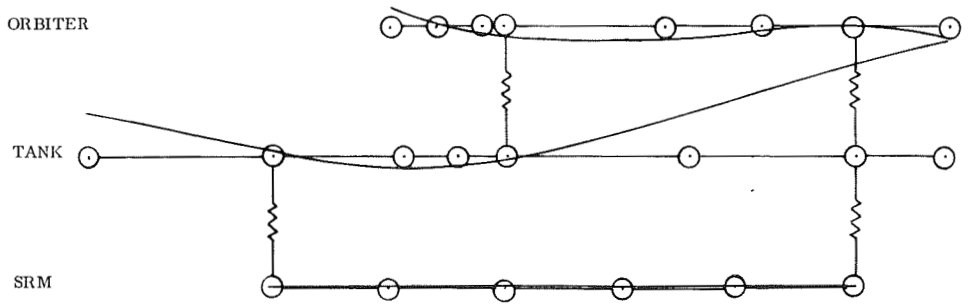

Mode 8, ω = 66.0 rad/sec (10.5 Hz)

Figure D3. — Concluded

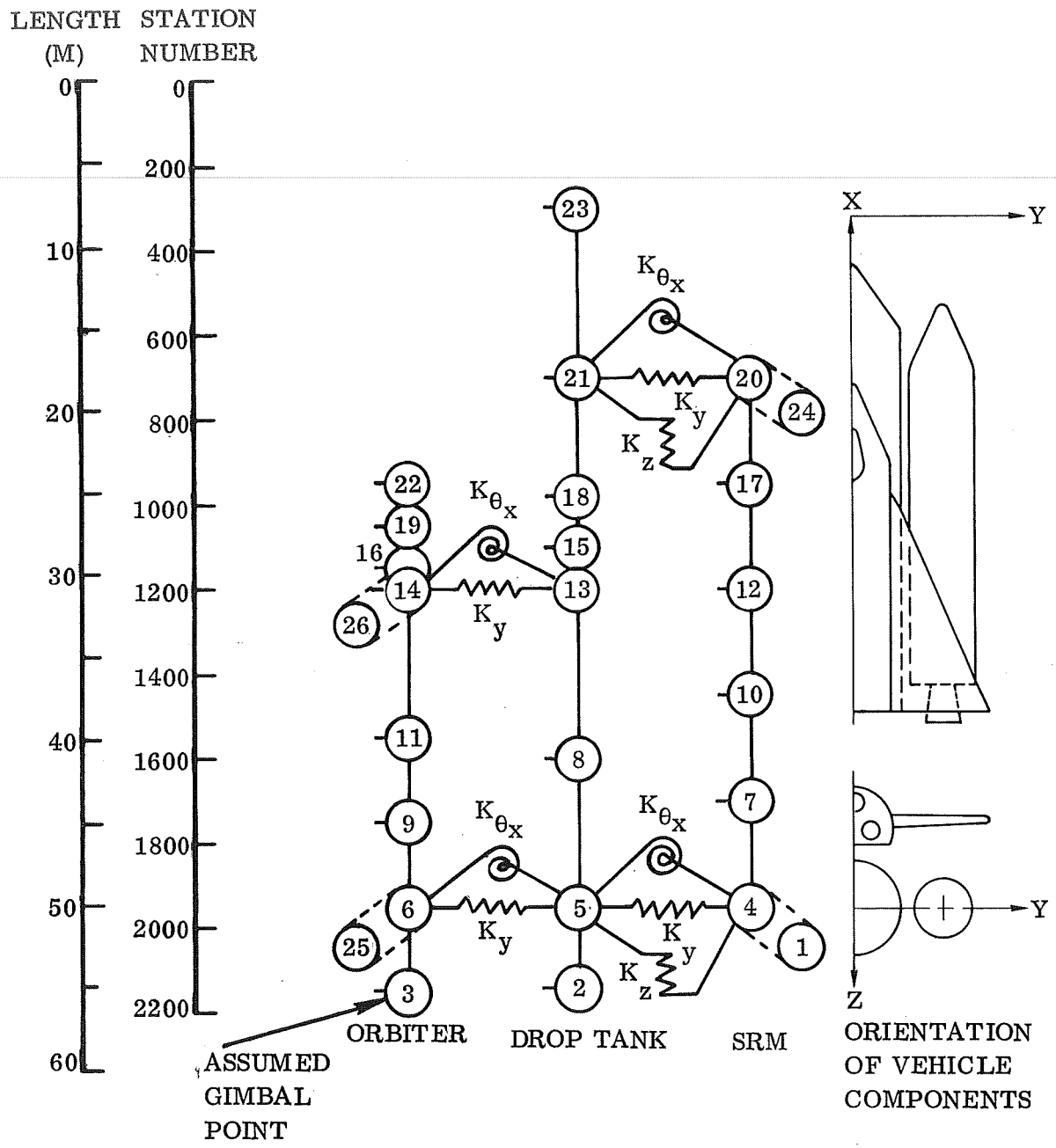

Figure D4.– Elastic Model Schematic (Antisymmetric Boundary Conditions)

TABLE D8.— ELASTIC VEHICLE MODAL DATA (ANTISYMMETRIC BOUNDARY CONDITIONS)

Mode Number	$\mathcal{M}$ kg (slugs)	ω rad/sec (Hz)	Φ_{yT} $\frac{m}{m} \times 10^2$	Φ_{yP} $\frac{m}{m} \times 10^2$	σ_{xT} rad/m $\times 10^3$ (rad/ft $\times 10^3$)	σ_{yT} rad/m $\times 10^3$ (rad/ft $\times 10^3$)	Φ_{yTS} $\frac{m}{m} \times 10^3$	Φ_{zTS} $\frac{m}{m} \times 10^2$	σ_{xTS} rad/m $\times 10^4$ (rad/ft $\times 10^4$)	σ_{yTS} rad/m $\times 10^4$ (rad/ft $\times 10^4$)	σ_{zTS} rad/m $\times 10^4$ (rad/ft $\times 10^4$)
1	350.3 (24)	13.73 (2.19)	-5.75	-0.275	-2.55 (-0.776)	2.18 (0.666)	1.28	-1.08	-12.57 (-3.83)	8.92 (2.72)	13.32 (4.06)
2	350.3 (24)	16.25 (2.59)	0.00824	-0.531	-2.85 (-0.870)	0.807 (0.246)	8.80	-1.39	-9.02 (-2.75)	-20.34 (-6.20)	4.99 (1.52)
3	350.3 (24)	17.92 (2.85)	-3.64	-0.840	-1.95 (-0.593)	2.303 (0.702)	10.6	0.367	-8.04 (-2.45)	-16.63 (-5.07)	12.47 (3.80)
4	350.3 (24)	19.12 (3.04)	-4.89	-1.11	11.45 (3.49)	4.59 (1.40)	3.09	0.980	16.08 (4.95)	-1.840 (-0.561)	-17.82 (-5.43)
5	350.3 (24)	21.17 (3.37)	2.59	0.926	12.07 (3.68)	-3.35 (-1.02)	1.83	-1.22	-16.54 (-5.04)	-4.23 (-1.29)	17.62 (5.37)
6	350.3 (24)	25.87 (4.12)	0.567	2.97	1.57 (0.480)	-3.94 (-1.20)	12.7	1.28	14.27 (4.35)	-16.57 (-5.05)	-17.03 (-5.19)
7	350.3 (24)	29.51 (4.70)	0.0396	-0.584	26.51 (8.08)	0.047 (0.0143)	-1.40	-0.286	-1.339 (-0.408)	1.857 (0.566)	2.66 (0.811)
8	350.3 (24)	32.49 (5.17)	-2.13	5.64	1.59 (0.484)	4.86 (1.48)	9.51	-0.500	-2.671 (-0.814)	-13.39 (-4.08)	5.97 (1.82)
9	350.3 (24)	40.68 (6.48)	-0.602	0.242	-3.84 (-1.17)	1.52 (0.462)	0.212	0.183	-1.657 (-0.505)	-0.525 (-0.160)	-1.89 (-0.575)
10	350.3 (24)	46.38 (7.38)	5.34	0.445	-0.459 (-0.140)	-13.42 (-4.09)	0.810	-0.284	10.86 (3.31)	-1.145 (-0.349)	3.26 (0.994)
11	350.3 (24)	47.69 (7.59)	1.08	0.0549	0.774 (0.236)	-2.46 (-0.750)	0.281	0.919	-56.17 (-17.12)	-1.831 (-0.558)	-11.55 (-3.52)
12	350.3 (24)	50.96 (8.11)	-0.235	-4.40	0.0886 (0.0270)	0.297 (0.0905)	9.09	0.000105	1.670 (0.509)	-42.32 (-12.9)	0.633 (0.193)

TABLE D9. – YAW CONTROL PLANE AUTOPILOT SENSOR ELASTIC MODAL DATA
(ANTISYMMETRIC BOUNDARY CONDITIONS)

	σ_{yRS} or σ_{yA} $\frac{rad}{m} \times 10^3 \left(\frac{rad}{ft} \times 10^4\right)$				
Mode Number	Model Node 22 S.N. 950 on Orbiter	Model Node 14 S.N. 1200 on Orbiter	Model Node 6 S.N. 1950 on Orbiter	Model Node 18 S.N. 980 on Tank	Model Node 5 S.N. 1950 on Tank
1	1.799 (5.483)	1.80 (5.50)	1.96 (5.96)	0.0101 (0.03078)	-0.2501 (-0.7622)
2	0.689 (2.10)	0.623 (1.90)	0.8058 (2.456)	-0.5647 (-1.721)	0.3311 (1.009)
3	1.73 (5.27)	1.66 (5.07)	2.05 (6.26)	-0.6454 (-1.967)	0.286 (0.873)
4	3.389 (10.33)	3.14 (9.58)	4.20 (12.8)	-0.5223 (-1.592)	0.3734 (1.138)
5	-2.31 (-7.04)	-2.053 (-6.256)	-3.093 (-9.426)	0.3438 (1.048)	-0.3826 (-1.166)
6	-2.12 (-6.45)	-1.55 (-4.71)	-3.858 (-11.76)	1.073 (3.27)	-1.445 (-4.404)
7	0.0156 (0.0475)	0.0028 (0.0084)	0.0541 (0.165)	-0.2249 (-0.6854)	0.2808 (0.8557)
8	0.709 (2.16)	0.175 (0.533)	4.387 (13.37)	2.1582 (6.578)	-2.699 (-8.227)
9	-1.03 (-3.13)	-0.988 (-3.01)	1.305 (3.977)	0.07967 (0.2428)	-0.1186 (-0.3615)
10	22.1 (67.5)	18.1 (55.3)	-10.96 (-33.41)	0.1272 (0.3878)	-0.179 (-0.545)
11	4.63 (14.1)	3.67 (11.2)	-1.937 (-5.905)	-0.0100 (-0.03048)	-0.101 (-0.3076)
12	-0.492 (-1.50)	-0.3376 (-1.029)	0.167 (0.510)	-1.7248 (-5.257)	0.0827 (0.2521)

TABLE D10. – ROLL CONTROL PLANE AUTOPILOT SENSOR ELASTIC MODAL DATA (ANTISYMMETRIC BOUNDARY CONDITIONS)

	σ_{RRS} or σ_{RA} $\frac{rad}{m} \times 10^3$ $\left(\frac{rad}{ft} \times 10^3\right)$			
Mode Number	Model Node 22 S. N. 950 on Orbiter	Model Node 6 S. N. 1950 on Orbiter	Model Node 13 S. N. 1200 on Tank	Model Node 5 S. N. 1950 on Tank
1	-1.32 (-0.403)	-2.374 (-0.7237)	-0.8124 (-0.2476)	-1.585 (-0.4831)
2	-0.8127 (-0.2477)	-2.58 (-0.787)	-0.1374 (-0.04188)	-1.339 (-0.4081)
3	-1.961 (-0.5978)	-1.718 (-0.5237)	-1.066 (-0.3248)	-0.4193 (-0.1278)
4	7.162 (2.183)	9.918 (3.023)	2.084 (0.6351)	1.564 (0.4766)
5	4.708 (1.435)	10.12 (3.084)	-1.848 (-0.5632)	-1.576 (-0.4803)
6	-1.87 (-0.57)	1.193 (0.3636)	-0.2206 (-0.06723)	1.195 (0.3641)
7	-12.72 (-3.878)	18.17 (5.538)	-0.3685 (-0.1123)	-0.0932 (-0.02841)
8	2.764 (0.8423)	0.9791 (0.2984)	1.484 (0.4523)	-0.141 (-0.0431)
9	-67.19 (-20.48)	-1.532 (-0.4669)	-1.025 (-0.3124)	-0.1414 (-0.04311)
10	-5.804 (-1.769)	-0.1016 (-0.03097)	1.473 (0.4491)	0.3901 (0.1189)
11	2.192 (0.668)	0.1363 (0.04154)	-0.6601 (-0.2012)	-1.308 (-0.3986)
12	0.5988 (0.1825)	0.00524 (0.001597)	-0.2723 (-0.08298)	-0.0834 (-0.02543)

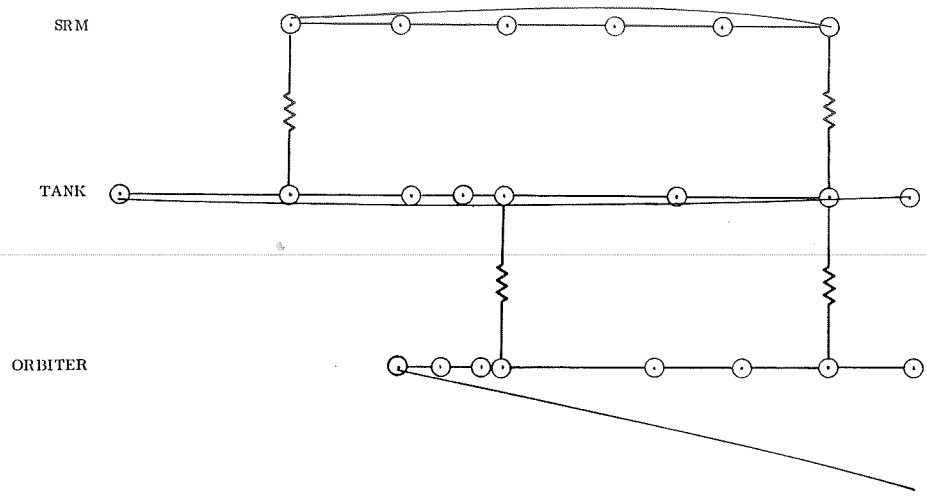

Mode 1, ω = 13.73 rad/sec (2.19 Hz)

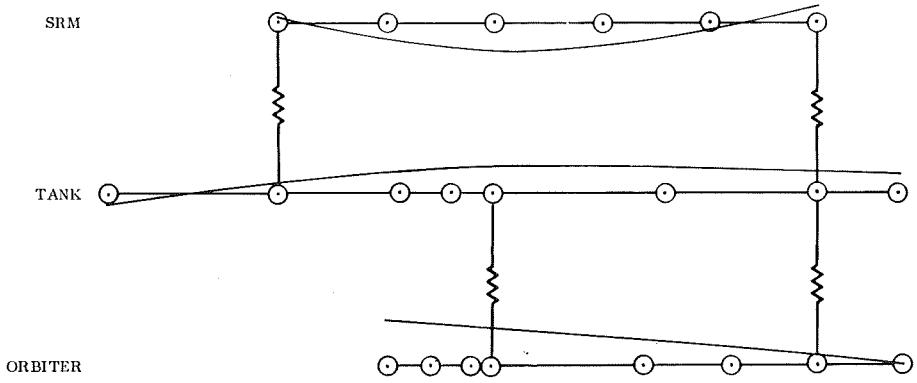

Mode 2, ω = 16.25 rad/sec (2.59 Hz)

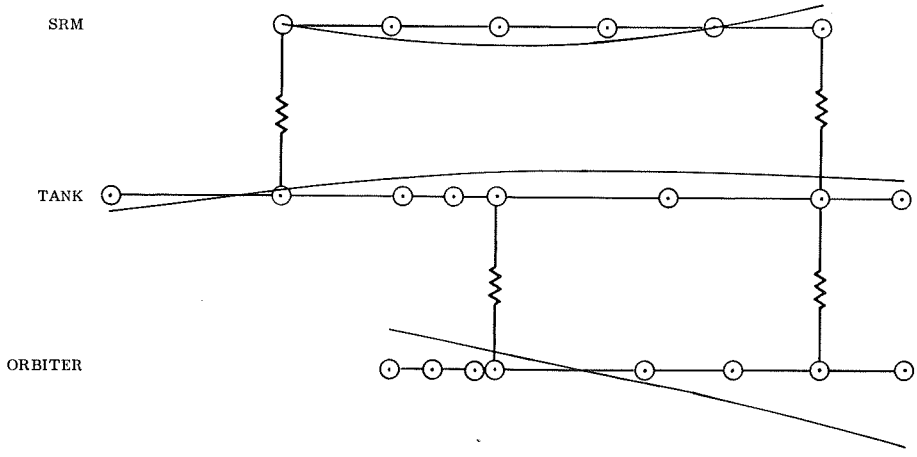

Mode 3, ω = 17.92 rad/sec (2.85 Hz)

Figure D5. – Lateral Component of Elastic Mode Shapes (Antisymmetric Boundary Conditions)

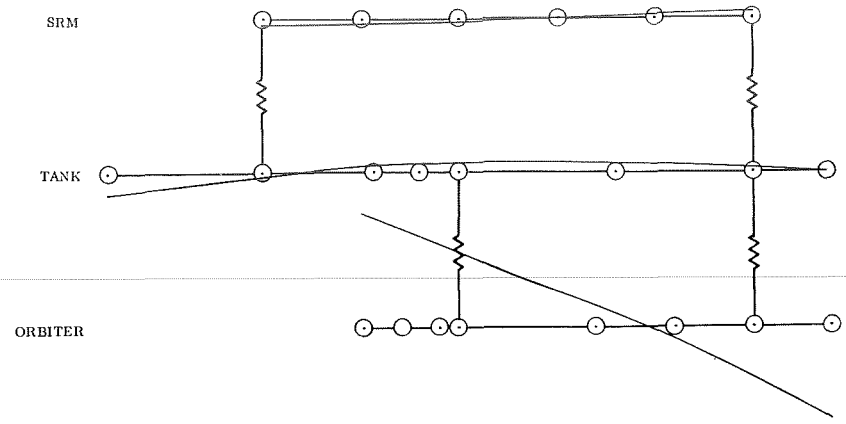

Mode 4, ω = 19.12 rad/sec (3.04 Hz)

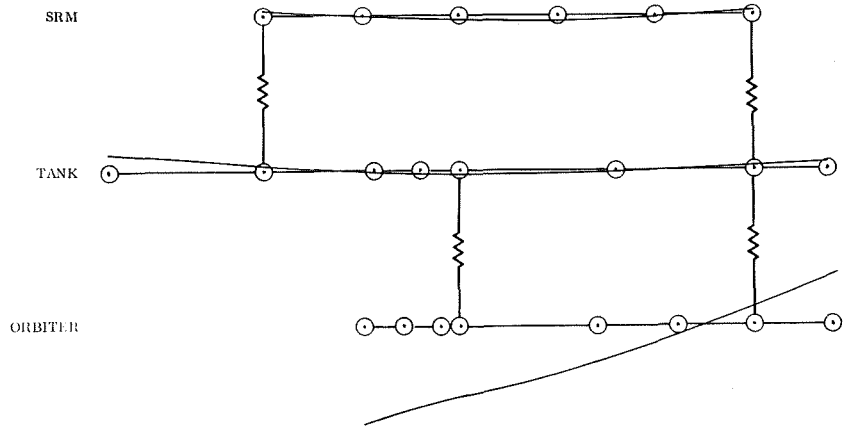

Mode 5, ω = 21.17 rad/sec (3.37 Hz)

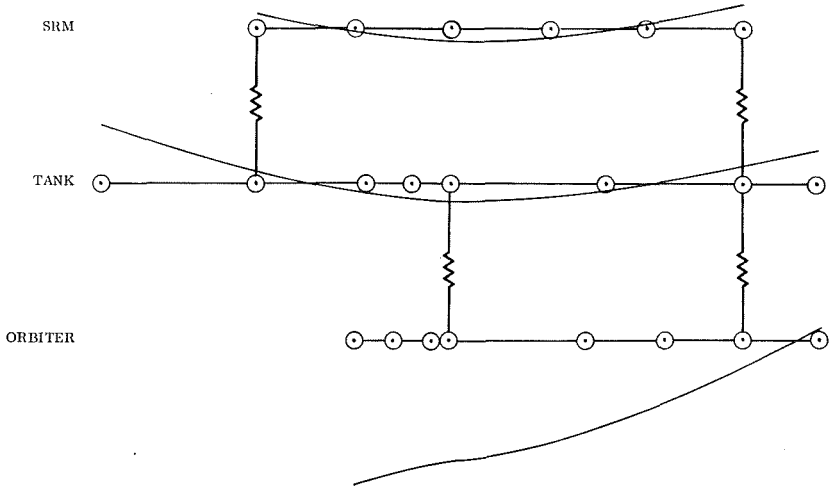

Mode 6, ω = 25.87 rad/sec (4.12 Hz)

Figure D5. – Continued

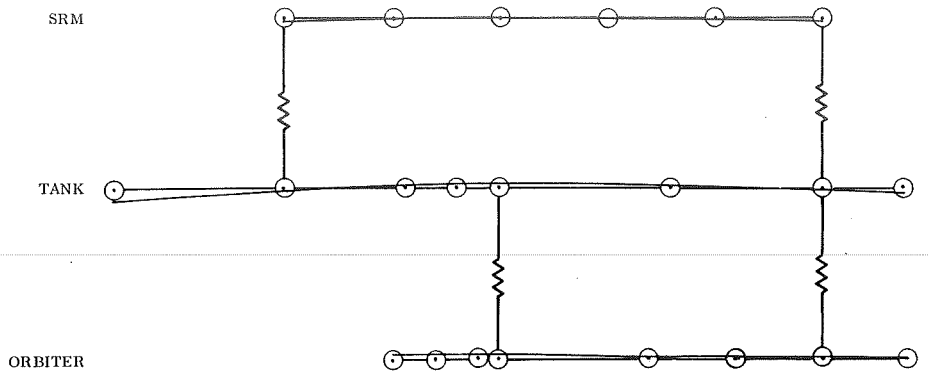

Mode 7, $\omega = 29.51$ rad/sec (4.70 Hz)

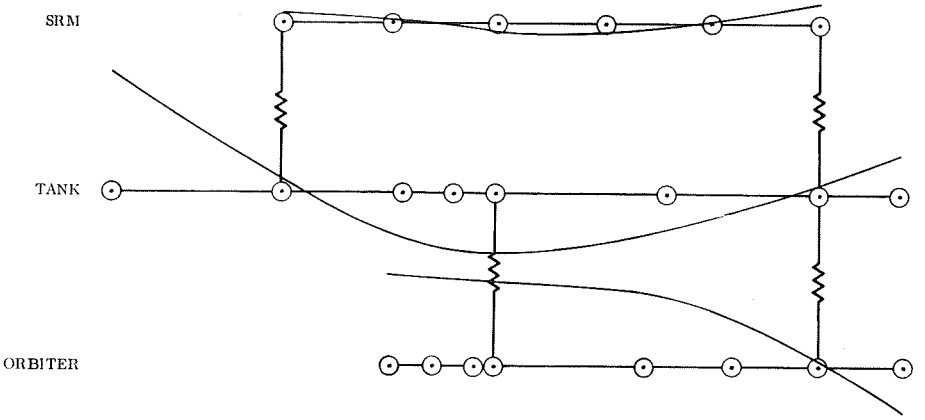

Mode 8, $\omega = 32.49$ rad/sec (5.17 Hz)

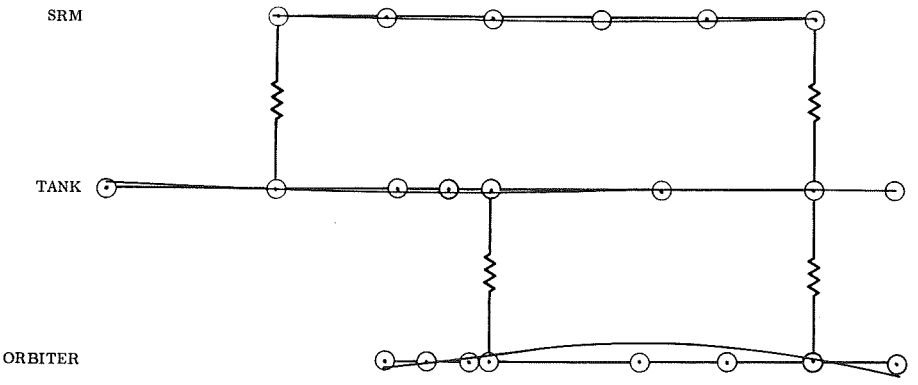

Mode 9, $\omega = 40.68$ rad/sec (6.47 Hz)

Figure D5. — Continued

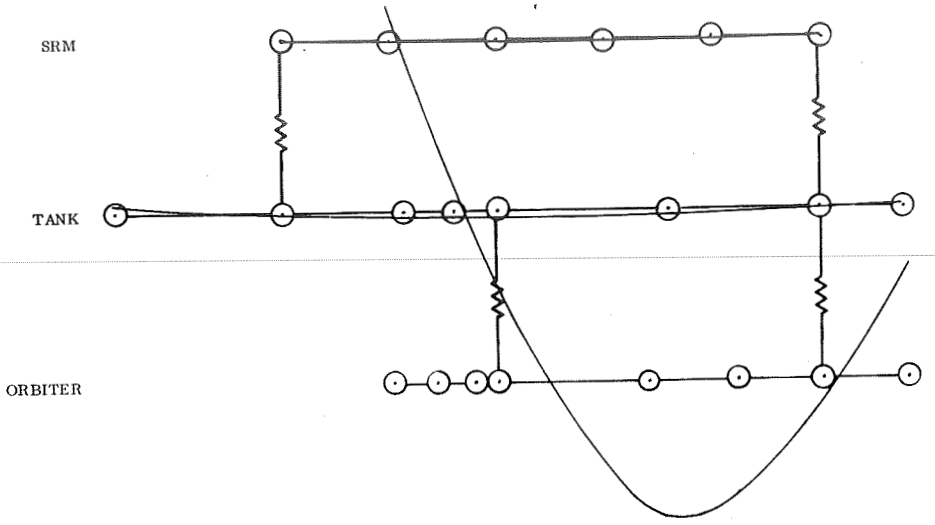

Mode 10, ω = 46.38 rad/sec (7.38 Hz)

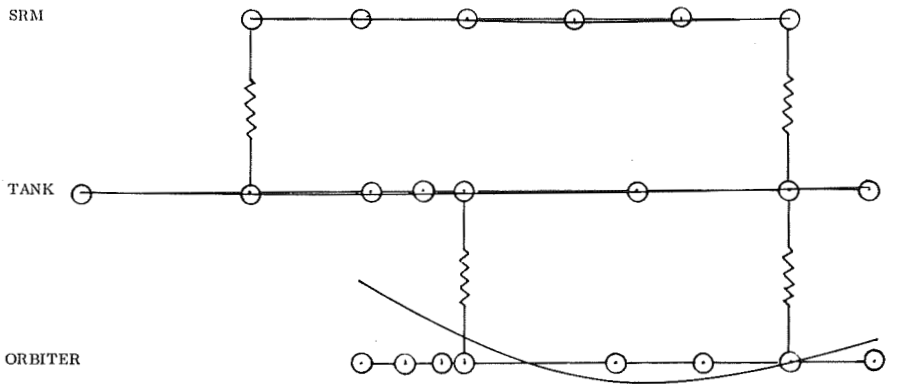

Mode 11, ω = 47.69 rad/sec (7.59 Hz)

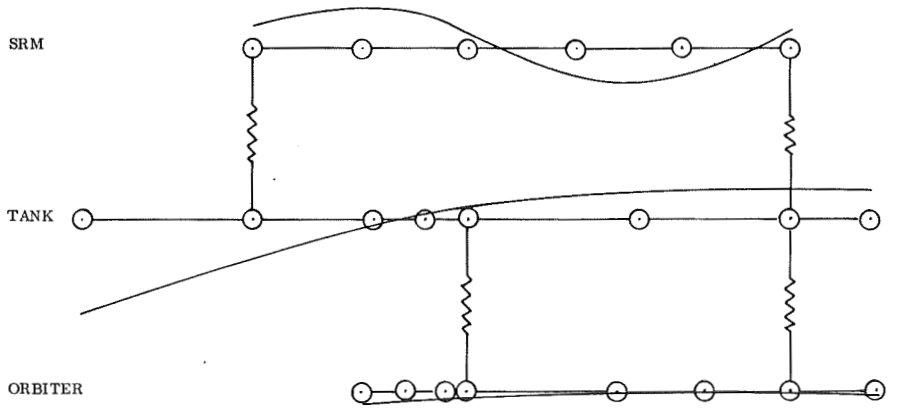

Mode 12, ω = 50.96 rad/sec (8.11 Hz)

Figure D5. — Concluded

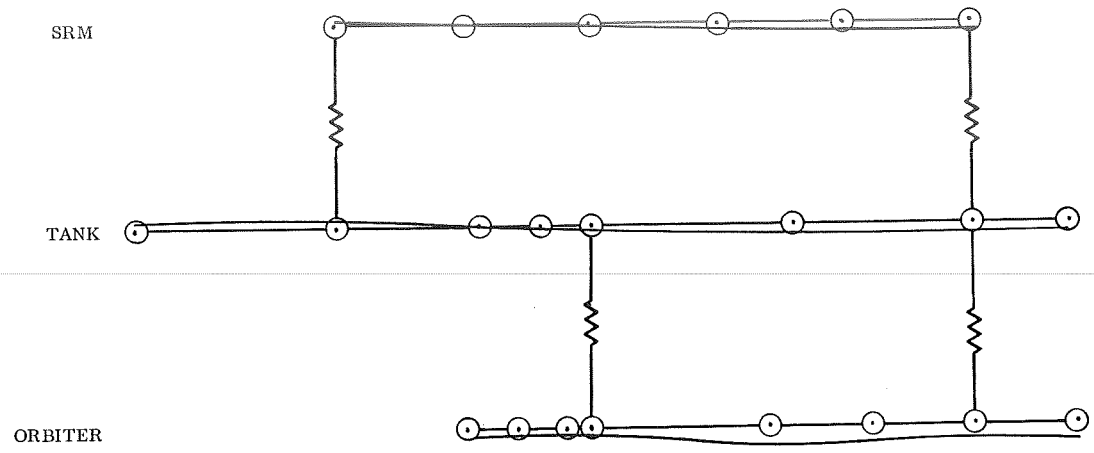

Mode 1, ω = 13.73 rad/sec (2.19 Hz)

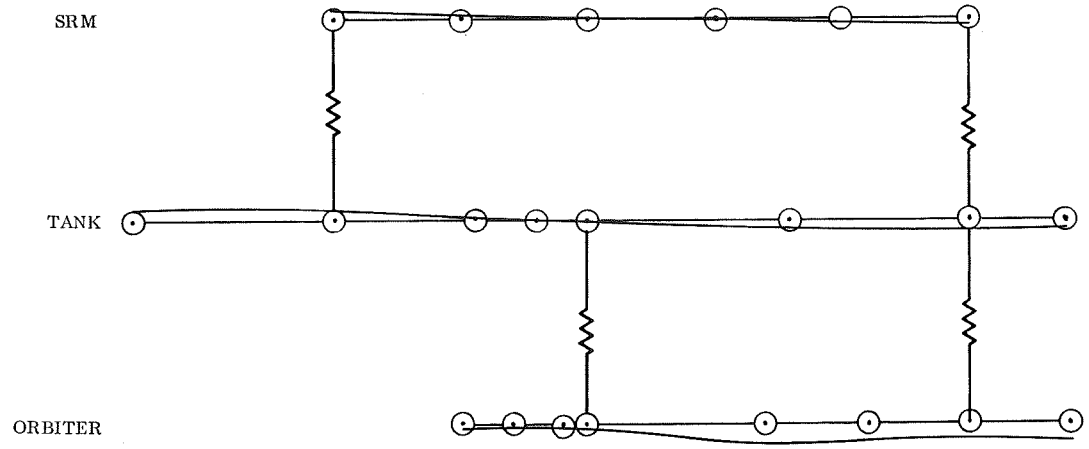

Mode 2, ω = 16.25 rad/sec (2.59 Hz)

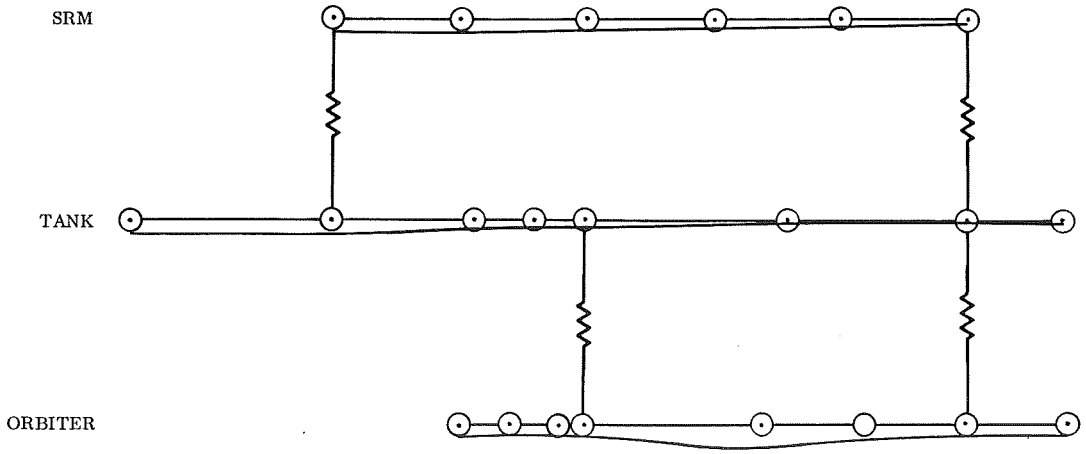

Mode 3, ω = 17.92 rad/sec (2.85 Hz)

Figure D6.– Roll Component of Elastic Mode Shapes (Antisymmetric Boundary Conditions)

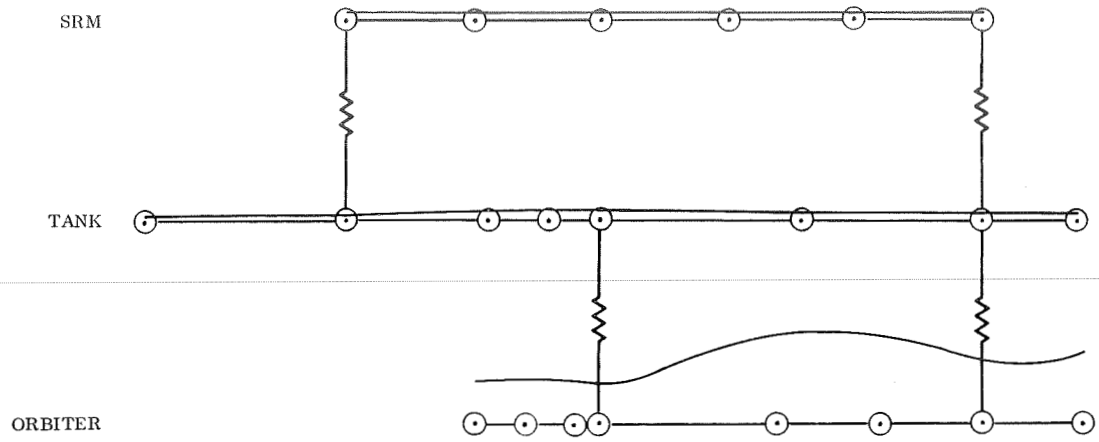

Mode 4, ω = 19.12 rad/sec (3.04 Hz)

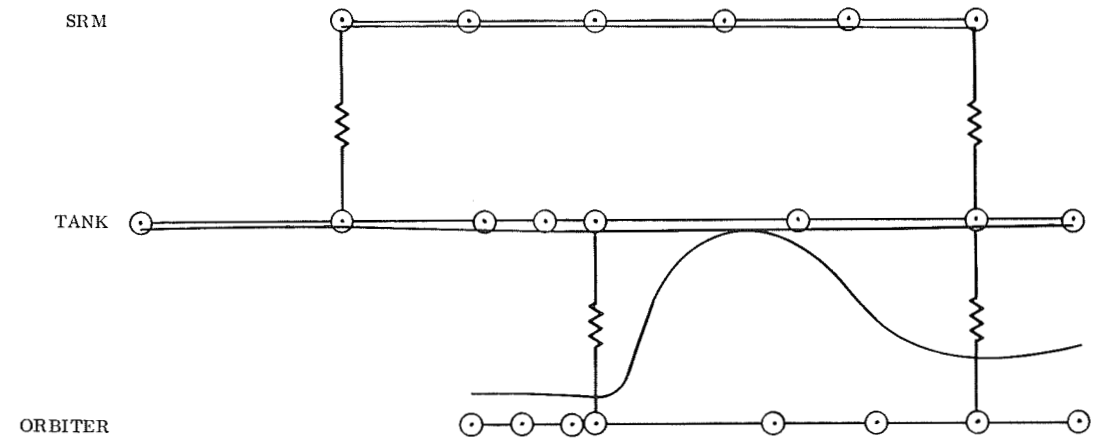

Mode 5, ω = 21.17 rad/sec (3.37 Hz)

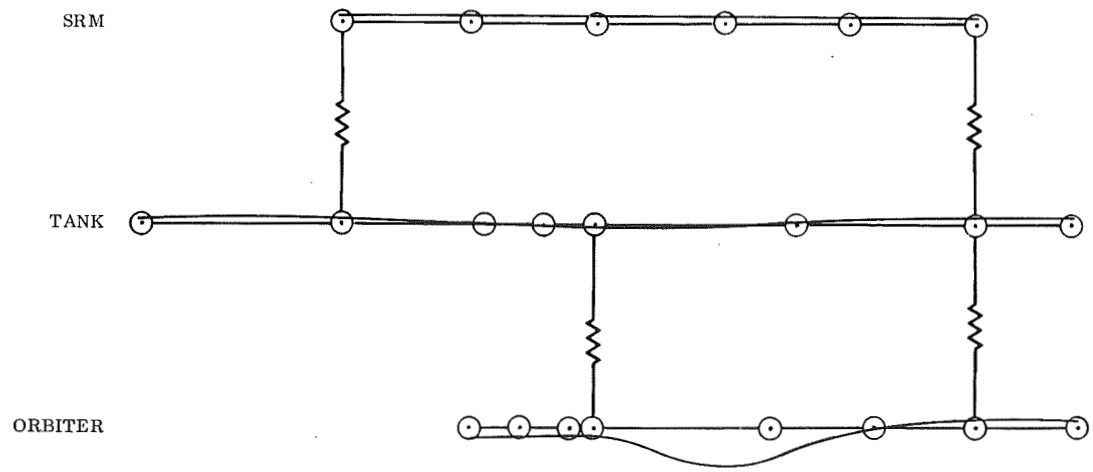

Mode 6, ω = 25.87 rad/sec (4.12 Hz)

Figure D6. — Continued

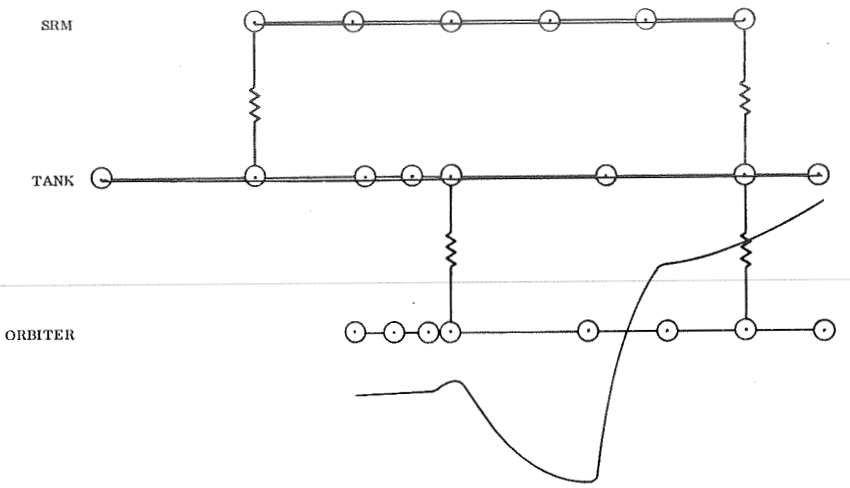

Mode 7, ω = 29.51 rad/sec (4.70 Hz)

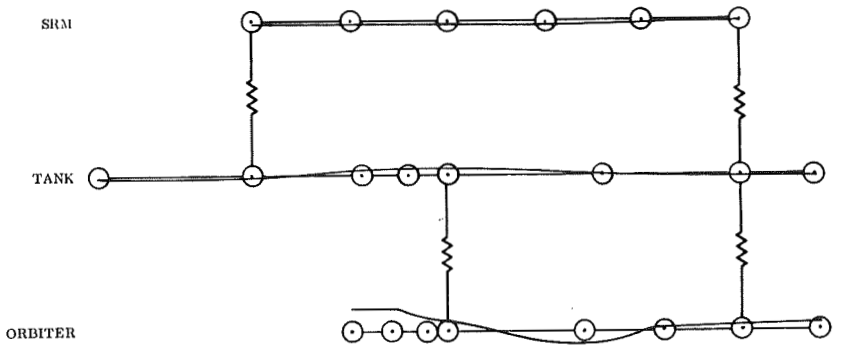

Mode 8, ω = 32.49 rad/sec (5.17 Hz)

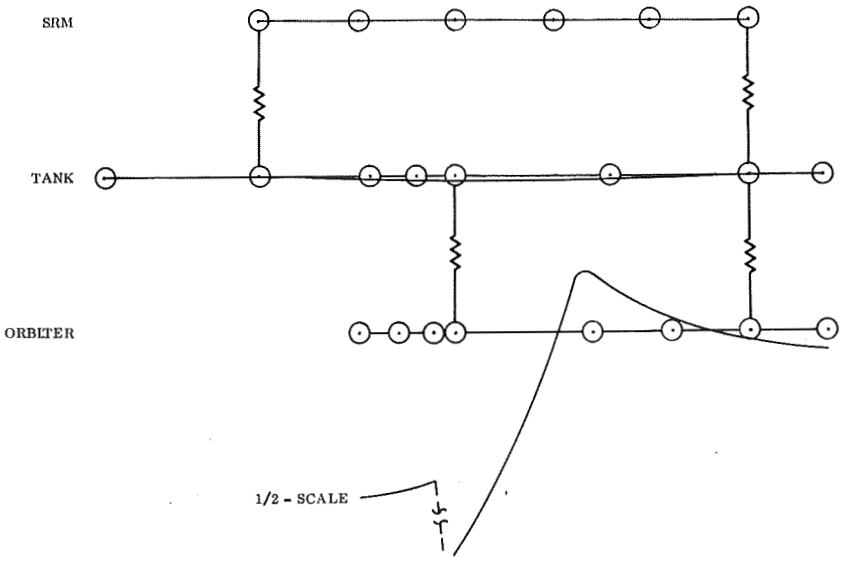

Mode 9, ω = 40.68 rad/sec (6.47 Hz)

Figure D6. — Continued

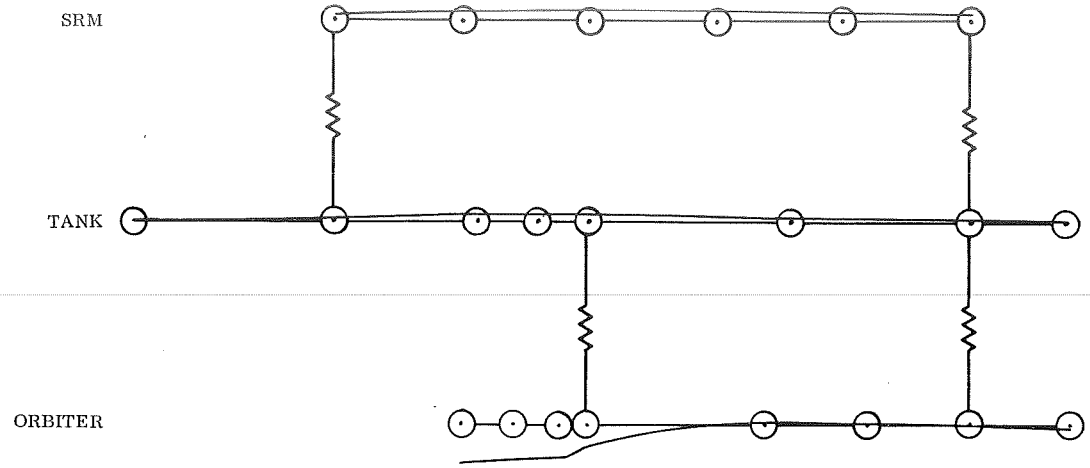

Mode 10, ω = 46.38 rad/sec (7.38 Hz)

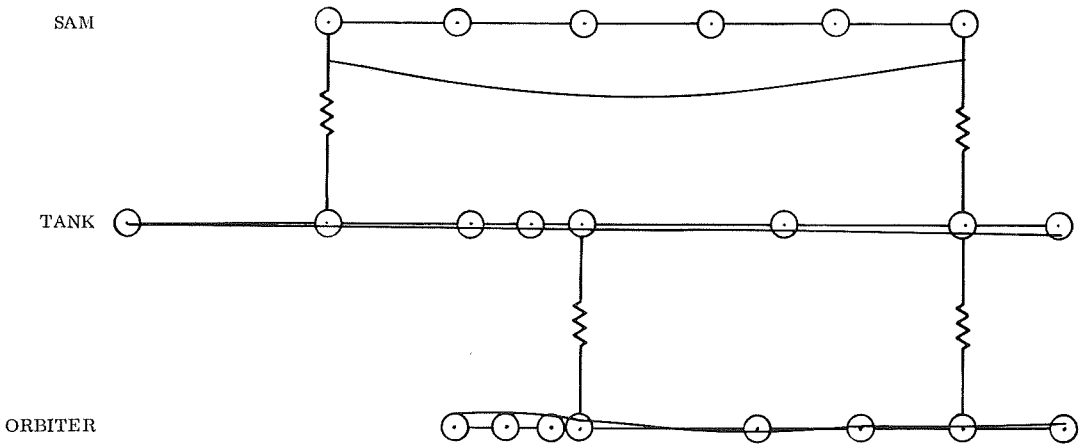

Mode 11, ω = 47.69 rad/sec (7.59 Hz)

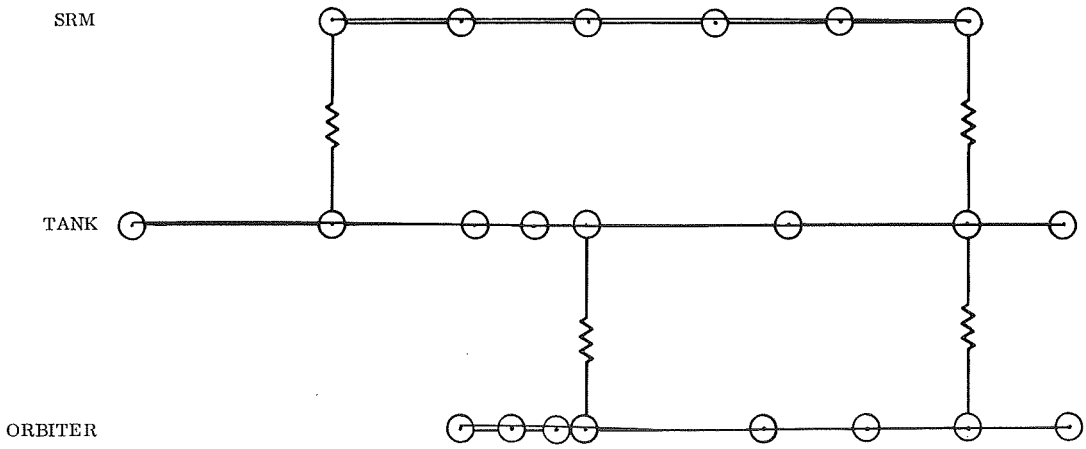

Mode 12, ω = 50.96 rad/sec (8.11 Hz)

Figure D6.— Concluded

APPENDIX E

THE ROOT LOCUS METHOD

One of the most powerful tools applicable to the analysis and synthesis of launch vehicle flight control systems is the root locus technique. Its chief virtue is the graphical display of the motion of system roots as functions of various system parameters. This enables the control engineer to evaluate the effects of these changes directly. The root locations can be translated immediately into an estimate of the system time response or, if desired, its frequency response. The following discussion is an exposition on the root locus method where the theoretical background is considerably abbreviated. It can be found in varying states of clarity and completeness in almost any textbook on linear control theory; for example, References 4 and 5.

Definitions

The roots of the characteristic equation are a set of complex numbers that depend upon the coefficients of the equation. These roots are continuous functions of the coefficients, hence of the system parameters. If the roots of the characteristic equation are plotted on the complex s-plane, they will trace out continuous curves as the several system parameters are varied. The path followed for a particular root is a root locus. For a given set of parameter values there is a single set of roots but through these roots a different set of loci will pass for each parameter variation. The question is then one of determining these loci.

Theory

The characteristic equation of a linear control system may be written in the form:

$$1 + GH(s) = 1 + K\frac{\prod_{i=1}^{m}(s - z_i)}{\prod_{j=1}^{n}(s - p_j)} = 0 \qquad \text{(E1)}$$

where the z_i and p_j are respectively the zeros and poles of the system, both real and complex, and K is the "high-frequency open-loop gain" — proportional to the low-frequency system gain. The function GH (s) is the open-loop transfer function for the system (see Figure E1). Suppose the complex number, s_0, is a root of Equation E1. Then, since gain K is a real number, the characteristic equation is equivalent to two relations:

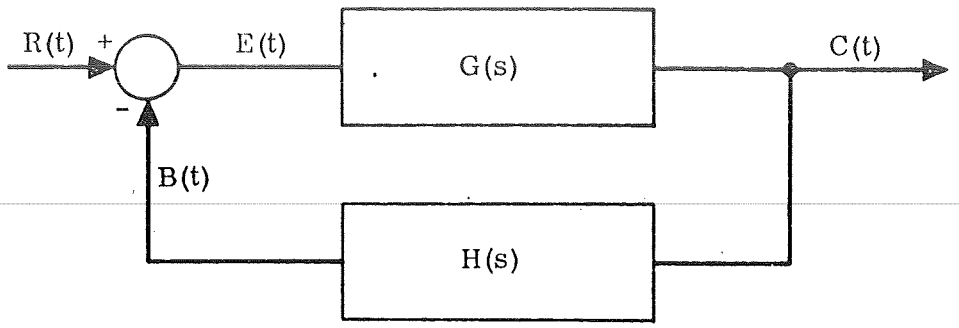

C (t)	Controlled Variable
R (t)	Reference (Command) Variable
E (t)	Error Variable
B (t)	Feedback Variable
G (s)	Forward Loop Transfer Function (Including Compensation)
H (s)	Feedback Loop Transfer Function (Including Compensation)

Figure E1. Generalized Block Diagram for Control Systems

$$K = \frac{\prod_{j=1}^{n} |s_0 - p_j|}{\prod_{i=1}^{m} |s_0 - z_i|} \qquad \text{(E2)}$$

$$\text{Arg}\left[\frac{\prod_{i=1}^{m} (s_0 - z_i)}{\prod_{j=1}^{n} (s_0 - p_j)}\right] = \sum_{i=1}^{m} \text{Arg}\,(s_0 - z_i) - \sum_{j=1}^{n} \text{Arg}\,(s_0 - p_j) = (2r + 1)\pi \qquad \text{(E3)}$$

where r is any integer. If a point can be found in the s-plane satisfying Equation E3, there will be only one value of K for which Equation E2 is satisfied. The root locus for s_0 under variation of the open-loop gain is the locus of points satisfying Equation E3 with K a parameter.

This procedure will define the motion of the system roots as a function of K. A few observations are in order. On the s-plane there may exist "saddle points," points where the derivative of the complex gain function given by

$$\frac{d}{ds}K(s) = -\frac{d}{ds}\left[\frac{\prod_{j=1}^{n}(s - p_j)}{\prod_{i=1}^{m}(s - z_i)}\right] \tag{E4}$$

goes to zero. If the locus passes through a region surrounding a saddle point it will be found that the distance along the locus for a given percentage change in gain increases dramatically; furthermore, in plotting the locus the points s_0 lying on the locus will be difficult to find. This situation usually occurs when two separate loci approach each other from opposite directions, when it will be difficult to determine if the locus is as shown (for example) in Figure E2a or E2b. From the engineering point of view, it makes little difference; the location of a root lying in the region of a saddle point will be sensitive to parameter variations, and the system should be designed accordingly, i.e., to be insensitive to the precise location of the root. This figure shows a typical situation encountered when analyzing the low-frequency parasitic modes (represented by the pole-zero dipole near the $j\omega$ axis). If the operating gain is either K_1 or K_2, the situation is clear. But an intermediate value of gain will result in two complex conjugate pairs of roots within the region of the saddle point that are difficult to locate with precision. This can best be appreciated by one familiar with the use of the Spirule: the locus is hard to "pin down." The difficulty is less severe if the brute-force methods of machine computation are used, but even here the number of iterations required to locate the roots will be somewhat larger than usual. It is not at all unusual to run across difficult cases where sophisticated computational techniques are required; the ordinary routines fail to converge.

For synthesis purposes, one is concerned with the effect of lead or lag compensation in the open-loop transfer function on the root location or, what amounts to the same thing, on the configuration of the loci. In essence the effect is as follows: in the upper half of the s-plane, loci emanating from complex poles will rotate clockwise about the pole as lag compensation is added. They also will tend to decrease in length

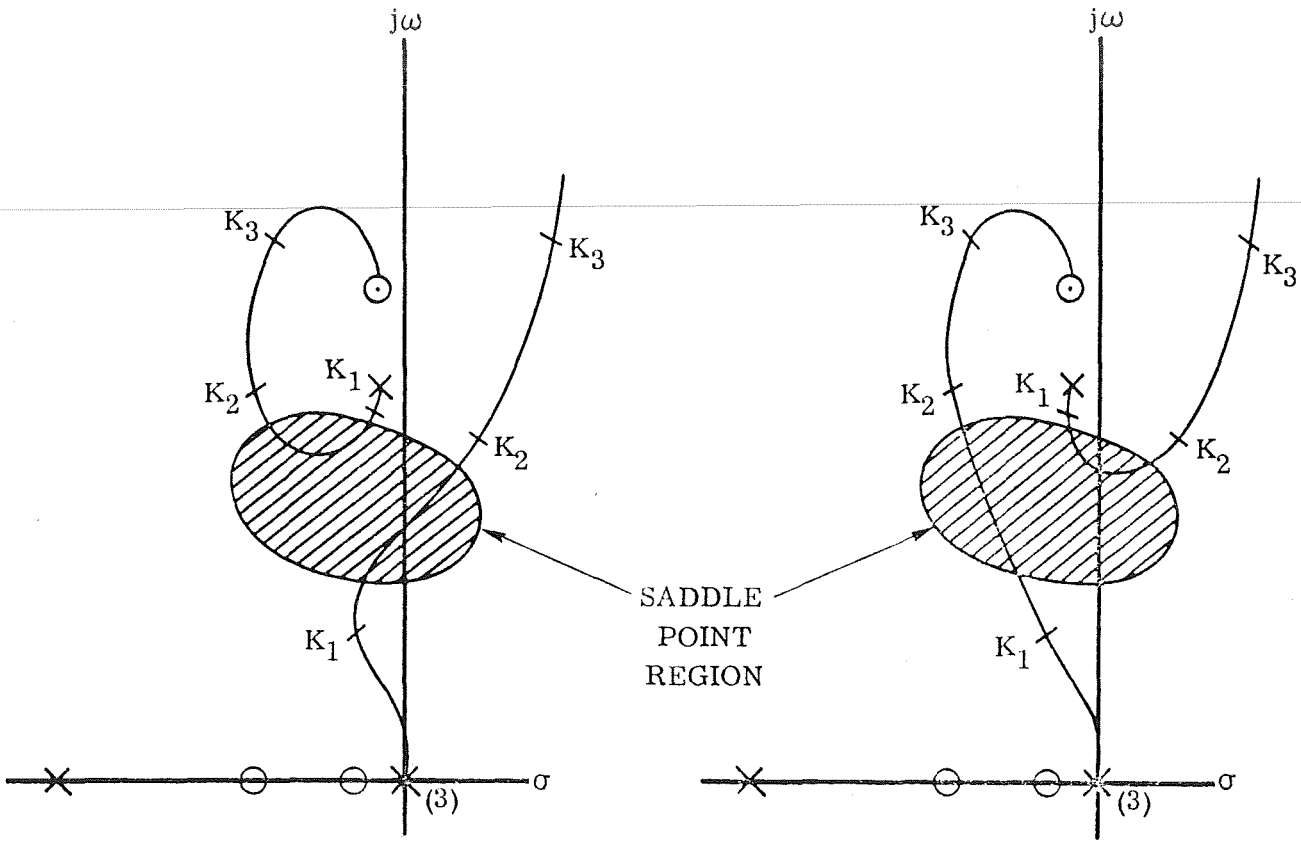

a. Variation 1

b. Variation 2

Figure E2. Variations in Root Loci Behavior in the Region of a Saddle Point

(the closed-loop roots move closer to the open-loop poles) by an amount proportional to the attenuation introduced by the lag. The amount of rotation is (approximately) equal to the phase lag introduced at the frequency corresponding to the system root of interest. In terms of Figure E2, the situation shown in (a) represents somewhat more lag than (b). It also shows the effects of lag on loci emanating from poles on the real axis: the loci will tend to move toward the right-half plane. For lead compensation, the situation is exactly reversed: the loci tend to increase in length and rotate counter-clockwise.

Phase and gain margins are conveniently measured for parasitic mode roots on root locus plots if the definitions in Figure E3 are used. One draws a vector between the pole and the nominal closed-loop root location, and inscribes a circular arc about the open-loop pole of radius equivalent to the distance of the closed-loop root from the pole. A vector is drawn from the pole to the intersection of the arc with the jω axis. The angle ϕ_m between the two vectors is the phase margin. The gain margin is the

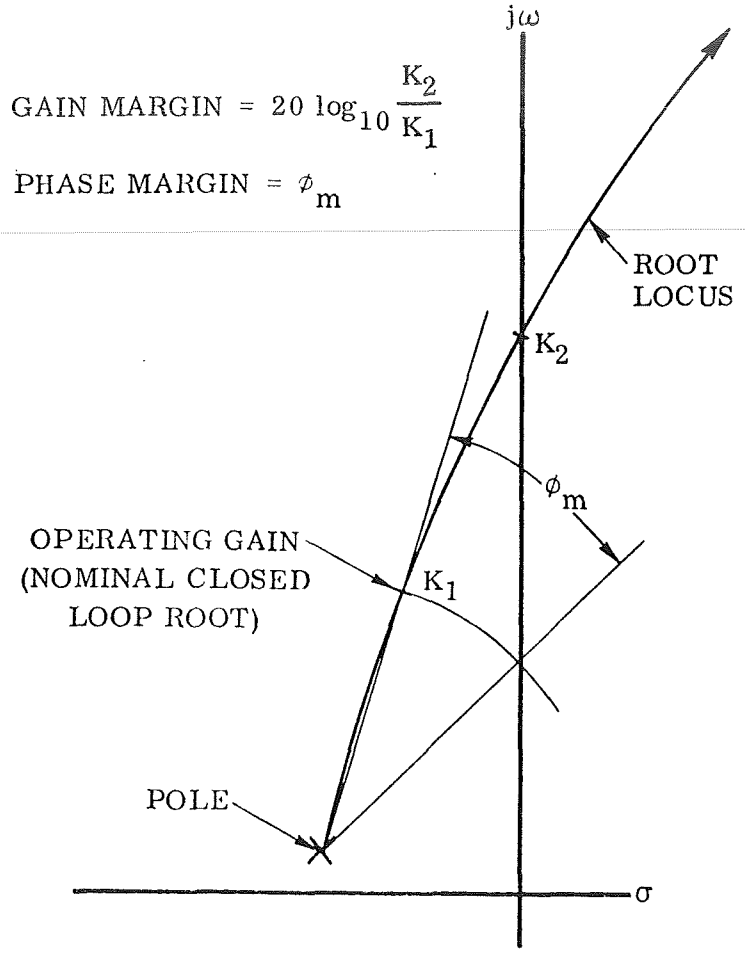

Figure E3. Gain and Phase Margin, Root Locus Interpretation

ratio between the gain at the point where the locus crosses the axis and the gain at the operating point (in decibels):

$$\text{Gain Margin} = 20 \log_{10} \frac{K_2}{K_1} \tag{E5}$$

Time and Frequency Response

The root locus technique is fundamentally a means of locating the roots of the characteristic equation. Its chief virtue is the display of these roots as functions of various system parameters. But most important are the system response properties to command or disturbance inputs, both inferred from the location of the open-loop

system poles and zeros. The s-plane diagram of these poles and zeros serves as a graphical means for determining the time and frequency response of the system.

The transfer function of a system can be represented by

$$T(s) = \frac{K \prod_{i=1}^{m} (s - z_i)}{\prod_{j=1}^{n} (s - p_j)} \tag{E6}$$

The input can be a command, a disturbance, or a test input; the output is the variable whose response is of interest. Consider the frequency response obtained by substituting $j\omega$ for s,

$$T(j\omega) = \frac{K \prod_{i=1}^{m} (j\omega - z_i)}{\prod_{j=1}^{n} (j\omega - p_j)}$$

$$= |T(j\omega)| e^{j \operatorname{Arg} T(j\omega)} \tag{E7}$$

This may be evaluated graphically from the s-plane plot of the poles and zeros for any desired ω by picking a point on the positive $j\omega$ axis corresponding to the desired frequency and measuring off distances to all the poles and zeros and their respective phase angles according to

$$|T(j\omega)| = \frac{K \prod_{i=1}^{m} |j\omega - z_i|}{\prod_{j=1}^{n} |j\omega - p_j|}$$

$$\operatorname{Arg} T(j\omega) = \sum_{i=1}^{m} \operatorname{Arg} (j\omega - z_i) - \sum_{j=1}^{n} \operatorname{Arg} (j\omega - p_j) \tag{E8}$$

where the angles are measured at the poles and zeros counterclockwise from the 3 o'clock position to the $j\omega$ point on the $j\omega$ axis.

Consider the transform of the time response to an input, C(s).

$$C(s) = R(s)\,T(s)$$

$$= \frac{K \prod_{i=1}^{m} (s - z_i)}{\prod_{j=1}^{n} (s - p_j)} R(s) \qquad \text{(E9)}$$

If R(s) is in closed form having only first-order poles (this excludes ramp inputs, for example) at frequencies different from the system poles, the response may be evaluated from an s-plane plot of the poles and zeros of C(s). C(s) may then be represented by:

$$C(s) = \frac{K' \prod_{i=1}^{k} (s - z_i)}{\prod_{j=1}^{\ell} (s - p_j)} \qquad \text{(E10)}$$

where the indices k and ℓ (rather than m and n) indicate additional poles and zeros in C(s) due to R(s). C(s) has the partial fraction expansion,

$$C(s) = \sum_{j=1}^{\ell} \frac{A_j}{(s - p_j)} \qquad \text{(E11)}$$

where the p^{th} residue is

$$A_p = (s - p_p)\,C(s)\Big|_{s=p_p}$$

$$= |A_p|\, e^{j\phi} \qquad \text{(E12)}$$

That is,

$$\left.\begin{aligned} |A_p| &= K' \prod_{i=1}^{k} |p_p - z_i| \Big/ \prod_{\substack{j=1 \\ j\neq p}}^{\ell} |p_p - p_j| \\ \phi &= \sum_{i=1}^{k} \text{Arg}\,(p_p - z_i) - \sum_{\substack{j=1 \\ j\neq p}}^{\ell} \text{Arg}\,(p_p - p_j) \end{aligned}\right\} \qquad \text{(E13)}$$

In short, the residue at the p^{th} pole of C (s) is determined by measuring the distance and angles as before from the s-plane plot. The time response is given by

$$C(t) = \sum_{j=1}^{\ell} A_j e^{p_j t} \qquad \text{(E14)}$$

If some of the poles are complex, the residues appear in complex conjugate pairs. Suppose there are poles at $p_1 = (\sigma_1 + j\omega_1)$ and $p_2 = (\sigma_1 - j\omega_1)$ with residues $A_1 e^{j\phi}$ and $A_1 e^{-j\phi}$. The corresponding contribution to the time response C (t) is

$$C_1(t) = 2 A_1 e^{\sigma_1 t} \cos(\omega_1 t + \phi) \qquad \text{(E15)}$$

The corresponding time functions may be graphically added to give the overall time response.

REFERENCES

1. Dodge, F. T., and Garza, L. R.: Propellant Dynamics in an Aircraft Type Launch Vehicle. NASA report by Southwest Research Institute, July 1971. Contract NAS8-25920.

2. Lomen, D.O.: Digital Analysis of Liquid Propellant Sloshing in Mobile Tanks with Rotational Symmetry. NASA CR-61540, 1968.

3. Gieseke, R. K.: Modal Analysis of the Mated Space Shuttle Configuration, NASTRAN User's Colloquim, NASA Langley Research Center, NASA TMX-2378, Volume I, September 1971. Paper No. 14.

4. D'Azzo, J. J., and Houpis, C. H.: Feedback Control System Analysis and Synthesis, 2nd Edition, McGraw-Hill Book Company, New York, 1966.

5. Truxal, J.G.: Automatic Feedback Control System Synthesis, McGraw-Hill Book Company, New York, 1955.

Unclassified

Security Classification

DOCUMENT CONTROL DATA - R & D

(Security classification of title, body of abstract and indexing annotation must be entered when the overall report is classified)

1. ORIGINATING ACTIVITY *(Corporate author)*	2a. REPORT SECURITY CLASSIFICATION
Convair Aerospace Division of General Dynamics San Diego, California	Unclassified
	2b. GROUP

3. REPORT TITLE

Influence of Vibration Modes on Control System Stabilization for Space Shuttle Type Vehicles

4. DESCRIPTIVE NOTES *(Type of report and inclusive dates)*

Final

5. AUTHOR(S) *(First name, middle initial, last name)*

Herbert G. Greiner

6. REPORT DATE	7a. TOTAL NO. OF PAGES	7b. NO. OF REFS
November 1972	189	5

8a. CONTRACT OR GRANT NO.	9a. ORIGINATOR'S REPORT NUMBER(S)
NAS1-10795	GDCA-DDE72-005
b. PROJECT NO.	
c.	9b. OTHER REPORT NO(S) *(Any other numbers that may be assigned this report)*
d.	NASA CR-112202

10. DISTRIBUTION STATEMENT

Distribution of this document is unlimited

11. SUPPLEMENTARY NOTES	12. SPONSORING MILITARY ACTIVITY
	None

13. ABSTRACT

The influence of the vibration modes on the vehicle control system stabilization problem is examined with a conventional, non-adaptive, single rate sensor autopilot. Two different piggy-back space shuttle configurations are considered. In one the booster and orbiter are independent vehicles, each with complete fly-back capability. In the other only the orbiter vehicle has fly-back capability and the booster consists of two strap-on solid motors. The linear stability analyses are based on symmetric and antisymmetric modal data that was generated primarily from flexible beam models. The principal control system variables considered are the effective autopilot rate and attitude gains, rate and attitude sensor locations and lead/lag stability compensation.

The frequency density of the elastic vehicle modes within the control system bandwidth greatly complicate the autopilot stability compensation requirements. For the strap-on solid motor vehicle additional complications are introduced by the high modal gain, the location of the tail-wags-dog frequency relative to the modal frequencies, and the high degree of elastic coupling between the vehicle elements through the links that join these elements together. Results indicate that for this particular vehicle a multiple sensor autopilot configuration will be necessary to achieve satisfactory vibration mode stability margins.

DD FORM 1 NOV 65 1473

Unclassified

Security Classification

14. KEY WORDS	LINK A		LINK B		LINK C	
	ROLE	WT	ROLE	WT	ROLE	WT